

CHEMICAL AND PHYSICAL STUDIES OF SECONDARY ORGANIC
AEROSOL FORMED FROM β -PINENE PHOTOOXIDATION

MEHRNAZ SARRAFZADEH

A DISSERTATION SUBMITTED TO THE FACULTY OF GRADUATE
STUDIES IN PARTIAL FULFILMENT OF THE REQUIREMENTS
FOR THE DEGREE OF
DOCTOR OF PHILOSOPHY

GRADUATE PROGRAM IN CHEMISTRY
YORK UNIVERSITY
TORONTO, ONTARIO

January 2017

© Mehrnaz Sarrafzadeh, 2017

Abstract

Atmospheric organic aerosols have a significant impact on climate and human health. However, our understanding of the physical and chemical properties of these aerosols is inadequate, thus their climate and health influences are poorly constrained. In this study, we investigated the secondary organic aerosol (SOA) formation from OH-initiated oxidation of β -pinene which has seldom been investigated. The majority of experiments were conducted in the York University smog chamber. The main objective was to identify the gas and particle phase products with an atmospheric pressure chemical ionization mass spectrometer (APCI-MS/MS). A wide variety of products were identified containing various functional groups including alcohol, aldehyde, carboxylic acid, ketone and nitrate.

Following the chemical composition characterization of products, the shape, phase state and density of generated particles were determined. Images from a scanning electron microscope (SEM) revealed that SOA particles from β -pinene were commonly spherical in shape, and adopted an amorphous semi-solid/liquid state. Additionally, the density was determined for SOA particles generated from reactions of β -pinene with OH radicals and reactions of nopinone with OH and NO_3 radicals for the first time using a tapered element oscillating microbalance-scanning mobility particle sizer (TEOM-SMPS) method. Our results showed a correlation between the determined particle density and the particle chemical composition of the respective system. This demonstrates that changes in particle density can be indicative of the changes in chemical composition of particles. We also investigated the chemical aging of oxidation products by exposing them to additional OH radicals or ozone. The observed changes in chemical composition of products and additional SOA mass production during OH-induced aging were attributed to further oxidation of gas phase intermediate products.

The NO_x dependence of SOA formation from β -pinene photooxidation was investigated in the York University smog chamber and the Jülich Plant Atmosphere Chamber (JPAC). Consistent with previous NO_x studies, SOA yields increased with increasing $[\text{NO}_x]$ at low- NO_x conditions, whereas increasing $[\text{NO}_x]$ at high- NO_x conditions suppressed the SOA yield. This increase was attributed to an increase of OH concentration. After removing the effect of $[\text{OH}]$ on SOA yield in the JPAC, SOA yields only decreased with increasing $[\text{NO}_x]$. Finally, the formation mechanisms of identified products were probed based on the information acquired throughout our study.

Acknowledgements

I would like to acknowledge all those who have helped and supported me during my PhD studies, without whom the completion of this dissertation was not possible. First and foremost I would like to thank my supervisor Prof. Donald Hastie for his support, guidance and patience throughout my PhD journey. I owe my growth, personal and intellectual, to his leadership and directions along the way.

I would also like to thank my supervisory committee Prof. Harris, Prof. Morin and Prof. Rudolph for their helpful suggestions and continuous support over the years. And thank you to my examination committee, Prof. Rudolph, Prof. Morin, Prof. Gordon, and Prof. Kahan for their valuable comments and suggestions on this dissertation. My sincere appreciation to Nick Karellas and the Ministry of the Environment for their support and the use of the API 365 mass spectrometer, TEOM and SMPS instruments. Additionally, I would like to thank Greg Koyanagi for his assistance and guidance with the mass spectrometer.

I would like to express my sincere gratitude to Prof. Astrid Kiendler-Scharr and Dr. Jürgen Wildt for giving me the opportunity to work at Forschungszentrum Jülich. I found this collaboration a highly rewarding experience. Additionally, I would like to thank all the people I worked with in Jülich for their support; Monika Springer, Iida Pullinen, Cheng Wu, Einhard Kleist, Thomas Mentel, Ralf Tillmann, Sebastian Schmitt, Defeng Zhao and Patrick Schlag.

My sincere thanks go to numerous colleagues, who have helped and supported me in a number of ways through the course of my PhD; Zoya Dobrusin, Dana Aljawhary, Marina Saccon, Amanda Jameer, Julie Bennett and Janeen Auld. And all the past and current members of the Centre for Atmospheric Chemistry (CAC), especially Carol Weldon for all of her efforts and assistance.

I would like to thank my husband Arta, who always believed in me and wanted the best for me. He always supported and motivated me over the years, particularly during the writing phase of this dissertation. I am also thankful to my sister for her support during the frustrating days and for all the fun times we spent together during our PhDs. I owe my parents the deepest gratitude; for their unconditional support and love throughout my studies and life. They emphasized the importance of education and they always encouraged and inspired me to follow my dreams. I am grateful to them for always reminding me to enjoy my PhD journey and not become so focused on the destination.

I dedicate this dissertation to my wonderful parents.

Statement of Collaboration

A portion of the research described in this Dissertation (Section 3.3.2) was part of a collaboration with Prof. Astrid Kiendler-Scharr and Dr. Jürgen Wildt from the Institute for Energy and Climate Research (IEK-8) and the Institute of Bio- and Geosciences (IBG-2) at Forschungszentrum Jülich, Germany. These materials have already been published in the ACP journal (Sarrafzadeh et al., 2016).

Table of Contents

Abstract	ii
Acknowledgements	iii
Statement of Collaboration	iv
Table of Contents	v
List of Tables	ix
List of Figures	x
List of Abbreviations	xx
1. Introduction	1
1.1. Atmospheric Aerosols.....	1
1.1.1. SOA Formation and Partitioning	3
1.1.2. SOA Yield.....	4
1.2. Laboratory Studies	6
1.2.1. SOA Chemical Composition	6
1.2.2. SOA Physical Properties.....	10
1.2.3. Impact of Various Parameters on SOA Formation	12
1.3. Objectives of This Study.....	15
2. Experimental	18
2.1. Methods and Experimental Set-up.....	18
2.1.1. York University Smog Chamber	18
2.1.1.1 Experimental Procedure	18
2.1.1.2 General Instrumentation	21
2.1.1.3 Sampling Methods.....	23
2.1.2. Jülich Plant Atmosphere Chamber (JPAC)	26
2.1.2.1 Experimental Procedure	28
2.1.2.2 General Instrumentation	30
2.1.2.3 Uncertainties.....	31

2.2.	Measurement of SOA Properties	32
2.2.1.	Particle Size Distribution and Particle Mass.....	32
2.2.1.1	Instrument Theory, Operation and Analysis	32
2.2.1.2	Particle Mass Correction	35
2.2.2.	Particle Density	38
2.2.2.1	Instrument Theory and Measurement Principles.....	38
2.2.2.2	Evaluation of the TEOM-SMPS System.....	40
2.2.3.	Particle Morphology	42
2.2.4.	SOA Chemical Composition	44
2.2.4.1	Principle of APCI-MS/MS	44
2.2.4.1.1.	APCI Ion Source.....	44
2.2.4.1.2.	Quadrupole Mass Analyzer	46
2.2.4.2	Principle of DART-TOF-MS	49
3.	Results and Discussion	51
3.1.	Physical Nature of Particles	51
3.1.1.	Particle Morphology and Phase State	51
3.1.2.	Particle Density.....	60
3.1.2.1	Determination of SOA Density from β -pinene Oxidation by OH.....	60
3.1.2.2	Determination of SOA Density from Nopinone Oxidation by OH.....	63
3.1.2.3	Determination of SOA Density from Nopinone Oxidation by NO_3	65
3.2.	Chemical Composition of Oxidation Products	69
3.2.1.	Gas Phase Products from β -pinene/OH	72
3.2.2.	Particle Phase Products from β -pinene/OH	76
3.2.2.1	Online Analysis	76
3.2.2.2	Offline Analysis.....	86
3.2.3.	Oxidation Product Formation Profiles	90
3.2.4.	Identification of Nopinone Oxidation Products.....	92
3.2.4.1	Nopinone Oxidation by OH.....	92

3.2.4.2	Nopinone Oxidation by NO ₃	98
3.3.	Impact of NO _x on SOA Yield and Composition.....	101
3.3.1.	York University	101
3.3.1.1	Impact of NO _x on SOA Formation	101
3.3.1.2	NO _x Sensitivity of Identified Products	108
3.3.2.	Jülich Plant Atmosphere Chamber (JPAC)	113
3.3.2.1	Impact of NO _x on SOA Formation	113
3.3.2.2	[OH] Dependence of SOA Formation	117
3.3.2.3	Isolate the Effect of [OH] on SOA Formation	119
3.3.2.4	Impact of NO _x on SOA Formation in the Presence of Seed Aerosol... ..	121
3.3.2.5	Role of RO ₂ Chemistry and NO/NO ₂ Ratio in SOA Formation	125
3.4.	Impact of Chemical Aging on SOA.....	129
3.4.1.	SOA Chemical Composition	129
3.4.1.1	OH-induced Aging	129
3.4.1.2	Ozone-induced Aging.....	141
3.4.2.	SOA Mass Formation	143
3.4.2.1	OH-induced Aging	143
3.4.2.1.1.	Source of Additional SOA Formation during Aging	145
3.4.2.2	Ozone-induced Aging.....	149
3.4.3.	SOA Density	151
3.4.3.1	OH-induced Aging	151
3.5.	Mechanism of Formation of Identified Products.....	155
3.5.1.	Nopinone.....	155
3.5.2.	Hydroxyl and Carbonyl Containing Products.....	157
3.5.3.	Carboxylic Acid Products	162
3.5.4.	Organic Nitrate Products	167
4.	Conclusions and Future Directions.....	171
4.1	Conclusions.....	171

4.1.1.	Chemical Composition	171
4.1.2.	Physical Properties.....	172
4.1.3.	Chemical Aging	173
4.1.4.	[NO _x] and [OH] Dependence of SOA Formation.....	174
4.1.5.	Formation Mechanisms.....	177
4.2	Future Directions	177
Bibliography		181
Appendices.....		199
Appendix A. Dilution Correction		199
Appendix B. Determination of J(O¹D).....		200
Appendix C. Nitrate Radical (NO₃) Concentration Modelling.....		203
Appendix D. Summary of Identified Reaction Products.....		204
Appendix E. Potential Products for m/z 187		210

List of Tables

Table 2.1 Summary of the particle density measurements for (NH ₄) ₂ SO ₄	42
Table 3.1 Summary of the density measurements for β-pinene SOA particles.....	62
Table 3.2 Summary of reported α- and β-Pinene SOA density.....	63
Table 3.3 Summary of the SMPS-TEOM measurements for nopinone/OH generated SOA.	65
Table 3.4 Summary of the SMPS-TEOM measurements for nopinone/NO ₃ generated SOA.	66
Table 3.5 Possible molecular formulas for β-pinene oxidation products for the m/z 169 product ion (measured accurate mass of 169.087 u). These molecular formulas are established for singly protonated molecular species. Mass errors are expressed in both terms of millimass units (mmu) and parts per million (ppm).....	88
Table 3.6 Experimental conditions and results for β-pinene/NO _x photooxidation experiments conducted in the York University smog chamber.....	102
Table 3.7 Experimental conditions and results for β-pinene/NO _x photooxidation experiments.....	116
Table 3.8 Experimental conditions and results for β-pinene photooxidation experiments at two OH levels.....	118
Table 3.9 Experimental conditions and results for OH-induced β-pinene aging experiments.	131
Table D.1 Summary of the molecular formula, m/z, functional groups, structure and NO _x sensitivity of identified products in the gas and particle phase. The exact masses as well as the confirmed molecular formula based on the exact mass for particle phase products are written in blue. The products that are indicated by * exist predominantly in the particle phase.	204
Table E.1 List of potential products for the m/z 187, obtained from the Master Chemical Mechanism (MCM).....	210

List of Figures

Figure 1.1 The structure of β -pinene.	15
Figure 2.1 Schematic diagram of the counter flow membrane denuder (CFMD) used for gas/particle separation, adapted from Bennett et al. (2009). The arrows indicate the direction of the air flows and the diffusion of the trace gases.	25
Figure 2.2 The effect of the in-line heater temperature on the signal of a few particle phase products formed from β -pinene photooxidation.	26
Figure 2.3 Time profiles of particle volume and mass concentrations evolution in the smog chamber for a $(\text{NH}_4)_2\text{SO}_4$ experiment. The particle density was calculated by taking the ratio between the particle mass and volume concentrations ($\rho = 1.75 \pm 0.08 \text{ g cm}^{-3}$).	41
Figure 2.4 SEM images of “clean” filters; (a) quartz fiber which is made up of quartz fibers of different diameters and (b) polycarbonate membrane filter, which contains $0.2 \mu\text{m}$ pores.	43
Figure 2.5 Schematic representation of the triple quadrupole analyzer.	47
Figure 3.1 SEM image of $(\text{NH}_4)_2\text{SO}_4$ seed particles collected on a polycarbonate membrane filter ($0.2 \mu\text{m}$ pore size). Note that the black holes are the filter pores and the white spheres are the $(\text{NH}_4)_2\text{SO}_4$ seed particles.	52
Figure 3.2 Size distribution of $(\text{NH}_4)_2\text{SO}_4$ seed particles measured during sample collection (every 5 minutes). The size distribution does not vary much over time ($< 5\%$ in mode diameter).	52
Figure 3.3 SEM image of SOA particles generated from β -pinene photooxidation collected on a polycarbonate membrane filter. Three selected regions identified by red circles, were magnified. Some particles in these regions appeared to be either a mixture of two phases or entirely liquid phase.	54
Figure 3.4 Size distributions of SOA particles generated from β -pinene photooxidation measured during the sample collection. The black curve is the size distribution of the $(\text{NH}_4)_2\text{SO}_4$ seed particles ($t=0 \text{ min}$) and the blue curves are the size distributions of SOA particles measured every 5 minutes, demonstrating the particle growth over time.	55

Figure 3.5 SEM images of SOA particles generated from β -pinene photooxidation collected on a polycarbonate membrane filter after aging. The magnified images at the bottom show the clogged pores upon focusing the beam on them and the agglomeration of two or more particles.....	56
Figure 3.6 Size distributions of SOA particles generated from β -pinene photooxidation measured during the sample collection. The black, blue and red curves are the size distribution of seed particles (t=0 mins), SOA particles before initiating aging and SOA particles upon aging respectively. This demonstrates the increase in particle number and size during aging.	57
Figure 3.7 SEM images of aged SOA particles generated from β -pinene photooxidation collected on a quartz filter.	58
Figure 3.8 Drops of n-hexadecane deposited on the quartz filter observed by SEM (Sutter et al., 2010).	59
Figure 3.9 Time profiles of particle volume and mass concentrations evolution in the smog chamber for one of the β -pinene photooxidation experiments. The particle density time series is also presented here. Time zero indicates the initiation of OH exposure (lights on). The average particle density after t=30 min was determined as $1.19 \pm 0.05 \text{ g cm}^{-3}$	61
Figure 3.10 Time profiles of particle volume and mass concentrations evolution as well as particle density in the smog chamber for one of the nopinone photooxidation experiments. Time zero indicates the initiation of OH exposure (lights on). The average particle density was determined as $1.20 \pm 0.07 \text{ g cm}^{-3}$	64
Figure 3.11 Time profiles of particle volume and mass concentrations evolution as well as particle density in the smog chamber for one of the nopinone + NO_3 experiments. The average particle density was $1.40 \pm 0.03 \text{ g cm}^{-3}$	67
Figure 3.12 Full mass spectrum of oxidation products formed from β -pinene photooxidation (400 ppb NO) in the gas phase. m/z 37 and 55 correspond to water cluster reagent ions. ...	73
Figure 3.13 Comparison of (+)MS/MS spectra of the target ion m/z 139 from A. a β -pinene/OH experiment in the gas phase and B. the nopinone standard. Both spectra were acquired at collision energy of 10 eV.	74

Figure 3.14 (+)MS/MS spectrum of target ion m/z 157 from β -pinene/OH experiment in the gas phase.	75
Figure 3.15 Potential β -pinene oxidation product structures with molar mass 156 g mol^{-1} .75	
Figure 3.16 Full mass spectrum of particle phase oxidation products formed from β -pinene photooxidation (400 ppb NO), obtained with the APCI-MS/MS. m/z 37 and 55 correspond to water cluster reagent ions.	78
Figure 3.17 (+)MS/MS spectrum of target ion m/z 169 from β -pinene/OH experiment in the particle phase.	78
Figure 3.18 Potential β -pinene oxidation product structures with molar mass 168 g mol^{-1}	79
Figure 3.19 Comparison of (+)MS/MS spectra of the target ion m/z 187 from A. a β -pinene/OH experiment in the particle phase and B. the pinic acid standard. Both spectra were acquired at collision energy of 10 eV.	80
Figure 3.20 Proposed fragmentation pathways for deprotonated pinic acid, adopted from Yasmeeen et al. (2010).	82
Figure 3.21 Proposed fragmentation pathways for deprotonated homoterpenylic acid, adopted from Yasmeeen et al. (2010).	82
Figure 3.22 Comparison of (-)MS/MS spectra of the target ion m/z 185 from A. a β -pinene/OH experiment in the particle phase and B. the pinic acid standard. Both spectra were acquired at collision energy of 10 eV.	83
Figure 3.23 (+)MS/MS spectrum of target ion m/z 246 from β -pinene/OH experiment in the particle phase.	84
Figure 3.24 Proposed organic nitrate product with molar mass 245 g mol^{-1} in the MCM. .	86
Figure 3.25 Full mass spectrum of oxidation products in the positive ion mode formed from β -pinene photooxidation (400 ppb NO) in the particle phase, obtained with the DART-TOF-MS.	87
Figure 3.26 SRM time profiles for the ion pairs 137→81 (black circles) and 139→121 (blue squares) representing β -pinene and nopinone respectively, during the A. gas phase and B. particle phase β -pinene experiments. The initial NO concentrations were 0.7 ppm and 0.4	

ppm for the gas and particle phase experiments, respectively. These profiles include the mixing time of the experiments before the lights were turned on and time zero indicates the initiation of OH exposure (lights on).....	91
Figure 3.27 β -pinene experiment SRM time profiles for the ion pairs A. 139 \rightarrow 121, 157 \rightarrow 121, 157 \rightarrow 139 and B. 157 \rightarrow 111 showing the formation of m/z 139 and m/z 157 products. It has been identified that some additional products contribute to the target ion m/z 157 besides nopinone's water cluster.	92
Figure 3.28 The structure of nopinone, primary product of β -pinene oxidation.	93
Figure 3.29 Full mass spectrum of oxidation products formed from nopinone photooxidation in the particle phase.	94
Figure 3.30 Comparison of (+)MS/MS spectra of the target ion m/z 201 from A. a β -pinene/OH experiment in the particle phase and B. a nopinone/OH experiment in the particle phase. Both spectra were acquired at collision energy of 10 eV.	96
Figure 3.31 Proposed C ₉ -organic nitrate product with molar mass of 245 g mol ⁻¹ in the MCM.....	96
Figure 3.32 Nopinone experiment SRM time profiles for the ion pairs A. 216 \rightarrow 152 and 216 \rightarrow 170, B. 214 \rightarrow 168, C. 232 \rightarrow 151 and D. 218 \rightarrow 200 and 218 \rightarrow 154. These profiles demonstrate low signal intensities for these organic nitrates, as well as the decay of their signal intensities due to possibly further reaction with OH radicals.	98
Figure 3.33 Full mass spectrum of oxidation products formed from nopinone oxidation with NO ₃ in the particle phase. The MS spectrum is subtracted from that of the chamber background.....	100
Figure 3.34 Measured SOA yield for the β -pinene photooxidation as a function of the initial NO _x concentration. Each point corresponds to one experiment.	102
Figure 3.35 Measured OH concentration during β -pinene photooxidation experiments as a function of initial NO _x concentration ([NO _x] ₀).....	104
Figure 3.36 β -pinene decay profile (A) and organic particle mass formation as a function of reacted β -pinene (B) over the course of β -pinene photooxidation experiments under different NO _x conditions. Each curve represents a single experiment. Here, lower-NO _x conditions	

($[\text{NO}_x]_0 < 0.2$ ppm), moderate- NO_x conditions ($0.2 < [\text{NO}_x]_0 < 1$ ppm) and higher- NO_x conditions ($[\text{NO}_x]_0 > 1$ ppm) were plotted in green, blue and red, respectively. 106

Figure 3.37 SRM time profiles for the ion pairs 139→121 representing nopinone during particle phase β -pinene experiments under varied NO_x conditions. Time zero indicates the initiation of OH exposure (lights on). 107

Figure 3.38 SRM time profiles for the ion pairs 173→127, 187→141 and 201→155 representing the norpinic acid, pinic acid and C10-hydroxy pinonic acid respectively, acquired at varied NO_x levels. These profiles demonstrated to be dependent on NO_x level. 110

Figure 3.39 SRM time profiles for the ion pairs 216→152, 218→200, 232→151 and 246→200 representing the C10-bicyclic hydroxy nitrate, C10-monocyclic hydroxy nitrate, C10-dihydroxy nitrate and C10-PAN respectively, acquired at varied NO_x levels..... 112

Figure 3.40 Measured SOA yield from PM_{max} (black circles) and rates of new particle formation (blue squares) for the β -pinene photooxidation as a function of the ratio of the initial hydrocarbon to the initial NO_x concentration and as a function of the initial NO_x concentration. Each point corresponds to one experiment. The errors in nucleation rate and $[\text{NO}_x]$ were estimated to be $\pm 10\%$. The error in SOA yield was estimated from error propagation using the sum of the systematic error, correction procedure error and error in BVOC data. Note that the horizontal error bars are associated with the BVOC/ NO_x axis. 114

Figure 3.41 Measured SOA yield from PM_{max} and from steady state PM (black and blue circles respectively) and measured OH concentration (red squares) as a function of initial ($[\text{NO}_x]_0$) and steady state ($[\text{NO}_x]_{\text{ss}}$) NO_x concentrations. The errors in $[\text{OH}]$ and $[\text{NO}_x]$ were estimated to be $\pm 20\%$ and $\pm 10\%$ respectively. The error in SOA yield was estimated from error propagation using the sum of the systematic error, correction procedure error and error in BVOC data..... 115

Figure 3.42 Total aerosol mass concentration as a function of the amount of reacted β -pinene under low- $[\text{OH}]$ (blue open circles) and high- $[\text{OH}]$ (red open squares) conditions. The SOA yield was estimated from the aerosol mass linear regression slope as a function of consumed

β -pinene, which resulted in approximately 20 ± 1 % and 31 ± 3 % for low- and high-OH conditions respectively. The error in [consumed β -pinene] was estimated to be ± 10 % and the error in particle mass was estimated from the sum of the systematic error and the correction procedure error. 119

Figure 3.43 Comparison of [OH] before (black squares) and after (blue squares) adjusting OH concentration during steady state in NO_x experiments. The errors in [OH] and [NO_x] were estimated to be ± 20 % and ± 10 % respectively. 120

Figure 3.44 Comparison of SOA yield before (black circles) and after (blue circles) adjusting OH concentration during steady state in NO_x experiments. The error in [NO_x] was estimated to be ± 10 % and the error in SOA yield was estimated from error propagation using the sum of the systematic error, correction procedure error and error in BVOC data. 121

Figure 3.45 Comparison of measured particle mass and particle number concentration after adjusting [OH] as a function of [NO_x] during steady state in the absence of seed aerosol. The error in particle number concentration was estimated to be ± 10 %..... 122

Figure 3.46 Comparison of SOA yield before (black circles) and after (blue circles) adjusting OH concentration during steady state in NO_x experiments performed in the presence of seed aerosol. The error in [NO_x] was estimated to be ± 10 % and the error in SOA yield was estimated from error propagation using the sum of the systematic error, correction procedure error and error in BVOC data. 123

Figure 3.47 Comparison of [OH] before (black squares) and after (blue squares) adjusting OH concentration during steady state in NO_x experiments performed under lower [NO]/[NO_2] ratio. The errors in [OH] and [NO_x] were estimated to be ± 20 % and ± 10 % respectively. 126

Figure 3.48 Comparison of SOA yield before (black circles) and after (blue circles) adjusting OH concentration during steady state in NO_x experiments performed under lower [NO]/[NO_2] ratio. The error in [NO_x] was estimated to be ± 10 % and the error in SOA yield was estimated from error propagation using the sum of the systematic error, correction procedure error and error in BVOC data. 127

Figure 3.49 MS scans of β -pinene photooxidation experiment in the particle phase during A. the reagent mixing period, B. two hours following initiation of the reaction (β -pinene+OH), and C. after aging ((β -pinene+OH)+OH, after approximately 6 hours). 132

Figure 3.50 SRM time profiles for the ion pairs 137→81 (green circles) and 139→121 (blue diamonds) representing β -pinene and nopinone respectively, during OH induced β -pinene aging experiment. The vertical red lines indicate the time at which the OH exposure started. 133

Figure 3.51 SRM time profiles for the ion pair 139→121 in the gas phase (green circles) and particle phase (blue diamonds) during OH induced β -pinene aging experiment. The vertical red lines indicate the time at which the OH exposure started..... 134

A detailed description of a few categories of compounds will be given here to illustrate the differences in their behaviour during aging. 134

Figure 3.52 SRM time profiles for A. hydroxy nopinone (155→109) and B. oxo-nopinone (153→111). The gas and particle phases are distinguished using green and blue markers, respectively. The vertical red lines indicate the time at which the OH exposure started. . 135

Figure 3.53 SRM time profiles for the ion pairs A. 171→125, B. 173→127 and C. 187→141, representing pinalic 3-acid (or pinalic 4-acid), norpinic acid and pinic acid respectively. The gas and particle phase are distinguished using green and blue symbols respectively. The vertical red lines indicate the time at which the OH exposure started..... 137

Figure 3.54 SRM time profiles for the ion pairs A. 214→168, B. 216→152 and C. 232→151, representing C10-aldehyde nitrate, C10-bicyclic hydroxy nitrate and C10-dihydroxy nitrate respectively. The gas and particle phase are distinguished using green and blue symbols respectively. The vertical red lines indicate the time at which the OH exposure started. . 139

Figure 3.55 SRM time profiles for the ion pairs A. 200→168 and B. 246→200, representing nitroxy nopinone and C10-PAN respectively. The gas and particle phase are distinguished using green and blue symbols respectively. The vertical red lines indicate the time at which the OH exposure started..... 140

Figure 3.56 SRM time profiles for the particle phase β -pinene and nopinone during β -pinene O_3 -induced aging experiment. The O_3 addition time after β -pinene depletion is shown by red vertical lines and O_3 levels are marked by arrows for each addition.....	142
Figure 3.57 SRM time profile for nopinone during nopinone/ O_3 experiment. The O_3 addition time is shown by red vertical lines and the overall O_3 levels are marked by arrows for each addition.	142
Figure 3.58 Particle size distribution during β -pinene OH-induced aging. The black dashed line (0 minutes) shows the time before β -pinene+OH reaction started and the blue solid lines represent the particle growth while oxidizing β -pinene. The black dashed line (Aging-175 minutes) shows the time before initiating the aging and the red solid lines demonstrate particle growth during aging.....	144
Figure 3.59 Time profile of organic particulate mass concentration during β -pinene OH-induced aging experiment ($NO_x \sim 1$ ppm). The vertical red lines indicate the initiation of OH exposure (lights on).	145
Figure 3.60 SRM time profiles for the β -pinene (green circles), nopinone (blue diamonds) during β -pinene OH-induced aging experiment and nopinone (purple triangles) during nopinone photooxidation experiment.	148
Figure 3.61 Comparison of the organic particulate mass concentration evolution from a β -pinene OH-induced aging experiment (blue diamonds) and three nopinone photooxidation experiments (purple triangles).	148
Figure 3.62 Particle size distribution during β -pinene O_3 -induced aging. The black dashed line (0 minutes) shows the time before β -pinene+ O_3 reaction started and the blue solid lines represent the particle growth while oxidizing β -pinene. The black dashed line (Aging-340 minutes) demonstrates the time before starting aging and the red solid lines show particle size distributions during aging.	149
Figure 3.63 Time profile of organic particulate mass concentration during β -pinene O_3 -induced aging experiment. The O_3 addition time is shown by red vertical lines and the overall O_3 levels are marked by arrows for each addition.	150

Figure 3.64 The time evolution of SOA volume, number and mass concentrations as well as SOA density in the smog chamber. Dashed grey and red lines indicate the time of the second IPN injection in the dark and turning on the UV lights, respectively. SOA density before and after aging were $1.20 \pm 0.04 \text{ g cm}^{-3}$ and $1.19 \pm 0.04 \text{ g cm}^{-3}$, respectively.....	152
Figure 3.65 A schematic of the proposed mechanistic pathways to nopinone through OH-initiated oxidation of β -pinene, compiled from the MCM.....	156
Figure 3.66 Structures of hydroxyl and carbonyl containing products identified during OH-initiated oxidation of β -pinene in this study.	158
Figure 3.67 A schematic mechanism illustrating the formation pathway from β -pinene to the C10-dihydroxy carbonyl product. This mechanism has not been incorporated in the MCM, although it is presented by Davis et al. (2005).	159
Figure 3.68 A schematic mechanism illustrating formation pathways from nopinone to hydroxy nopinone, oxo-nopinone, and hydroxy oxo-nopinone products, compiled from the MCM.....	161
Figure 3.69 Structures of carboxylic acid products identified during OH-initiated oxidation of β -pinene in this study.....	162
Figure 3.70 A schematic mechanism illustrating formation pathways from nopinone to a number of carbocyclic acid products (norpinalic acid, C8-keto acid, pinalic 3-acid, pinalic 4-acid, norpinic acid and pinic acid) identified in this study. These mechanisms are compiled from the MCM, Larsen et al. (2001) and Jaoui and Kamens (2003).....	164
Figure 3.71 A schematic mechanism illustrating formation pathways from β -pinene to the C10-hydroxy pinonic acid (MCM; Jaoui and Kamens (2003)).....	165
Figure 3.72 A schematic mechanism illustrating formation pathway from β -pinene to homoterpenylic acid (Yasmeen et al., 2010).	166
Figure 3.73 Structures of organic nitrate products identified during OH-initiated oxidation of β -pinene in this study.....	167
Figure 3.74 A schematic mechanism illustrating formation pathways from β -pinene to a number of organic nitrates (C10-dihydroxy nitrate, C10-bicyclic hydroxy nitrate, C10-aldehyde nitrate and C10-PAN) identified in this study.....	169

Figure 3.75 A schematic mechanism illustrating formation pathway from nopinone to nitroxy nopinone. 170

List of Abbreviations

APCI	atmospheric pressure chemical ionization
APM	aerosol particle mass analyzer
CCN	cloud condensation nuclei
CE	collision energy
CFMD	counter flow membrane denuder
CIMS	chemical ionization mass spectrometry
CPC	condensation particle counter
DART	direct analysis in real time
DMA	differential mobility analyzer
ELVOC	extremely low volatile organic compound
FID	flame ionization detector
GC	gas chromatography
IPN	isopropyl nitrite
JPAC	Jülich plant atmosphere chamber
LC	liquid chromatography
MCM	master chemical mechanism
MS	mass spectrometry
MS/MS	tandem mass spectrometry
m/z	mass to charge ratio
NO _x	sum of nitric oxide and nitrogen dioxide
NPF	new particle formation
OM	organic material
PAN	peroxyacyl nitrate
PM	particulate matter
POA	primary organic aerosol
PTR-MS	proton transfer reaction mass spectrometry
SEM	scanning electron microscope
SMPS	scanning mobility particle sizer
SOA	secondary organic aerosol
SRM	selected reaction monitoring
TEOM	tapered element oscillating microbalance
TOF	time of flight
UV	ultraviolet
VOC	volatile organic compound

1. Introduction

1.1. Atmospheric Aerosols

Atmospheric particular matter (PM), liquid or solid particles suspended in air, plays a key role in global climate and many environmental processes. The direct climate effect of PM involves scattering and absorption of solar radiation, resulting in reduced visibility as well as alteration of the earth's radiation budget (Jacob, 1999; Bauer et al., 2012). These aerosols also influence the climate indirectly by acting as cloud condensation nuclei (CCN) which alters clouds formation and properties (e.g. cloud albedo, lifetime) (Twomey et al., 1984; Finlayson-Pitts and Pitts 2000). PM has been also linked to have an adverse impact on human health as it has been found that exposure to fine particular matter (PM_{2.5}) is associated with cardiovascular and respiratory diseases and mortality (Harrison and Yin, 2000; Davidson et al., 2005; Pope and Dockery, 2006; Miller et al., 2007; Mauderly and Chow, 2008; Brook et al., 2010). A better understanding of the true impact of atmospheric PM on climate and health requires more detailed information of their sources, properties, chemical composition and mechanisms of formation.

PM can be classified into two categories; primary PM and secondary PM. Primary PM is directly emitted into the atmosphere such as wind-driven suspension of soil, dust or sea salt. In contrast, secondary PM results from reactions and the subsequent nucleation of gaseous species, which is called new particle formation (NPF), or through the condensation of gases onto existing particles. In case of organic PM, primary particles are emitted directly into the

atmosphere from sources such as biomass burning, combustion of fossil fuels and volcanic eruptions which is referred to as primary organic aerosol (POA) (Hallquist et al., 2009). However, secondary organic PM is formed in the atmosphere by the nucleation or condensation of the oxidation products formed from volatile organic compounds (VOC), which is referred to secondary organic aerosol (SOA).

VOCs are classified into two groups based on their emission sources; anthropogenic VOCs and biogenic VOCs (BVOC). Anthropogenic sources include vehicle exhaust, industrial emissions, fuel combustion and human-induced biomass burning, while exclusively biogenic (natural) emission sources include vegetation, soil microbes and the oceans. Large quantities of VOCs are emitted into the atmosphere from vegetation globally. At a global level, the biogenic VOC emissions exceed those of anthropogenic VOCs. BVOC emissions were estimated as 1150 Tg C yr⁻¹ (Guenther et al., 1995), whereas the total global anthropogenic non-methane VOC emissions were approximately 150 Tg C yr⁻¹ (Müller, 1992). One of the major BVOC groups is monoterpenes which are emitted mainly by forest vegetation. Monoterpenes consist of two isoprene units and have the molecular formula C₁₀H₁₆. The blue haze that surrounds forested areas is associated with the emission of monoterpenes and their subsequent SOA formation.

In the atmosphere, VOCs undergo oxidation by oxidants such as O₃, hydroxyl (OH) radicals and nitrate (NO₃) radicals, resulting in the formation of a diverse range of organic products. These reaction products can vary in volatility; volatile products remain in the gas phase, low volatility products go into the particle phase and semivolatiles partition between the gas and

particle phases. The low volatility and semivolatile products can produce new particles or condense onto existing particles, both resulting in an increase in mass concentration of PM (Pankow, 1994; Odum et al., 1996; Seinfeld and Pandis, 2003). Thus, SOA is composed predominantly of low volatility and semivolatile organics.

1.1.1. SOA Formation and Partitioning

The SOA formation can be described in terms of gas/particle partitioning. Partitioning of semivolatile organic compounds demonstrates how much of a gas phase compound can be absorbed and become incorporated into the particle phase. The gas/particle partitioning at equilibrium is described by a partitioning coefficient ($K_{p,i}$) for absorptive uptake into the particle phase, developed by Pankow (1994). The $K_{p,i}$ gives a measure of the ability of a compound i to remain in the particle phase in equilibrium with the gas phase (Eq. 1.1)

$$K_{p,i} = \frac{C_i (ng/\mu g)_{particle\ phase}}{C_i (ng/m^3)_{gas\ phase}} = \frac{F_i}{TSP} = \frac{760RTf_{om}}{10^6 MW_{om} \gamma_i P_{L,i}^o} \quad (1.1)$$

Where F_i ($ng\ m^{-3}$) is the mass concentration of the semivolatile compound i in the organic material (OM) particle phase, TSP ($\mu g\ m^{-3}$) is the mass concentration of the total suspended PM, A_i ($ng\ m^{-3}$) is the mass concentration of the semivolatile compound i in the gas phase, R is the ideal gas constant ($8.2 \times 10^{-5}\ m^3\ atm\ mol^{-1}\ K^{-1}$), T (K) is temperature, f_{om} is the mass weight fraction of the absorbing OM phase present in the TSP, MW_{om} ($g\ mol^{-1}$) is the average molecular weight of the absorbing OM phase, γ_i is the activity coefficient of the

compound i in the particle phase and $P_{L,i}^o$ (Torr) is the compound's vapor pressure as a pure liquid at the temperature of interest.

Equation 1.1. shows that the partitioning coefficient $K_{p,i}$ ($\text{m}^3 \mu\text{g}^{-1}$) is inversely proportional to the saturation vapor pressure of the pure semivolatile compound. Therefore, compounds with higher vapor pressures have smaller partitioning coefficients, contributing less to the particulate mass, while compounds with lower vapor pressures and thus higher partitioning coefficients will enhance particle formation.

1.1.2. SOA Yield

The SOA formation potentials of VOC species are represented by SOA mass yields (Y), which are generally defined as the ratio of the SOA mass concentration produced (ΔM) from the oxidation of the SOA precursor to the mass of the precursor consumed (ΔVOC) ($Y = \Delta M / \Delta \text{VOC}$) (Odum et al., 1996).

Comparison of atmospheric models with field and laboratory measurements have shown that SOA mass is often significantly under predicted by models (Heald et al., 2005; Morris et al., 2005; Volkamer et al., 2006; Yu et al., 2008). This underestimation points to the limited understanding of SOA chemical composition, properties and formation pathways. Identification and quantification of oxidation products is very difficult due to the diversity and complexity of oxidation products and their formation pathways. Thus, the specific composition and formation pathways of these products remain poorly known. Therefore, comprehensive laboratory studies of SOA formation are required to gain additional insight

into chemical composition, properties and formation pathways of the oxidation products to improve the current atmospheric models.

Additionally, uncertainties in measured SOA yields influence the accuracy of model predictions as SOA formation rates used in atmospheric models are generally based on SOA yields derived from chamber measurements. Despite the fact that many laboratory studies have focused on the production of SOA from a number of VOCs (e.g. Toluene, m-xylene and monoterpenes such as α -pinene, β -pinene), reported SOA yields have shown high variability for a given precursor (Pandis et al., 1991; Hoffmann et al., 1997; Griffin et al., 1999; Larsen et al., 2001; Presto et al., 2005; Song et al., 2005; Kroll et al., 2006; Ng et al., 2007a; Mentel et al., 2009; Eddingsaas et al., 2012a). For instance, reported SOA mass yield from α -pinene photooxidation ranges from 8 to 37 % (Eddingsaas et al., 2012a). This variability points to the numerous factors that can influence the partitioning of semivolatile compounds and thus the SOA yields, such as the inorganic and organic mass loading, particle acidity, concentration of the oxidants, NO_x ($\text{NO}_x = \text{NO} + \text{NO}_2$) level, humidity, and temperature. This continues to show that ambient SOA yields cannot be represented by a unique value for a given VOC as the yields are heavily dependent on the conditions under which the SOA is formed. Therefore, the detailed characterization of the impact of different parameters on SOA yields must be implemented into atmospheric models.

1.2. Laboratory Studies

Laboratory studies are a requirement for a detailed understanding of formation, chemical composition, properties and transformation of SOA. These studies must be sufficiently extensive that their results can be extrapolated to the real atmosphere and incorporated into atmospheric models.

1.2.1. SOA Chemical Composition

Investigating the composition of organic products generated from oxidation of hydrocarbons, requires detection and identification of the oxidation products. Several techniques have been developed for the identification (and sometimes quantification) of organic compounds present in ambient air or those produced in laboratory studies. These measurement techniques are carried out either offline or online.

Offline measurement techniques involve the collection of the samples, followed by sample treatment and preparation and then analyses. Gas phase samples are usually collected using cartridges (Ligocki and Pankow, 1985) or denuders (Edney et al., 2003) by adsorbing the products onto a coated surface, whereas particle samples are generally collected onto filters or impactor plates. These samples are then recovered by thermal desorption or chemical extraction using solvents. Although offline techniques have the advantage of pre-concentrating the samples when products are low in concentration, there are also several drawbacks. Offline techniques require long sampling times and may introduce artefacts during the processing of samples. In addition, collected products on a surface have the

tendency to evaporate, undergo reaction (e.g. with oxidants in the gas phase) or decompose (e.g. during thermal desorption). In online measurement techniques, samples are introduced directly into the analysis system reducing the chance of sample contamination, modification or loss. Additionally, online techniques allow measurement of the chemical compositions of the individual species present in SOA simultaneously and in real time. Online gas and particle separation can be carried out by either placing a filter in line to remove particles from the sample flow to analyze gas phase products, or using a denuder to remove trace gases from the sample flow to acquire particles. Two types of denuder can be used for particle analysis. One is a denuder with absorbent surfaces such as charcoal, where gases that have much higher diffusion coefficient than particles diffuse to the surfaces, while particles pass through the denuder. The use of these denuders, however, is limited in laboratory studies with high gas and particle concentrations as they get saturated fairly quickly and need to be regenerated or replaced. The other type is a membrane diffusion denuder that uses a membrane to separate gases from particles. In this type of denuder, gases diffuse from the sample into a clean air flow or a liquid flow. Membrane denuders remove gases nonselectively and also they are not subjected to surface saturation.

After sample collection and preparation or gas/particle separation, a number of instruments can be used for analysis and identification of oxidation products. Mass spectrometry (MS) is one of the analytical techniques that is most commonly used for identification of unknown compounds. Combination of the mass spectrometric technique with chromatographic techniques such as gas chromatography (GC) and liquid chromatography (LC) enables

separation of a number of compounds as well as their identification. GC-MS and LC-MS have been used extensively in offline methods for identification and quantification of compounds (Forstner et al., 1997; Kleindienst et al., 1999; Larsen et al. 2001; Jaoui and Kamens, 2003). However, these techniques require long collection times to obtain sufficient amounts of sample, resulting in low time resolution.

Online gas/particle separation coupled with mass spectrometry is an ideal online technique for composition analysis of products. MS techniques offer high sensitivity and selectivity. Some of the most commonly used mass spectrometric techniques for the composition analysis of VOC and SOA are aerosol mass spectrometry (AMS), chemical ionization mass spectrometry (CIMS), proton transfer reaction mass spectrometry (PTR-MS) and atmospheric pressure chemical ionization mass spectrometry (APCI-MS).

AMS has been particularly widely used to quantitatively characterize the size-resolved composition of PM. AMS provides mass concentration analysis of species by thermal vaporization of aerosol components (typically at 600 °C) followed by 70-eV electron-impact ionization (EI). Produced sample ions are then analyzed with either a quadrupole (Q), time-of-flight (TOF) or high-resolution (HR)-TOF mass analyzer (Jayne et al., 2000; DeCarlo et al. 2006). AMS provides quantitative mass concentrations of the chemical species present in the bulk particles including ammonium, nitrate, sulfate, chloride and total organics. However, this technique is not suitable for identification of individual molecular species due to the hard EI ionization, which is a highly energetic form of ionization and results in excessive fragmentation.

CIMS has been widely used for atmospheric trace gases measurements and recently has been applied to investigate atmospheric particles (Thornton et al., 2003; Thornton and Abbatt, 2005; Aljawhary et al., 2013). Chemical ionization is a relatively soft ionization technique and therefore does not cause fragmentation of the analyte ions. This results in molecular ions to remain largely intact, allowing molecular weight information to be obtained. The major advantage of the CIMS is the ability to use multiple reagent ions for the chemical ionization. The choice of reagent ion allows detecting a class of compounds with a high degree of sensitivity. The common reagent ions used in CIMS instruments are protonated water clusters ($(\text{H}_2\text{O})_n\text{H}^+$), acetate (CH_3CO^-), iodide water clusters ($\text{I}(\text{H}_2\text{O})_n^-$) and nitrate (NO_3^-). CIMS instruments have been mainly used with the quadrupole mass analyzer and more recently with the high resolution time-of-flight (HR-TOF) to better resolve the organic composition.

Both PTR-MS and APCI-MS can be used for identification of oxidation products which provide individual compound characterization (Wisthaler et al., 2001; Lee et al., 2006). PTR and APCI are soft chemical ionization techniques. Samples are usually ionized by proton transfer reactions, producing $(\text{M}+\text{H})^+$ ions. PTR is often coupled with a single quadrupole and TOF mass analyzers (Blake et al., 2009), whereas APCI is commonly used with triple quadrupole and ion trap mass analyzers (Aschmann et al., 1998; Hoffmann et al., 2002; Warscheid et al., 2003). One of the drawbacks of PTR-MS with a single quadrupole is that identification of compounds is limited to the molecular mass of the protonated product ion. Tandem mass spectrometry in APCI technique allows fragmentation of a specified ion which

produces a mass spectrum of its fragment ions (MS/MS). This helps with structural elucidation of the target ion. In this study, APCI-MS/MS system has been mainly used to analyze products of β -pinene oxidation.

1.2.2. SOA Physical Properties

To better understand the influences of aerosols in the atmosphere, knowledge is required not only on their chemical composition but also on their physical properties such as particle shape, phase and density.

Atmospheric aerosol particles may occur as liquid, semi-solid or solid. By definition the viscosity of the liquids is $\leq 10^2$ Pa s, viscosity of the semi-solids ranging from 10^2 Pa s to 10^{12} Pa s, and solids typically have viscosities $\geq 10^{12}$ Pa s. Depending on viscosity, the semi-solid amorphous state may be classified as rubbery, gel-like or ultra-viscous liquids (Mikhailov et al., 2009). Knowledge of the shape and phase state of aerosol particles is crucial since it can influence atmospheric processes such as heterogeneous chemistry, gas/particle partitioning, chemical transformation and aging as well as their light scattering and absorption properties. Until recently, it has been assumed that organic particles formed in the atmosphere are liquids based on gas/particle partitioning theory (Pankow, 1994). Some recent studies have shown that highly mixed organic/inorganic aerosols are in a liquid-like phase even at low relative humidities (Cappa et al. 2008; Mikhailov et al., 2009). However, Virtanen et al. (2010) showed that biogenic SOA particles can adopt an amorphous solid state (most probably glassy state) by investigating particles bounce behaviour. The work by

Renbaum-Wolff et al. (2013) has also shown that based on the measured particle viscosity, particles produced by α -pinene ozonolysis range from liquid to semi-solid or solid over a range of relative humidities. Furthermore, studies on particles morphology have reported different shapes for atmospheric particles (i.e., spheres, aggregates, and irregular shapes) (Dye et al., 2000; Xiong and Friedlander, 2001; Okada and Heintzenberg, 2003). This shows that current knowledge of the shape and phase of aerosols is still highly uncertain. Therefore, it would be beneficial to perform more detailed studies to better characterize the morphology of aerosol particles.

Aerosol density can be an important parameter for characterizing the particles formed. Monitoring the density of SOA particles over the course of experiments or during ambient measurements can improve our understanding of changes in particle composition that are occurring. In addition, to calculate SOA mass yield from the SOA volume data requires knowledge of the SOA density. Early chamber studies estimated particle mass concentration assuming an aerosol density of 1 g cm^{-3} due to absence of density measurements. However, the density associated with the SOA particles produced in different systems vary widely. The SOA density have been estimated to range from 0.6 g cm^{-3} to 1.6 g cm^{-3} in recent studies (Kalberer et al., 2000; Bahreini et al. 2005; Surratt et al. 2006; Kostenidou et al. 2007; Zelenyuk et al. 2008; Malloy et al., 2009).

Several techniques have been developed in the past to estimate aerosol particle density. Early density measurements were based on detailed chemical speciation of the SOA particles, independent of particle mass and volume (Forstner et al., 1997; Kalberer et al., 2000; Rogge

et al., 1993). However, due to the complexity of aerosol composition only a small fraction of the compounds in particle phase can be identified and quantified which makes this method less practical. More recently, densities of SOA were measured using a scanning mobility particle sizer and an aerosol mass spectrometer (SMPS-AMS). In this method the density is derived by comparing the mass distribution and volume distribution of particles measured from an AMS and a SMPS respectively (DeCarlo et al. 2004). Furthermore, Wirtz and Martin-Reviejo (2003) determined the density of aerosols by combining a tapered element oscillating microbalance (TEOM) and a SMPS to obtain the mass concentration and volume of particles, respectively. Another recent technique for particle density measurements was introduced by McMurry et al. (2002), where particle volume is integrated from a SMPS and mass concentration is obtained utilizing an aerosol particle mass analyzer (APM). The technique used in this project to measure particles density was the SMPS-TEOM.

1.2.3. Impact of Various Parameters on SOA Formation

The high degree of variability in SOA yields measured from a number of VOCs suggests that SOA yield is highly sensitive to the reaction conditions. There are several parameters that contribute to the observed variations such as temperature, relative humidity (RH), particle acidity, oxidant level (e.g. OH concentration) and NO_x level.

Temperature influences SOA yields mainly by altering the gas/particle partitioning and phase equilibrium of semivolatile products as the partitioning coefficient is dependent on temperature (Eq. 1.1). Apart from the temperature term in Eq. 1.1, vapor pressure is highly

dependent on temperature (Sheehan and Bowman, 2001; Jenkin, 2004; Saathoff et al., 2009). Relative humidity may affect oxidation products by influencing the amount of liquid water in the particles, potentially resulting in heterogeneous reactions of water-soluble organic compounds and changes in gas/particle partitioning of products. The effect of particle acidity on SOA formation is mainly due to acid-catalyzed reactions in the particle phase which may enhance the reactive uptake of particle phase organics (Jang et al., 2003; Garland et al., 2006; Liggio and Li, 2006).

Oxidant level may influence the chemical reactions of intermediate products, thus reflecting the oxidative aging of the oxidation products and may affect the SOA yields. During oxidative aging, organic products can undergo further oxidation which could influence their chemical and physical properties (e.g. density, chemical composition, toxicity). Proposed pathways for the oxidative aging of SOA include: 1) further oxidation of gas phase semivolatile products that condense into the particle phase (Robinson et al., 2007); 2) particle phase semivolatile products evaporates to the gas phase, get oxidized and re-condense back into the particle phase (Qi et al., 2010); 3) oxidation of particle phase organics via heterogeneous reactive uptake of gas phase oxidants such as O_3 , OH and NO_3 (Ellison et al., 1999); 4) further oxidation of organic semivolatile monomers in the SOA particles to form oligomers (Rudich, 2003). Therefore, concentration of oxidants can play a role in the chemical aging of SOA. Understanding the oxidative aging mechanisms that SOA undergo in the atmosphere and incorporating such knowledge into atmospheric models is crucial for better prediction of models.

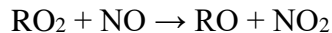
One of the critical factors that results in variation in SOA yields appears to be the impact of NO_x on SOA formation. Over the past few decades, numerous studies have been investigating the influence of NO_x level on the SOA production for a variety of compounds and it has been shown that NO_x has a significant influence on the formation of SOA. For larger VOCs, such as sesquiterpenes, SOA yields increase with increasing NO_x (Ng et al., 2007a), whereas the photooxidation and ozonolysis of monoterpenes, benzene, toluene, and m-xylene have demonstrated that SOA yields are higher under low- NO_x conditions (Hatakeyama et al., 1991; Kroll et al., 2006; Presto et al., 2005; Song et al., 2005; Ng et al., 2007a,b; Chan et al., 2010). It is generally assumed that the impact of NO_x results from altering the balance between competing peroxy-radical (RO_2) reactions and thus from the changes in the distribution of secondary reactions.

Under low- NO_x conditions, the reaction of RO_2 radicals with HO_2 (Reaction R1.1) is the dominant pathway, which leads to the formation of low volatility hydroperoxides that can participate in NPF and contribute to SOA mass (Johnson et al., 2005; Camredon et al., 2007).



Under high- NO_x conditions, RO_2 radicals react with NO resulting in the formation of organic nitrates (Reaction R1.2a) or alkoxy radicals (Reaction R1.2b) that either fragment, or react to form more volatile products. This implies that higher NO_x concentrations will suppress the formation of low volatility products, and thereby suppress NPF and SOA mass formation.



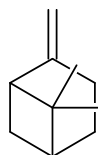


R1.2b

All these factors (e.g. temperature, RH, oxidant level and NO_x level) show that the high degree of variability in measured SOA yields can be related to different factors. Thus it would be valuable to investigate the impact of each parameter on SOA formation for individual VOCs.

1.3. Objectives of This Study

In this study, a series of chamber experiments have been conducted to investigate the chemical and physical properties of oxidation products formed from β -pinene photooxidation. β -pinene is the second most abundant monoterpene compound, which contains a single exocyclic double bond (Fig. 1.1).



β -pinene
 $\text{C}_{10}\text{H}_{16}$
(M136)

Figure 1.1 The structure of β -pinene.

The double bond makes β -pinene highly reactive in the atmosphere, reacting with OH radicals, NO_3 radicals and ozone with an atmospheric lifetime in the order of a few hours.

The primary objective of this study was to investigate the chemical composition of β -pinene photooxidation products in both gas and particle phases. Although the identification of

products formed from β -pinene oxidation has been studied before, a significant fraction particularly in the particle phase is yet to be identified (Aschmann et al., 1998, Larsen et al., 2001, Jaoui and Kamens, 2003). In addition, the detailed chemical mechanisms of SOA production from β -pinene remain uncertain, due to the extreme complexity of the reaction systems. Thus improved knowledge of the composition of organic products can be used to gain some insights into their formation pathways. In this work, gas and particle phase products were generated from OH-initiated oxidation of β -pinene in the York University smog chamber, followed by APCI-MS/MS analysis to identify the unknown compounds in the mixture.

Since the current knowledge of the SOA's physical properties (e.g. morphology, density) is limited, we also aimed to investigate the physical properties of the oxidation products formed from β -pinene oxidation. We explored the shape and phase state of generated particles using scanning electron microscopy (SEM) as well as measuring the SOA density using the TEOM-SMPS system. Determination of the SOA density is beneficial to produce more accurate SOA yield estimates for β -pinene since no density measurements have yet been taken for β -pinene photooxidation particles. Additionally, monitoring the density of SOA particles over the course of experiments would allow us to improve our understanding in changes in particle composition that may occur. Consistency in changes in the measured particle density over time with the results of the APCI-MS/MS, could demonstrate that monitoring particle density is a valuable technique to gain insight into particles composition changes.

This study also examined the chemical aging processes of oxidation products produced from the photooxidation of β -pinene to investigate the extent of further oxidation with OH radicals or O_3 in both condensed and gas phases. The objective was to examine whether aging induced by OH radicals or O_3 can alter the chemical composition and physical properties of products or influence the organic particulate mass concentration generated from β -pinene photooxidation.

One of the other goals of this study was to explore the impact of NO_x on SOA formation from β -pinene photooxidation under varied NO_x levels. Understanding the NO_x sensitivity of products is important since the NO_x level is variable between rural and urban areas. In this study, the NO_x dependence of SOA formation from β -pinene photooxidation was comprehensively investigated in the York University smog chamber as well as the Jülich Plant Atmosphere Chamber (JPAC) to gain more insight into the impact of NO_x on SOA yield and to better characterize the mechanisms leading to effects of NO_x on SOA yield.

In this dissertation, the instruments used in this study are presented in detail in Chapter 2 and the results achieved from each research project are discussed in Chapter 3. Lastly, Chapter 4 provides a summary of the study, general conclusions and potential future research directions.

2. Experimental

2.1. Methods and Experimental Set-up

The York University smog chamber and Jülich Plant Atmosphere Chamber (JPAC) were used for the studies discussed in this dissertation, and are described in detail in the following Sections.

2.1.1. York University Smog Chamber

The York University smog chamber has been used for an extensive study of the chemical composition of products from β -pinene photooxidation, impact of aging and NO_x on products formation as well as determining the density and phase state of particles. The smog chamber is described in detail elsewhere (Auld and Hastie, 2009). In short, the chamber consists of a cylindrical 8 m^3 Teflon bag with Teflon coated circular endplates. The outside is a mobile frame backed by a Mylar reflector, containing 24 UV lights (Philips F40BL, 40 Watt) which have a radiation range of 350 - 400 nm. Reagents are injected at one end where an internal large fan rotates to enhance mixing and samples are taken at the other end. Temperature and relative humidity (RH) were typically $\sim 22 - 26^\circ\text{C}$ and $<10 \%$ in the chamber.

2.1.1.1 Experimental Procedure

Prior to each experiment, the chamber was flushed with purified air from an Aadco clean air generator (Aadco Instruments Inc., Cleves, OH) for at least 24 hours. Most oxidations were

initiated by OH radicals, where the reagents used include isopropyl nitrite (IPN, hydroxyl radical source synthesized in house according to the method used by Noyes (1936)), β -pinene or nopinone (Sigma Aldrich, > 99%), nitric oxide (NO, Linde) and ammonium sulfate ((NH₄)₂SO₄) seed particles.

Inorganic seed particles were introduced into the chamber to act as condensation sites onto which the generated semivolatile SOA may condense. For seeded experiments, (NH₄)₂SO₄ seed particles were generated from a 0.5 g L⁻¹ solution of (NH₄)₂SO₄ in water by a Collison nebulizer (BGI, Waltham, MA). The particles were then passed through a calcium sulfate drier and a Po-210 source before entering the chamber, to dry and neutralize the particles respectively. Neutralizing the particles prevents the highly charged particles from getting lost to the Teflon surfaces of the chamber. This resulted in average particle number concentration of $\sim 3.2 \times 10^4$ particles cm⁻³ and an average particle mass of $\sim 22 \mu\text{g cm}^{-3}$.

Once the seed stabilized (no more significant changes in particle growth), β -pinene (or nopinone), IPN and NO were introduced to the chamber through the injection ports and all reagents were allowed to mix in the dark for approximately one hour. Generally the initial reagent concentrations were: 0.1-0.4 ppm β -pinene (or nopinone), 0.1-0.4 ppm IPN and 0-2 ppm NO. Finally, the reaction was initiated by irradiating the chamber with the UV lights for IPN photolysis and OH radical formation (R2.1-2.3). The reaction mixture was typically analyzed for approximately 2-3 hours.





The photolysis of NO_2 produced from Reaction 2.3 results in ozone formation in the chamber (R2.4-2.5). Addition of NO into the system can suppress the ozone formation (R2.6). Since the initial NO concentration was varied between 0-2 ppm during our β -pinene experiments, minimal ozone interference is expected at low NO_x concentrations.



For ozonolysis experiments, the ozonized gas stream from the ozone generator was fed to the chamber after β -pinene was mixed in the presence of seed particles. Prior to introducing ozone to the chamber, the generated ozone was passed through a bypass line for a few minutes to ensure a constant level of ozone production. The initial ozone concentration was between 2 – 4 ppm.

To balance the sampling flow drawn by the instruments, purified air was continuously added to the chamber. Thus, a dilution correction (which was less than 2% in most cases) applied for all the quantitative results (the detail of the correction method is outlined in Appendix A).

2.1.1.2 General Instrumentation

A number of analytical instruments sampled from the chamber for the quantitative and qualitative analysis of the physical and chemical properties of the contents. NO concentrations were measured by chemiluminescence NO_x analyzer (TE Inc. Model 42S). Particle size distributions were measured between 8 and 700 nm using a scanning mobility particle sizer (SMPS; TSI 3071 DMA–TSI 3010 CPC or TSI 3081 DMA–TSI 3010 CPC). The measured size distributions were used to determine the SOA mass concentrations (details in Section 2.2.1), assuming homogeneous spherical particles and a density of 1.2 g m⁻³. The temperature and relative humidity of the chamber were continuously monitored before and during experiments using an Omegaette HH311 humidity and temperature meter (OMEGA, Laval, QC). For those experiments conducting with O₃ or NO₃ radicals as the oxidant, an ozone generator (Model GL-1; PCI Ozone Corp. West Caldwell, N.J.) and an ozone monitor (U.V. Photometric Ambient Ozone Analyzer Model 49) were used to produce and monitor ozone levels in the chamber, respectively. The β-pinene concentration was monitored by a Hewlett Packard (HP) 5890 gas chromatograph coupled to a flame ionization detector (GC-FID). The GC-FID was calibrated using a gravimetrically calibrated β-pinene permeation tube (VICI Valco Instruments Co. Inc.). The permeation tube was stored in a temperature controlled housing at 100°C. The permeation rate was determined by monitoring the mass loss of the permeation tube periodically. The average permeation rate was found to be 75 ± 5 ng min⁻¹. This permeation rate was applied to determine the β-pinene concentration released by the permeation housing. A constant flow of nitrogen (15 ml min⁻¹,

Linde, purity 99.999%) was used to sweep the emitted β -pinene from the housing which was further diluted with varied flow of Aadco air to produce a range of concentrations (20 – 100 ppb, 6 points) for the calibration of the GC-FID.

The average OH concentration was estimated from the initial decay profiles of β -pinene. Assuming a pseudo first order decay of β -pinene, a plot of $\ln[\beta\text{-pinene}]$ as a function of time results in a straight line for the first 30 minutes of the reaction with the slope of $k^{\text{OH}} [\text{OH}]$ (Eq. 2.1). Given the k^{OH} value ($k \sim 7.4 \times 10^{-11} \text{ cm}^3 \text{ s}^{-1}$) (Atkinson and Arey, 2003)), an estimated OH concentration could be determined for each experiment. Based on our β -pinene experimental conditions, the average OH concentration was found to be $\sim 4\text{-}9 \times 10^6 \text{ cm}^{-3}$ ($\sim 0.1\text{-}0.3 \text{ ppt}$), which is slightly more than daytime atmospheric OH concentrations ($\sim 1\text{-}2 \times 10^6 \text{ cm}^{-3}$, (Prinn et al., 2001; Mao et al., 2009)).

$$\frac{d[\beta p]}{dt} = -k^{\text{OH}} \cdot [\text{OH}] \cdot [\beta p] \quad (2.1)$$

Chemical composition of oxidation products was probed using a triple quadrupole mass spectrometer, coupled with an atmospheric pressure chemical ionization (APCI) ion source (APCI-MS/MS, MDS Sciex, Concord, ON, Canada). Particle phase products were also subjected to accurate-mass time-of-flight mass spectrometric analysis (AccuTOF-MS, JEOL USA, Peabody, MA) coupled with a direct analysis in real time (DART) ion source. The APCI-MS/MS and DART-TOF-MS will be described in detail in Section 2.2.4. More details on gas measurements with the NO_x analyzer and the GC-FID are provided in Auld (2009).

2.1.1.3 Sampling Methods

For gas phase analysis with the APCI-MS/MS, the reaction mixture was drawn from the chamber through 1/4" Teflon tubing at a flow rate of $\sim 2 \text{ L min}^{-1}$. This tubing was attached to a 2 cm diameter quartz glass tube where the reaction mixture was diluted with $\sim 2 \text{ L min}^{-1}$ purified Aadco air. The output of the glass tube was fed directly into the ion source.

In the previous study by Auld (2009), an in-line 25 mm diameter quartz fiber filter (PALL (Canada) Ltd, Toronto, ON) was placed in the sampling line to remove particles from the sample flow prior to gas phase analysis. In this study we found that using the filter in the sampling line caused time delays in the onset of a detectable signal increase over the course of the experiments. This indicates the adsorption of gas phase products onto the filter. When adsorption occurs, after a certain time the filter gets saturated and gases that adsorbed onto the filter start to pass through the filter and reach the ion source. Due to concerns of the filter interference in accurate time profiles measurements, the experiments were conducted with no filter in place. This raises the question of whether the evaporation of particulate phase products could contribute to the gas phase signal. On sampling, the gas particle mixture from the chamber is not perturbed (either by dilution or temperature changes) until it is diluted immediately before the ion source. Thus the time available for the particle phase to evaporate is extremely short (estimated as $< 6 \text{ sec}$) and it was therefore assumed that the particle phase products did not contribute significantly to the APCI-MS/MS signals of the gas phase products.

For online particle phase analysis, a counter flow membrane denuder (CFMD) was coupled to the smog chamber and the APCI-MS/MS. The CFMD is described in detail in Bennett et al. (2009). A schematic diagram of CFMD is shown in Fig. 2.1 and a summary is provided here. CFMD allows for online separation of gas phase products from particle phase products. The denuder consists of three aluminium channels (90 cm long and 10 cm wide) separated by membranes. The sample gas from the chamber which contains both gas and particle phase products is introduced into the center channel and purified Aadco air to the upper and lower channels in an opposite direction to the center channel. Since the flow in the centre channel is laminar, trace gases diffuse through the membrane into the outer Aadco air channel unlike particles, which cannot diffuse as quickly due to their higher inertia and therefore, remain in the center channel. The flow rates for the sample gas and Aadco air are as Bennett et al. (2009); 0.6 L min^{-1} for the centre channel and 6 L min^{-1} for the outer channels in order to have the trace gas signal in the center channel below detectable levels.

Particle phase products cannot be directly analyzed by the mass spectrometer, thus it is necessary to convert them to the gas phase before being introduced to the ion source of the mass spectrometer. Therefore, an in-line heated probe was placed after the denuder to volatilize particles. In order to find the optimum temperature in which particles have the significant evaporation with the limited molecular decomposition, the effect of temperature on the signal of a few particle phase products formed from β -pinene oxidation was investigated. As shown in Fig. 2.2, by increasing the in-line heater temperature from 50°C to 200°C , higher amount of particle compounds were evaporated resulting in higher signals

for most of the products. Although a few products (e.g. m/z 157 and 201) showed an increase in their signal at 250°C, the majority of the particle phase products almost stabilized. Therefore, temperature of 200°C was selected as a suitable heater set point for particle phase analysis since the majority of particle phase products could be analyzed. We avoided excessive heating (higher than 200°C) as it could cause some products to decompose which results in interferences of their fragments ions in the mass spectrum.

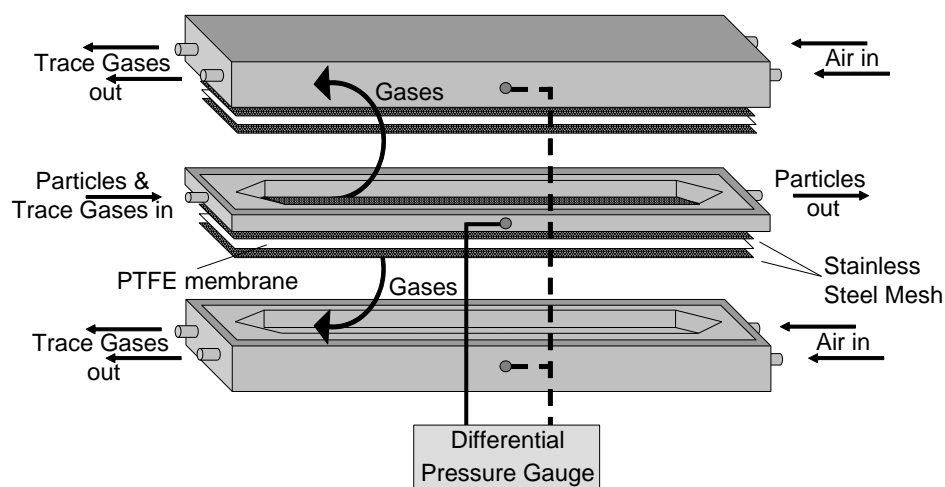


Figure 2.1 Schematic diagram of the counter flow membrane denuder (CFMD) used for gas/particle separation, adapted from Bennett et al. (2009). The arrows indicate the direction of the air flows and the diffusion of the trace gases.

For offline particle phase analysis, a sample of the reaction mixture was drawn from the chamber after the end of the reaction (when the aerosol mass reached a constant value) through a 25mm diameter quartz fibre filter at a sampling flow rate of 10 L min^{-1} for approximately 3 hours. The filter was then ultrasonically extracted with 5 ml acetonitrile (pesticide residue analysis grade from Sigma Aldrich). This was followed by filtration using

a syringe equipped with a 0.2 μm PTFE Chromspec filter. The solvent was then evaporated to dryness under a gentle stream of nitrogen. Finally, the residues were dissolved in ~ 1 mL dichloromethane ($\geq 99.5\%$) and analyzed by DART-TOF-MS.

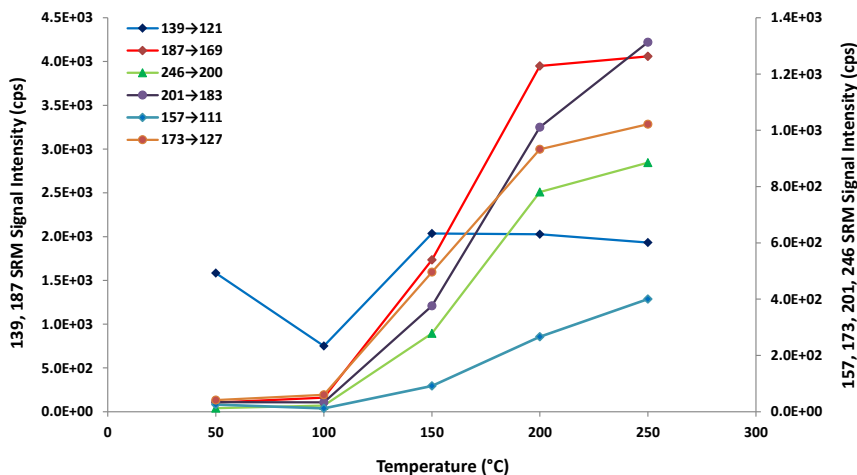


Figure 2.2 The effect of the in-line heater temperature on the signal of a few particle phase products formed from β -pinene photooxidation.

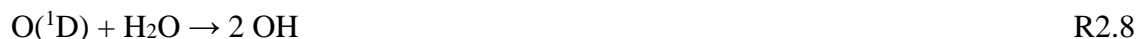
2.1.2. Jülich Plant Atmosphere Chamber (JPAC)

Similar to the York University chamber, the JPAC has been used to study OH-initiated oxidation of β -pinene, but with a different OH source and under a humid condition. The experimental setup of JPAC is described in detail elsewhere (Mentel et al., 2009, 2015). The chamber is 1450 liter in volume, made of borosilicate glass in a climate-controlled housing. The chamber was operated as a continuously stirred tank reactor (CSTR) with a residence time of approximately 46 min. A Teflon fan inside the chamber ensures good mixing. The

temperature and relative humidity inside the chamber were held at $16 \pm 1^\circ\text{C}$ and $63 \pm 2\%$, respectively over the course of the experiments.

The flow into the chamber consisted of two purified air streams. One stream was passed through an ozonator and was humidified with double distilled water. The other stream contained β -pinene emitted from a diffusion/permeation source held at 38°C . Where necessary seed particles could be generated externally and introduced using a third air stream. Air was purified by an adsorption drying device (KEA 70; Zander Aufbereitungstechnik GmbH & Co. KG, Essen, Germany) and by a palladium catalyst operating at 450°C . To increase the relative humidity of the air in the chamber to about 60%, water vapor was added by passing a part of the inflowing air through a water containing glass vessel.

The chamber was equipped with several lamps; 12 discharge lamps (metal halide lamps; HQI 400 W/D, Osram) to simulate the solar light spectrum in the chamber, 12 discharge lamps (Philips, TL 60 W/10-R, 9 60W, $\lambda_{\text{max}} = 365 \text{ nm}$, from here on termed UVA lamps according to the spectral distribution of their light) for NO_2 photolysis, and one internal UVC lamp (Philips, TUV 40W, $\lambda_{\text{max}} = 254 \text{ nm}$; here termed as TUV lamp) to produce OH radicals from ozone photolysis and subsequent reaction of water vapor with $\text{O}(^1\text{D})$ atoms (Reactions 2.7-2.8).



The TUV lamp could be shielded by glass tubes to control the amount of UV radiation entering the chamber. Thus by controlling the length of the lamp exposed, the OH production rate could be adjusted by varying the photolysis rate coefficient $J(O^1D)$. The detail of $J(O^1D)$ calculation is provided in Appendix B. It has to be noted that the short wavelength cut off of the glass vessel is around 350 nm and thus no light with wavelength short enough to produce O^1D is in the chamber when the TUV lamp is off. Furthermore, the absorption cross section of NO_2 at the wavelengths of the TUV lamp is more than an order of magnitude lower than at wavelengths around 365 nm (Davidson et al., 1988). Together with the lower energy of the TUV lamp compared to the UVA lamps, this allowed independent variation of $J(O^1D)$ and $J(NO_2)$.

2.1.2.1 Experimental Procedure

A series of β -pinene photooxidation experiments were performed in the JPAC to investigate the SOA formation under low- NO_x (here defined as $[NO_x]_0 < 30$ ppb, $[BVOC]_0 / [NO_x]_0 > 10$) and high- NO_x (here defined as $[NO_x]_0 > 30$ ppb, $[BVOC]_0 / [NO_x]_0 < 10$) conditions. In these experiments, the inflow of β -pinene (95 %, Aldrich) to the chamber was kept constant, leading to initial mixing ratios of 37 ± 0.6 ppb. The initial O_3 concentration was 40 ± 5 ppb. NO_2 (Linde, diluted from a 104 ± 3 ppm NO_2 in nitrogen cylinder) was introduced into the β -pinene air stream. Initial NO_x concentrations, $[NO_x]_0$, in the chamber were varied between < 1 and 146 ppb. The chamber was illuminated with one of the HQI lamps and all the UVA lamps, resulting in an NO_2 photolysis frequency ($J(NO_2)$) of $4.3 \times 10^{-3} s^{-1}$. When VOC, NO_x and O_3 concentrations in the chamber were near to steady state, the experiment was initiated

by turning on the TUV lamp resulting in OH radical production. During experiments a constant $J(\text{O}^1\text{D})$ was maintained. Experiments without NO_x addition were performed amongst NO_x experiments. In these cases, residual NO_x concentrations from chamber walls were below 1 ppb.

After initiating the OH production, β -pinene and NO_x concentrations decreased due to their reactions with OH radicals. The majority of the results presented in this study are from steady state measurements, when all physical and chemical parameters were constant in the chamber. However, for the purpose of comparison with the literature, the initial concentration of NO_x , $[\text{NO}_x]_0$, and β -pinene, $[\text{BVOC}]_0$, were also presented here.

To investigate the role of NO_x on SOA formation in the presence of inorganic aerosol, similar to York University experiments, β -pinene photooxidation/ NO_x experiments were repeated in the presence of seed aerosol. The seed particles were generated using a constant output aerosol generator (TSI, Model 3076) by atomizing $(\text{NH}_4)_2\text{SO}_4$ solutions (typical concentration $\sim 40 \text{ mg L}^{-1}$) at a pressure of around 1.4 bar. The generated aerosol then passed through a silica gel diffusion drier before entering the reaction chamber. In the control experiments, distilled water was used for atomization to keep the experimental conditions constant. For these experiments, the organic particle mass was determined by subtracting the initial seed aerosol mass from the total particle mass.

2.1.2.2 General Instrumentation

A suite of instruments were used for both gas and particle phase measurements. Ozone concentration was determined by UV photometric devices (Thermo Environmental 49 and Ansyco, O₃ 42M ozone analyzers), NO was measured by chemiluminescence (Eco Physics, CLD 770 AL ppt), NO₂ by chemiluminescence after photolysis (Eco Physics, PLC 760) and relative humidity was measured by a dew point mirror (TS-2, Walz). Furthermore, a condensation particle counter (CPC; TSI 3783) and a scanning mobility particle sizer (SMPS; combination of a TSI 3081 DMA and a TSI 3025 CPC) were used to count the total particle number greater than 3 nm and to measure the particle size distribution between 13 and 740 nm respectively. The total particle mass concentration was estimated from the measured total aerosol volume assuming spherical particles with a density of 1.2 g cm⁻³. The β-pinene mixing ratio in the chamber was determined by gas chromatography-mass spectrometry (GC-MS; Agilent GC-MSD system with HP6890 GC and 5973 MSD) or a proton transfer reaction mass spectrometer (PTR-MS; Ionicon). The GC-MS and PTR-MS were calibrated using a β-pinene diffusion/permeation source containing pure β-pinene in a vial in combination with a dynamic dilution system. The GC-MS and PTR-MS were switched periodically between the outlet and the inlet of the chamber to quantify concentrations of β-pinene entering and exiting the chamber. Equation (2.2) is the basic rate equation for a CSTR resulting from mass balance.

$$\frac{d[\beta p]}{dt} = \frac{F}{V} \cdot ([\beta p]_{in} - [\beta p]) - (k^{OH} \cdot [OH] + k^{O_3} \cdot [O_3]) \cdot [\beta p] \quad (2.2)$$

In Eq. (2.2), V is the volume of the chamber and F is the total air flow through the chamber. $[\beta p]_{in}$ and $[\beta p]$ are the concentrations of β -pinene in the inlet air and in the chamber respectively. For a well-mixed continuously stirred tank reactor, $[\beta p]$ is the concentration of β -pinene measured in the outlet flow. k^{OH} and k^{O_3} are the rate constants of reactions of β -pinene with OH and with O_3 . The OH concentration was calculated by recognizing that Eq. (2.2) results in Eq. (2.3) under steady state conditions.

$$[OH] = \frac{\frac{F}{V} \cdot \frac{[\beta p]_{in} - [\beta p]}{[\beta p]} - k^{O_3} \cdot [O_3]}{k^{OH}} \quad (2.3)$$

Since β -pinene has a relatively low rate constant with O_3 ($k^{O_3} = 1.5 \times 10^{-17} \text{ cm}^3 \text{ s}^{-1}$; Atkinson and Arey, 2003), the reaction of β -pinene with O_3 could be neglected from Eq. (2.3) for our ozone (50-100 ppb) and OH concentrations ($9 \times 10^6 - 1.6 \times 10^8 \text{ cm}^{-3}$). The uncertainty in OH concentration was estimated to be approximately 20% (Wildt et al., 2014).

2.1.2.3 Uncertainties

Error limits for the SOA yields were calculated from error propagation using the sum of the 10 % systematic (analytical) error for SMPS data and BVOC data and the error from the correction procedure. In the case of SOA yields plotted versus NO_x , we showed 10 % systematic (analytical) error for NO_x data (Figs. 3.41, 3.44, 3.46 and 3.48). Plotting [OH] versus NO_x we used 20 % error for [OH] (estimate of both statistical and systematic errors) and 10 % error for $[NO_x]$, respectively (Figs. 3.43 and 3.47). For the plot of particle mass versus β -pinene consumption (Fig. 3.42) we showed the error limits as estimated for particle

mass, i.e. sum of 10 % systematic error for SMPS data, error from the correction method and 10 % for the BVOC consumption. The error limits given in the text for the yields (in Fig. 3.42) represent the statistical error from the plot only. For the plot of particle number versus NO_x (Fig. 3.45) we showed 10 % systematic error for particle number and NO_x data. Considering that the ratio $[\text{BVOC}]_0/[\text{NO}_x]_0$ contains possible errors in both quantities, the error for $[\text{BVOC}]_0/[\text{NO}_x]_0$ was calculated according to error propagation (Fig. 3.40).

2.2. Measurement of SOA Properties

Here we focus on the physical and chemical properties of SOA. A comprehensive range of measurements were employed to investigate the chemical composition of the SOA formed from β -pinene as well as the SOA physical properties such as particle density and phase state. In the following Sections, a description of the measurement system and the instruments involved for these measurements will be provided.

2.2.1. Particle Size Distribution and Particle Mass

2.2.1.1 Instrument Theory, Operation and Analysis

Particle size distribution measurements are acquired by the SMPS and the measured size distributions are then used to estimate the particle mass concentration produced during an experiment. The SMPS consists of a differential mobility analyzer (DMA) and a condensation particle counter (CPC). The DMA separates particles according to their electrical mobility, which is a function of size and the CPC counts the particles.

Particles are drawn from the chamber to the DMA, charged by passing through a Kr-85 radioactive source and then separated based on their electrical mobility while traveling through the DMA. Electrical mobility (Z_p , $\text{cm}^2 \text{V}^{-1} \text{s}^{-1}$) is dependent on both the diameter and charge of the particle as shown in Eq. 2.4 (Seinfeld and Pandis, 2006; TSI, 2002).

$$Z_p = \frac{qC \times 10^7}{3\pi\mu D_p} \quad (2.4)$$

Where q is the charge on the particle in coulombs, C is the slip correction factor, μ is the gas viscosity in poise, D_p is the particle diameter in cm and the factor of 10^7 is included for the conversion of the units. As shown, the electrical mobility is proportional to the charge on particle and inversely proportional to the particle diameter.

Inside the DMA there are two concentric metal cylinders; the inner is held at a certain voltage and the outer is grounded, which creates an electric field within the annular space. A polydisperse aerosol flow (q_p) and a purified sheath air flow (q_s) are continuously flowing down the annular space between the cylinders in laminar streams. While positively charged particles traveling inside the DMA, they migrate towards the inner rod. Based on the voltage of the inner rod, only particles of a certain range in electrical mobility can exit through the monodisperse aerosol flow (q_m). Smaller particles with the higher mobility will impact the inner rod, whereas larger particles with the lower mobility will exit the DMA with the excess airflow. The monodisperse aerosol flow is then transferred to the CPC for particle counting. The mean electrical mobility of particles inside the DMA is proportional to the flows of the

DMA, dimension of the DMA and the voltage of the inner rod according to Equation 2.5 (DMA manual).

$$Z_p = \frac{(q_t - \frac{1}{2}(q_m + q_p)) \ln\left(\frac{r_2}{r_1}\right)}{2\pi VL} \quad (2.5)$$

Where q_t is total flow inside the DMA, q_m and q_p are the monodisperse and polydisperse aerosol flows respectively ($\text{cm}^3 \text{ s}^{-1}$), r_1 and r_2 are the inner and outer radii of the annular space (cm), V is the applied voltage on the inner rod (volts) and L is the length of the inner rod between the inlet of the polydisperse aerosol flow and the exit slit (cm). By varying the voltage of the inner rod, particles can be separated according to their size.

Particles are counted in the CPC by passing through an environment of saturated butanol vapour to grow the particles to a larger size by condensation which then can be optically detected. The final output of the DMA-CPC, processed by a software, is particle size distributions in the form of $dN/d\ln(D_p)$ for particle size ranging from ~ 8 to 700 nm. The q_p and q_s were set to specific flows to obtain measurements of particle numbers within this diameter range. To determine the particle mass concentration, the total number of particles at each size interval ($N(D_p)$) should be calculated for each D_p . Then the total particle mass per size interval, $M(D_p)$ can be calculated from Eq. 2.6 in $\mu\text{g cm}^{-3}$.

$$M(D_p) = \rho V \left(N(D_p) \right) = \rho \left(\frac{\pi}{6} \right) (D_p)^3 N(D_p) \quad (2.6)$$

Where ρ is the particle density and V is the particle volume which is equal to $V = \frac{\pi D_p^3}{6}$ (assuming spherical particles). The total particle mass concentration per time step (every 2 or 5 minutes) can be subsequently determined by summing the individual particles masses computed for each size interval.

2.2.1.2 Particle Mass Correction

York University smog chamber

For the experiments conducted in the York University smog chamber, the particle mass concentration was corrected for two loss processes; particle loss to the walls and dilution. The detail of the wall loss correction for this chamber is described in detail in Bienenstock (2001). In summary, the size dependent deposition loss rate constant (k_{dep} , s^{-1}) was determined for the particles in the chamber using succinic acid disodium salt monodispersed particles ranging from 30 to 420 nm in diameter (Eq. 2.7).

$$k_{dep} = a + b \exp \left[\left(-0.5 \left(\frac{\ln(D_p)}{\frac{c}{d}} \right)^2 \right) \right] \quad (2.7)$$

Where the constants a , b , c and d were determined as 0.0105, -0.0105, 0.1605 and 30.72 respectively, and D_p is the particle diameter (in μm). It should be noted that these constant values are only valid for the chamber used in this study with the fan running. The particulate mass lost due to deposition on the wall was determined for each size bin in a given time step

according to Eq. 2.8. The total mass lost in each time interval was then determined by summing the mass loss of each size. The mass correction was less than 1%.

$$Mass\ loss(D_p) = k_{dep} Mass(D_p) \Delta t \quad (2.8)$$

To account for the dilution due to sampling and addition of Aadco air to the chamber, a dilution correction had to be applied. The detail of this correction, which is similar for all instruments, is provided in Appendix A. The particle masses obtained from the corrections were then added cumulatively over the course of the experiment to the measured particle mass to correct for the mass lost due to deposition and dilution.

JPAC

Since the experiments carried out in the JPAC were conducted at lower β -pinene concentrations, a different loss correction method was necessary to correct the particle mass concentration. The derivation of the correction method is described in detail in the supplement of Sarrafzadeh et al. (2016). Here, we briefly describe how the measured particle masses were corrected for wall losses, as well as how SOA yields were obtained from steady state conditions.

Important precursors of particles in the JPAC are extremely low volatility organic compounds (ELVOC) which are recently detected as a class of compound that contributes to SOA at low mass loadings (Ehn et al., 2014). Previous experiments in JPAC studied losses of ELVOCs on particles and chamber walls. In these experiments, first ELVOCs were generated from α -pinene (or β -pinene) oxidation, then their formation was stopped during

steady state by ceasing OH production, which allowed measuring their lifetimes. In absence of particles, the lifetimes of the dominant ELVOCs were in the range of 2 to 3 minutes. The lifetime of ELVOCs was dependent on the presence of particles and they were much shorter (down to a few seconds) in the presence of particles (when seed particles were added). The lifetimes were shorter the higher the particle surface area was and this was attributed to the condensation of the ELVOCs on the particles. ELVOCs losses on the particles were determined from wall loss rates and the total loss rates. The outflow of ELVOCs from the chamber was negligible compared to the dominant losses. Knowing the loss rates on particles and the total loss allowed determining the fraction of ELVOCs contributing to particle mass formation and not lost on the walls of the chamber, which is defined as F_p (Eq. 2.9).

$$\left(F_p = \frac{\text{Loss on particles}}{\text{Loss on particles} + \text{loss on walls}} \right) \quad (2.9)$$

Knowing this ratio allowed correcting the measured mass by the inverse of this ratio i.e. the measured mass was divided by F_p . Experiments with α -pinene and β -pinene and variations of particle surface by adding different amounts of ammonium sulfate seed allowed verifying this correction procedure for a wide range of particle surfaces. Note that the numerical data obtained for wall loss correction are only valid for the chamber used in this study.

SOA yields were determined mainly at steady state conditions in this study. Correcting measured particle masses by the procedure described above, revealed that after an induction time of ~ 20 minutes, the wall loss corrected particle mass was constant as long as the OH production rate was constant. This allowed determining yields using steady state

assumptions. Yields were determined by dividing the particle mass formed in the experiments by oxidation rate of the β -pinene. Based on our method of [OH] determination, using the β -pinene consumption according to Eq. (2.3), and at the negligible inflow of particle mass into the chamber, this equals the simple mass balance assumption: produced particle mass divided by β -pinene consumption (Eq. 2.10).

$$Yield = \frac{\textit{Particle mass}}{\beta - \textit{pinene consumption}} \quad (2.10)$$

Determining SOA yield during steady state conditions was advantageous since adjustments of [OH] were required during many experiments conducted in the JPAC (more details on yield determination is provided in Sarrafzadeh et al. (2016)).

2.2.2. Particle Density

2.2.2.1 Instrument Theory and Measurement Principles

The technique that was used in this project to measure particle density was a combination of a SMPS and a tapered element oscillating microbalance (TEOM, Rupprecht and Patashnick series 1400a). The SMPS-TEOM method involves simultaneous measurements of particle size and mass. The particle density is determined by taking the ratio between the particle mass concentration (from TEOM) and the volume concentration (from SMPS).

The TEOM monitor is a gravimetric instrument that measures real-time particle mass concentrations. It consists of a highly sensitive mass transducer (sensor unit) and a control unit. The sample flow is normally drawn to the instrument through a size selective (PM 2.5)

inlet which is then split into a 3 L min^{-1} flow directed to the mass transducer while the remainder is sent to exhaust. The inlet was bypassed in our setup since the particles formed in the smog chamber are less than a micron in size. Inside the mass transducer, the sample flow passes through an exchangeable filter cartridge (Teflon-coated borosilicate glass) which is mounted over the tip of a hollow tube (tapered element). The tapered element vibrates at its natural frequency. As particles deposit on the filter, the vibration frequency of the tapered element changes which is then used to calculate the total accumulated mass as it is illustrated in Equation 2.11 (TEOM series 1400a manual, 2001).

$$\Delta M = K_0 \left(\frac{1}{f_f^2} - \frac{1}{f_i^2} \right) \quad (2.11)$$

Where ΔM is the mass change, K_0 is the calibration (spring) constant, f_i is the initial oscillation frequency of the system and f_f is the oscillation frequency after the addition of mass (ΔM). K_0 was determined by measuring the frequencies with and without a known mass (pre-weighed filter cartridge, $106921 \mu\text{g}$). The final output of the TEOM is the total particle mass concentration (in $\mu\text{g m}^{-3}$) averaged over a 2-minute time step.

The TEOM sensor is generally heated to 50°C to prevent water vapour condensation on the tapered element. However, we found this elevated temperature could cause some of the semivolatile fraction of the particles to be lost. Since the experiments were performed under dry conditions in the York University smog chamber ($\text{RH} < 10\%$), the use of such a high temperature was avoided. Therefore, the TEOM operating temperature was set to 27°C .

2.2.2.2 Evaluation of the TEOM-SMPS System

The performance of the SMPS-TEOM system was evaluated first with test particles of known density such as ammonium sulfate ($\rho = 1.77 \text{ g/cm}^3$). Ammonium sulfate particles were generated from a 0.5 g L^{-1} solution of $(\text{NH}_4)_2\text{SO}_4$ using a Collison nebulizer, passed through a diffusion drier followed by a neutralizer and then introduced into the smog chamber.

Figure 2.3 shows the total particle mass concentration and the total particle volume concentration that were recorded every 2 minutes by the TEOM and SMPS respectively. The observed decrease in the particle volume and mass concentration is due to dilution and wall loss in the chamber. The particle density was then calculated by taking the ratio between the particle mass and volume concentrations and plotted versus time (Fig. 2.3). The first 20 minutes was not taken into account for the average density, to allow the instruments to converge (differences in sampling time between the instruments leads to errors when the particle mass and volume are changing rapidly). The particle density measurements for $(\text{NH}_4)_2\text{SO}_4$ particles are summarized in Table 2.1. The average particle density measured for $(\text{NH}_4)_2\text{SO}_4$ was in agreement with the reported density (1.77 g cm^{-3} (Lide, 2003)), which confirmed accurate performance of the TEOM-SMPS system. The average particle density for each experiment was determined by taking the sum of the measured particle density over the course of the experiment (every 2 minutes) and dividing it by the number of measurements. An estimate standard deviation (SD) was calculated for the average particle density based on the standard deviation of the measured particle density over the course of

the experiment (avoiding the first 20 minutes). The relative standard uncertainty (RSD) for the average density was estimated as the standard deviation of the average density divided by the average density. The standard error of the mean (SE) was calculated by dividing the standard deviation by the square root of the number of measurements ($SE = \frac{SD}{\sqrt{n}}$).

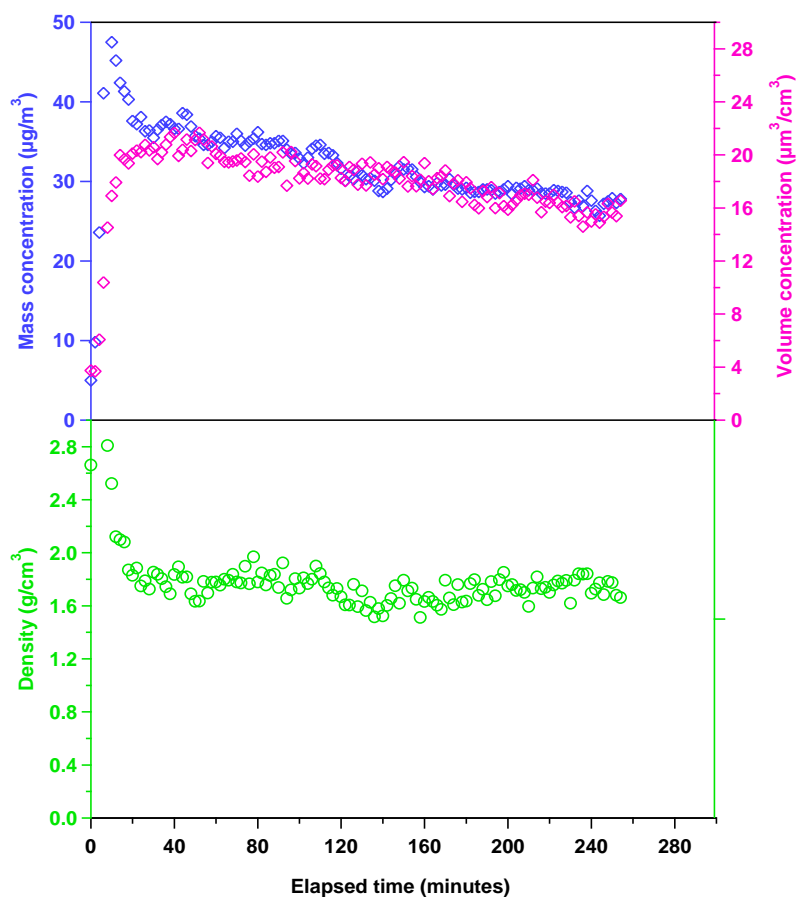


Figure 2.3 Time profiles of particle volume and mass concentrations evolution in the smog chamber for a $(\text{NH}_4)_2\text{SO}_4$ experiment. The particle density was calculated by taking the ratio between the particle mass and volume concentrations ($\rho = 1.75 \pm 0.08 \text{ g cm}^{-3}$).

Table 2.1 Summary of the particle density measurements for (NH₄)₂SO₄.

Date	Average density (g cm ⁻³)	n ^a	SD (g cm ⁻³) ^b	RSD (%) ^c	SE (g cm ⁻³) ^d
10-27-13	1.79	40	0.09	4.87	0.01
10-28-13	1.80	101	0.10	5.70	0.01
10-29-13	1.75	113	0.08	4.82	0.01
11-15-13	1.83	94	0.14	7.57	0.01

Average density (g cm ⁻³)	SD (g cm ⁻³)	N ^e	RSD (%)	SE (g cm ⁻³)	Reported density (g cm ⁻³) ^f
1.79	0.10	4	5.60	0.005	1.77

^a n is number of density measurements in each experiment, ^b SD is standard deviation, ^c RSD is relative standard deviation, ^d SE is standard error of the mean, ^e N is number of experiments, ^f (Lide, 2003).

2.2.3. Particle Morphology

Images of particles were recorded using a scanning electron microscope (SEM, Quanta 3D FEG) to investigate the shape and phase state of aerosol particles. The filters were prepared for SEM analysis in a few steps. Initially, particles were collected on a filter by drawing the gas stream from the chamber. The collection time for the sampling was between 1 to 2 hours at a flow rate of 2 L min⁻¹. Both quartz fiber filter (25 mm diameter; PALL) and polycarbonate membrane filter (25 mm diameter, 0.2 μm pore size; Millipore) were used for these experiments to better define optimal conditions to investigate the shape and phase of particles. Figure 2.4 shows the SEM images of polycarbonate membrane and quartz filters, with no particles collected on them. Polycarbonate filters provide a flat surface upon which

all the particles can be observed which are more commonly used for SEM analysis. After collection, filters were refrigerated under dry conditions for analysis within 24 hours.

A small piece of the filter was cut and mounted with a carbon tape on the aluminum SEM stub. Filters were then coated with a thin layer of conducting material (Au/Pd) using a sputter coater (coated for ~ 30 sec under ~ 100 mtorr pressure). The samples were then viewed under the SEM, which is a type of electron microscope that focused a beam of electrons over a surface to create an image. In this study, the SEM was operated under high vacuum (10^{-5} torr), with an accelerating voltage of 10 kV, a probe current of 23-93 pico-amps and a spot size (electron beam diameter on the specimen surface) of 4-5 nm. We aimed to use low beam voltage and current to avoid evaporating the particles. We considered using the environmental SEM mode as it has the advantage of observing samples under higher pressures (up to 30 Torr). However, its use was avoided because it would introduce water vapour into the system which could interact with the particles. After acquiring the SEM images, particle size distributions were determined from the SEM images by image analysis using the ImageJ program (available online at <https://imagej.nih.gov/ij/>).

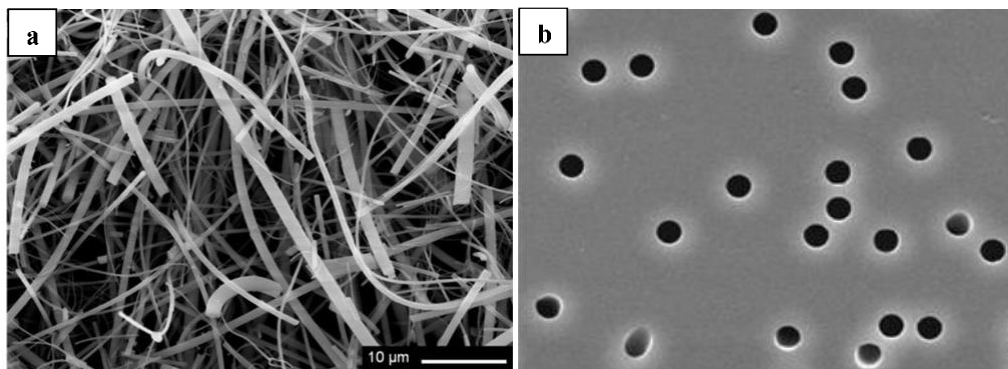


Figure 2.4 SEM images of “clean” filters; (a) quartz fiber which is made up of quartz fibers of different diameters and (b) polycarbonate membrane filter, which contains 0.2 μm pores.

2.2.4. SOA Chemical Composition

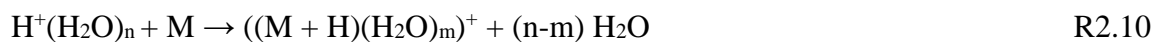
2.2.4.1 Principle of APCI-MS/MS

Real time analysis of particle and gas phase products formed during the oxidation reactions, was performed using the APCI-MS/MS. As mentioned previously (Section 2.1.1.3), the reaction mixture from the chamber is introduced directly into the ion source for gas phase analysis or is passed through the CFMD and the in-line heater before entering the ion source for particle phase analysis.

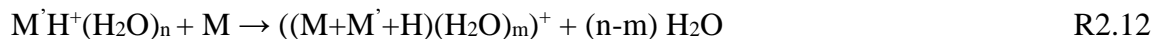
2.2.4.1.1. APCI Ion Source

In the APCI ion source, the air sample undergoes direct ionization at atmospheric pressure. Since the ionization takes place in air, the primary positive and negative ions formed by the point-to-plane corona discharge are N_2^+ , O_2^+ and O_2^- (Bruins, 1991). The discharge current is generated between the corona discharge needle at applied electrical potential of $\sim 5\text{kV}$ and the curtain plate. Due to the presence of water in the ion source, these primary ions can then form secondary reactant gas ions such as $\text{H}^+(\text{H}_2\text{O})_n$ and $\text{O}_2^-(\text{H}_2\text{O})_n$ (where $n = 0, 1, 2, 3$, etc) through collision with water vapour (Good et al., 1970). In the positive mode, the dominant ions in the background mass spectra are the hydronium ion clusters, such as m/z 37 $(\text{H}+2\text{H}_2\text{O})^+$ and m/z 55 $(\text{H}+3\text{H}_2\text{O})^+$. Thus, protonated molecular ions are formed through a proton transfer by ion–molecule reactions with these water cluster ions (R2.9). It should be noted that only compounds with higher proton affinity than water (696 kJ mol^{-1}) or its water

clusters can undergo proton transfer. In addition to protonated ions, water clusters of protonated molecule ions can also form in the ion source (R2.10).



Furthermore, molecules may undergo charge transfer or association reactions to produce the M^+ or $(\text{M}+\text{M}'+\text{H})^+$ molecular ions (R2.11-2.12). The association reactions occur as a result of interaction with other species present in relatively high amounts in the ion source, which are observed as protonated oligomers consisting of the same compound (dimers) or combinations of two different species.



Generally, protonated molecular ions are the most dominant ions observed in the APCI source.

In the positive ionization mode, the mechanisms are protonation, adduct formation, and charge transfer. Whereas, in the negative mode ions are formed via proton abstraction or charge transfer (R2.13-2.14) as well as via association (R2.15).



APCI is a relatively soft ionization technique and produces mainly $(M+H)^+$, $(M-H)^-$, but it does produce some degree of fragmentation.

The generated ions are then drawn towards the orifice into an area of intermediate vacuum through a nitrogen curtain gas, followed by focusing ring and skimmer that transports ions into the high vacuum mass analyzer region.

2.2.4.1.2. Quadrupole Mass Analyzer

The analyzer region of the API instrument consists of four quadrupoles, which are called q0, Q1, q2 and Q3. A schematic of the analyzer is shown in Fig. 2.5. Each quadrupole consists of four circular parallel rods (or electrodes) arranged across from each other. Electrical potential of direct current (DC) or radio frequency (RF) or both, are applied to the electrodes of these quadrupoles. For a given applied DC and RF voltages, only ions of a specific mass to charge ratio (m/z) will be transmitted by the quadrupole. The quadrupoles q0 and q2 are ion guides (RF only), which only transmit ions. Whereas, Q1 and Q3 are mass filters (RF and DC), which separate ions according to their m/z . q2 can also be used as a collision cell where target ions are fragmented by colliding with the collision gas (nitrogen, N_2) (Medley, 1978; Dass, 2007). Those ions that successfully pass through the quadrupoles will reach the detector (channel electron multiplier (CEM, Photonis, Sturbridge, MA)).

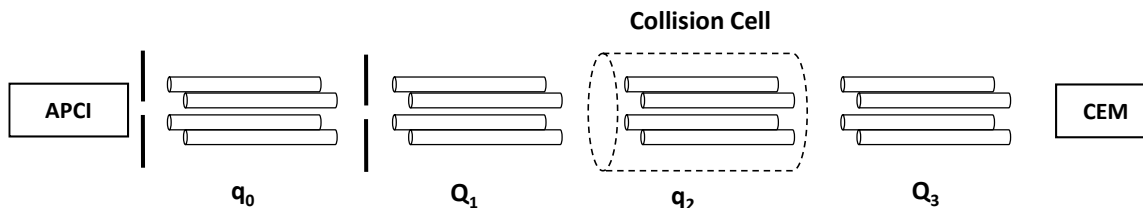


Figure 2.5 Schematic representation of the triple quadrupole analyzer.

The mass analyzer was operated under multiple scan modes in this study; full scan mass spectrum (MS) mode, MS/MS mode and selected reaction monitoring (SRM) mode which allow us to identify reaction product ions. The MS mode is used to acquire a full mass spectrum of all generated ions for a given range of m/z values. In this mode, Q1 is set to scan a particular range of m/z , while q2 and Q3 are set to focus and transmit ions to the detector. The full scan MS mode gives an overview of the species present for further mass spectrometry analysis. In our experiments, the full mass spectra were usually acquired between 10-400 u, with a 5 s dwell time.

The MS/MS mode, which is also known as collision-induced dissociation (CID) or product ion scan mode, provides structural or functionality information of the target ion. In the MS/MS mode, only a single target ion with a specific m/z ratio is selected in the Q1 and passed into the q2, which acts as a collision cell. The pressure inside the q2 of our APCI-MS/MS is approximately 8 mTorr. The target (precursor) ion is then fragmented in the q2 through collisions with the nitrogen molecules. The resultant fragment (product) ions are then analyzed by the Q3, which is set to scan over a specific m/z range. This results in a MS/MS spectrum. During the collision process, a portion of the ion's kinetic energy is converted to internal energy, resulting in bonds breaking and fragmentation. Varying the

collision energy (CE) influences the degree of fragmentation of precursor ions, as higher collision energies are required to break stronger bonds. The collision energy can be adjusted between 5 and 40 eV in the APCI-MS/MS. In this study, a collision energy of 10 eV was mainly used for the MS/MS scan. The dwell time was varied between 100-200 ms.

The selected reaction monitoring (SRM), formerly multiple reaction monitoring (MRM), mode monitors a specific precursor/product ion pair (SRM ion pair). For each chamber experiment, this creates an experimental time profile for each identified product. After performing the MS/MS scan and gaining the knowledge of which product ions formed from a particular precursor ion, SRM ion pairs can be assigned to the reaction products. In this mode, a precursor ion is selected by the Q1, fragmented in the q2, and then a specific product ion is selected by the Q3. Only ions pairs with this exact precursor → product transition will be detected. Therefore, SRM scan mode offers the highest sensitivity towards the product ions, as it spends more measurement time on a particular precursor and a product ion. Multiple SRM ion pairs were analyzed simultaneously over the course of the experiment with consistent parameters (e.g. CE, dwell time), to allow comparison of time profiles. A collision energy of 10 eV and dwell time of 150 ms were used for each ion pair in all the SRM acquisitions.

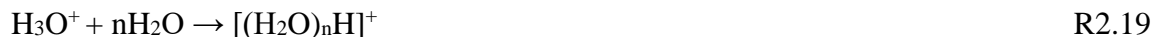
In this study, both positive and negative mode MS and MS/MS spectra were acquired for reaction product ions. All masses that were used for MS/MS and SRM scan modes were the nominal mass; which is the sum of the integer mass of the most abundant isotope of each element in the ion/molecule.

2.2.4.2 Principle of DART-TOF-MS

For offline chemical analysis, aerosol samples from the filter extracts were analyzed by the DART-TOF-MS, which is a DART ionization source coupled to the AccuTOF-MS. The DART-TOF-MS allows high-resolution, accurate mass measurements of reaction products. DART is an atmospheric pressure thermal electron source where samples undergo ionization under atmospheric pressure. The ionization process involves interactions of the electronically excited atoms or vibronically excited molecules (M^*) with the analyte (S) (Cody et al., 2005, Iaramee et al., 2007). This transfers the energy from the excited gas M^* to the analyte S, which produces a radical molecular cation and an electron upon collision (R2.16).



This is termed Pinning ionization, which only occurs when analyte S possess a lower ionization potential than the energy of the excited molecule M^* . The resultant molecular cation is then ejected from the sampling surface and transferred to the mass analyzer with the gas stream (nitrogen or neon). When helium is used as the carrier gas, a different ionization process takes place. Helium primarily produces the (2^3S) electronic excited state, which rapidly reacts with atmospheric water vapor (R2.17). The ionized water then reacts with other water molecules, leading to the formation of ionized water clusters which is followed by the proton transfer reaction with the analyte. This yields a protonated molecule (R2.18-2.20).



Therefore, DART generates mass spectra similar to the APCI which is characterized by M^+ and/or $(\text{M}+\text{H})^+$, usually dominated by $[\text{M}+\text{H}]^+$, in the positive mode.

The DART source is operated with gas flows between 1.5 and 3 L min⁻¹, and the gas temperature can be adjusted from ambient temperature up to ~ 350 °C. In this study, helium was used as the carrier gas with the temperature at 200 °C. One of the main advantages of DART source is that samples can be directly analyzed on a surface of a glass, paper, etc. In this study, a cotton swab was inserted into a vial containing ~ 1-3 ml of our sample and then simply placed in front of the DART source (against the mass spectrometer sampling orifice). Subsequently, product ions were observed in the mass spectrum within seconds.

TOF mass analyzer detects ions based on the time that it takes ions to reach a detector at a known distance. This time is dependent on the molecular mass of ions, resulting in ions to hit the detector at different times, which allows discriminating isobaric compounds. The TOF-MS instrument was operated at a resolving power (mass resolution) of approximately 6000 (FWHM). The full mass spectrum was acquired between 50 and 400 u. The elemental composition of products were determined from the measured exact masses.

3. Results and Discussion

3.1. Physical Nature of Particles

3.1.1. Particle Morphology and Phase State

This study explored the shape and phase state of aerosol particles using the SEM. Here, we collected SEM samples for ammonium sulfate ((NH₄)₂SO₄) seed particles as well as a mixture of organic aerosols formed from β-pinene photooxidation in the presence of seed particles.

Firstly, the seed particles were examined. Figure 3.1 shows SEM images of (NH₄)₂SO₄ particles collected on a polycarbonate membrane filter. The particles were spherical in shape, and solid as expected from the high density of (NH₄)₂SO₄ particles (1.77 g cm⁻³). The spherical shape of the particles is likely due to many small crystals forming upon drying of aqueous solution droplets. The particle size distribution derived from the SEM image ranged from 40 nm to 180 nm. This was consistent with the SMPS size distribution obtained during the collection period, implying that there is little evaporation of volatile compounds during sampling (Figure 3.2).

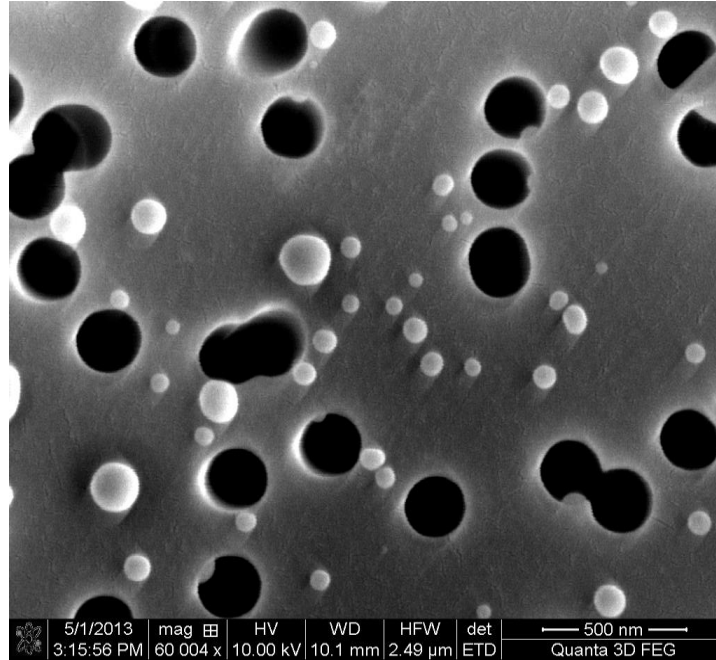


Figure 3.1 SEM image of $(\text{NH}_4)_2\text{SO}_4$ seed particles collected on a polycarbonate membrane filter (0.2 μm pore size). Note that the black holes are the filter pores and the white spheres are the $(\text{NH}_4)_2\text{SO}_4$ seed particles.

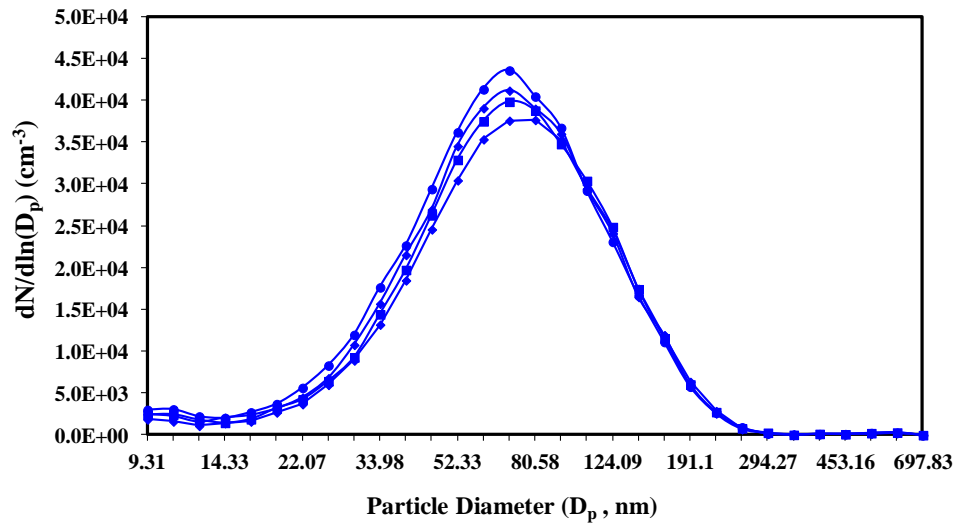


Figure 3.2 Size distribution of $(\text{NH}_4)_2\text{SO}_4$ seed particles measured during sample collection (every 5 minutes). The size distribution does not vary much over time ($< 5\%$ in mode diameter).

Figure 3.3 shows the SEM image of particles formed from β -pinene photooxidation in the presence of $(\text{NH}_4)_2\text{SO}_4$ seed particles collected on a polycarbonate membrane filter. These particles were produced from approximately 0.4 ppm β -pinene reaction with OH radicals ($\sim 10^6 \text{ cm}^{-3}$), producing $\sim 5.5 \times 10^4$ particles cm^{-3} and particle mass concentrations of $\sim 2000 \mu\text{g m}^{-3}$. The smallest particles appeared to be uncoated seed particles of about 25-30 nm with the largest particles ranging from 400 to 450 nm, which were consistent with the result of SMPS size distributions (Figure 3.4). These particles were most commonly imaged as spheres; however, some particles were somewhat irregular. These particles seemed to either consist of two small spheres, likely as a result of coagulation, or resembled an ellipsoid in shape, possibly resulting from particles being flattened on the filter surface during collection. This demonstrates that these organic particles tend to form amorphous rather than crystalline phases.

In addition, as illustrated in Fig. 3.3 some particles were observed in a mixed phase state; liquid phase and solid phase, or entirely as liquid phase. This indicates that particles might not be as dense as a solid. These particles clearly exhibited very different behaviours. This may be due to some of these particles undergoing a partial phase transition and became more fluid like, either during the sample collection or during the analysis with SEM.

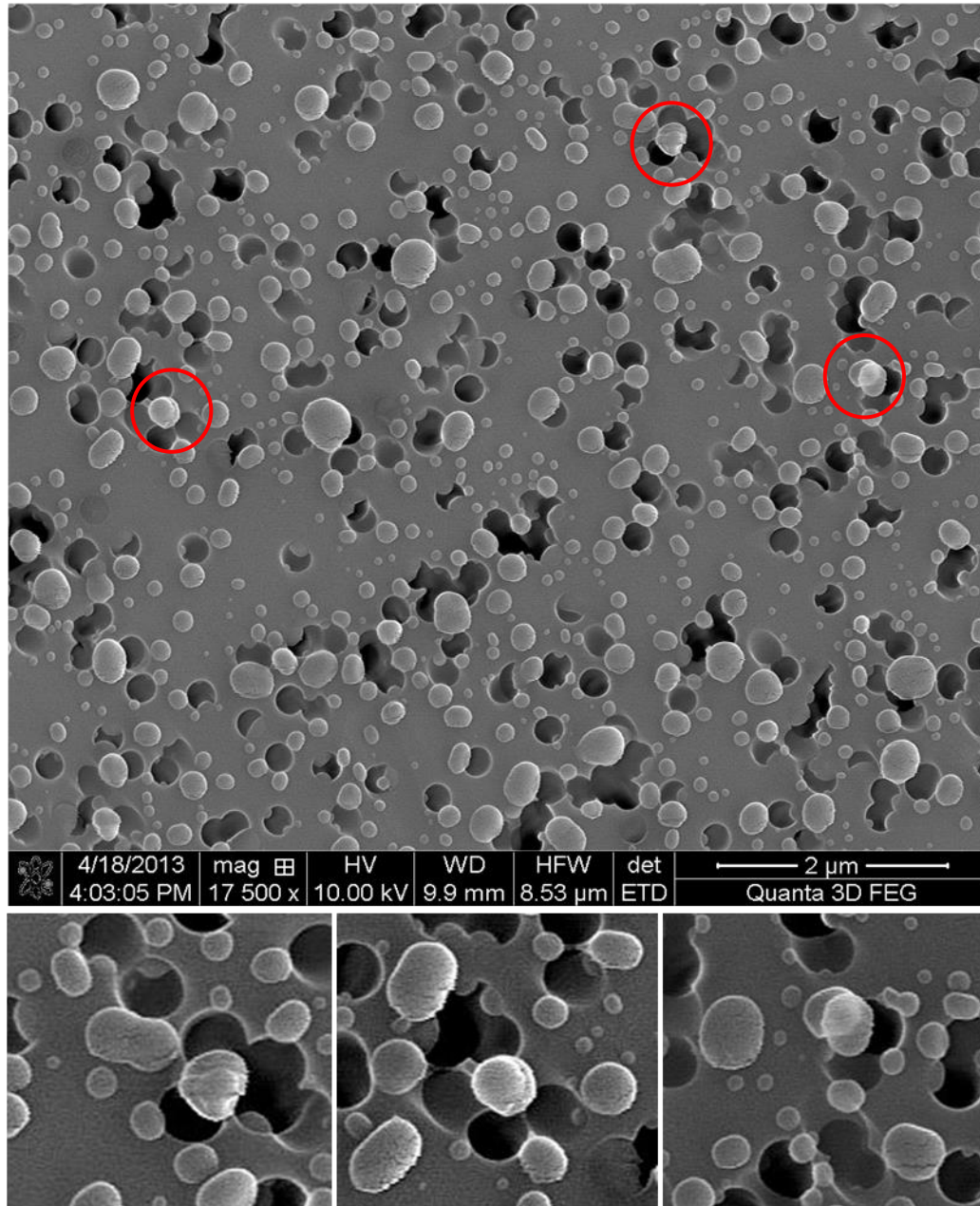


Figure 3.3 SEM image of SOA particles generated from β -pinene photooxidation collected on a polycarbonate membrane filter. Three selected regions identified by red circles, were magnified. Some particles in these regions appeared to be either a mixture of two phases or entirely liquid phase.

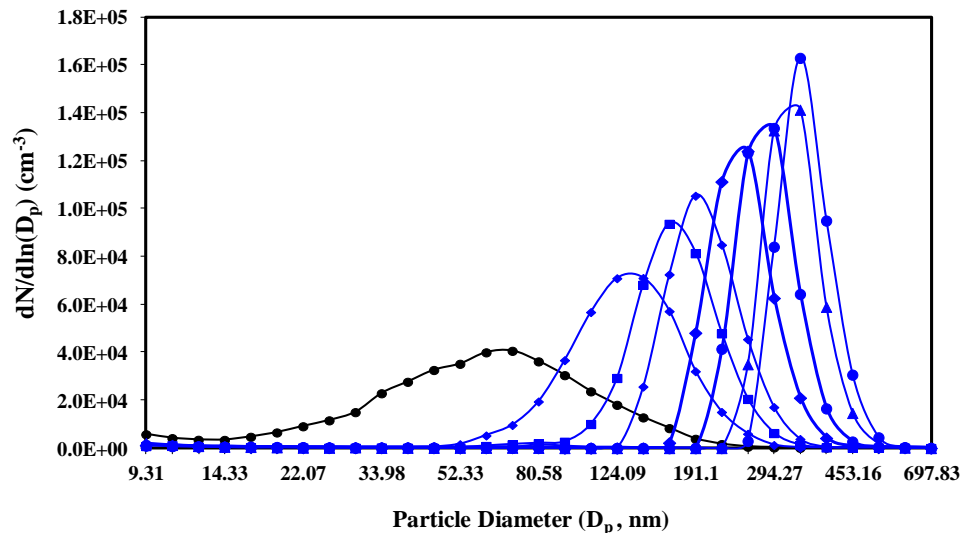


Figure 3.4 Size distributions of SOA particles generated from β -pinene photooxidation measured during the sample collection. The black curve is the size distribution of the $(\text{NH}_4)_2\text{SO}_4$ seed particles ($t=0$ min) and the blue curves are the size distributions of SOA particles measured every 5 minutes, demonstrating the particle growth over time.

In addition, particle phase samples from aging experiments were examined to investigate the impact of further reaction of the oxidation products with OH radicals on the morphology of the particles. Shown in Figure 3.5 are SEM images taken from aged particles, which were formed by further reaction of products from the first oxidation step ($\text{OH} + \beta$ -pinene) with additional OH radicals. The largest particles observed in the SEM images were in the size range of 600 to 640 nm consistent with the SMPS size distribution (Figure 3.6). The first observation from figure 3.5 is that the filter was clogged significantly due to the particles with greater sizes. It appears that the particles collapsed and deformed on the surface of the filter during the collection period as a result of applied forces exerted by pumping. This is consistent with the particles being in a semi-solid/liquid state rather than a solid state; otherwise they would have accumulated on top of each other forming a layer. In addition, it

was observed that upon focusing the SEM beam on the samples, the particle residues on the clogged pores started to vanish, which can be a consequence of evaporation of the liquid components of particles. Furthermore, some particles were agglomerated from two or more particles, but it is not clear if this occurred in the particle phase or during the collection period.

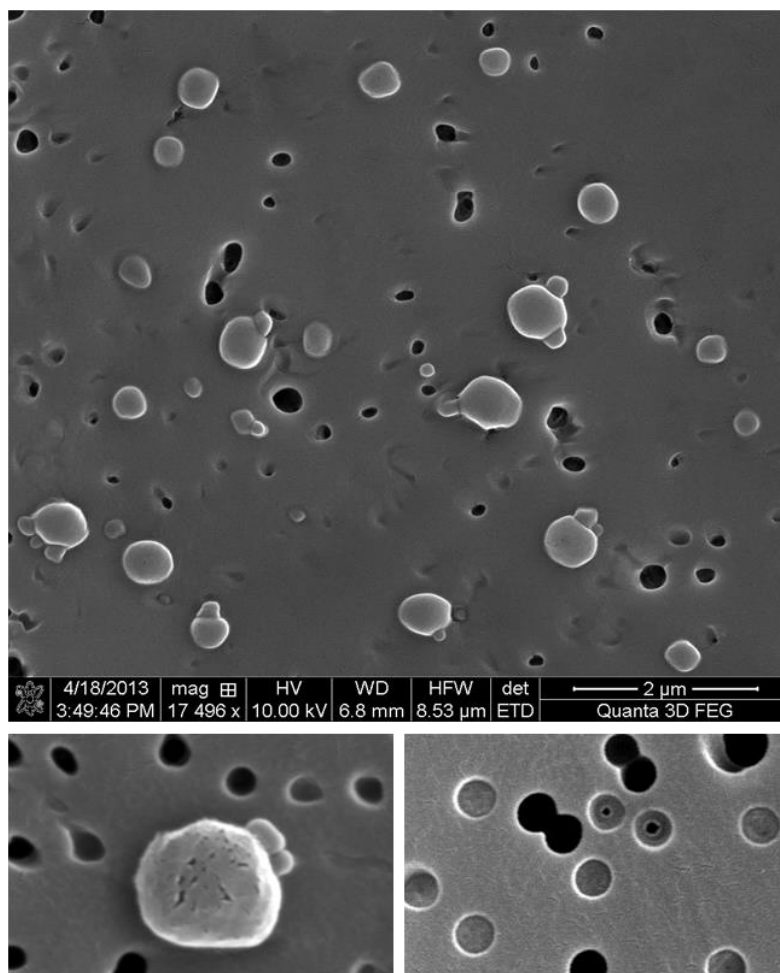


Figure 3.5 SEM images of SOA particles generated from β -pinene photooxidation collected on a polycarbonate membrane filter after aging. The magnified images at the bottom show the clogged pores upon focusing the beam on them and the agglomeration of two or more particles

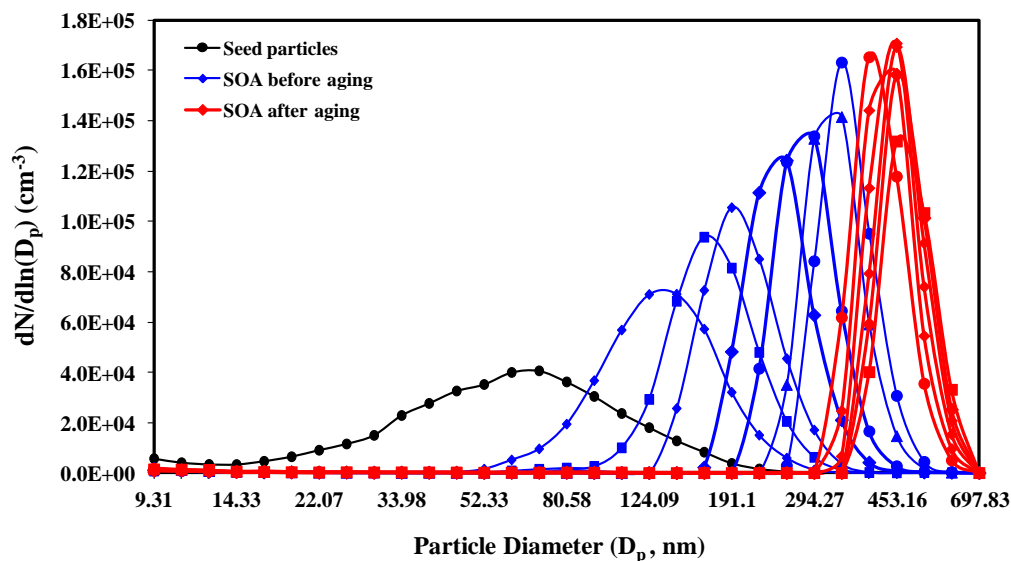


Figure 3.6 Size distributions of SOA particles generated from β -pinene photooxidation measured during the sample collection. The black, blue and red curves are the size distribution of seed particles ($t=0$ mins), SOA particles before initiating aging and SOA particles upon aging respectively. This demonstrates the increase in particle number and size during aging.

Aged particles were also collected on a quartz filter to see whether any additional information on the phase state of particle can be obtained. The results demonstrate that the particles developed different shapes when they were in contact with fibers (Figure 3.7). Smaller particles (up to 200 nm) settled on the thicker fibers (Figure 3.7b) while larger particles (up to 1 μm) formed spherical and ellipsoidal shapes (Figure 3.7c-d) around the fibers. Particle shapes vary depending on the diameter of the particles, the diameter of the fiber and the particle surface tension. Figure 3.7c-d illustrates that particles can be described as fluid phase. If the figures are compared with those of n-hexadecane (C16) liquid drops deposited on a quartz filter (Sutter et al., 2010), it can be concluded that particles behave

more like liquid particles with high viscosity (Figure 3.8). It is worth noting that the surface of particles is not as smooth as the liquid n-hexadecane drops.

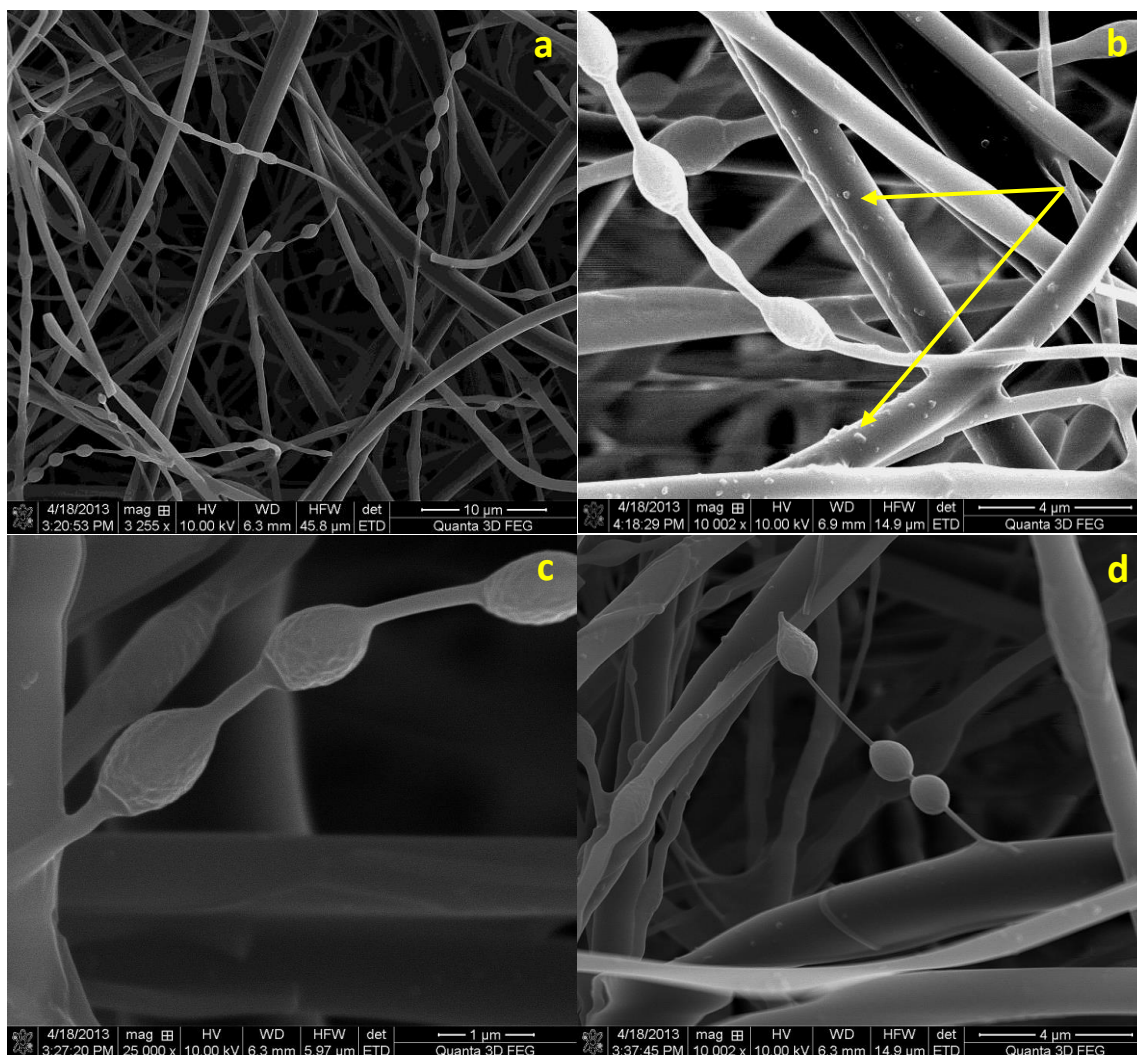


Figure 3.7 SEM images of aged SOA particles generated from β -pinene photooxidation collected on a quartz filter.

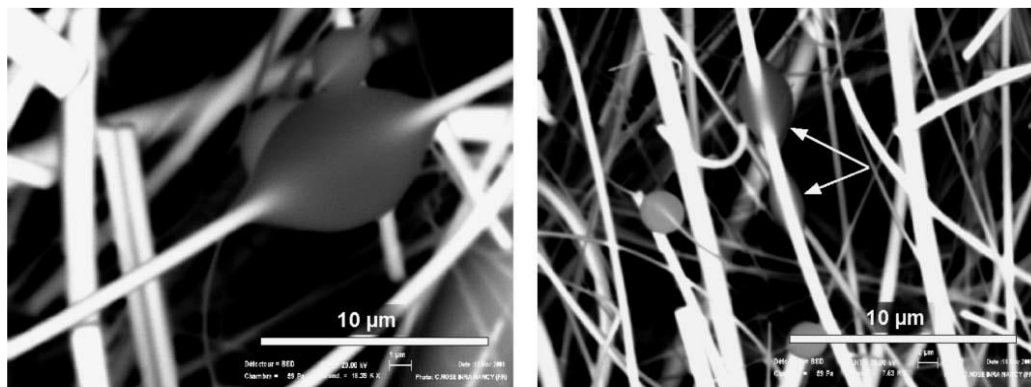


Figure 3.8 Drops of n-hexadecane deposited on the quartz filter observed by SEM (Sutter et al., 2010).

Overall, the analysis of the SEM samples in our study revealed that laboratory generated SOA particles were most commonly spherical and ellipsoidal in shape. Consistency of the SEM size distribution results with those of the SMPS, indicates that evaporation of semivolatile components was not significant, specifically for aged particles, when they were exposed to pressure reductions in the vacuum.

In addition, the SEM images revealed the amorphous phase of particles. This is consistent with this fact that atmospheric aerosols are multi-component mixtures, for which properties differ from those expected from pure substances. Thus, they are more likely to form amorphous rather than crystalline phases (Marcolli et al., 2004; Cappa et al., 2008). Moreover, the SEM images indicated that particles generated from β -pinene oxidation may adopt an ultra-viscous liquid state. This is in contrast to some recent studies that suggested that SOA particles might be in an amorphous solid state under low relative humidity (Virtanen et al., 2010; Renbaum-Wolff et al., 2013).

In published laboratory experiments, phase of particles depends on the chemical composition of SOA, chamber humidity and the precursor concentrations (Bahreini et al., 2005; Mikhailov et al., 2009). The products of the β -pinene oxidation by OH radicals include diols, aldehydes, ketones and nitrates as well as carboxylic acids and hydroperoxides. Based on the vapour pressures of these products, some may adopt a solid phase (e.g. dicarboxylic acids and hydroperoxides) whereas the other compounds with higher vapour pressure (e.g. aldehydes and ketones) may adopt a liquid phase under the conditions of our experiments. The phase for a well-mixed particle will be the sum of all of its components phases. Thus, depending on the nature and proportion of the compounds in the particles, they can adopt various phases. Furthermore, high humidity and high precursor concentrations have been shown to enhance the partitioning of greater volatility (smaller molar mass) species into the particle phase and hence increase the chances for liquid phase particles.

3.1.2. Particle Density

3.1.2.1 Determination of SOA Density from β -pinene Oxidation by OH

The density of SOA particles produced from β -pinene photooxidation was determined in a series of β -pinene experiments conducted in the York University smog chamber in the absence of $(\text{NH}_4)_2\text{SO}_4$ seed particles. In these experiments approximately 100 ppb β -pinene was oxidized with OH radicals generated from ~ 100 ppb isopropyl nitrite (IPN) in the presence of ~ 400 ppb NO. SOA density was determined by measuring the mass of SOA using the TEOM and integrating the particle volume distribution obtained by the SMPS.

Figure 3.9 shows the total particle mass concentration and the total particle volume concentration recorded as well as SOA density time profile during one of the β -pinene photooxidation experiments.

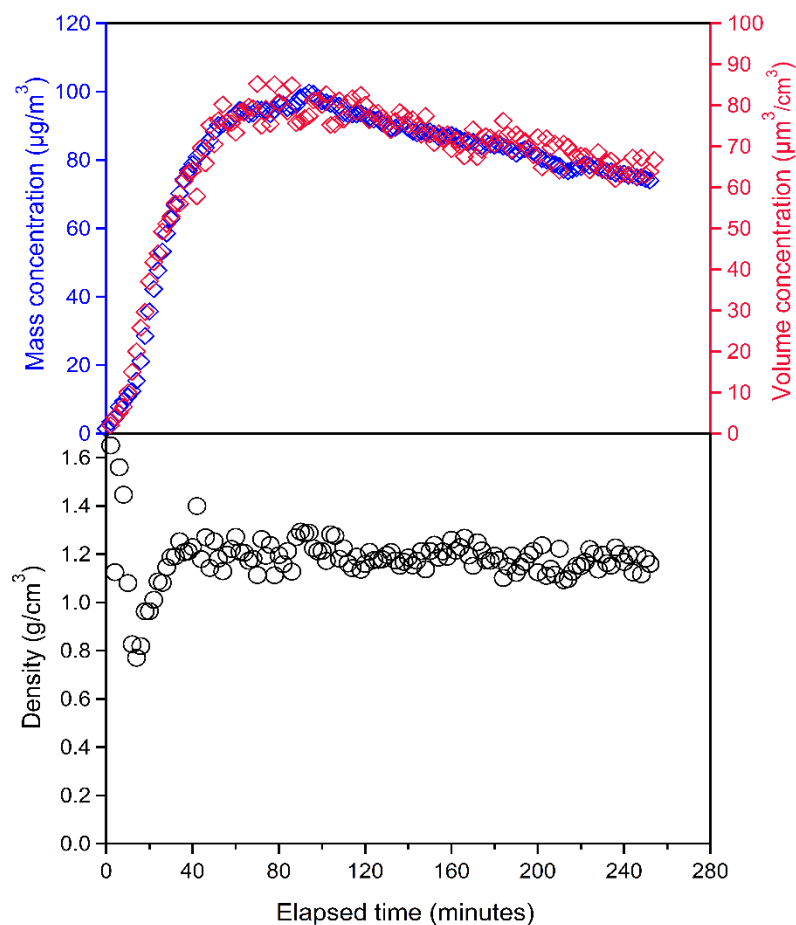


Figure 3.9 Time profiles of particle volume and mass concentrations evolution in the smog chamber for one of the β -pinene photooxidation experiments. The particle density time series is also presented here. Time zero indicates the initiation of OH exposure (lights on). The average particle density after $t=30$ min was determined as 1.19 ± 0.05 g cm^{-3} .

The results of density measurements for generated SOA from β -pinene photooxidation are summarized in Table 3.1. Similar to the $(\text{NH}_4)_2\text{SO}_4$ seed experiments (Section 2.2.2.2), the

first 20-30 minutes were not considered for the average SOA density. The average SOA density measured from several β -pinene photooxidation experiments found to be 1.20 ± 0.05 g cm^{-3} which was consistent with that determined previously from the majority of β -pinene and α -pinene experiments (Bahreini et al., 2005; Alfarra et al., 2006, Shilling et al., 2008; Saathoff et al., 2009; Malloy et al., 2009). The reported densities for α - and β -pinene SOA particles based on a few different techniques are summarized in Table 3.2.

Table 3.1 Summary of the density measurements for β -pinene SOA particles.

Date	Average density (g cm^{-3})	n ^a	SD (g cm^{-3}) ^b	RSD (%) ^c	SE (g cm^{-3}) ^d
11-05-13	1.19	111	0.05	4.33	0.005
11-06-13	1.20	108	0.05	4.22	0.005
11-11-13	1.18	60	0.04	3.07	0.005
11-18-13	1.20	126	0.05	4.50	0.005
11-26-13	1.21	74	0.04	3.27	0.005

Average density (g cm^{-3})	SD (g cm^{-3})	N ^e	RSD (%)	SE (g cm^{-3})	Reported density (g cm^{-3}) ^f
1.20	0.05	5	4.47	0.002	1.20 – 1.30

^a n is number of density measurements in each experiment, ^b SD is standard deviation, ^c RSD is relative standard deviation, ^d SE is standard error of the mean, ^e N is number of experiments, ^f Bahreini et al., 2005; Alfarra et al., 2006, Shilling et al., 2008; Saathoff et al., 2009; Malloy et al., 2009.

Table 3.2 Summary of reported α - and β -Pinene SOA density.

Author	Technique	Particle Type	Density (g/cm ³)
Wirtz & Martin- Reviejo, 2003	SMPS-TEOM	α -pinene ozonolysis	1.04 \pm 0.09
Bahreini et al., 2005	SMPS-AMS	β -pinene ozonolysis	1.20
Alfarra et al., 2006	SMPS-AMS	α -pinene photooxidation	1.29 - 1.32
Kostenidou et al., 2007	SMPS-AMS	β -pinene ozonolysis	1.41 - 1.50
Shilling et al., 2008	SMPS-AMS	α -pinene ozonolysis	1.23
Saathoff et al., 2009	SMPS-AMS	α -pinene ozonolysis	1.25 \pm 0.10
Malloy et al., 2009	SMPS-APM	α -pinene ozonolysis	1.24 \pm 0.03

3.1.2.2 Determination of SOA Density from Nopinone Oxidation by OH

Nopinone has been identified in this work and previous studies (Larsen et al., 2001; Jaoui and Kamens, 2003) as the major product of β -pinene photooxidation. A series of nopinone experiments were conducted in the chamber to examine if the density of SOA generated from nopinone reaction with OH radicals was consistent with that from β -pinene as a precursor. The experiments were initiated by introducing 200 ppb of nopinone and NO to the chamber along with higher concentration of IPN (200 ppb) to account for the lower reactivity of nopinone. These experiments were carried out without (NH₄)₂SO₄ seed particles. Time series of particle volume and mass concentrations as well as SOA density for one of the nopinone/OH experiments are presented in Figure 3.10. The measured particle densities are shown in Table 3.3. The average particle density of SOA generated from nopinone/OH was found to be 1.21 \pm 0.06 g cm⁻³ which is not statistically different from

that measured during β -pinene/OH experiments. This is consistent with nopinone being an intermediate in SOA produced from β -pinene photooxidation.

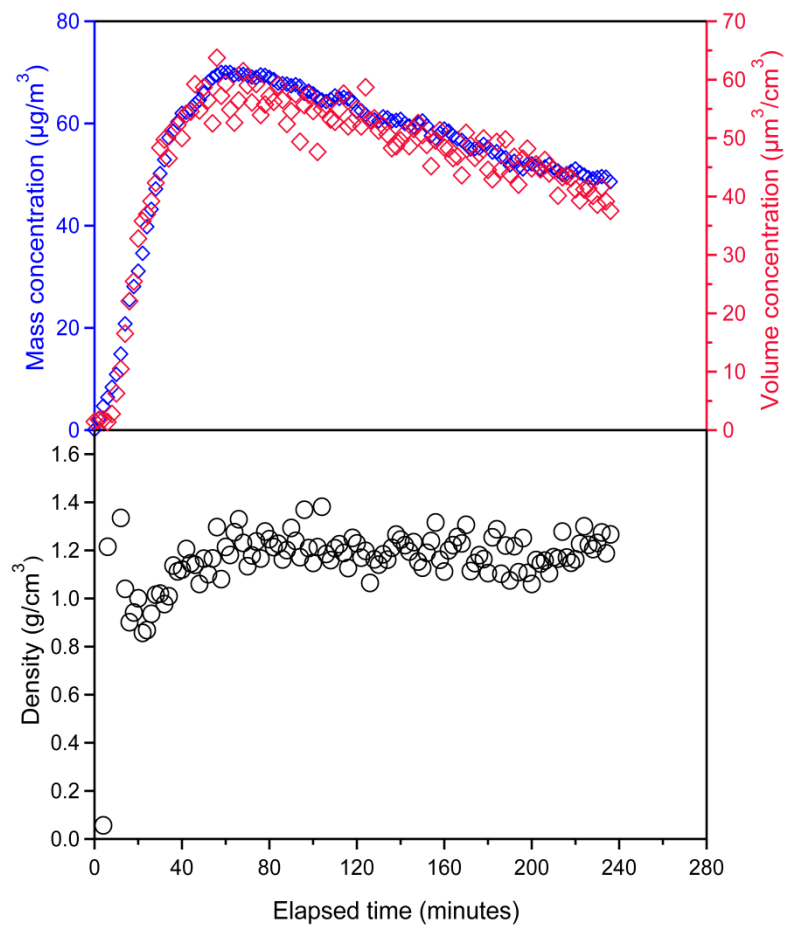


Figure 3.10 Time profiles of particle volume and mass concentrations evolution as well as particle density in the smog chamber for one of the nopinone photooxidation experiments. Time zero indicates the initiation of OH exposure (lights on). The average particle density was determined as $1.20 \pm 0.07 \text{ g cm}^{-3}$.

Table 3.3 Summary of the SMPS-TEOM measurements for nopinone/OH generated SOA.

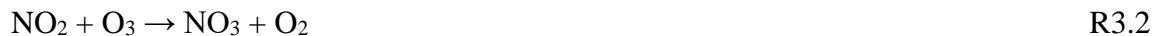
Date	Average density (g cm ⁻³)	n ^a	SD (g cm ⁻³) ^b	RSD (%) ^c	SE (g cm ⁻³) ^d
01-13-14	1.21	75	0.06	4.67	0.007
01-14-14	1.22	90	0.07	5.83	0.007
01-15-14	1.20	101	0.07	5.49	0.006

Average density (g cm ⁻³)	SD (g cm ⁻³)	N ^e	RSD (%)	SE (g cm ⁻³)	Reported density (g cm ⁻³)
1.21	0.06	3	5.36	0.004	-----

^an is number of density measurements in each experiment, ^bSD is standard deviation, ^cRSD is relative standard deviation, ^dSE is standard error of the mean, ^eN is number of experiments.

3.1.2.3 Determination of SOA Density from Nopinone Oxidation by NO₃

Additional nopinone experiments were carried out in the chamber to evaluate the effect of other oxidants, such as nitrate radicals (NO₃) on the density of generated SOA from nopinone. In these experiments nopinone and NO (~ 200 ppb and ~ 6 ppm, respectively) were introduced to the chamber and allowed to mix in the dark for one hour followed by O₃ (~ 8 ppm) injection to initiate the reaction. NO₃ radicals in the chamber are formed by the following reactions:



Since O₃ does not react with nopinone due to the absence of a double bond ($k = 5.0 \times 10^{-21}$ cm³ s⁻¹ (Calogirou et al., 1999)), SOA is only formed by oxidation of nopinone with NO₃

radicals in the chamber ($k < 2 \times 10^{-15} \text{ cm}^3 \text{ s}^{-1}$) (Atkinson and Arey, 2003)). Accuchem modelling (see appendix C for the details of the model) was used to predict the NO_3 radical concentration in the chamber based on a simplified reaction scheme which estimated NO_3 radicals to be approximately $2 \times 10^{10} \text{ cm}^{-3}$ ($\sim 0.8 \text{ ppb}$). Nopinone reactions were not considered in this estimation. Figure 3.11 shows the time series of particle volume and mass concentrations as well as SOA density for nopinone/ NO_3 experiment. Particle formation was observed 5 minutes after O_3 injections by an increase in the particle mass concentration in the TEOM and a growth in the particle size distribution formation in the SMPS. The observed sharp increase in mass concentration upon initiation of the reaction is possibly due to the reaction of ozone with the collected samples on the TEOM filter. Thus, the average density was calculated after it reached a plateau which was found to be $1.39 \pm 0.03 \text{ g cm}^{-3}$. Table 3.4 summarizes the average density for the SOA density measurements.

Table 3.4 Summary of the SMPS-TEOM measurements for nopinone/ NO_3 generated SOA.

Date	Average density (g cm^{-3})	n^a	SD (g cm^{-3})^b	RSD (%)^c	SE (g cm^{-3})^d
03-05-14	1.40	106	0.04	2.74	0.004
03-31-14	1.39	65	0.03	2.08	0.004
04-08-14	1.40	81	0.03	2.37	0.004

Average density (g cm^{-3})	SD (g cm^{-3})	N^e	RSD (%)	SE (g cm^{-3})	Reported density (g cm^{-3})
1.39	0.03	3	2.42	0.002	-----

^a n is number of density measurements in each experiment, ^b SD is standard deviation, ^c RSD is relative standard deviation, ^d SE is standard error of the mean, ^e N is number of experiments.

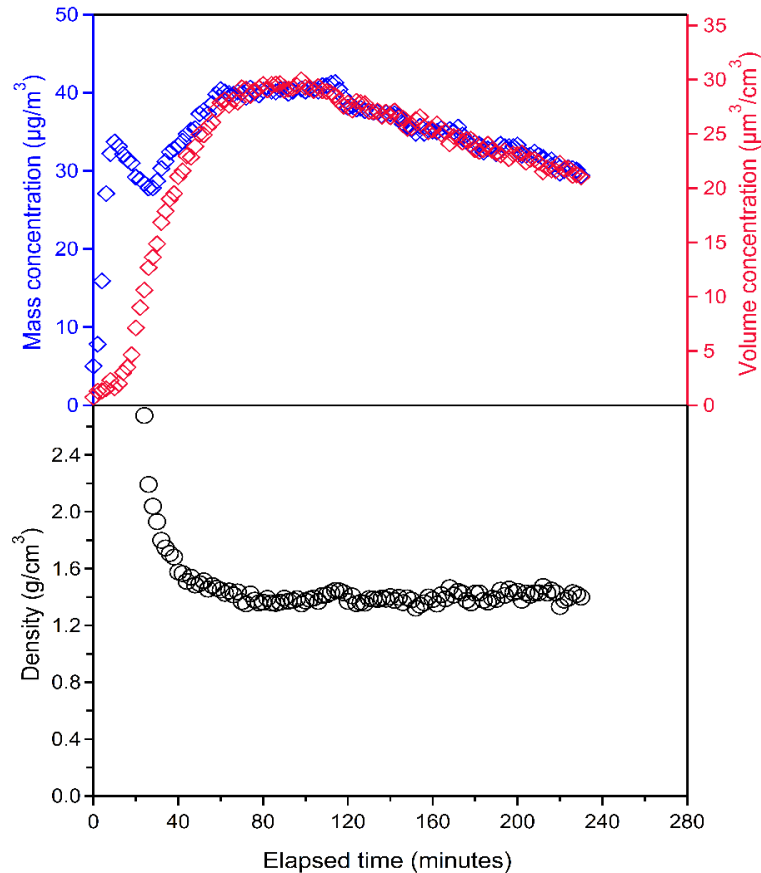


Figure 3.11 Time profiles of particle volume and mass concentrations evolution as well as particle density in the smog chamber for one of the nopinone + NO₃ experiments. The average particle density was $1.40 \pm 0.03 \text{ g cm}^{-3}$.

The result of this work indicates that the measured SOA density from nopinone/NO₃ experiments is significantly higher than the average particle density values reported here and in literature (Bahreini et al., 2005; Alfarra et al., 2006, Shilling et al., 2008; Malloy et al., 2009; Saathoff et al., 2009) for monoterpenes oxidation with OH radicals and O₃ ($\sim 1.2 \text{ g cm}^{-3}$). Explaining the higher SOA density for the nopinone/NO₃ system requires further

information on the chemical composition of the generated particles. However, studies have not yet investigated the chemical composition of these products.

In this study, we implemented several nopinone experiments to gain insight into the chemical composition of formed particles from nopinone oxidation with NO_3 radicals, and the differences between OH and NO_3 chemistry through particle density measurements. The distribution of products in the SOA formed from NO_3 - and OH-induced oxidation of nopinone revealed to have different particle compositions. We found the particle composition to be influenced by NO_3 oxidation, leading to contribution of high molecular weight organic nitrates with considerably lower vapour pressures (e.g. peroxyacyl nitrates (PANs, $\text{C}_x\text{H}_y\text{O}_3\text{NO}_2$)) into the particle contents (the detail of identified products is discussed in the Section 3.2.4). The density of liquid peroxyacetyl nitrate ($\text{C}_2\text{H}_3\text{NO}_5$) is reported as $1.4 \pm 0.1 \text{ g cm}^{-3}$ (ChemSpider). This is consistent with the observed higher SOA density measured for nopinone/ NO_3 system.

The present study was carried out with relatively high NO_2 concentrations which will favour PAN formation. However, under atmospheric conditions where NO_3 concentration is low, the formation of these PAN products is not likely due to the low rate constant of the nopinone + NO_3 reaction. However, the result of this study shows that there is a correlation between the SOA density and the particle composition. This demonstrates that measuring particle density can be a useful technique to gain insight into particle compositions.

3.2. Chemical Composition of Oxidation Products

The APCI-MS/MS has been used to identify the gas and particle phase organic products formed in the York University smog chamber. For β -pinene photooxidation experiments, the initial reagent mixing ratios were approximately 0.4 ppm β -pinene, 0.4 ppm IPN and 0-2 ppm NO. Online chemical analysis of products in the gas and particle phases were performed in separate experiments, conducted under the same conditions.

Multiple scan modes have been used to identify the oxidation products including; mass spectrum (MS) mode, MS/MS mode and selected reaction monitoring (SRM) mode. Identification of reaction products starts with the MS mode in the APCI-MS/MS to acquire a full mass spectrum of all generated ions within the mass range of 10 - 400 u. The formation of organic products is determined by observation of an increase in ion signal intensities upon reaction initiation, by turning the UV lights on. Depending on the proton affinity of hydrocarbons, M^+ or $(M+H)^+$ ions are formed in the positive ion mode, where M is the nominal mass, which appear at $m/z = M+1$ and $m/z = M$. Due to the relative high pressure in the APCI ion source, water clusters of protonated product $(M+H+(H_2O)_n)^+$, and clusters of protonated products with other highly abundant species, $(M1+H+M2)^+$, are also produced. In the negative mode ions appear at $m/z = M-1$, $m/z = M$ and $m/z = M+32$ (Warscheid & Hoffmann, 2001).

Based on the nominal mass obtained from the mass spectra, there are numerous molecular formulas possible. However, these numbers can be reduced with knowledge of likely atom

ratios. Potential products of β -pinene are expected to have molecular formulas of $\leq C_{10}$. In addition, ratios of carbon to hydrogen, and nitrogen to oxygen should be reasonable for structures associated with β -pinene. For instance, nitrogen containing products are expected in the form of nitrates (R-ONO₂), which requires a minimum 1:3 ratio of nitrogen to oxygen in the molecular formula. Therefore, we can develop a list of possible molecular formulas as either C_xH_yO_z or C_xH_yO_zN_q based on the observed m/z.

In order to narrow down the number of potential products further, information regarding the functional groups content is necessary, which can be obtained using the MS/MS mode. The unique MS/MS spectrum of products can be used for compound identification only when standards are available to allow comparison of their fragmentation patterns. However in this work, commercial standards for β -pinene oxidation products are limited to nopinone and pinic acid. For compounds without commercially available standards, surrogate compounds can be used to provide some additional information. Surrogates could help in predicting the structure and functional groups of unidentified products by associating the losses and fragments found in their MS/MS spectra with those of unidentified products.

In general, structure elucidation of products based solely on their neutral losses or fragments is very challenging. However, knowing which characteristic losses and fragments are associated with which functional groups, can help in determining the molecular structure. The reaction products formed from β -pinene photooxidation contain a variety of functional groups such as aldehyde, ketone, alcohol, carboxylic acid, hydroperoxy or nitrate. Compounds with aldehyde and ketone functionality usually give a strong loss of 28,

associated with the loss of CO in the (+)MS/MS mode. Products containing carboxylic acid functionality result in a mass loss of 18 u (H₂O), 28 u (CO) and 46 u (CO + H₂O). Negative mode APCI-MS/MS has been found to be useful for the identification of acid products. Compounds with acid functionality form (M-H)⁻ and (M+32)⁻ ions in the negative MS mode, and in the negative MS/MS mode, show intense signals from a loss of CO₂, [M-H-CO₂]⁻, and weak signals from a loss of H₂O, [M-H-H₂O]⁻. Furthermore, the characteristic neutral loss of 34 u (hydrogen peroxide, H₂O₂) in the (+)MS/MS spectra is a clear indication for the existence of an organic peroxide, containing a hydroperoxy functional group. Finally, nitrate products with odd numbers of nitrogen have odd nominal masses which are observed at even m/z in the MS mode for the protonated ion [M+H]⁺. In the (+)MS/MS mode, the dominant losses of nitrate products ions include: 46 u (NO₂), 63 u (HNO₃), 64 u (H₂O + NO₂) and 81 u (H₂O + HNO₃).

One of the main challenges in identifying products is to distinguish between isobaric product ions (defined as molecular species with the same nominal mass but different exact masses, which can have the same or different functional groups). SRM scan mode monitors precursor/product ion pairs and provides time profiles of individual products. SRM time profiles provide information on how different products behave over the course of the experiments. Products with different chemical composition exhibit different SRM time profiles. Hence, acquiring the SRM scan mode is beneficial in differentiating between the isobaric products.

Due to the limited availability of standards and their fingerprints, a large number of identified products in this study have either a proposed unique molecular formula with multiple structural isomers or have more than one proposed molecular formula and structure (isobaric products).

3.2.1. Gas Phase Products from β -pinene/OH

As mentioned previously, for gas phase analysis the reaction mixture was sampled from the chamber directly to the APCI-MS/MS due to the observed delayed onsets in the SRM time profiles caused by adsorption of gas phase products onto the filter.

Figure 3.12 shows an example of the positive ion full spectrum for the gas phase products generated from β -pinene photooxidation. The most intense peak was detected at m/z 139 which corresponds to the nominal mass of the oxidation product nopinone ($C_9H_{14}O$). To confirm the presence of nopinone, (+)MS/MS spectra was acquired from the $(M+H)^+$ target ion, m/z 139, of the reaction mixture and compared with that of the nopinone standard, as shown in Figure 3.13. The consistency of the fragmentation patterns in the two spectra confirmed the formation of nopinone during the β -pinene photooxidation experiment. Additionally, the observed fragmentation pattern demonstrates reasonable losses for nopinone as a ketone; 18 u (H_2O), 46 u (C_2H_6O), and 56 u (C_3H_4O) which results in m/z 121 (C_9H_{13}), m/z 93 (C_7H_9), and m/z 83 (C_6H_{11}), respectively.

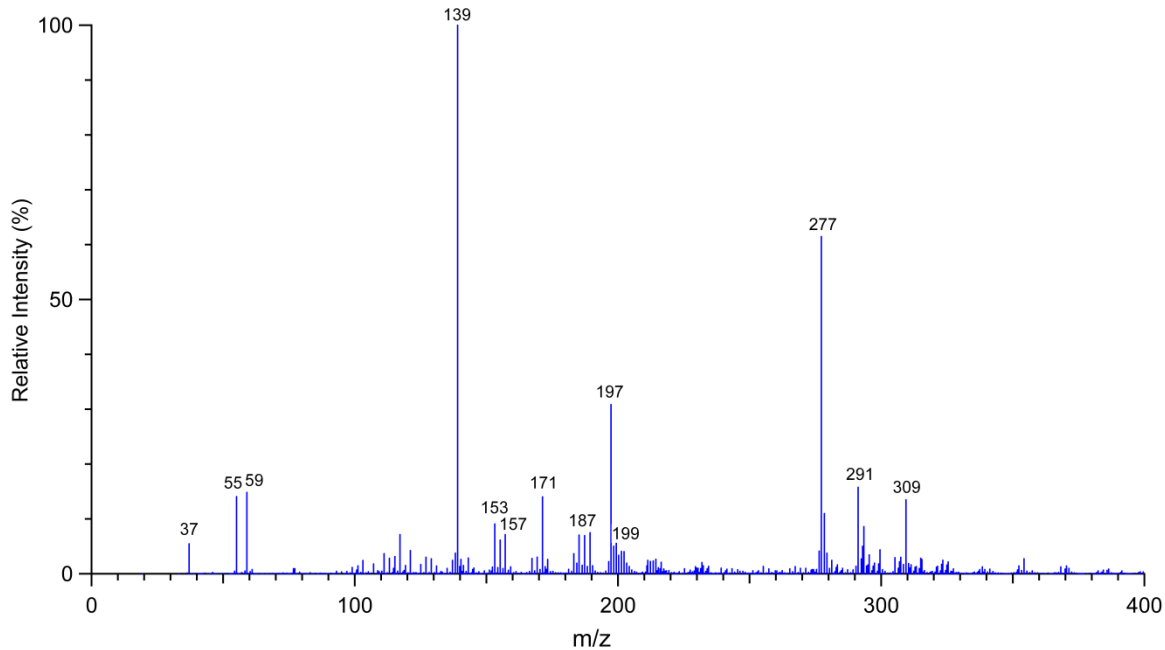


Figure 3.12 Full mass spectrum of oxidation products formed from β -pinene photooxidation (400 ppb NO) in the gas phase. m/z 37 and 55 correspond to water cluster reagent ions.

Some of the other intense $(M+H)^+$ mass peaks observed in the MS scan of oxidation products were m/z 153, 155, 157, 171, 187, 197, 214, 216, 232, 277 and 291 (Figure 3.12). The MS/MS spectra of target ions m/z 157, 197 and 277 from the reaction illustrated that these peaks are associated with the water cluster of nopinone $[M+H+H_2O]^+$, the acetone adduct of nopinone $[M+H+CH_3COO]^+$ and nopinone dimer $[M+M+H]^+$, respectively. It should be noted that even though this product confirms the arrangement given here, this may not be the only product confirmation to the mass spectra. It is challenging to distinguish these clusters from products as they may produce characteristic fragment ions such as neutral loss of water, as exemplified for oxidation products containing hydroxyl and carbonyl functional groups. For instance, the (+)MS/MS spectrum of m/z 157 suggests contributions from one

or more species other than nopinone's water cluster at m/z 157 since one of the fragments present in the spectrum (m/z 111) is not associated with the fragments of m/z 157 from a sample of pure nopinone (Figure 3.14).

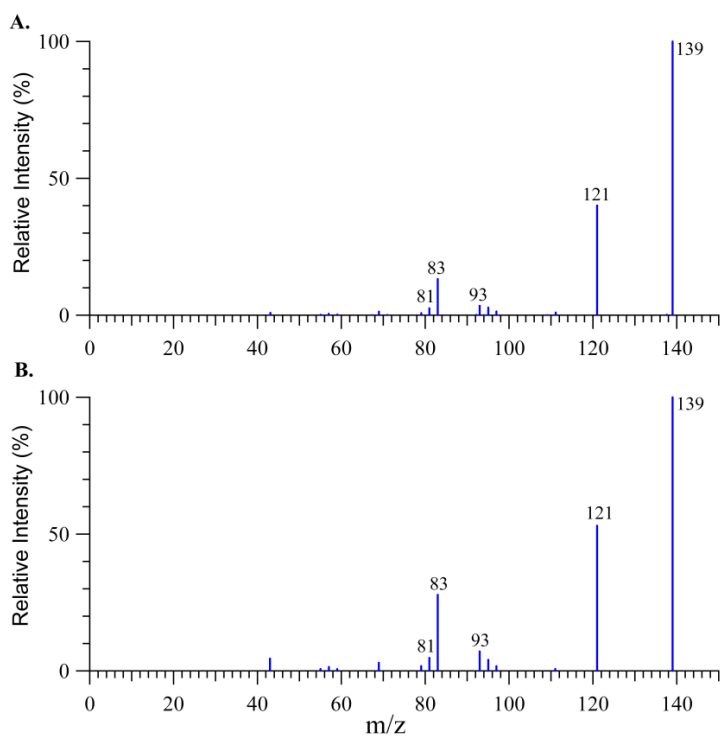


Figure 3.13 Comparison of (+)MS/MS spectra of the target ion m/z 139 from A. a β -pinene/OH experiment in the gas phase and B. the nopinone standard. Both spectra were acquired at collision energy of 10 eV.

Potential products for m/z 157 were proposed to be either norpinalic acid or a C8-keto acid which both have the same molecular formula ($C_8H_{12}O_3$) (Fig. 3.15). These tentatively identified products have the same characteristic losses of one and two H_2O molecules ($(M+H-H_2O)^+$ at m/z 139 and $(M+H-2H_2O)^+$ at m/z 121), CO ($(M+H-CO)^+$ at m/z 129, with higher signals at higher collision energies), CH_2OO ($(M+H-CH_2OO)^+$ at m/z 111) and

$\text{H}_2\text{O}+\text{CH}_2\text{OO}$ ($(\text{M}+\text{H}-\text{H}_2\text{O}-\text{CH}_2\text{OO})^+$ at m/z 93). Norpinalic acid has been previously identified as a product of β -pinene reaction with OH radicals (Auld, 2009; Larsen et al., 2001).

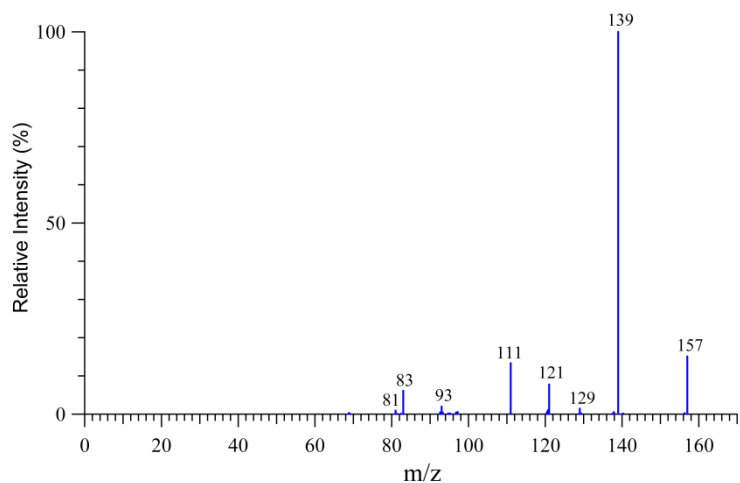


Figure 3.14 (+)MS/MS spectrum of target ion m/z 157 from β -pinene/OH experiment in the gas phase.

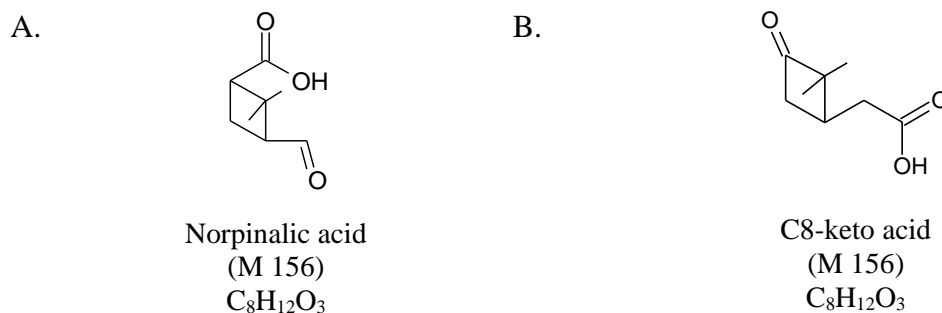


Figure 3.15 Potential β -pinene oxidation product structures with molar mass 156 g mol^{-1} .

Additionally, oxo-nopinone (m/z 153), hydroxy nopinone (m/z 155), pinalic 3-acid (or pinalic 4-acid, m/z 171), norpinic acid (m/z 173), pinic acid (m/z 187), C10-aldehyde nitrate (m/z 214), C10-bicyclic hydroxy nitrate (m/z 216) and C10-dihydroxy nitrate (m/z 232) have

been identified in the gas phase in the current study. The identification of gas phase products from β -pinene photooxidation is discussed in detail in Auld (2009). A summary of the tentatively identified products from our study is presented in Appendix D (Table D.1).

3.2.2. Particle Phase Products from β -pinene/OH

3.2.2.1 Online Analysis

The detection and identification of low volatility products in the particle phase was one of the primary objectives of this study. Here, the APCI-MS/MS coupled with the CFMD was used for characterization of particle phase products from β -pinene photooxidation. As soon as β -pinene reaction with OH radicals begins, oxidation products are produced in the chamber. These products may be found in the gas phase or in the particle phase or both phases, depending on their vapor pressures. It is believed that oxidation products initially build up in the gas phase and then transfer to the particle phase. Gas phase products with low saturation vapor pressure either nucleate to form new particles or condense onto existing particles.

Oxidation products with relatively high vapor pressures such as singly substituted carbonyl and alcohol compounds may never reach saturation in the gas phase under our experimental conditions or atmospheric conditions and thus, would not nucleate to form particles. Whereas, multifunctional secondary products such as carboxylic acids, dicarboxylic acids, hydroxy-carboxylic acids, oxo-carboxylic acids, peroxy acids, hydroxy ketones, and diols,

which have strong intermolecular forces and resulting low vapour pressures, are expected to constitute the majority of the particle phase products (Larsen et al., 2001).

Figure 3.16 shows the positive full spectrum of the particle phase products in this study. A number of dissimilarities were observed by comparing the mass spectrum in the particle phase with that of gas phase; 1) there appears to be a lot more ions in the particle phase, consistent with the observed higher total ion counts; 2) relatively a number of ions stand out such as m/z 173, 185, 187, 201 and 246; 3) a number of different compounds are observed; 4) the large number of m/z ratios suggests it is very difficult to unravel.

Many products were identified in the particle phase which were categorized as hydroxyl and carbonyl containing compounds, carboxylic acids and organic nitrates. Here, a detailed description is given on the interpretation of the mass spectral data for each category of compounds to illustrate their differences. All the identified products in the particle phase are tabulated in Appendix D (Table D.1).

Hydroxyl and Carbonyl Containing Compounds

A number of hydroxyl and carbonyl compounds were found in this study. As an example, a product with molar mass of 168 g mol^{-1} has been identified at the target ion m/z 169 ($M+H$)⁺ in this study. The (+)MS/MS of this ion shows fragment ions attributed to the presence of carbonyl and hydroxyl functionalities at m/z 151 (-18 u, H₂O), 141 (-28 u, CO), 133 (-36 u, 2 H₂O) and 123 (-46 u, CH₂O₂ or C₂H₆O) (Figure 3.17).

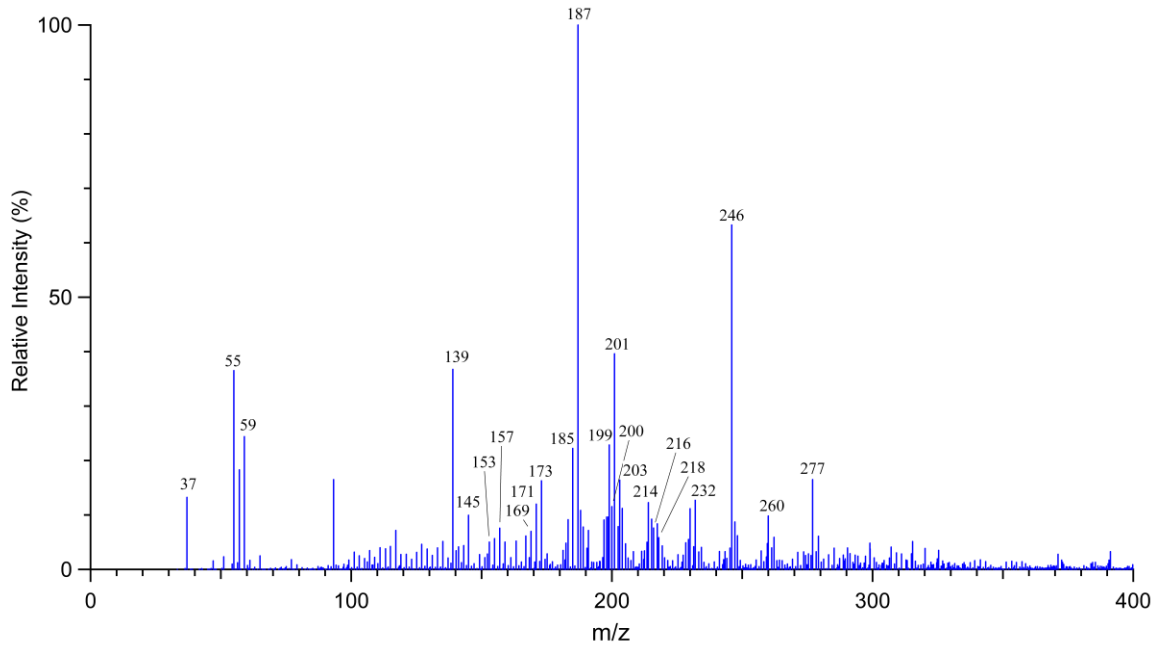


Figure 3.16 Full mass spectrum of particle phase oxidation products formed from β -pinene photooxidation (400 ppb NO), obtained with the APCI-MS/MS. m/z 37 and 55 correspond to water cluster reagent ions.

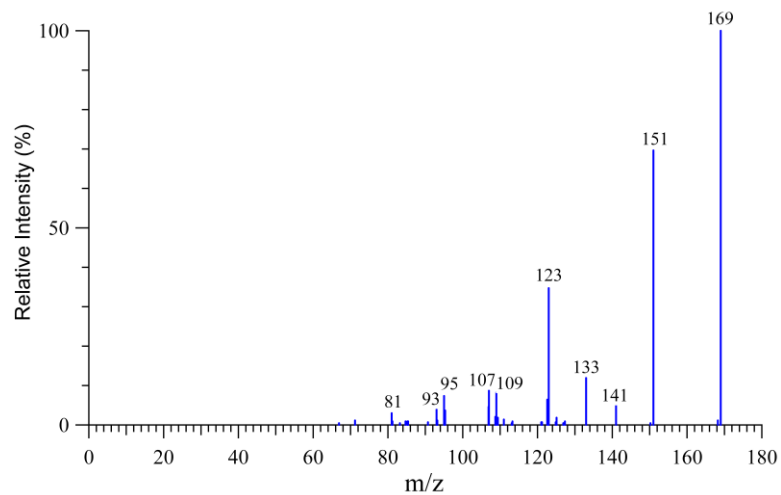


Figure 3.17 (+)MS/MS spectrum of target ion m/z 169 from β -pinene/OH experiment in the particle phase.

Based on the nominal mass and the functionalities, two products were determined to be possibly present; a C10-hydroxy aldehyde and a hydroxy oxo-nopinone (Figure 3.18). However, without having a high resolution mass spectrometer it would not be possible to differentiate between these two products.

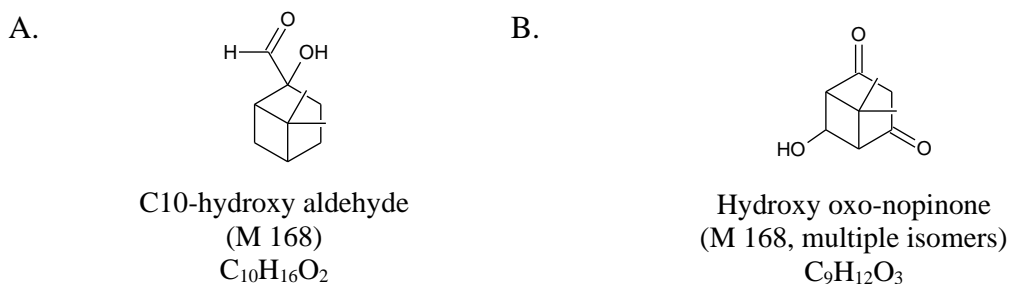


Figure 3.18 Potential β -pinene oxidation product structures with molar mass 168 g mol⁻¹.

Carboxylic Acids

A number of carboxylic acid products were identified in the particle phase including m/z 157, 171, 173, 185, 187, 199 and 201 (Fig. 3.16). The most intense peak was detected at m/z 187. This mass peak was attributed to pinic acid (M = 186) as a dominant product in the particle phase from α - and β -pinene oxidation in a number of studies (Larsen et al., 2001; Jaoui et al., 2003; Kourtchev et al., 2008; Lewandowski et al., 2007). To confirm the presence of pinic acid, the (+)MS/MS spectra was acquired from the reaction mixture and compared with that of a pinic acid standard. As shown in figure 3.19, the reaction product and the pinic acid fingerprint MS/MS spectra are consistent in m/z with each other, strongly suggesting the presence of pinic acid in the reaction mixture. However, the ratio of fragments does not entirely match with each other.

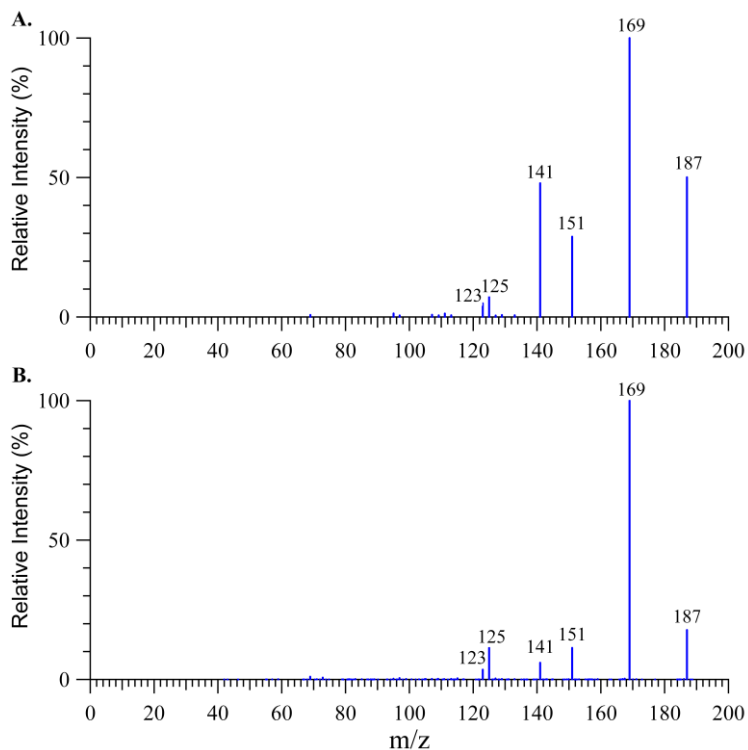


Figure 3.19 Comparison of (+)MS/MS spectra of the target ion m/z 187 from A. a β -pinene/OH experiment in the particle phase and B. the pinic acid standard. Both spectra were acquired at collision energy of 10 eV.

Two reasons could be attributed to this inconsistency; first, the pinic acid standard obtained from Sigma-Aldrich was a mixture of cis and trans isomers and the ratios of cis and trans isomers in the standard and the reaction mixture were likely different which influenced the ratios of the fragments. Second, there could be a contribution of other compounds to m/z 187.

Water cluster of the m/z 169 ($M+H$)⁺ product ion could potentially overlap with m/z 187. However, the fragment ions observed in the (+)MS/MS for m/z 169 and m/z 187 are not

completely consistent (Figure 3.17 and 3.19) with each other, indicating contribution of some other product ions.

A number of other products with the molar mass of 186 g mol^{-1} are proposed in the Master Chemical Mechanism (MCM) from either β -pinene or nopinone oxidation (see Table E.1 in Appendix E). All these proposed products, except for pinic acid, are either peroxide or peroxy acids. As it was mentioned earlier, compounds with peroxide functionality show a neutral loss of 34 u (H_2O_2) in the (+)MS/MS spectra. However, the loss of 34 was not observed in the particle phase reaction mixture (Figure 3.19). This suggests that this contribution cannot be from a peroxide product.

In recent studies (Claeys et al., 2009; Yasmeeen et al., 2010), m/z 187 was assigned to both pinic acid and homoterpenylic acid. It has been reported that the homoterpenylic acid ($M = 186$) which is a lactone-containing monocarboxylic acid, is formed from both ozonolysis and photooxidation of α - and β -pinene. In the study by Clasey et al. (2009), emphasis is given to the differentiation of these isobaric carboxylic acids using negative MS/MS mode based on the fragmentation of m/z 185 ($M\text{-H}^-$). It has been shown that the fragmentation of deprotonated pinic acid is very similar to the deprotonated homoterpenylic acid with only minor differences. The proposed fragmentation routes for deprotonated pinic and homoterpenylic acid are presented in Figures 3.20 and 3.21. In the case of pinic acid the (-)MS/MS of m/z 185 results in m/z 99 through a loss of 42 u (propene, C_3H_6) from m/z 141 fragment, while homoterpenylic acid fragmentation show a loss of 44 u (CO_2) from m/z 141

fragment which results in m/z 97. The other described difference was the relative abundance of m/z 123 which is higher in homoterpenylic acid fragmentation (Claeys et al., 2009).

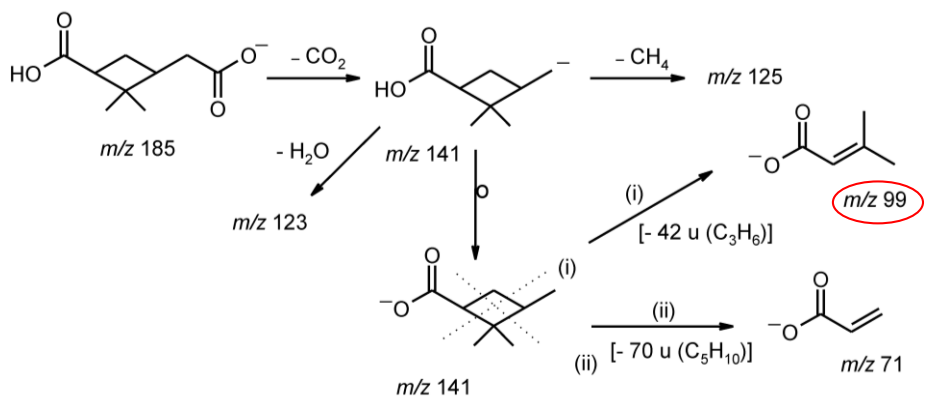


Figure 3.20 Proposed fragmentation pathways for deprotonated pinic acid, adopted from Yasmeen et al. (2010).

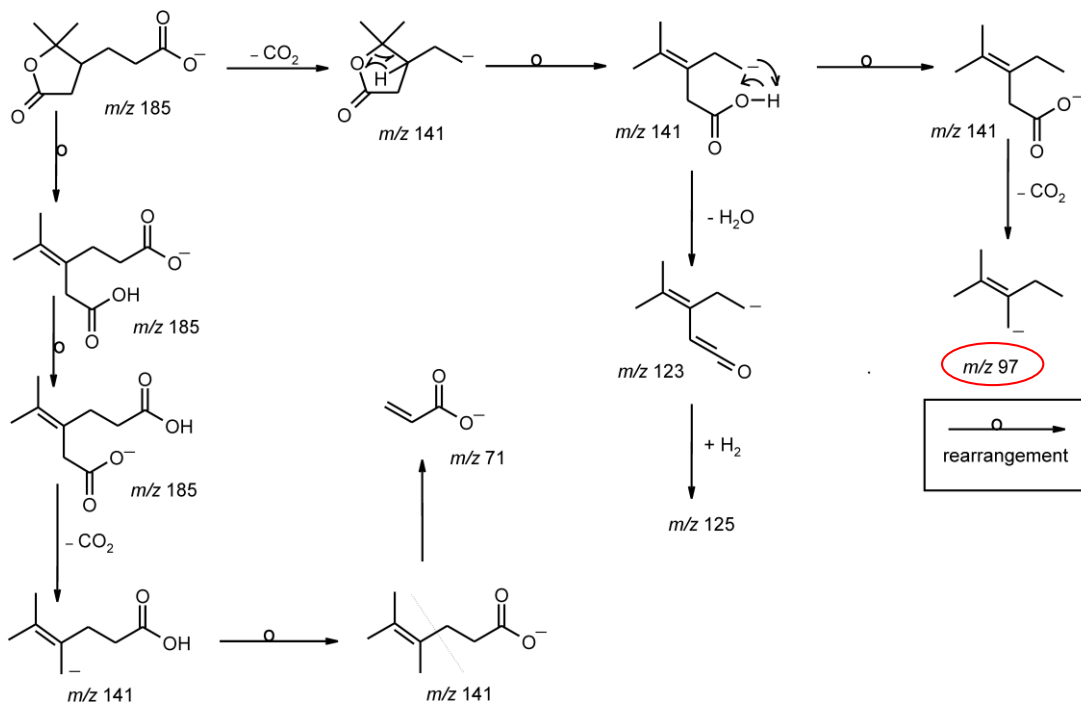


Figure 3.21 Proposed fragmentation pathways for deprotonated homoterpenylic acid, adopted from Yasmeen et al. (2010).

To investigate whether our result is in agreement with the results of these studies (Claeys et al., 2009; Yasmeen et al., 2010), (-)MS/MS of m/z 185 was performed on both reaction mixture and pinic acid standard. As illustrated in Figure 3.22, pinic acid standard only showed a fragment at m/z of 99, whereas the reaction mixture showed fragments at both m/z 97 and 99. This suggests that homoterpenylic acid may contribute to the m/z 187 peak in the (+)MS spectrum. However, we are not able to confirm the presence of homoterpenylic acid due to non-availability of its standard.

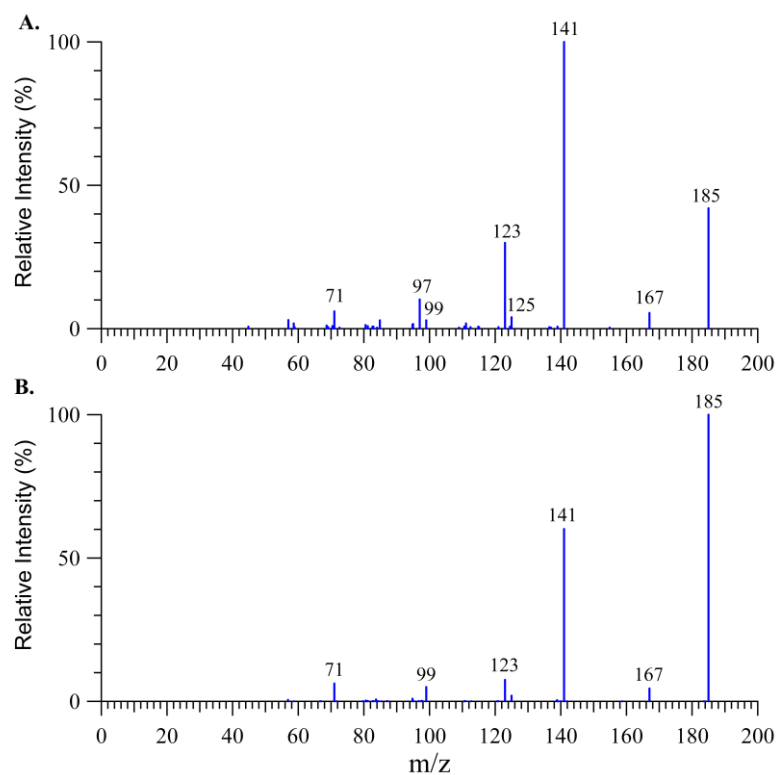


Figure 3.22 Comparison of (-)MS/MS spectra of the target ion m/z 185 from A. a β -pinene/OH experiment in the particle phase and B. the pinic acid standard. Both spectra were acquired at collision energy of 10 eV.

Organic Nitrates

Several products containing nitrate functional groups have been identified in the particle phase from β -pinene/OH experiments in this study (Fig. 3.16). These products were observed at m/z 200, 214, 216, 218, 232, 246 and 260. Here the target ion m/z 246 will be discussed as it was the most intense peak observed in the full spectrum of oxidation product.

The (+)MS/MS spectrum of the target ion m/z 246 during the β -pinene experiments is presented in Fig. 3.23. Identification of the presence of nitrate functionality occurs through even m/z observation for $(M+H)^+$ and the fragment ions observed at m/z 200 (-46 u, NO_2), 182 (-64 u, $\text{H}_2\text{O} + \text{NO}_2$) and 165 (-81 u, $\text{H}_2\text{O} + \text{HNO}_3$).

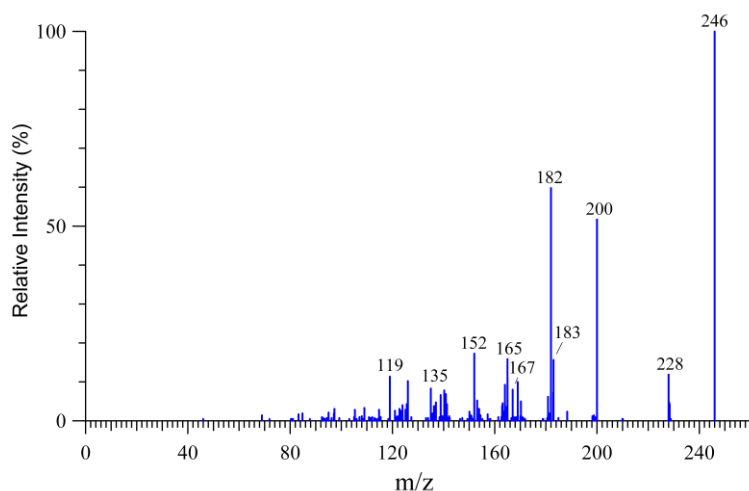


Figure 3.23 (+)MS/MS spectrum of target ion m/z 246 from β -pinene/OH experiment in the particle phase.

These fragment ions indicate the presence of a nitrate as well as other oxygenated functionalities. For instance, there are two fragment ions observed at m/z 183 (-63 u) and

167 (-79 u) which can be associated with losses of HONO₂ and HOONO₂ respectively. These losses are common for the peroxyacyl nitrates (referred to as PANs) compounds. Considering a molar mass of 245 g mol⁻¹ and these fragments, C₁₀H₁₅NO₆ is one reasonable molecular formula that can be associated with this mass. Other potential molecular formulas containing C ≤ 10 and odd number of nitrogen atoms have more than six oxygen atoms, which are not expected to form from β-pinene/OH reaction under our chamber conditions. Formation of molecules containing three or more nitrogen atoms is also not expected.

The double bond equivalent (DBE) (also known as degree of unsaturation) was then calculated for C₁₀H₁₅NO₆ as follow (Badertscher et al., 2001):

$$DBE = C - \frac{H}{2} + \frac{N}{2} + 1 \quad (\text{Eq. 3.1})$$

Where C, N and H are the number of carbon, nitrogen and hydrogen atoms in the molecule, respectively. DBE gives the sum of the number of rings, double bonds and triple bonds. In this case, DBE is four. Since NO₂ functional group counts for one DBE, this indicates this product is either a C₁₀ bicyclic product that contains one carbonyl functionality or a C₁₀ monocyclic product that contain two carbonyl functionalities. There is no organic nitrate product with these characteristics identified in literature. However, this molecular formula has been proposed in the MCM to form from β-pinene photooxidation where its structure is shown in Figure 3.24. The structure illustrates that this is a bicyclic compound which contains one carbonyl functional group. Therefore, m/z 246 was identified as C₁₀-PAN in our study.

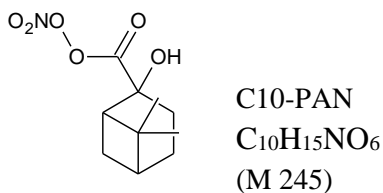


Figure 3.24 Proposed organic nitrate product with molar mass 245 g mol⁻¹ in the MCM.

3.2.2.2 Offline Analysis

Characterization of the reaction products based on only the observed nominal mass and the MS/MS fragmentation was very challenging in this study due to the possibility of multiple isobaric products. Hence, to help with the determination of the elemental composition and structure elucidation, DART-TOF-MS was used to provide high resolution and accurate masses for the product ions. The obtained accurate masses of the product ions combined with the functional groups information from the APCI-MS/MS analysis, made the identification of oxygenated compounds more precise.

In the DART-TOF-MS, reaction products were detected as (M+H)⁺ in the positive ion mode. Thus the acquired full mass spectrum was expected to be similar to that obtained from the APCI-MS/MS. Shown in Figure 3.25 is the full spectrum of particle phase products formed during β-pinene photooxidation. For easy viewing, only the most abundant peaks are labelled in this Figure.

Although the mass spectrum is quoted to 4 decimal places, the mass uncertainty for a pure sample in the DART-TOF-MS is approximately ± 0.0025 u. However, in this spectrum, high mass accuracy cannot be expected for the observed peaks, since there are certain

interferences which will make it impossible to assign a molecular formula with confidence. Therefore, in analyzing the data the mass accuracy was taken to be no more than ± 0.01 u. Even at this resolution, narrowing the m/z window from 1 to 0.01 u largely eliminates isobaric interferences that were observed in the nominal-mass spectrum. In the following, one example will be discussed as to how the accurate mass helps to distinguish between two or more possible products.

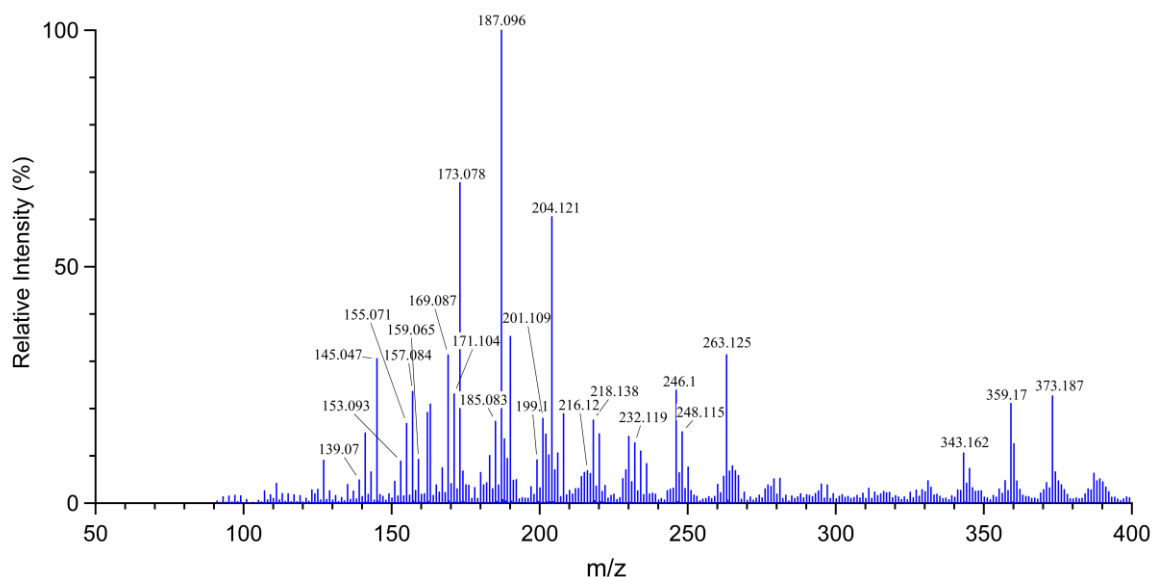


Figure 3.25 Full mass spectrum of oxidation products in the positive ion mode formed from β -pinene photooxidation (400 ppb NO) in the particle phase, obtained with the DART-TOF-MS.

As discussed previously, the product with nominal mass 168 has been identified in the particle phase. However, based on the fragmentation pattern two isobar products have been assigned to the m/z 169 target ion; a C₁₀-hydroxy aldehyde (C₁₀H₁₆O₂) and a hydroxy oxopinone (C₉H₁₂O₃) (see Figure 3.18). The measured accurate mass of this target ion was

found to be 169.087 u. A list of possible compounds with elemental compositions that match the measured m/z was acquired and is given in Table 3.5.

Table 3.5 Possible molecular formulas for β -pinene oxidation products for the m/z 169 product ion (measured accurate mass of 169.087 u). These molecular formulas are established for singly protonated molecular species. Mass errors are expressed in both terms of millimass units (mmu) and parts per million (ppm).

Possible Formula (M+H) ⁺	Calc. Exact Mass	Mass Error (mmu)	Mass Error (ppm)
C ₉ H ₁₃ O ₃	169.086	0.510	3.016
C ₁₀ H ₁₇ O ₂	169.123	-35.999	-212.862
C ₈ H ₉ O ₄	169.050	37.0	218.870

Differentiation between these possible molecular formulas is based on the mass difference between their monoisotopic calculated exact masses and the measured accurate mass. This is defined as mass error (or mass accuracy) and expressed in both terms of millimass units (mmu) and parts per million (ppm). This value can be positive or negative. The mass measurement error is typically described as ppm and it is defined as

$$\text{Mass Error (ppm)} = \frac{\text{Mass Error (accurate mass} - \text{exact mass) (u)}}{\text{Exact Mass}} \times 10^6 \quad (\text{Eq. 3.2})$$

As it can be seen from the Table 3.5, the most likely elemental formula for this target ion is C₉H₁₃O₃ which is the protonated hydroxy oxo-nopinone. The measured accurate mass (169.087) falls within a few parts per million of the theoretical exact mass of this compound. However, the exact mass for the protonated C10-hydroxy aldehyde (C₁₀H₁₇O₂) was about

212 ppm greater than the respective accurate mass. Therefore, the product with molar mass of 168 g mol^{-1} was identified as the hydroxy oxo-nopinone ($\text{C}_9\text{H}_{12}\text{O}_3$) in the particle phase.

These results indicate that mass accuracy is a valuable tool to differentiate between isobaric compounds. However, this method does not help with distinguishing isomeric compounds (molecules with the same molecular formula but different chemical structures). As it was mentioned previously in Section 3.2.2.1, two products were identified to contribute to m/z 187 in the particle phase; pinic acid (M 186, $\text{C}_9\text{H}_{14}\text{O}_4$) and homoterpenylic acid (M 186, $\text{C}_9\text{H}_{14}\text{O}_4$). Since these two products are isomers with the same molecular formula and thus the same accurate mass, they require further analysis for differentiation such as chromatographic separation.

The measured accurate masses for other products were also used in this study for the confirmation of their tentative identification based on the APCI-MS/MS results. In summary, identification of 18 products was confirmed in the particle phase based on their obtained accurate masses with mass accuracy of less than 30 ppm, including differentiating between 9 isobaric compounds. It should be noted that even though this analysis rejected the presence of some of the isobaric compounds, this is only true for the particle phase products and they may be present in the gas phase. The measured accurate masses for all the identified products are provided in the Table D.1 of Appendix D.

3.2.3. Oxidation Product Formation Profiles

Another approach to assist us with product characterization was through comparison of SRM time profiles of reaction products. Thus, the SRM time profiles of products were acquired by monitoring selected precursor to product ion pair signals over the course of the experiment to examine their formation during the photooxidation of β -pinene.

Nopinone has been identified as the major primary product of β -pinene photooxidation (Aschmann et al., 1998; Larsen et al., 2001; Jaoui and Kamens, 2003). Here the nopinone SRM time profile of the $(M+H)^+$ ion pair 139 \rightarrow 121 was acquired to probe the formation of nopinone from β -pinene photooxidation in both gas and particle phases. The SRM profile of β -pinene (target ion m/z 137 ($(M+H)^+$)) was also monitored during the same time period with SRM ion pair 137 \rightarrow 81. As shown in Figure 3.26, the signal associated with β -pinene decreased after initiation of the reaction until almost no β -pinene remained in the chamber, meanwhile, nopinone signal increased due to its formation and finally reached a plateau.

The 139 \rightarrow 121 SRM profile overall is what expected for nopinone. A slight decay in the 139 \rightarrow 121 time profile is due to nopinone reaction with OH radicals after β -pinene was completely depleted. This SRM profile also indicates that there is an equilibrium between nopinone in the gas and particle phase.

In the following example, we demonstrate how comparison of SRM time profiles of reaction products helps to distinguish between products. As mentioned in Section 3.2.1, the MS/MS spectrum of m/z 157 implied contributions from one or more products other than the

nopinone water cluster at m/z 157, as the fragment m/z 111 was not present in the MS/MS spectrum of pure nopinone. Here the SRM profiles of $139 \rightarrow 121$, $157 \rightarrow 139$, and $157 \rightarrow 121$ (nopinone related product ions) were acquired in the gas phase and compared with that of $157 \rightarrow 111$ (unknown). The comparison of the time profiles showed differences in their shape (Fig. 3.27). The nopinone related profiles ($139 \rightarrow 121$, $157 \rightarrow 139$, and $157 \rightarrow 121$) matched in shape over the course of the experiment and reached a plateau, while the $157 \rightarrow 111$ time profile showed a totally different shape as the signal decayed with time. This discrepancy confirms that there is a contribution from at least two products to the m/z 157 target ion.

This shows that SRM scan provides time evolution of oxidation products which could give insights into the identity of the products. Acquiring SRM time profiles was extensively practical for interpreting our aging experiments which is discussed in Section 3.4.

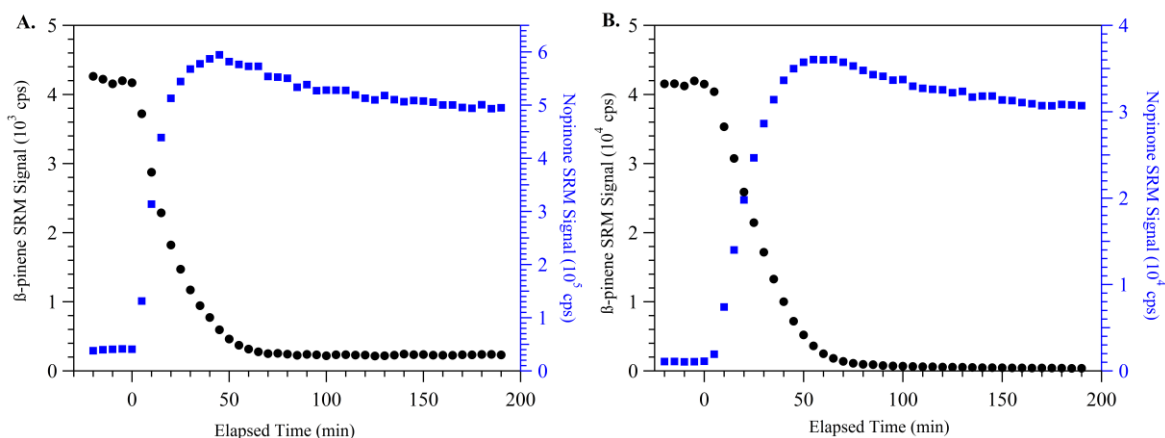


Figure 3.26 SRM time profiles for the ion pairs $137 \rightarrow 81$ (black circles) and $139 \rightarrow 121$ (blue squares) representing β -pinene and nopinone respectively, during the A. gas phase and B. particle phase β -pinene experiments. The initial NO concentrations were 0.7 ppm and 0.4 ppm for the gas and particle phase experiments, respectively. These profiles include the mixing time of the experiments before the lights were turned on and time zero indicates the initiation of OH exposure (lights on).

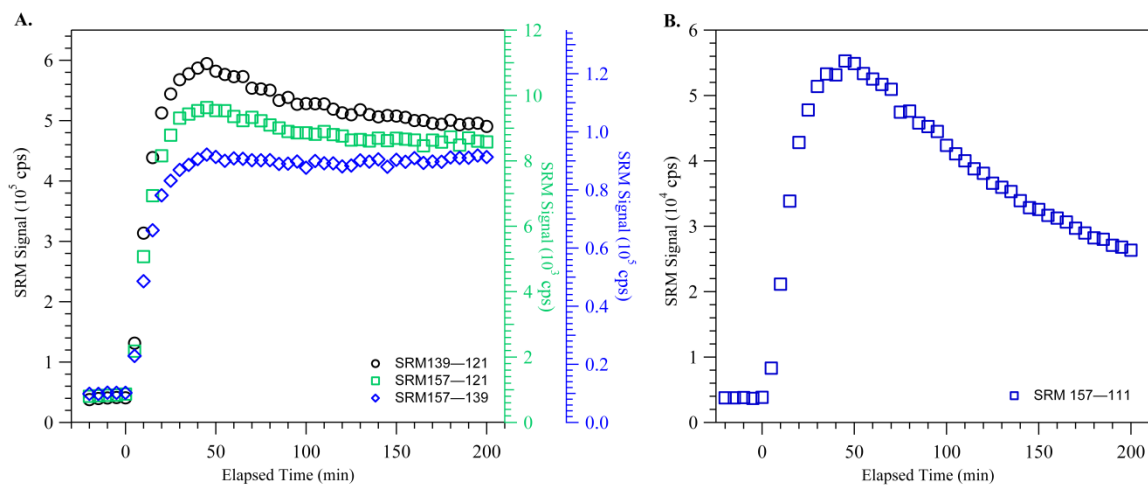
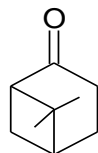


Figure 3.27 β -pinene experiment SRM time profiles for the ion pairs A. 139 \rightarrow 121, 157 \rightarrow 121, 157 \rightarrow 139 and B. 157 \rightarrow 111 showing the formation of m/z 139 and m/z 157 products. It has been identified that some additional products contribute to the target ion m/z 157 besides nopinone's water cluster.

3.2.4. Identification of Nopinone Oxidation Products

3.2.4.1 Nopinone Oxidation by OH

Nopinone has been identified as a primary product in this study (Figure 3.28). The rate constant for the reaction of nopinone with OH radicals ($k \sim 1.5 \times 10^{-11} \text{ cm}^3 \text{ s}^{-1}$) is approximately one fifth of that of β -pinene ($k \sim 7.4 \times 10^{-11} \text{ cm}^3 \text{ s}^{-1}$) (Atkinson and Arey, 2003). Thus, when β -pinene is depleted, there is still an appreciable concentration of nopinone in the chamber. As a result, OH radicals react dominantly with nopinone and result in further formation of secondary oxidation products.



Nopinone
(M138)
C₉H₁₄O

Figure 3.28 The structure of nopinone, primary product of β -pinene oxidation.

In this study we performed several OH-initiated nopinone experiments to identify the products formed from the nopinone+OH reaction, to gain more insight into the previously identified products from β -pinene experiments. For these experiments, the initial reagent mixing ratios were approximately 0.4 ppm nopinone, 2 ppm IPN and 0.4-2 ppm NO. Note that due to the lower rate of nopinone+OH reaction, five times higher IPN concentration was used for nopinone experiments. Figure 3.29 shows the positive full spectrum of particle phase reaction products within the mass range of 10 - 400 u acquired during a nopinone photooxidation experiment.

Comparison of the positive full spectrum of β -pinene particle phase oxidation products (Figure 3.16) with that of nopinone (Figure 3.29) indicates numerous similarities. A number of peaks that have been observed during β -pinene photooxidation were also detected in nopinone photooxidation experiments, including m/z 155, 157, 171, 173, 185, 187, 201 and 246. The comparison of the MS/MS fragmentation patterns of these detected peaks from nopinone/OH with those of β -pinene/OH confirmed the formation of hydroxy nopinone (m/z 155), norpinalic acid (or C8-keto acid, m/z 157), pinalic 3-acid (or pinalic 4-acid, m/z 171),

norpinic acid (m/z 173), a C₉ carboxylic acid (m/z 185) and pinic acid (m/z 187) during nopinone photooxidation experiments. However, since the previously identified C₁₀-hydroxy pinonic acid (m/z 201) and the C₁₀-PAN (m/z 246) from β-pinene oxidation contain 10 carbons, they cannot form from nopinone oxidation. This indicates contributions from different species to these masses.

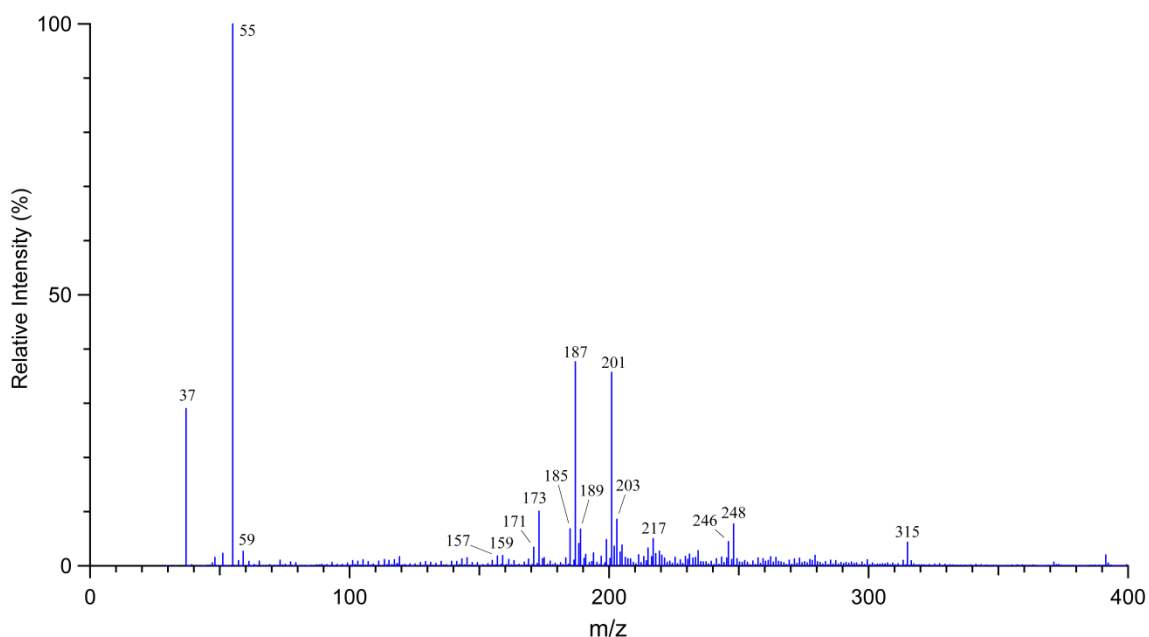


Figure 3.29 Full mass spectrum of oxidation products formed from nopinone photooxidation in the particle phase.

The β-pinene (+)MS/MS of m/z 201 shows a fragment ion at m/z 169 corresponding to a loss of 32 u (CH₃OH), which was not observed in the nopinone (+)MS/MS of m/z 201 (Fig. 3.30). This mass loss is consistent with the structure of the C₁₀-hydroxy pinonic acid (Table D.1, Appendix D). The differences observed in the (+)MS/MS fragmentation spectra of m/z 201 during the β-pinene and nopinone experiments, further supports the contribution from

two or more species into the m/z 201. No studies in the literature have yet investigated the formation of products from nopinone oxidation. In addition no possible carboxylic acid product with molar mass of 200 g mol^{-1} was proposed in the MCM to form from nopinone oxidation. Therefore, at this point the identification of the m/z 201 produced from nopinone oxidation is limited to be proposed as a carboxylic acid with a maximum C9 backbone.

The observed product during the nopinone photooxidation at m/z 246 $(M+H)^+$, is an organic nitrate which should contain a maximum of C9. A C9 organic nitrate with molar mass of 245 g mol^{-1} will have the molecular formula of $C_9H_{12}NO_7$. According to the MCM, there is a PAN compound that is proposed to form from nopinone oxidation with the same molecular formula (Fig. 3.31). Thus, this product could potentially contribute to the m/z 246 during nopinone experiments.

The majority of the detected products from nopinone photooxidation were carboxylic acids. The previously identified organic nitrates from β -pinene photooxidation, such as the C10-aldehyde nitrate (m/z 214), the C10-bicyclic hydroxy nitrate (m/z 216), the C10-monocyclic hydroxy nitrate (m/z 218), and the C10-dihydroxy nitrate (m/z 232) were not observed as intense peaks in the obtained full mass spectrum from nopinone experiments (Fig. 3.29). This is consistent with the fact that all these organic nitrates are C10 and are not expected to form from nopinone oxidation. The possible formation of these masses via nopinone indicates that the structure of these organic nitrates will contain a maximum of C9. As shown in Table D.1 (Appendix D), there are C9-bicyclic dioxo nitrate (m/z 214, $C_9H_{11}NO_5$), C9-monocyclic dioxo nitrate (m/z 216, $C_9H_{13}NO_5$), C9-dihydroxy nitrate (m/z 218, $C_9H_{15}NO_5$)

and C9-dihydroxy-oxo nitrate (or C9-oxo nitrate acid, C9-dioxo hydroxy nitrate; m/z 232, $C_9H_{13}NO_6$) compounds that may form from β -pinene oxidation. Due to their very low signal intensities during the nopinone experiments, the MS/MS was unable to be used on these organic nitrates to help with their identification.

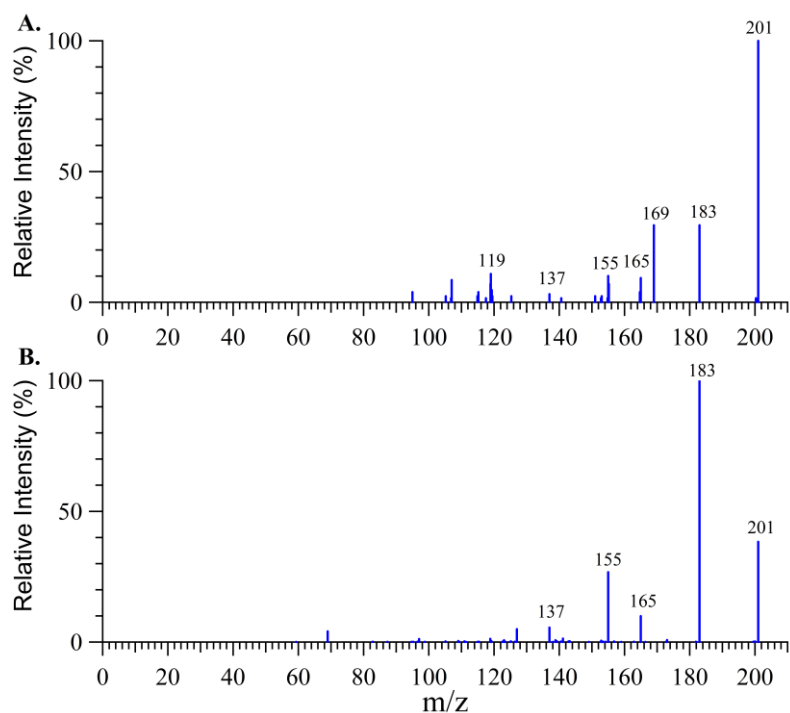


Figure 3.30 Comparison of (+)MS/MS spectra of the target ion m/z 201 from A. a β -pinene/OH experiment in the particle phase and B. a nopinone/OH experiment in the particle phase. Both spectra were acquired at collision energy of 10 eV.

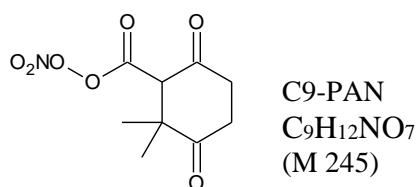


Figure 3.31 Proposed C9-organic nitrate product with molar mass of 245 g mol^{-1} in the MCM.

To check for the presence of these organic nitrates, their SRM time profiles were obtained during a nopinone experiment as SRM offers the highest sensitivity towards the products. Looking at these nitrates' SRM time profiles (Figure 3.32), it was found that the SRM signal intensities for these nitrates were very low (< 100 cps). Moreover, these nitrates react with OH radicals upon formation. This behaviour was not observed for organic nitrates generated during β -pinene photooxidation experiments, most likely due to the fact that the OH concentration was 5 times lower than the nopinone experiments. This suggests that organic nitrates form during nopinone photooxidation, but they are not as dominant as the carboxylic acids. It should be noted that since five times higher IPN concentration was used during nopinone/OH experiments, the formation of these C9 nitrates may not be expected during β -pinene photooxidation experiments.

Information obtained from nopinone experiments were beneficial in interpreting the results of our aging experiments as well as in evaluating the formation mechanisms of identified products which is discussed in detail in Sections 3.4 and 3.5, respectively.

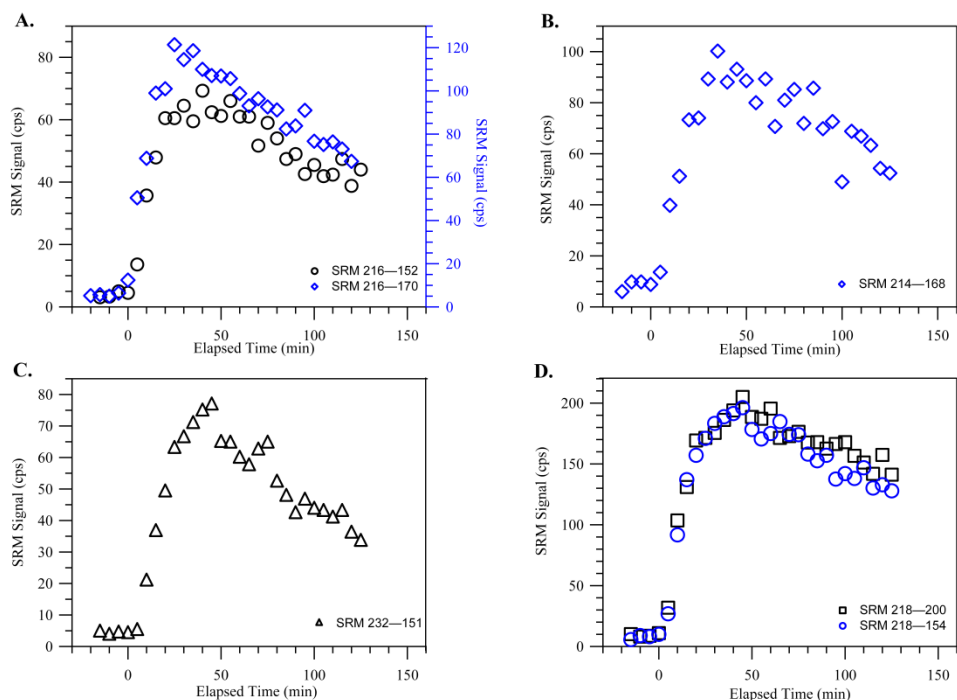


Figure 3.32 Nopinone experiment SRM time profiles for the ion pairs A. 216→152 and 216→170, B. 214→168, C. 232→151 and D. 218→200 and 218→154. These profiles demonstrate low signal intensities for these organic nitrates, as well as the decay of their signal intensities due to possibly further reaction with OH radicals.

3.2.4.2 Nopinone Oxidation by NO_3

We conducted several NO_3 -initiated nopinone experiments to identify the products formed from the nopinone+ NO_3 reaction to gain insight into the differences between OH and NO_3 chemistry. This was towards our objective to understand if there is a correlation between the SOA density and the particle composition, as discussed in Section 3.1.2.3.

Figure 3.33 shows the positive full spectrum of particle phase reaction products within the mass range of 10 - 400 u acquired during a nopinone/ NO_3 experiment. A number of even

m/z were detected at 218, 220, 232, 234, 238, 248 and 262, which are suspected to be organic nitrates. The acquired (+)MS/MS scan for each individual m/z demonstrated similar losses of 18, 46, 63, 79 and 81 where the most intense fragment corresponded to the loss of 46. These losses were consistent with the structure of PAN compounds and therefore, were interpreted as PANs. In addition, (+)MS/MS spectra for the observed $[M+H]^+$ peaks at m/z 159, 171, 173, 185, 187, 189, 199, 201, 215, 279 and 295 were obtained. The fragmentation spectra of these compounds consistently showed an abundant loss of H₂O (18) and a loss of CO and H₂O (46) as well as a minor loss of 2 H₂O (36) and a loss of CO (28). Furthermore, the fragmentation spectra of the corresponding $[M-H]^-$ ions in the negative mode showed a dominant loss of CO₂ (44) which further proves the presence of acid functionality in these compounds. Therefore, these compounds can be assigned to one of the dicarboxylic acid, oxocarboxylic acid or hydroxycarboxylic acid classes. It should be noted that m/z 215, 279 and 297 were not observed during nopinone photooxidation experiments.

Comparison of products formed from NO₃-induced oxidation of nopinone with that of OH indicates different particle compositions. It was observed that the nopinone/NO₃ oxidation leads to contribution of high molecular weight organic nitrates (PANs) to the particle contents. This is consistent with the observed higher SOA density measured for nopinone/NO₃ system in Section 3.1.2.3, as these PANs are expected to have low vapour pressures.

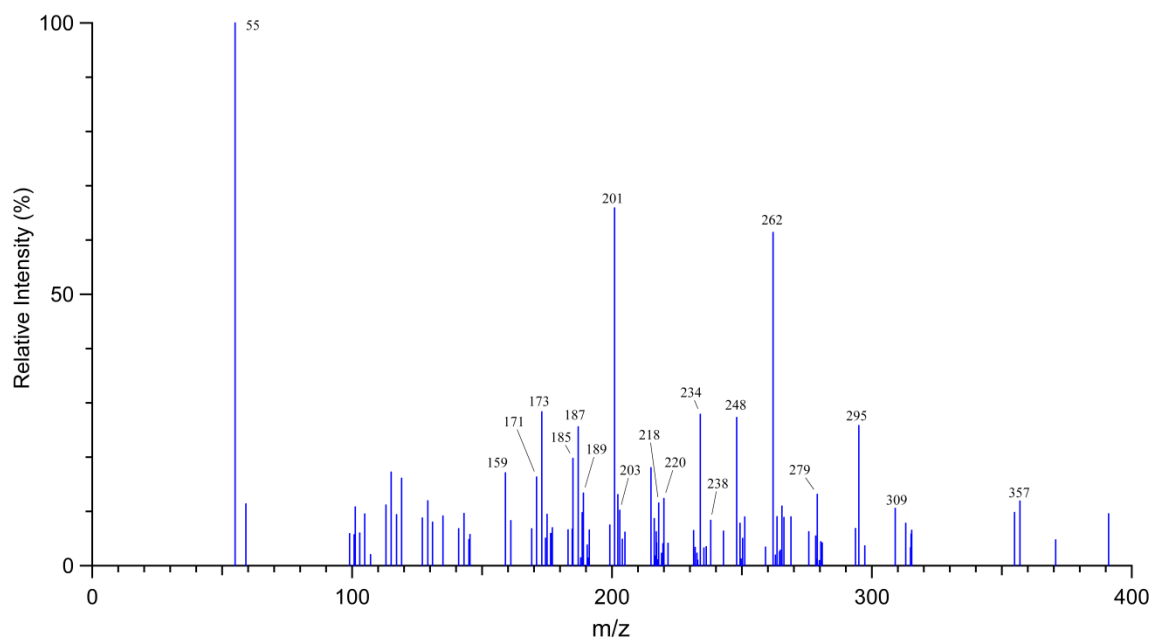


Figure 3.33 Full mass spectrum of oxidation products formed from nopinone oxidation with NO_3 in the particle phase. The MS spectrum is subtracted from that of the chamber background.

3.3. Impact of NO_x on SOA Yield and Composition of Products

In this study, we investigated SOA formation from β -pinene photooxidation in the York University smog chamber as well as Jülich Plant Atmosphere Chamber (JPAC) under a range of NO_x concentrations which will be described in the following Sections.

3.3.1. York University

3.3.1.1 Impact of NO_x on SOA Formation

To investigate the dependence of SOA yield on the NO_x level, the organic particulate yield was obtained for a series of β -pinene photooxidation experiments with varied NO_x levels. These experiments were performed in the presence of ammonium sulfate seed aerosol. SOA yields were determined by taking the ratio of the organic particle mass formed, obtained from SMPS and corrected for wall losses, to the mass of consumed β -pinene, measured by GC-FID (Eq. 3.3).

$$Y = \frac{\textit{Particle mass}}{\beta - \textit{pinene consumption}} \quad \text{Eq. 3.3}$$

Table 3.6 shows a summary of the experimental conditions and results for the β -pinene/NO_x photooxidation experiments. Figure 3.34 shows SOA yields as a function of initial NO_x concentration, [NO_x]₀.

Table 3.6 Experimental conditions and results for β -pinene/ NO_x photooxidation experiments conducted in the York University smog chamber.

$[\text{NO}_x]_0$ (ppm) ^a	β -pinene reacted/ 10^3 ($\mu\text{g m}^{-3}$)	$[\text{OH}]/10^6$ (cm^{-3})	$\text{PM}/10^3$ ($\mu\text{g m}^{-3}$) ^b	$[\text{BVOC}]_0/[\text{NO}_x]_0$ (ppbC ppb ⁻¹)	SOA yield (%)
0.16	3.1	3.1	2.9	32.7	94
0.17	2.5	4.6	3.0	26.4	119
0.28	2.3	8.9	4.1	14.6	177
0.35	2.4	9.9	3.9	11.2	166
0.55	2.6	9.2	3.6	8.3	138
0.56	2.5	9.8	3.6	8.2	143
0.83	2.6	7.2	3.2	5.4	122
1.43	2.4	5.7	1.6	3.1	67
1.59	2.7	4.7	1.4	3.2	51
1.65	2.6	4.3	1.2	2.9	45

^aInitial NO_x concentration before OH production, ^b Particle mass concentration (PM), assuming a SOA density of 1.2 g cm^{-3} . These values have been corrected for wall losses.

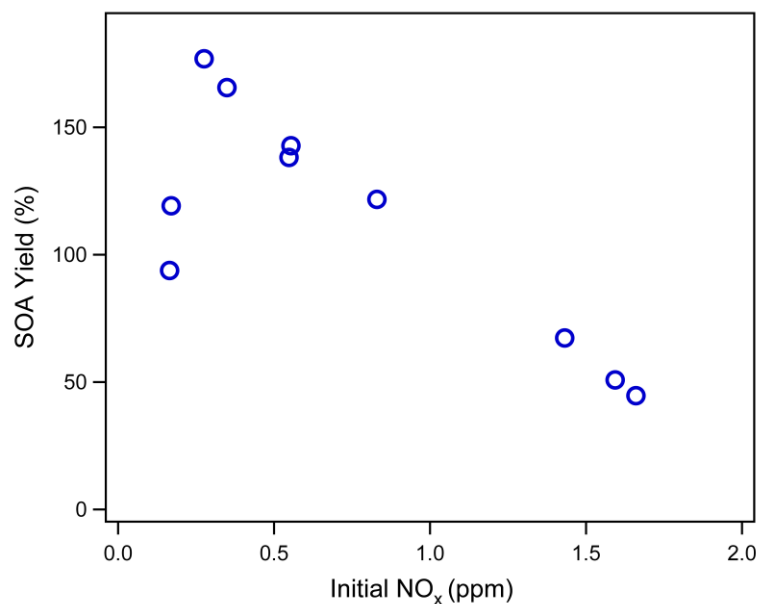


Figure 3.34 Measured SOA yield for the β -pinene photooxidation as a function of the initial NO_x concentration. Each point corresponds to one experiment.

The yield profile showed an inverse dependence to NO_x level, with higher SOA yield found under lower-NO_x condition. However, SOA yield increased with increasing NO_x under lower-NO_x conditions. It should be noted that since SOA yield is defined on a mass basis, the addition of O and N atoms on oxidation can result in a yield higher than 100%. The observed high β-pinene SOA yield is consistent with the previous β-pinene photooxidation experiments carried out in the York University smog chamber, which ranged from 40% under high initial NO mixing ratios (2-2.5 ppm) up to approximately 100% under lower initial NO mixing ratios (0-0.2 ppm) based on a SOA density of 1 g cm⁻³ (Auld, 2009).

At low-NO_x concentrations we observed an increase in SOA yield with increasing NO_x, whereas at high-NO_x levels the yields decreased. Having different NO_x dependencies in different NO_x regimes suggests multiple factors at play. Kroll et al. (2006) suggested that the increase in SOA yield of isoprene with NO_x could be due to changes in the [NO]/[HO₂] ratio. As experiments in batch reactors proceed, NO_x concentrations decrease due to their reactions with OH resulting in a switch from high-NO_x to low-NO_x conditions. The lowered NO concentrations cause increasing HO₂ concentrations due to the suppression of reaction (R3.4):



In such experiments, peroxy radicals initially react mainly with NO, whereas peroxy radicals formed later from first generation products, primarily react with HO₂.

In addition, Camredon et al. (2007) noted that SOA formation enhancement under lower- NO_x condition could be due to the influence of OH levels. However, in the majority of studies investigating the impact of NO_x on SOA formation, OH concentration was either not measured or the potential influence of OH was not discussed in detail (Eddingsaas et al., 2012a, 2012b; Xu et al., 2014).

The measured OH concentration profile during our study indicates that concentration of OH varies by NO_x level. As illustrated in Fig. 3.35, OH concentration increased at lower NO_x levels, passed through a maximum ($\sim 1 \times 10^7 \text{ cm}^{-3}$) at $[\text{NO}_x]_0 \sim 0.35 \text{ ppm}$ and then declined at higher NO_x levels.

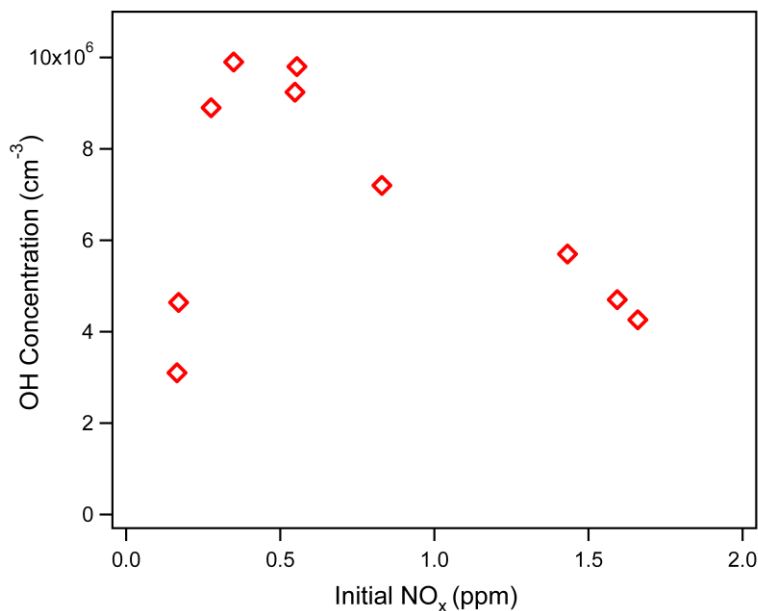


Figure 3.35 Measured OH concentration during β -pinene photooxidation experiments as a function of initial NO_x concentration ($[\text{NO}_x]_0$).

The variation in OH is explained by two reactions. At low- NO_x levels, OH production is expected to increase with NO_x addition due to the increased rate of the OH recycling reaction

(R3.4). As the $[\text{NO}_x]$ is further increased, the OH termination reaction (R3.5) dominates and thus NO_x is acting as a sink for OH.



Hence, OH concentration increased with increasing NO_x , reached a maximum value and then declined. In general terms this is consistent with the nonlinear dependence of OH concentration on NO_x level in the lower troposphere (Ehhalt and Rohrer, 1995).

Comparison of the SOA yield profile (Fig. 3.34) with that of OH concentration (Fig. 3.35) shows their correlation with each other, indicating that the SOA yield is dependent on changes in $[\text{OH}]$. One possible reason for the impact of OH on SOA formation is secondary reactions. SOA yields depend on the extent of the secondary reactions, which means to what extent the first generation products undergo further oxidation to form secondary products. For instance, nopinone is the main intermediate product from β -pinene oxidation. When β -pinene is depleted, an increased OH concentration results in further reaction of nopinone with OH radicals, leading to further formation of condensable species. As a result, SOA mass will be higher at higher OH concentrations and therefore, SOA yield based on only β -pinene consumption will be higher.

We examined the dependence of SOA mass formation on OH concentration through the β -pinene decay and organic mass formation profiles under varied NO_x levels in our β -pinene photooxidation experiments (Fig. 3.36). These profiles show that under lower- NO_x conditions, β -pinene reacts away with OH radicals more rapidly and results in higher particle

mass formation, which is consistent with the higher OH concentration. To better show the correlation of β -pinene decay and particle mass formation profiles with that of [OH] and SOA yield, we color coded the NO_x levels as green for lower- NO_x levels ($[\text{NO}_x]_0 < 0.2$ ppm), blue for moderate- NO_x levels ($0.2 < [\text{NO}_x]_0 < 1$ ppm) and red for higher- NO_x levels ($[\text{NO}_x]_0 > 1$ ppm) (Fig. 3.36). At moderate- NO_x conditions where the OH concentration reached the maximum, aerosol growth was sustainably higher. In addition, at moderate- NO_x level, the particle mass continues to increase after all β -pinene was consumed which results in a vertical section in the curve. This further supports the importance of secondary reactions.

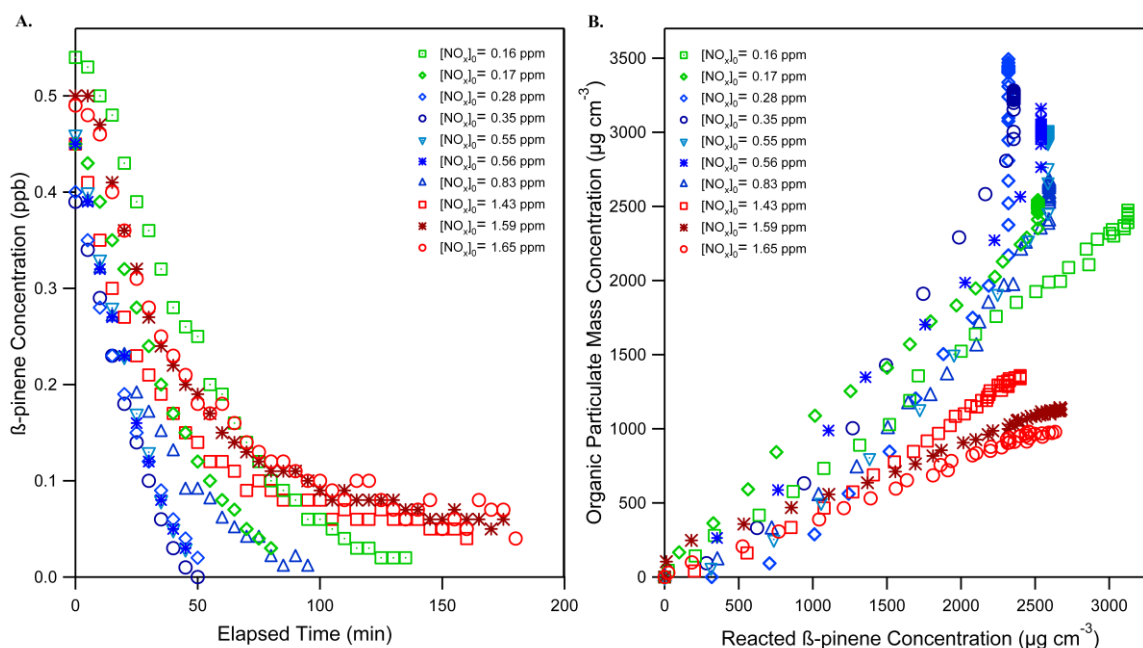


Figure 3.36 β -pinene decay profile (A) and organic particle mass formation as a function of reacted β -pinene (B) over the course of β -pinene photooxidation experiments under different NO_x conditions. Each curve represents a single experiment. Here, lower- NO_x conditions ($[\text{NO}_x]_0 < 0.2$ ppm), moderate- NO_x conditions ($0.2 < [\text{NO}_x]_0 < 1$ ppm) and higher- NO_x conditions ($[\text{NO}_x]_0 > 1$ ppm) were plotted in green, blue and red, respectively.

In addition, nopinone formation profiles under varied NO_x levels demonstrated further reaction of nopinone under moderate- NO_x levels (Fig. 3.37). This is consistent with the hypothesis discussed above, stating that nopinone further reacts under moderate- NO_x levels due to the higher OH concentration in the system. It is noted that only NO_x experiments with similar water peaks intensity (m/z 55 and 37) were selected for the purpose of comparison to avoid the impact of protonation on reaction products' SRM signal. As illustrated in Figure 3.37, nopinone SRM signals at two of the moderate- NO_x levels (0.28 and 0.35 ppm) start to decline at approximately 60-70 minutes. Comparing this with the corresponding β -pinene decay for these two NO_x levels in Figure 3.36A, indicates that almost all the measurable β -pinene was removed in about 50-60 minutes. Due to the detection limit of GC we are not able to determine the exact time that no measurable β -pinene is present in the system. This ascertains that OH radicals further react with the first generation products such as nopinone after β -pinene is depleted, resulting in further particle mass production.

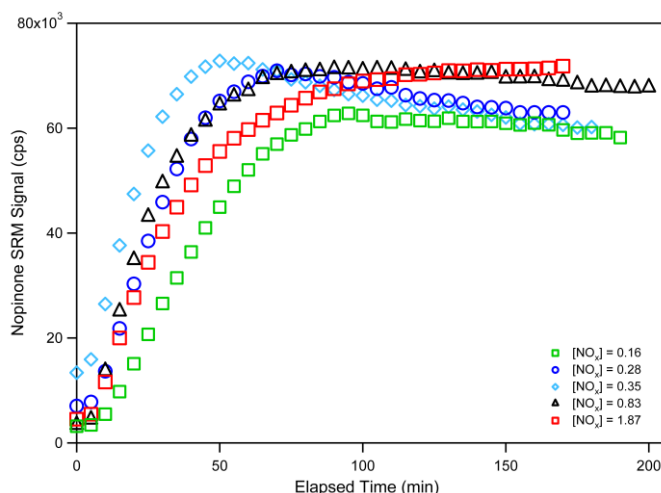


Figure 3.37 SRM time profiles for the ion pairs 139→121 representing nopinone during particle phase β -pinene experiments under varied NO_x conditions. Time zero indicates the initiation of OH exposure (lights on).

These findings are consistent with the results of other studies (Song et al., 2007; Eddingsaas et al., 2012a, 2012b; Ng et al., 2007a) illustrating that the unsaturated first-generation products formed from some parent hydrocarbon could further react with the oxidants (OH, O₃, or NO₃) to generate more oxidized products, contributing to the SOA growth.

3.3.1.2 NO_x Sensitivity of Identified Products

In this study, besides investigating the dependence of SOA yield on NO_x, we also examined the NO_x sensitivity of individual oxidation products. This was intended to provide insights into the dependence of the formation mechanism of individual products on NO_x level. The SRM time profiles, using the (M+H)⁺ precursor ion, for selected β-pinene/OH reaction products were acquired to examine the products formation under different NO_x levels. The impact of NO_x on the formation of nopinone (M 138), a few carboxylic acids (norpinic acid (M 172), pinic acid (M 186), and C10-hydroxy pinonic acid (M 200)) and a few organic nitrates (C10-bicyclic hydroxy nitrate (M 215), C10-monocyclic hydroxy nitrate (M 217), C10-dihydroxy nitrate (M 231) and C10-PAN (M 245)) are presented here.

As illustrated in Figure 3.37, nopinone formation was found to be insensitive to the variation in NO_x levels, whereas the formation of norpinic acid, pinic acid and C10-hydroxy pinonic acid demonstrated inverse NO_x dependence; enhanced under low-NO_x (Fig. 3.38). As discussed in Section 3.3.1.1, SOA yield is dependent on OH concentration. Since [OH] changes with NO_x level, this complicates investigating the impact of NO_x on SOA production. The same applies for interpreting the NO_x sensitivity of reaction products.

Although the majority of carboxylic acids showed inverse NO_x dependency, the SRM signal of the lowest NO_x experiment was not the highest in the SRM time profiles for these acids (green markers in Fig. 3.38). This is due to the fact that the respective OH concentration was the lowest for this NO_x level (Fig. 3.35). This indicates that the SRM signal of the carboxylic acid products followed the same pattern as SOA yield; it was relatively low at the lowest NO_x levels, reached maximum at the moderate- NO_x levels and then declined at the highest NO_x levels. Since carboxylic acid dependency on NO_x is consistent with that of SOA yield, this agrees well with our expectation that carboxylic acids contribute the most to the organic particle mass.

It was observed that the SOA yields measured at $[\text{NO}_x]_0 \sim 143\text{-}165$ ppm were lower than that at $[\text{NO}_x]_0 < 0.2$ ppm while their respective OH concentrations were higher (Figs. 3.34-3.35). In addition, the SRM signal for the highest NO_x experiment is lower than that of the lowest NO_x experiment in the SRM time profiles of these carboxylic acids (red markers compared with green markers in Fig. 3.38). This indicates that the impact on [OH] is not the sole consequence of NO_x addition and other possible effects of NO_x has to be considered.

Comparison of the NO_x dependence profiles with the proposed formation mechanism indicates that those products form via $\text{RO}_2 + \text{HO}_2$ pathway such as norpinic acid, pinalic 3-acid (or pinalic 4-acid), pinic acid and C10-hydroxy pinonic acid, showed formation enhancement under lower- NO_x conditions which is expected from the RO_2 competitive chemistry. The formation mechanisms is presented in detail in Section 3.5.

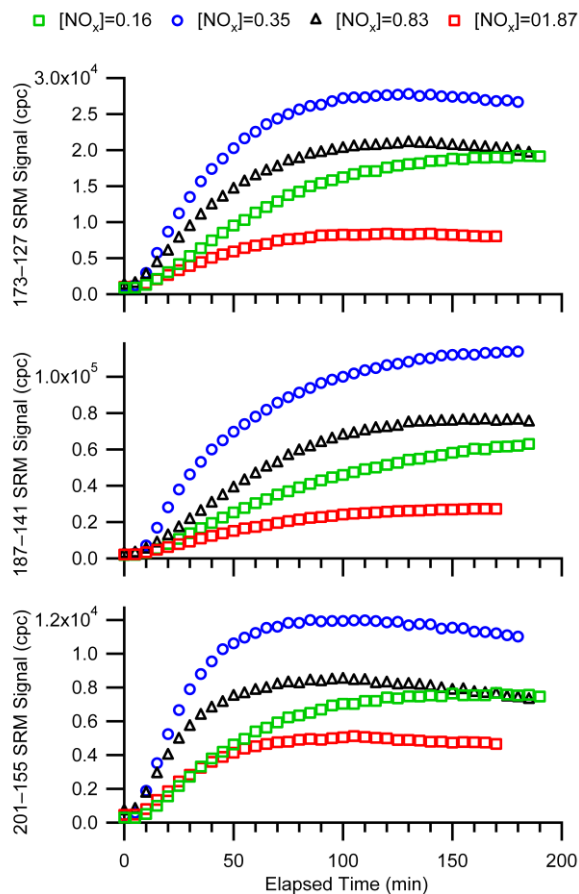


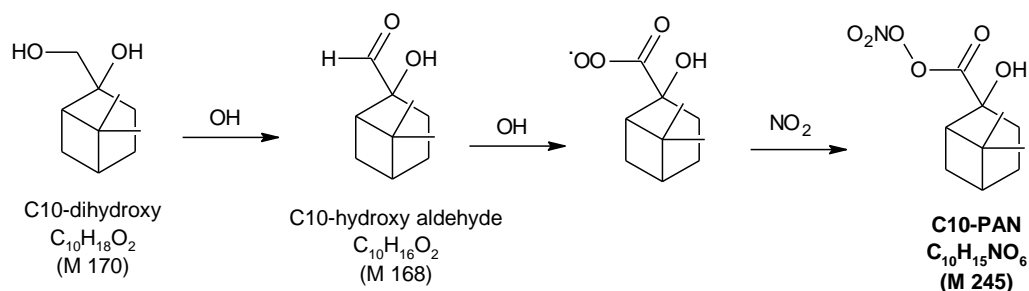
Figure 3.38 SRM time profiles for the ion pairs 173→127, 187→141 and 201→155 representing the norpinic acid, pinic acid and C10-hydroxy pinonic acid respectively, acquired at varied NO_x levels. These profiles demonstrated to be dependent on NO_x level.

The effect of NO_x on the formation of a few organic nitrates is presented in Figure 3.39. In contrast to carboxylic acids, nitrate products did not demonstrate a similar NO_x sensitivity profile among them. The interplay of the OH effect with that of NO_x is even more complicated for nitrate products. For instance, SRM time profile for the C10-bicyclic hydroxy nitrate (ion pair 216→152) exhibits almost a NO_x insensitive profile, if we assume that the SRM signal of the lowest NO_x experiment (0.16 ppm) is only low due to the very low OH concentration. However, the C10-bicyclic hydroxy nitrate formation could also be

enhanced under higher-NO_x condition and competed with the enhanced formation caused by higher OH concentration under moderate-NO_x condition. When these two effects (NO_x and OH) are comparable without one being dominated, it causes complication in determining the NO_x sensitivity of products. Hence, without being able to eliminate the impact of OH from that of NO_x it would not be possible to interpret the true impact of NO_x on the formation of all products.

SRM time profiles of the C10-monocyclic hydroxy nitrate (ion pair 218→200) and the C10-dihydroxy nitrate (ion pair 232→151) revealed to be nearly enhanced under higher-NO_x levels as on average the signals of the higher NO_x experiments are higher. This is consistent with the formation mechanism of organic nitrates which is through RO₂ + NO pathway and is favored under higher-NO_x conditions.

On the contrary, SRM time profile of C10-PAN (ion pair 246→200) demonstrates formation enhancement under low-NO_x condition. The formation mechanism for this product is proposed as:



According to this mechanism the pathway of C10-PAN is not through RO₂ + NO channel. We believe the formation of the C10-hydroxy aldehyde is the limiting step in the proposed

mechanism and since the C10-hydroxy aldehyde exhibited enhancement under low-NO_x conditions, thus C10-PAN follows the same NO_x sensitivity.

Observing different behaviours to changes in NO_x levels for organic nitrates, suggests that the general RO₂ + NO formation pathway for organic nitrates is not the only factor that controls the influence of NO_x.

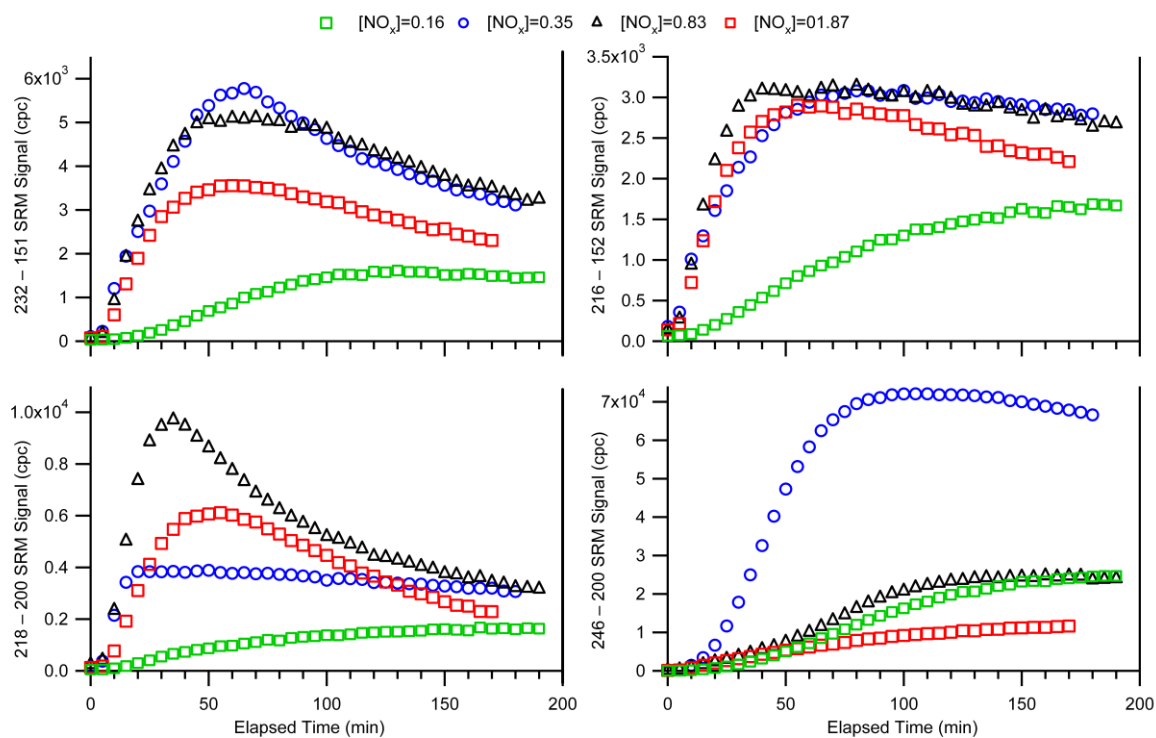


Figure 3.39 SRM time profiles for the ion pairs 216→152, 218→200, 232→151 and 246→200 representing the C10-bicyclic hydroxy nitrate, C10-monocyclic hydroxy nitrate, C10-dihydroxy nitrate and C10-PAN respectively, acquired at varied NO_x levels.

The NO_x sensitivity profiles have been investigated for other products in this study as well which is presented in Table D.1 of Appendix D.

3.3.2. Jülich Plant Atmosphere Chamber (JPAC)

3.3.2.1 Impact of NO_x on SOA Formation

To further explore the influence of NO_x on SOA formation, a series of NO_x experiments were conducted in the JPAC in which β-pinene was oxidized in the absence of inorganic seed aerosol. A summary of experimental conditions and results for the β-pinene/NO_x photooxidation experiments is provided in Table 3.7. Figure 3.40 illustrates SOA yields, calculated from wall-loss corrected maximum particle mass concentration (PM_{max}), as a function of [BVOC]₀/[NO_x]₀ ratio and [NO_x]₀. SOA yield demonstrates strong dependence on [BVOC]₀/[NO_x]₀ and [NO_x]₀ levels. At low-NO_x conditions an increase in the initial NO_x concentration increases the SOA yield, whereas at high-NO_x concentrations the opposite SOA yield dependence on NO_x was observed. Similar NO_x dependencies of SOA yields have been observed in our York University NO_x experiment as well as some of the previous studies (Pandis et al., 1991; Kroll et al., 2006; Zhang et al., 1992; Camredon et al., 2007, Xu et al., 2014).

Similar to the results of the NO_x experiments conducted in the York University chamber, the concentration of OH was found to change noticeably by varying NO_x concentration in the JPAC (Fig. 3.41). OH concentrations passed through a maximum ($\sim 3.8 \times 10^7 \text{ cm}^{-3}$) at [NO_x]_{ss} ~ 40 ppb ([NO_x]₀ ~ 70 ppb) which represented a 4-fold increase over that in the absence of NO_x. In this study, NO_x enhanced OH production in two ways: by recycling OH through reaction (R3.4), as well as by increasing [O₃] and thereby the photolytic OH source

(R2.7-2.8). As mentioned previously, NO_x is acting as a sink for OH at very high- NO_x concentrations due to Reaction (R3.5).

Correlation between changes in SOA yield and [OH] again proves that SOA yield is dependent on [OH] (Fig.3.41). Hence, we performed some experiments to investigate the dependence of SOA formation on OH concentration in more detail.

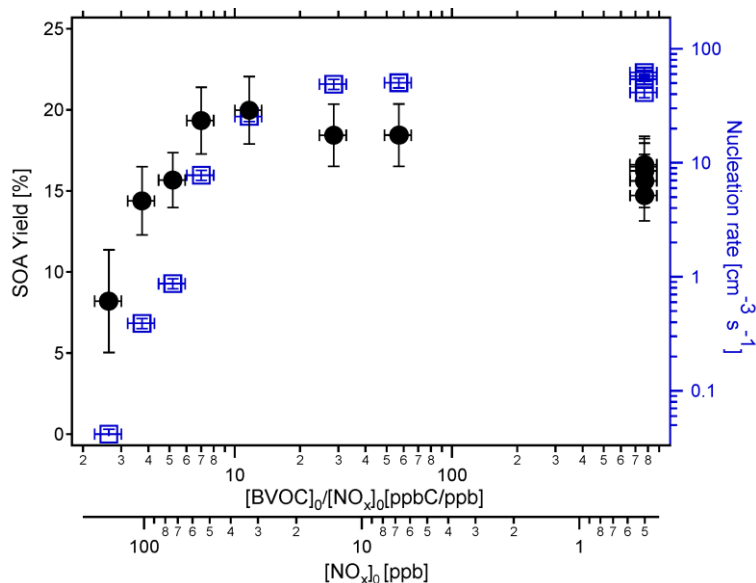


Figure 3.40 Measured SOA yield from PM_{max} (black circles) and rates of new particle formation (blue squares) for the β -pinene photooxidation as a function of the ratio of the initial hydrocarbon to the initial NO_x concentration and as a function of the initial NO_x concentration. Each point corresponds to one experiment. The errors in nucleation rate and $[\text{NO}_x]$ were estimated to be $\pm 10\%$. The error in SOA yield was estimated from error propagation using the sum of the systematic error, correction procedure error and error in BVOC data. Note that the horizontal error bars are associated with the BVOC/ NO_x axis.

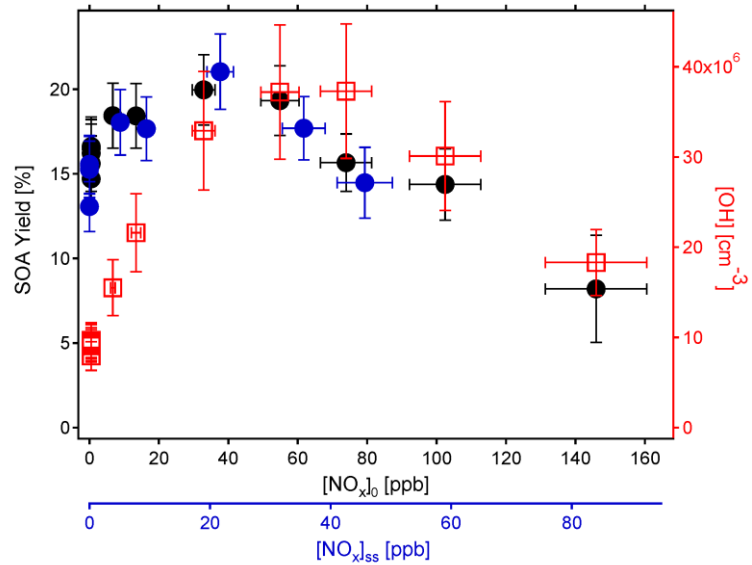


Figure 3.41 Measured SOA yield from PM_{max} and from steady state PM (black and blue circles respectively) and measured OH concentration (red squares) as a function of initial ([NO_x]₀) and steady state ([NO_x]_{ss}) NO_x concentrations. The errors in [OH] and [NO_x] were estimated to be ± 20 % and ± 10 % respectively. The error in SOA yield was estimated from error propagation using the sum of the systematic error, correction procedure error and error in BVOC data.

Table 3.7 Experimental conditions and results for β -pinene/ NO_x photooxidation experiments conducted in the JPAC.

β -pinene reacted (ppb)	$[\text{NO}_x]_0$ (ppb) ^a	$[\text{NO}_x]_{ss}$ (ppb) ^b	$[\text{OH}]/10^7$ (cm^{-3}) ^c	PM_{max} ($\mu\text{g m}^{-3}$) ^d	PM_{ss} ($\mu\text{g m}^{-3}$) ^e	J_3 ($\text{cm}^{-3} \text{s}^{-1}$) ^f	$[\text{BVOC}]_0/[\text{NO}_x]_0$ (ppbC ppb ⁻¹)	SOA yield ^g (%)	SOA yield ^h (%)
33.9	73.9	34.4	3.7	30.3	-----	0.9	5.2	15.7	----
34.0	54.8	35.5	3.7	37.6	34.4	7.8	7.0	19.3	17.7
30.4	145.9	86.1	1.8	14.3	-----	0.04	2.6	8.2	----
31.4	13.4	9.5	2.2	33.1	31.7	48.9	28.6	18.4	17.7
33.1	102.5	45.7	3.0	27.2	27.2	0.4	3.7	14.4	14.5
33.5	32.9	21.7	3.3	38.2	40.2	25.5	11.7	20.0	21.0
29.4	6.7	5.1	1.5	30.9	30.3	50.3	57.0	18.4	18.0
23.7	<0.5	<1.0	0.8	20.0	17.7	41.3	765	14.7	13.1
25.3	<0.5	<1.0	0.9	23.5	22.1	57.5	768	16.2	15.3
25.7	<0.5	<1.0	0.9	24.4	22.8	62.0	768	16.6	15.5
25.3	<0.5	<1.0	0.9	23.8	22.5	54.2	768	16.5	15.6
25.7	<0.5	<1.0	1.0	22.9	22.8	53.8	767	15.6	15.5

^a Initial NO_x concentration before OH production. The error in $[\text{NO}_x]$ was estimated to be $\pm 10\%$, ^b NO_x concentration during steady state, in cases without NO_x addition we found increasing NO_x which is assumed to be produced from residual HNO_3 that is photolyzed by the TUV lamp, ^c The error in $[\text{OH}]$ was estimated to be $\pm 20\%$, ^d Maximum formed particle mass concentration, assuming a SOA density of 1.2 g cm^{-3} . These values have been adjusted for wall losses and losses on particles, ^e Particle mass concentration during steady state, assuming a SOA density of 1.2 g cm^{-3} . These values have been adjusted for wall losses and losses on particles, ^f Rates of new particle formation for particles greater than 3 nm, ^g SOA yields determined from PM_{max} . The error in SOA yield was estimated from error propagation using the sum of the systematic error, correction procedure error and error in BVOC data, ^h SOA yields determined from PM_{ss} .

3.3.2.2 [OH] Dependence of SOA Formation

To examine the dependency of SOA yields on the OH concentration, additional experiments were carried out at two different OH production rates and the β -pinene concentration was varied to give a range of SOA mass. The detailed experimental conditions are given in Table 3.8. By setting the TUV gap to 15 cm and 45 cm, two different $J(O^1D)$ conditions ($1.9 \pm 0.2 \times 10^{-3} \text{ s}^{-1}$ and $5.7 \pm 0.5 \times 10^{-3} \text{ s}^{-1}$) were achieved that gave considerably different OH production rates at otherwise unchanged conditions. The OH concentrations were $4 \times 10^7 - 1 \times 10^8 \text{ cm}^{-3}$ and $1.2 - 1.6 \times 10^8 \text{ cm}^{-3}$ under low- and high-OH conditions, respectively. Approximately 90-95 % of the total β -pinene was consumed in these experiments.

The maximum particle mass corrected for wall losses was plotted as a function of consumed β -pinene, ranging from 20 to $140 \mu\text{g m}^{-3}$ (Fig. 3.42). The slopes were then used to determine the incremental mass yields. Figure 3.42 shows that the SOA yields were higher at higher OH levels ($31 \pm 3 \%$ and $20 \pm 1 \%$ for high- and low-OH conditions, respectively). It should be noted that forcing the intercept of the linear regression lines to zero has little effects on the slopes ($\sim 30 \%$ and 19%) and the SOA yield is still higher at higher [OH].

As we discussed previously, we believe secondary reactions play a major role for the observed OH dependence of SOA yield. However, in previous studies it was suggested that the cause of this dependence might be the more efficient NPF and/or higher abundance of low volatile vapors at higher oxidant levels. This results in a larger particle surface area, allowing more semivolatile vapors to condense on particles which will be less susceptible to

loss processes (Ng et al., 2007b; Healy et al., 2009). Since particle masses are corrected for wall losses in this study, this effect should be of minor importance. Another possibility might be the OH dependence of ELVOC formation. Formation of such molecules might require more than one OH reaction.

The results of these experiments confirm the importance of the OH concentrations in SOA mass formation. This complicates the assignment of the observed changes in SOA yield to the impact of NO_x on peroxy radical chemistry, as SOA yield was also varied with [OH]. Thus, we conducted a series of experiments to decouple the impacts of OH and NO_x on SOA formation.

Table 3.8 Experimental conditions and results for β -pinene photooxidation experiments at two OH levels.

$J(O^1D)/10^{-3}$ (s ⁻¹) ^a	Initial β - pinene (ppb) ^b	β -pinene reacted (ppb)	[OH]/10 ⁷ (cm ⁻³)	PM _{max} (μ g m ⁻³) ^b
1.9	3.8	3.6	12.5	4.2
1.9	9.2	8.8	11.3	6.5
1.9	9.2	8.9	11.3	6.9
1.9	9.2	8.9	11.3	7.7
1.9	15.9	14.8	6.2	14.4
1.9	24.8	22.0	3.7	23.8
1.9	24.8	22.0	3.7	23.2
1.9	24.8	22.0	3.7	22.0
5.7	3.8	3.6	12.5	4.1
5.7	9.2	9.0	14.5	9.8
5.7	15.9	15.5	15.7	21.3
5.7	24.8	23.9	12.4	39.6

^aJ(O¹D) was varied by altering the TUV gap, ^bThe error in [β -pinene] was estimated to be $\pm 10\%$, ^cMaximum formed particle mass concentration, assuming a SOA density of 1.2 g cm⁻³. These values have been adjusted for wall losses and losses on particles. The error in particle mass was estimated from the sum of the systematic error and the correction procedure error.

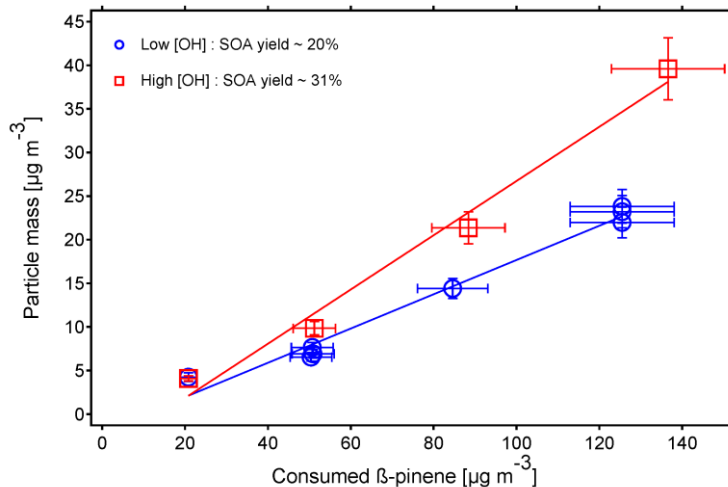


Figure 3.42 Total aerosol mass concentration as a function of the amount of reacted β -pinene under low-[OH] (blue open circles) and high-[OH] (red open squares) conditions. The SOA yield was estimated from the aerosol mass linear regression slope as a function of consumed β -pinene, which resulted in approximately $20 \pm 1\%$ and $31 \pm 3\%$ for low- and high-OH conditions respectively. The error in [consumed β -pinene] was estimated to be $\pm 10\%$ and the error in particle mass was estimated from the sum of the systematic error and the correction procedure error.

3.3.2.3 Isolate the Effect of [OH] on SOA Formation

To investigate the impact of NO_x on SOA production independent of [OH] changes, a series of experiments were performed where the steady state OH concentration was held constant by tuning the value of $J(\text{O}^1\text{D})$. This required constant [OH] monitoring as the system approached steady state. This was carried out by monitoring the consumption of β -pinene from GC-MS or PTR-MS, to ensure the [OH] was adjusted to the desired level.

Despite the significant variations of initial OH concentrations with NO_x when $J(\text{O}^1\text{D})$ was unchanged, it was possible to maintain the OH concentrations to within 5% across all NO_x concentrations by adjusting $J(\text{O}^1\text{D})$ (Fig. 3.43).

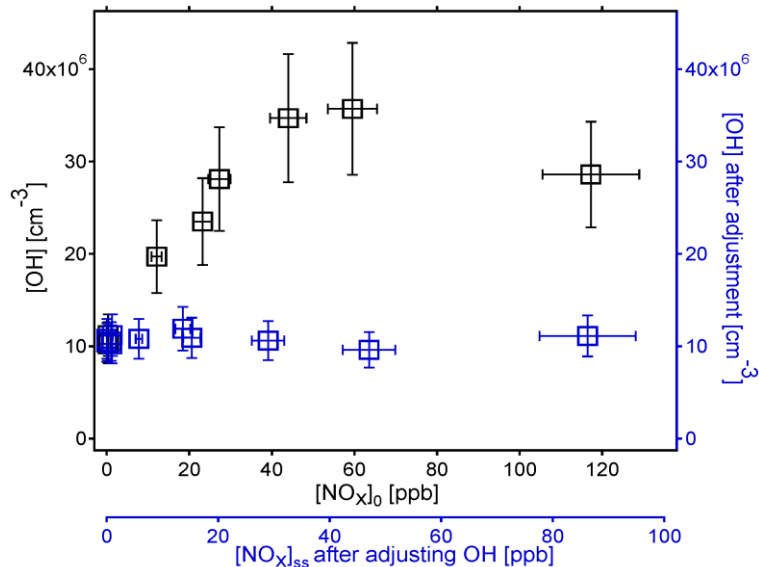


Figure 3.43 Comparison of [OH] before (black squares) and after (blue squares) adjusting OH concentration during steady state in NO_x experiments. The errors in [OH] and [NO_x] were estimated to be ± 20 % and ± 10 % respectively.

Figure 3.44 illustrates the SOA yield as a function of [NO_x] during the steady state, before and after [OH] adjustment. Before adjusting [OH], the yield profile was consistent with our previous results; SOA yield increased with increasing NO_x at low-NO_x levels and then decreased at high-NO_x levels. After adjusting [OH], the yield demonstrated no increase at low-NO_x levels and only suppressed by increasing NO_x. This indicates that the observed increase in SOA yield without keeping [OH] constant, is a result of NO_x enhancing [OH]. Hence, isolating the effect of [OH] revealed that increasing [NO_x] only suppressed particle mass formation, and therefore also suppressed SOA mass yield.

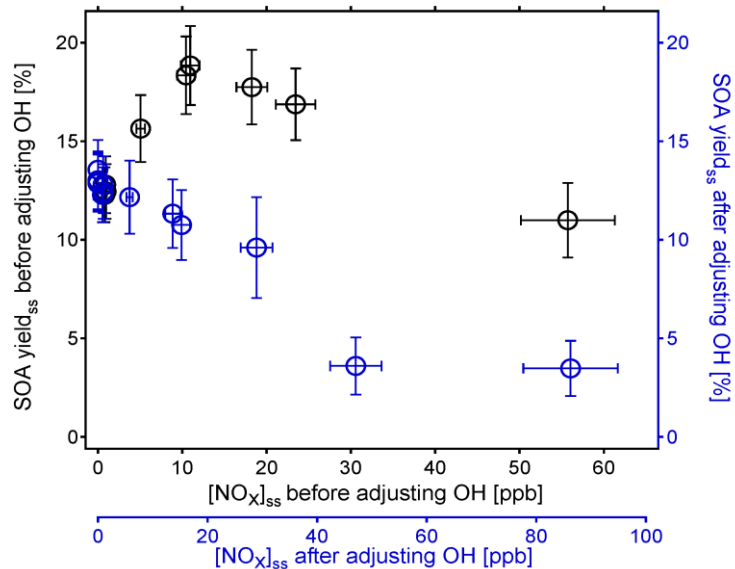


Figure 3.44 Comparison of SOA yield before (black circles) and after (blue circles) adjusting OH concentration during steady state in NO_x experiments. The error in [NO_x] was estimated to be ± 10 % and the error in SOA yield was estimated from error propagation using the sum of the systematic error, correction procedure error and error in BVOC data.

3.3.2.4 Impact of NO_x on SOA Formation in the Presence of Seed Aerosol

It was observed that the SOA yield measured at [NO_x]_{ss} ~ 86 ppb ([NO_x]₀ ~ 146 ppb) was lower than that at [NO_x]₀ < 1 ppb while [OH] was higher (Fig. 3.41). This indicates that there must be another effect of NO_x addition besides its impact on [OH]. As shown in Fig. 3.45, particle number concentrations were suppressed significantly by adding NO_x. The strong reduction of particle number concentration with increasing NO_x exhibits that NPF is suppressed by NO_x (see also Wildt et al., 2014). Therefore, the SOA formation is most probably hindered by low particle phase condensational sinks at high-NO_x levels, and thus

the observed suppression of SOA yield may be due to the lowering of available particle surface area.

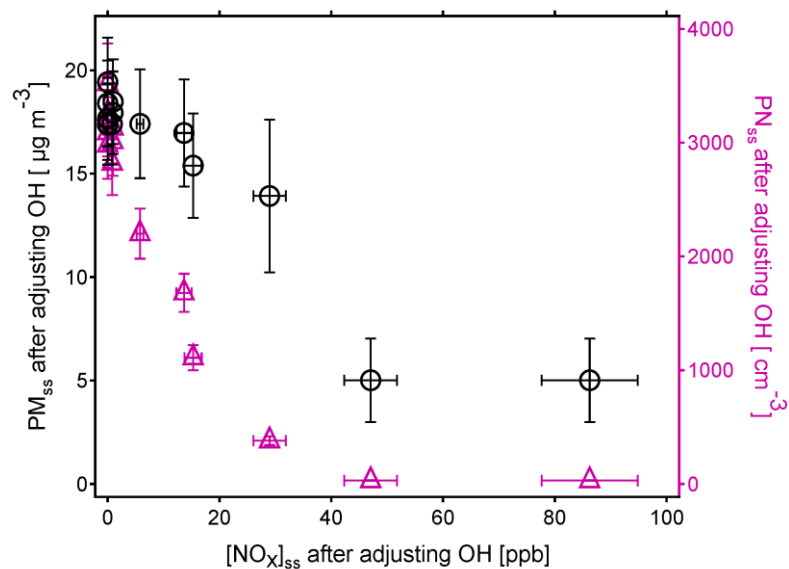


Figure 3.45 Comparison of measured particle mass and particle number concentration after adjusting [OH] as a function of [NO_x] during steady state in the absence of seed aerosol. The error in particle number concentration was estimated to be $\pm 10\%$.

Particle numbers and surface areas were quite low under high-NO_x conditions. Therefore, large correction factors had to be applied to correct the particle mass for wall losses of ELVOCs which includes high uncertainties. These uncertainties can be reduced by using seed particles since they provide a surface onto which the low volatile organics may condense. In the presence of seed aerosol, the growth of particles would not be limited by the surface of particles and would be much less affected by losses of SOA precursors on the chamber walls.

Therefore, NO_x experiments were also conducted in the presence of (NH₄)₂SO₄ seed particles (average seed mass and surface were approximately $9 \pm 1 \mu\text{g m}^{-3}$ and $1.3 \times 10^{-3} \text{ m}^2 \text{ m}^{-3}$, respectively). In these experiments [OH] was also adjusted during steady state to the same level as during the NO_x-free experiments. The comparison of SOA yield before and after [OH] adjustment for seeded NO_x experiments is presented in Figure 3.46 (seed mass is subtracted from the total particle mass to determine the organic mass used in the yield calculation).

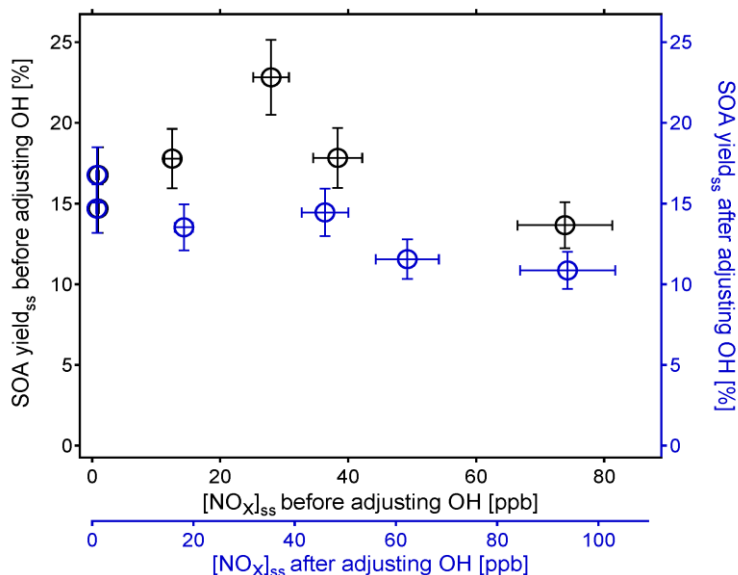


Figure 3.46 Comparison of SOA yield before (black circles) and after (blue circles) adjusting OH concentration during steady state in NO_x experiments performed in the presence of seed aerosol. The error in [NO_x] was estimated to be $\pm 10\%$ and the error in SOA yield was estimated from error propagation using the sum of the systematic error, correction procedure error and error in BVOC data.

The results from the seeded experiments showed that without adjustment of [OH], yields increased with increasing NO_x at low-NO_x levels and were only slightly suppressed with

further increasing NO_x . The most evident difference here to the experiments without seed is the fairly high yield at high- NO_x levels (Fig. 3.46). Even after $[\text{OH}]$ was adjusted, the decrease in SOA yield was not as significant as in the experiments without seed particles. This suggests that in the absence of seed particles, the accumulation of mass was indeed limited by low particle surface area caused by the NO_x -induced suppression of NPF.

In the presence of seed particles and at constant $[\text{OH}]$, the decrease in SOA yield was only moderate compared to those in the absence of seed particles. This suggests that other NO_x impacts such as its effect on RO_2 chemistry and formation of organic nitrates were moderate as well. The difference between yields determined with and without addition of seed particles indicates that at very small particle surface areas, our correction procedure underestimates wall losses of precursors. This might be due to either possible differences in uptake of the ELVOC by the type of particles (mainly organic particles versus inorganic ammonium sulfate particles), or the differences in the size of particles. However, the real reason for this underestimation is not known yet. Although our correction procedure may involve uncertainties and errors, it had to be applied to prevent overestimating the NO_x dependence.

NO_x suppresses NPF and thereby limits mass formation in the absence of seed particles. As both, the impacts of wall losses and impacts of suppressed NPF on SOA mass formation are certainly diminished in the presence of seed, we assume that the experiments with seed particles give the most reliable results on NO_x impacts on SOA mass formation from β -pinene.

3.3.2.5 Role of RO₂ Chemistry and NO/NO₂ Ratio in SOA Formation

The influence of the [NO]/[NO₂] ratio on SOA formation from β-pinene/NO_x mixtures was also investigated in this study. In order to change the [NO]/[NO₂] ratio, [O₃] was changed in the chamber. Ozone, NO and NO₂ are interrelated as illustrated in Reactions (R3.6) and (R3.7):



The [NO]/[NO₂] ratio is described by the photostationary steady state (Leighton, 1961) as:

$$\frac{[\text{NO}]}{[\text{NO}_2]} = \frac{J(\text{NO}_2)}{k^{3.6}[\text{O}_3]} \quad (\text{Eq.3.4})$$

where $J(\text{NO}_2)$ represents the photolysis rate coefficient of NO₂ and $k^{3.6}$ is the rate coefficient of Reaction (R3.6). Thus, adjusting O₃ concentration in the chamber allowed varying [NO]/[NO₂] ratios. In the previous NO_x experiments, the O₃ concentration and [NO]/[NO₂] ratio were 40 ± 5 ppb and 0.035 ± 0.005 ppb · ppb⁻¹, respectively. Here, NO_x experiments with no seed particles with approximately 50 % higher O₃ concentration (74 ± 7 ppb, [NO]/[NO₂] = 0.018 ± 0.004 ppb · ppb⁻¹) were performed to examine the dependency of SOA mass formation on relative NO and NO₂ concentrations. The remaining conditions were maintained the same.

Figure 3.47 shows the OH concentration as a function of NO_x before and after [OH] adjustment. Comparison of Fig. 3.43 with Fig. 3.47 shows that the high-O₃ experiments

(equivalent to lower NO/NO₂) demonstrate a different behavior than the experiments with lower [O₃]. Before adjusting, [OH] increased with increasing NO_x but the increase was less pronounced. With a lower [NO]/[NO₂] ratio, the maximum OH concentration increase was approximately 2-fold relative to the respective NO_x-free experiments (Fig. 3.47), compared to the 4-fold increase with the higher [NO]/[NO₂] (Fig. 3.43). This is consistent with the assumption that reaction (R3.4) recycles OH. As illustrated in Fig. 3.48, a slight increase was observed in SOA yield when [NO_x] increased up to ~ 15 ppb. Furthermore, the increase in SOA yield was less pronounced in the high-O₃ experiments again indicating the role of [OH] in SOA formation.

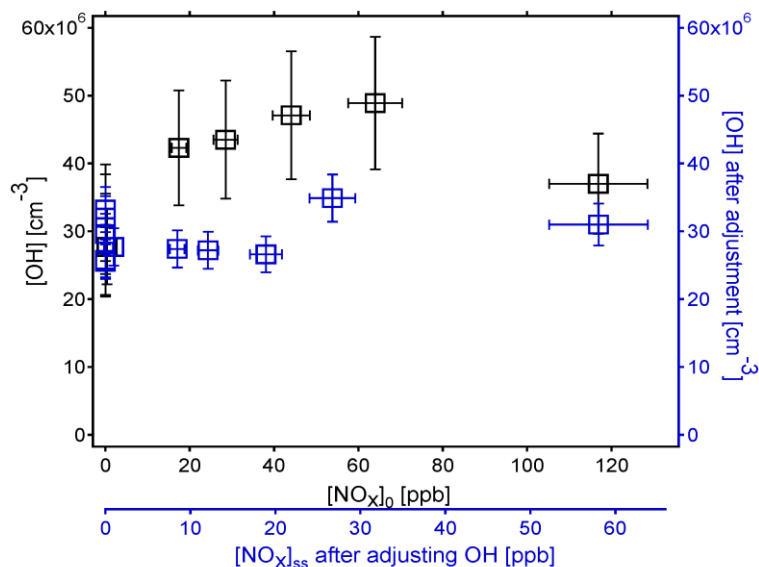


Figure 3.47 Comparison of [OH] before (black squares) and after (blue squares) adjusting OH concentration during steady state in NO_x experiments performed under lower [NO]/[NO₂] ratio. The errors in [OH] and [NO_x] were estimated to be ± 20 % and ± 10 % respectively.

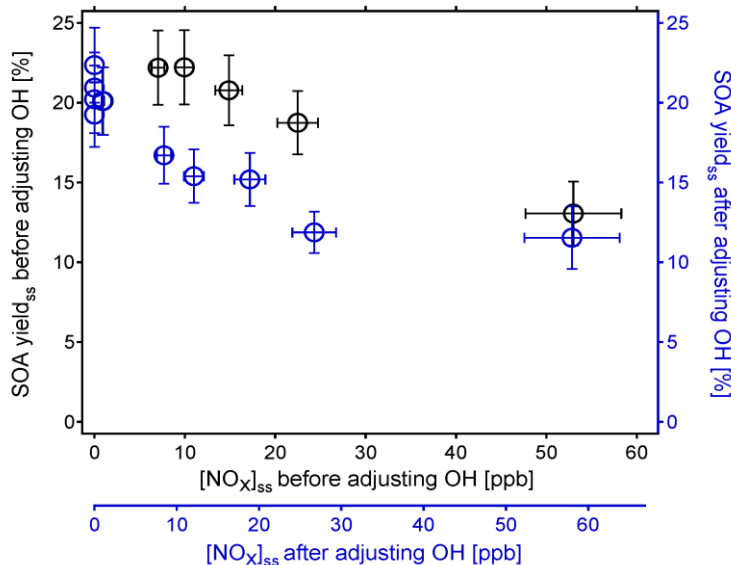


Figure 3.48 Comparison of SOA yield before (black circles) and after (blue circles) adjusting OH concentration during steady state in NO_x experiments performed under lower [NO]/[NO₂] ratio. The error in [NO_x] was estimated to be ± 10 % and the error in SOA yield was estimated from error propagation using the sum of the systematic error, correction procedure error and error in BVOC data.

After adjusting [OH] to the same level as in the NO_x-free experiments (Fig. 3.47), no increase in SOA yield was observed and increasing NO_x only suppressed SOA formation (Fig. 3.48). These results were in agreement with those found earlier in the low-O₃ experiments demonstrating that, after separating the effect of [OH], SOA yield was only suppressed with increasing NO_x also at higher [O₃]. Comparison of the SOA yield profiles obtained from the low-O₃ and the high-O₃ experiments (blue circles in Fig. 3.44 and Fig. 3.48), indicates that the reduction in SOA yield was ~ 35 % in the high-O₃ experiments, whereas it was approximately 70 % in the low-O₃ experiments.

In summary, after isolating the impact of NO_x on OH and NPF, there was a remaining NO_x impact on SOA formation (Fig. 3.46). According to the present knowledge (e.g. Hatakeyama

et al., 1991; Pandis et al., 1991; Kroll et al., 2006) this effect is caused by the impacts of NO_x on RO_2 chemistry. The most important effect of NO_x is the change in product composition. Under higher- NO_x conditions, organic nitrates are produced as an alternative to hydroperoxides and thus may have an influence on the average volatility of the products mixture. Furthermore, decomposition of alkoxy radicals may play a role here. Decomposition of alkoxy radicals can lead to products with higher volatility and thus to a mixture with an average higher volatility. We observed that SOA suppression was more pronounced under higher $[\text{NO}]/[\text{NO}_2]$ ratio. This points to NO as a major player responsible for the SOA yield diminishing effect of NO_x and thus to a role of alkoxy radical decomposition. As alkoxy radicals are produced by only $\text{RO}_2 + \text{NO}$ reactions, more effective suppression of SOA formation at higher $[\text{NO}]/[\text{NO}_2]$ would be consistent with alkoxy radical decomposition leading to decomposition products with on average high vapor pressures. However, from our results no clear conclusion can be given in this respect. In addition, the NO / NO_2 ratios in typical urban air are often much higher than the $[\text{NO}]/[\text{NO}_2]$ ratios used in this study (Kurtenbach et al., 2012; Frey et al., 2013). Therefore, the suppression capacity of NO_x might have been underestimated in this study.

3.4. Impact of Chemical Aging on SOA

This Section focuses on changes in chemical composition of products from β -pinene oxidation as well as changes in particle mass and particle density at longer reaction times than those described previously. This will allow us to investigate further reactions of the SOA and/or further reactions of the intermediate products.

3.4.1. SOA Chemical Composition

3.4.1.1 OH-induced Aging

In these experiments the produced SOA from β -pinene oxidation was subjected to additional exposure to hydroxyl radicals, generated by the addition of IPN/NO to the reaction mixture. A summary of the experimental conditions and results for OH-induced aging experiments is presented in Table 3.9. In the first step, MS scans were performed on the β -pinene reaction mixture in order to analyze the oxidation products prior and after aging. Figure 3.49 shows the mass spectrum of the particle phase sample during the reagent mixing period, two hours following initiation of the reaction and after aging (after third IPN/NO injections followed by lights on). The mass spectrum during mixing time shows the presence of proton reagent ions (m/z 37 and 55) as well as the ion peak corresponding to β -pinene (m/z 137). Upon initiating the reaction, the β -pinene peak disappeared, oxidation products were formed and new peaks appeared. A number of differences were observed when comparing the mass spectra before and after aging: 1) the peak m/z 139 ($M+H^+$) which corresponds to nopinone (major primary product of the β -pinene oxidation) disappeared during aging process. This

indicates further oxidation of nopinone has occurred; 2) the signal due to some of the products increased such as m/z 187, pinic acid. It is important to note that since all the mass spectra were obtained from one acquired MS scan, these changes cannot be due to signal variations that may occur by switching scans; 3) there is no indication of large molecular weight oligomeric compound formation, as no ions of significant intensity were observed beyond 300 u; and 4) subtracting the before from after aging spectra showed no evidence of previously undetected product formation. The same behaviour was observed in the gas phase products, with notably less change in the products during aging.

The SRM time profiles for selected oxidation products were acquired to provide more sensitive measures of their formation during the β -pinene photooxidation and also their fate under aging condition. The SRM time profiles were obtained for both gas and particle phase products, which will be presented in the following Sections.

Table 3.9 Experimental conditions and results for OH-induced β -pinene aging experiments.

β -pinene reacted/ 10^3 ($\mu\text{g cm}^{-3}$)	IPN injected (ppm) 1 st /2 nd /3 rd	[NO] injected (~ ppm) 1 st /2 nd /3 rd	[NO _x] (ppm) ^a 1 st /2 nd	[OH] ₀ /10 ⁶ (cm ⁻³) ^b	SOA mass ($\mu\text{g cm}^{-3}$) ^c 1 st /2 nd /3 rd	Δ SOA mass ($\mu\text{g cm}^{-3}$) ^d
Particle phase						
2.8	0.4 / 3 / 3	0.4 / 0.4 / 0.4	0.30 / 0.62 / 0.87	11.7	4204 / 5642 / 5940	1438 / 298
-----	0.4 / 3 / 2.5	0.4 / 0 / 0.8	-----	-----	4170 / 4750 / -----	580
2.8	0.4 / 2 / 2.5	1 / 1 / 0	1.13 / 0.70 / 0.84	6.4	2799 / 3407 / 3565	608 / 158
2.8	0.4 / 2 / 2.5	1 / 2 / 0	0.82 / 0.73 / 0.83	5.8	2172 / 2970 / 3160	798 / 190
Gas phase						
-----	0.4 / 2 / 2.5	0 / 0 / 0	-----	-----	4230 / 5562 / 5838	1332 / 276
2.9	0.4 / 2 / 2.5	1 / 0.4 / 0.2	1.2 / 0.73 / 0.84	6.7	2701 / 3632 / 3794	931 / 162

^aNO_x concentration after each NO injection during steady state, ^bThe OH concentration in the first step to react away β -pinene, ^cMaximum formed particle mass concentration after each OH production, assuming a SOA density of 1.2 g cm⁻³. These values have been adjusted for wall losses, ^dThe additional SOA mass produced during aging.

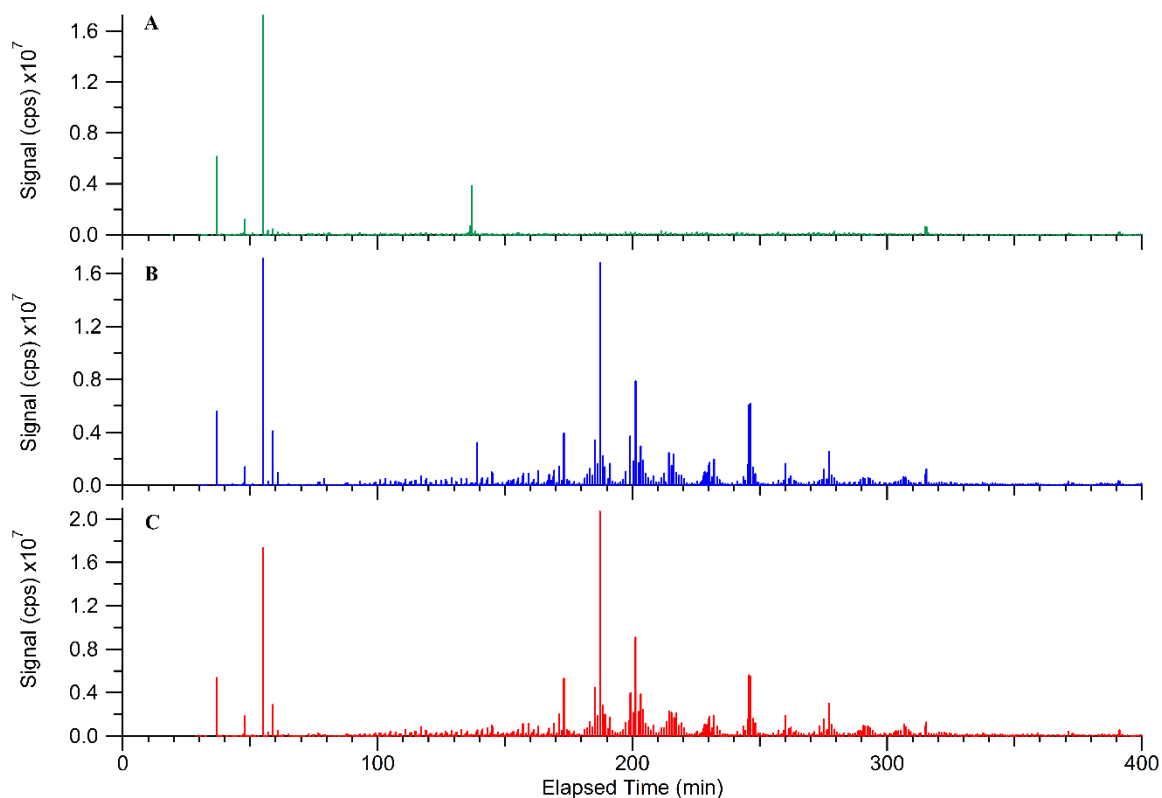


Figure 3.49 MS scans of β -pinene photooxidation experiment in the particle phase during A. the reagent mixing period, B. two hours following initiation of the reaction (β -pinene+OH), and C. after aging ($(\beta$ -pinene+OH)+OH, after approximately 6 hours).

Nopinone (M 138)

Figure 3.50 illustrates the time profiles of β -pinene and nopinone during the particle phase aging experiment. The signal associated with β -pinene decreased after initiation of the reaction until all measurable β -pinene was completely removed (approximately after 2 hours), meanwhile nopinone signal increased due to its formation and finally reached a plateau. At this point, OH radicals were no longer present in the chamber. The nopinone signal remained constant during the mixing with the additional IPN/NO in the dark. Then

the nopinone signal decays sharply upon additional OH exposure. A significant fraction of nopinone was reacted away after this period (approximately after 2 hours) and the majority of the remaining nopinone was almost consumed after the third OH exposure.

Nopinone SRM time profiles in both gas and particle phases are shown in Fig. 3.51. This demonstrates the correlation between gas and particle phase behaviour during OH-induced aging. As nopinone reacted with OH radicals in the gas phase, nopinone in the particle phase evaporated and partitioned back to the gas phase which further reacted away. This is consistent with the relatively high vapor pressure of nopinone ($p_{\text{vap}}=4.8\times 10^{-2}$ Torr = 6.4 Pa (Capouet and Müller, 2006)). Since nopinone is oxidized during aging, further formation of other products is expected.

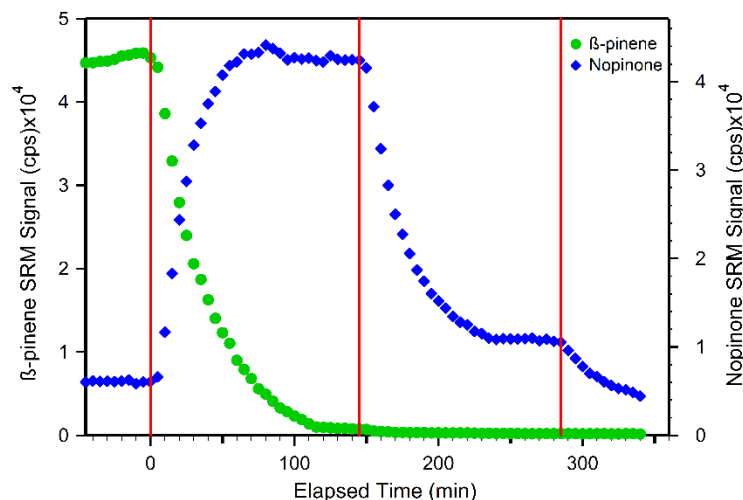


Figure 3.50 SRM time profiles for the ion pairs 137→81 (green circles) and 139→121 (blue diamonds) representing β -pinene and nopinone respectively, during OH induced β -pinene aging experiment. The vertical red lines indicate the time at which the OH exposure started.

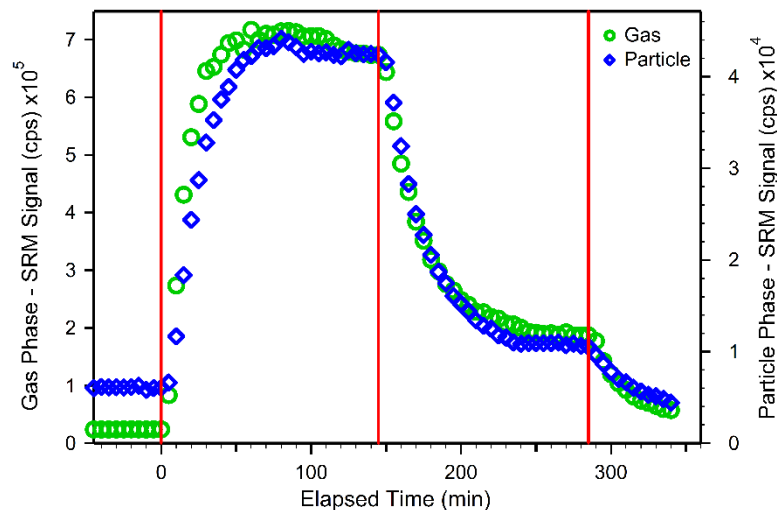


Figure 3.51 SRM time profiles for the ion pair 139→121 in the gas phase (green circles) and particle phase (blue diamonds) during OH induced β -pinene aging experiment. The vertical red lines indicate the time at which the OH exposure started.

A detailed description of a few categories of compounds will be given here to illustrate the differences in their behaviour during aging.

Hydroxyl and Carbonyl Containing Compounds (Hydroxy nopinone and Oxonopinone)

Hydroxy nopinone (M 154) which was previously identified from β -pinene photooxidation, is one of the other products that exhibited a sharp decay in the SRM time profile during aging (Fig. 3.52A). The rate constant of hydroxy nopinone reaction with OH radicals ($k \sim 1.8 \times 10^{-11} \text{ cm}^3 \text{ s}^{-1}$ (MCM)) is comparable with that of nopinone which explains the reason for its similar sharp decay to nopinone. The results show that the hydroxy nopinone gas phase signal decreased rapidly after the second OH exposure, whereas it decreased very slowly in the particle phase. This indicates that as hydroxy nopinone reacted rapidly in the gas phase,

in turn it evaporated slowly from the particle phase to the gas phase. This is consistent with the lower vapour pressure of hydroxy nopinone compared to that of nopinone. Thus, this resulted in a relatively slow decrease in the particle phase.

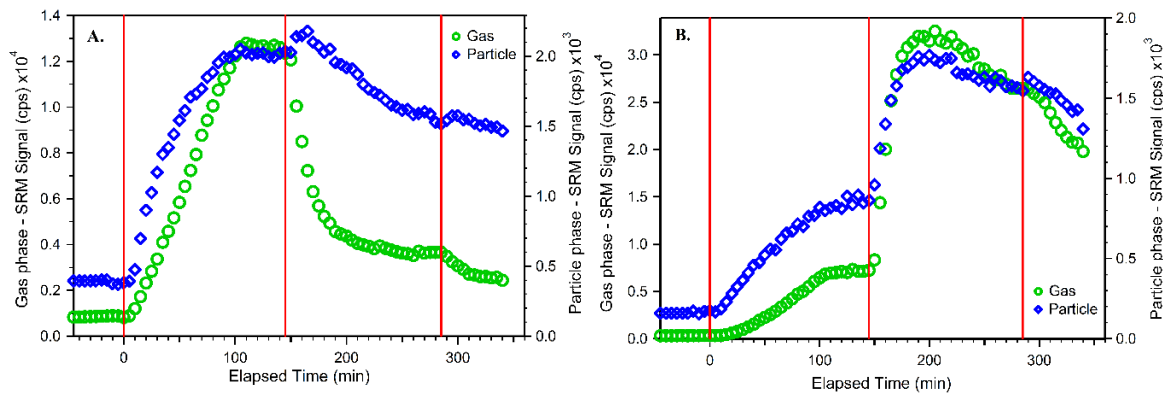


Figure 3.52 SRM time profiles for A. hydroxy nopinone (155→109) and B. oxo-nopinone (153→111). The gas and particle phases are distinguished using green and blue markers, respectively. The vertical red lines indicate the time at which the OH exposure started.

Oxo-nopinone (M 152) which is formed from nopinone oxidation during β -pinene photooxidation is also the product of the hydroxy nopinone oxidation with OH radicals. The mechanism of formation for oxo-nopinone is illustrated in Section 3.5.2 (Fig. 3.68). Figure 3.52B illustrates the formation of oxo-nopinone and its fate during aging. The SRM time profile of oxo-nopinone demonstrates a very sharp increase after the second OH exposure, confirming that nopinone and likely hydroxy nopinone are involved in its formation.

As oxo-nopinone formed during aging it is also oxidized by OH radicals, illustrated by the decrease in SRM signal with OH addition (Fig. 3.52B). When Oxo-nopinone was consumed in the gas phase, the oxo-nopinone in the particle phase evaporated back into the gas phase.

The similarity in the relative slope of the gas and particle phase decays suggests a fairly high vapour pressure for oxo-nopinone. The comparison between hydroxy nopinone and oxo-nopinone time profiles suggests that the oxo-nopinone gas phase concentration is higher than that of hydroxy nopinone. This is consistent with hydroxy nopinone being more polar.

Carboxylic Acids (Pinalic 3-acid, Norpinic acid and Pinic acid)

A number of carboxylic acid products have been previously identified from β -pinene photooxidation experiments including pinalic 3-acid (or pinalic 4-acid, M 170), norpinic acid (M 172) and pinic acid (M 186). The SRM time profiles of these acids during β -pinene aging experiments are shown in Figure 3.53. In all these profiles, a rise in signal was observed after the second OH exposure in both gas and particle phases. This indicates additional formation of these carboxylic acids upon aging. During the same time period, the nopinone profile showed a rapid decay in signal (Fig. 3.51), suggesting that nopinone was a source of the further formation of these acids. This agrees well with the formation mechanism of carboxylic acids, illustrating that all these acids are produced mainly via nopinone oxidation with OH radicals (these mechanisms are presented in Section 3.5.3). The observed SRM signal increase in both phases implies that additional formation of these acids was a result of nopinone oxidation in the gas phase with subsequent condensation to the particle phase. This is also consistent with the results of our nopinone photooxidation experiments, which demonstrated that the majority of the dominant identified products were carboxylic acids (Section 3.2.4.1). Similar behaviour was observed in some other identified carboxylic acids in this study, such as m/z 185, 199 and 201.

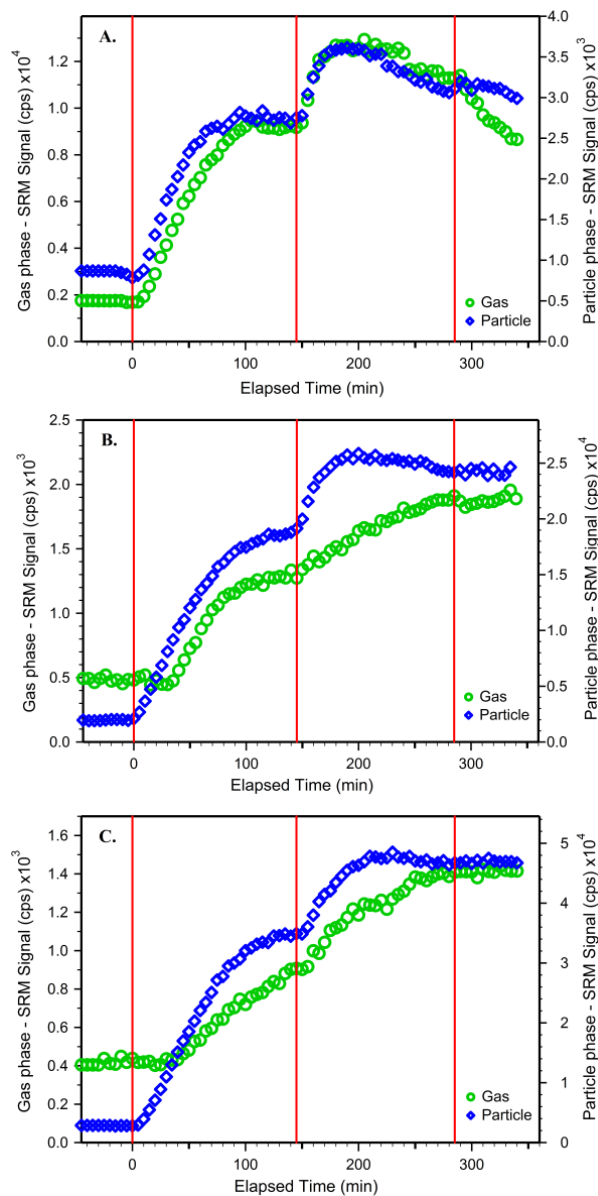


Figure 3.53 SRM time profiles for the ion pairs A. 171→125, B. 173→127 and C. 187→141, representing pinalic 3-acid (or pinalic 4-acid), norpinic acid and pinic acid respectively. The gas and particle phase are distinguished using green and blue symbols respectively. The vertical red lines indicate the time at which the OH exposure started.

Organic Nitrates (C10-aldehyde nitrate, C10-bicyclic hydroxy nitrate and C10-dihydroxy nitrate)

A number of organic nitrate products have been previously identified from β -pinene photooxidation experiments, including C10-aldehyde nitrate (M 213), C10-bicyclic hydroxy nitrate (M 215) and C10-dihydroxy nitrate (M 231). The SRM time profiles of these nitrate products were acquired during β -pinene aging experiments and are presented in Fig. 3.54. The main observation from the nitrate profiles is that their signal started to decay after they were exposed to additional OH radicals in both gas and particle phases. This indicates that nitrate products, in contrast to the carboxylic acid products, are more reactive towards OH radicals. In addition, although a slight increase was observed in the nitrate SRM time profiles upon initiation of the reaction during aging (second OH exposure), the rate of consumption is more than production for these nitrates. The observed slight increase in these profiles may be due to the formation of the C9 organic nitrates from nopinone oxidation, as discussed in Section 3.2.4.1. The reason for the slight differences in the behaviour of organics nitrates in the gas and particle phase is not clear at this time.

The proposed formation mechanisms of these C10 organic nitrates (MCM; Aschmann et al., 1998) indicate that they were formed via β -pinene oxidation. Since β -pinene was no longer present during the exposure to additional OH, further formation of these products was not possible. The formation mechanisms are presented in Section 3.5.4.

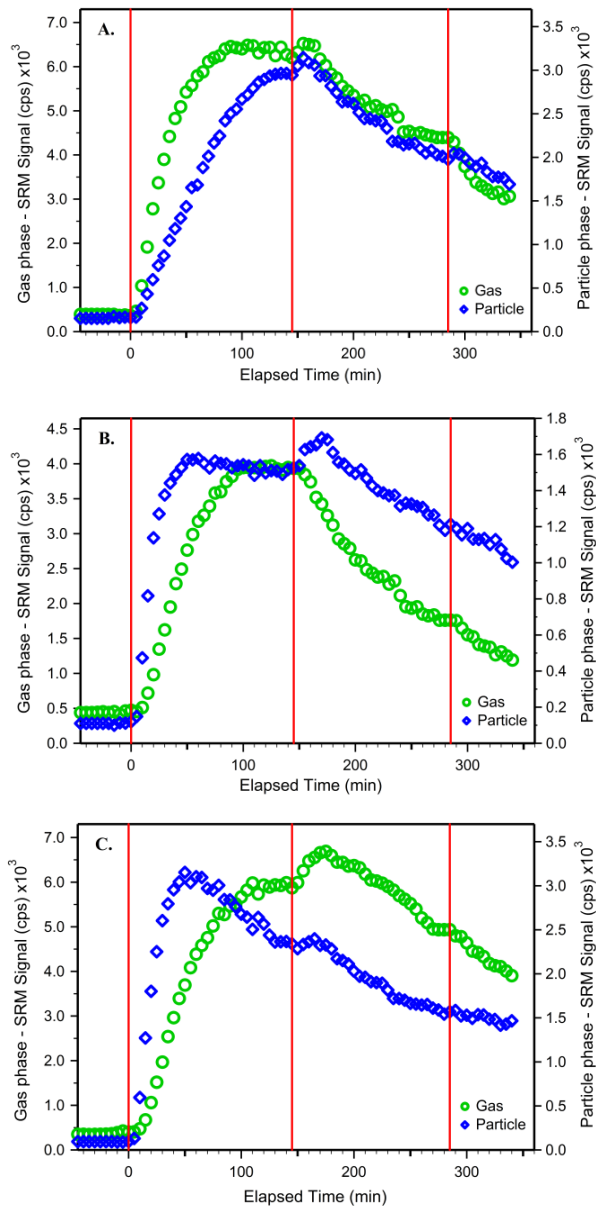


Figure 3.54 SRM time profiles for the ion pairs A. 214→168, B. 216→152 and C. 232→151, representing C10-aldehyde nitrate, C10-bicyclic hydroxy nitrate and C10-dihydroxy nitrate respectively. The gas and particle phase are distinguished using green and blue symbols respectively. The vertical red lines indicate the time at which the OH exposure started.

Organic Nitrates (Nitroxy nopinone and C10-PAN)

The SRM time profiles of two of the previously identified organic nitrates, nitroxy nopinone (M 199) and C10-PAN (M 245), demonstrated different profiles than the rest of the organic nitrates (M 213, 215 and 231). As shown in Fig. 3.55, the SRM signal for these nitrates increased after the additional OH exposure in both gas and particle phases, indicating their further formation upon aging. This suggests that the formation mechanisms of the C10-PAN and nitroxy nopinone are unlike the previously shown organic nitrates.

These results are consistent with the formation pathway of nitroxy nopinone which is proposed to occur via nopinone oxidation with OH radicals (presented in Section 3.5.4). In addition, as it was discussed in Section 3.3.1.2, the formation of C10-PAN is not through primary oxidation of β -pinene, and it is via C10-hydroxy aldehyde (M 168) oxidation with OH radicals. Therefore, further formation of these nitrates are expected during aging.

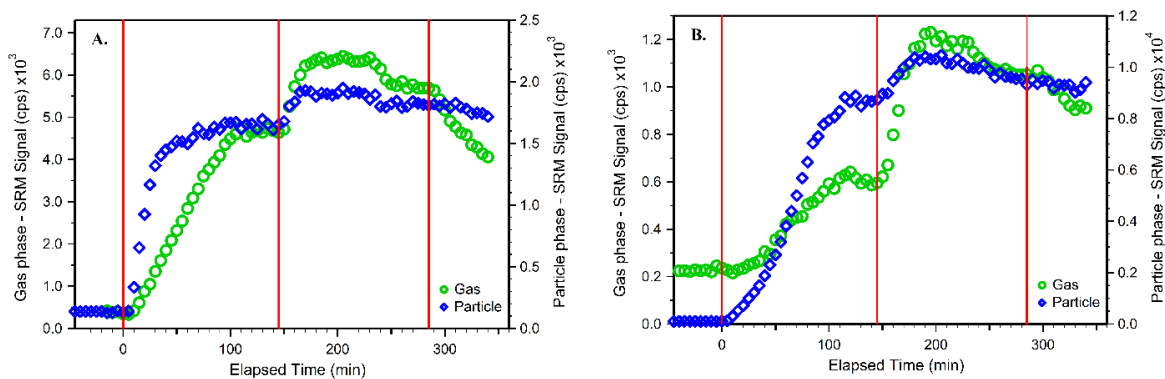


Figure 3.55 SRM time profiles for the ion pairs A. 200→168 and B. 246→200, representing nitroxy nopinone and C10-PAN respectively. The gas and particle phase are distinguished using green and blue symbols respectively. The vertical red lines indicate the time at which the OH exposure started.

3.4.1.2 Ozone-induced Aging

To further examine the effect of oxidants on the SOA produced from β -pinene oxidation, a series of O_3 -induced aging experiments were conducted following the reaction of β -pinene with O_3 . The full mass spectrum demonstrated no noticeable change during O_3 -induced aging experiments, suggesting no alterations in the chemical composition of products. To look further for any possible indication of O_3 impact on products, SRM time profiles of β -pinene and nopinone were acquired. As shown in Fig. 3.56, after complete removal of measurable β -pinene by reaction with O_3 , additional ozone was added twice in the presence of pre-existing oxidation products. Unlike the OH-induced aging experiments, O_3 did not have any influence on the nopinone time profile, demonstrating no further reaction of nopinone with O_3 . It is noted that nopinone's SRM signal slowly decays after its production due to wall losses as well as oxidation by OH radicals produced from β -pinene ozonolysis reaction. However, since no difference was observed in the slope of nopinone decay before and after the O_3 exposure, oxidation of nopinone was not associated with O_3 . In addition, no significant changes were observed for other identified products during O_3 induced aging. A slight increase in the SRM signal of norpinic acid and pinic acid was observed for O_3 level above 8 ppm. The reason for this increase is not well understood.

To confirm that nopinone is not oxidized by O_3 , a few nopinone ozonolysis experiments were performed. The nopinone time profile during these experiments is shown in Fig. 3.57. O_3 was injected to the chamber with concentrations of 2.5 ppm at time 0, 2.5 ppm at time 55 and 4 ppm at time 100. After each O_3 exposure, no change in nopinone signal was detected,

indicating that no oxidation had occurred. These observations are consistent with our expectation due to the very low rate constant of nopinone reaction with O_3 ($5.0 \times 10^{-21} \text{ cm}^3 \text{ s}^{-1}$) (Calogirou et al., 1999).

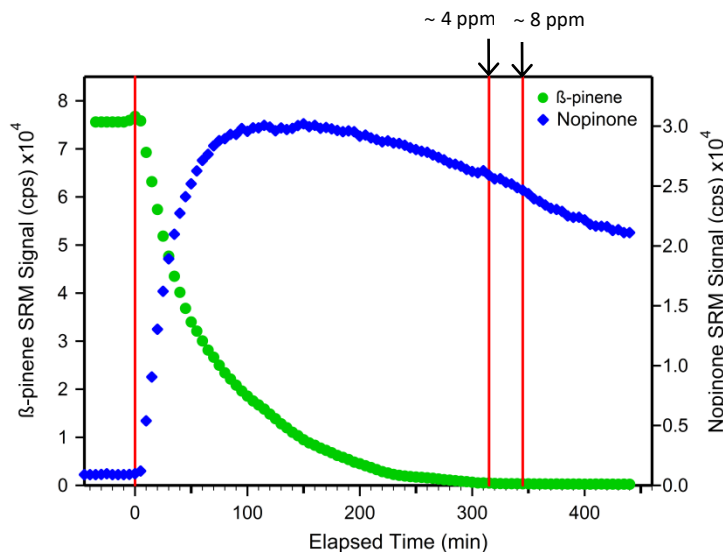


Figure 3.56 SRM time profiles for the particle phase β -pinene and nopinone during β -pinene O_3 -induced aging experiment. The O_3 addition time after β -pinene depletion is shown by red vertical lines and O_3 levels are marked by arrows for each addition.

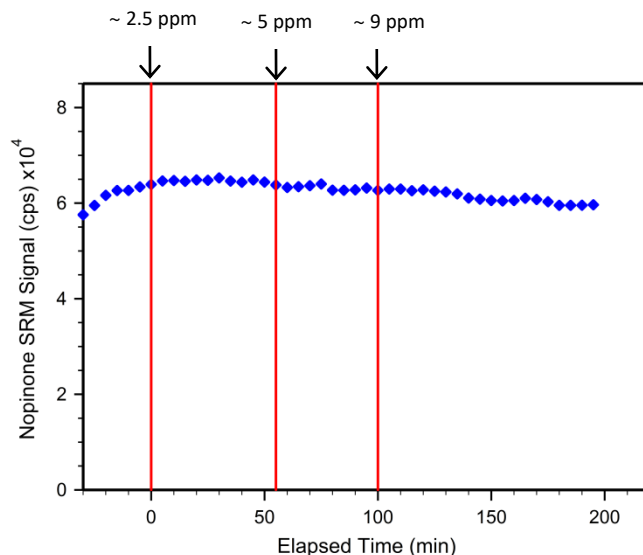


Figure 3.57 SRM time profile for nopinone during nopinone/ O_3 experiment. The O_3 addition time is shown by red vertical lines and the overall O_3 levels are marked by arrows for each addition.

3.4.2. SOA Mass Formation

3.4.2.1 OH-induced Aging

In this study, particle size distribution and organic particulate mass concentration were acquired during OH-induced β -pinene aging experiments. Figure 3.58 shows the size distribution of the seed particles ($t=0$ min) and the particle size distribution after 5 and 15 minutes of β -pinene photooxidation. Furthermore, it displays the last size distribution before starting aging (before addition of OH) and the size distribution 5 and 45 minutes following the second OH exposure. After aging was initiated, increases in number and size of particles were observed which indicate additional formation of organic particles. It should be noted that the particle size distribution is plotted on a logarithmic scale and therefore any growth at larger particle sizes (during aging) are less pronounced than that at smaller particle sizes which were formed initially by β -pinene oxidation. The growth after further OH addition (third OH exposure) during aging experiments was not significant and thus is not shown here.

The time profile of organic particulate mass concentration evolution during β -pinene photooxidation and aging is shown in Fig. 3.59. By initiating β -pinene oxidation, organic particles were formed resulting in an increase in the organic particulate mass concentration which reached the maximum value of $\sim 2200 \mu\text{g cm}^{-3}$. Over the period of time during which the UV lights have stayed off, the particulate mass remained constant and after lights being turned on for aging, a rise in the particulate mass was observed. After completion of the

aerosol growth from further reaction of oxidation products, the organic mass plateaued at approximately $3000 \text{ } (\mu\text{g cm}^{-3})$ and then after the third OH exposure, it showed a very small rise which did not result in a significant organic mass increase.

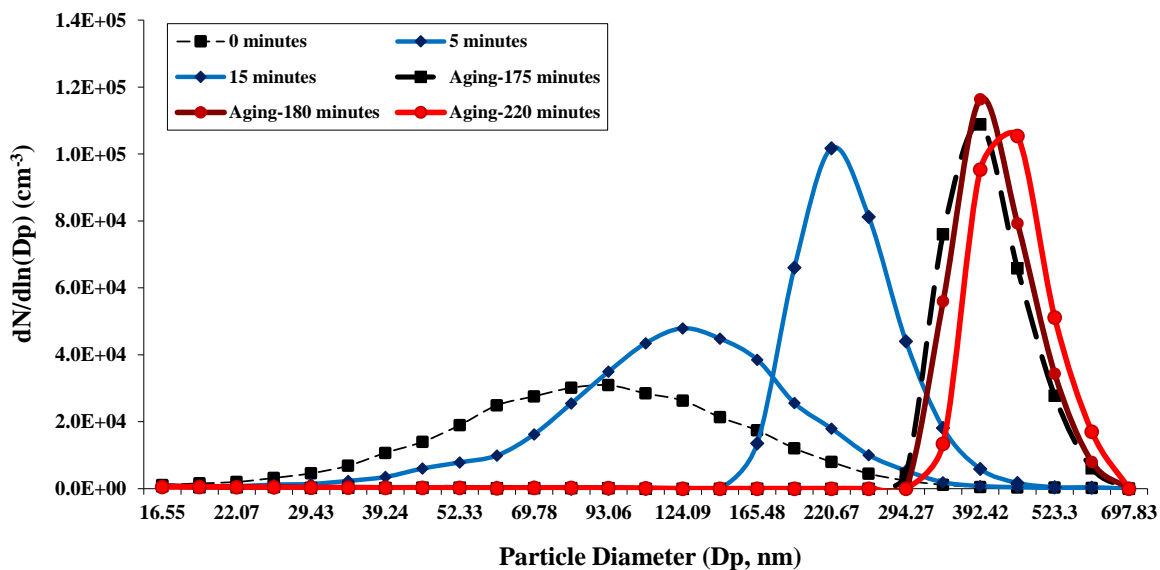


Figure 3.58 Particle size distribution during β -pinene OH-induced aging. The black dashed line (0 minutes) shows the time before β -pinene+OH reaction started and the blue solid lines represent the particle growth while oxidizing β -pinene. The black dashed line (Aging-175 minutes) shows the time before initiating the aging and the red solid lines demonstrate particle growth during aging.

The observed changes in particle size distribution and additional production of SOA mass during OH-induced aging appear to be simply explained by further oxidation of first generation products in the gas phase, mainly nopinone, which produces compounds partitioning to the particle phase.

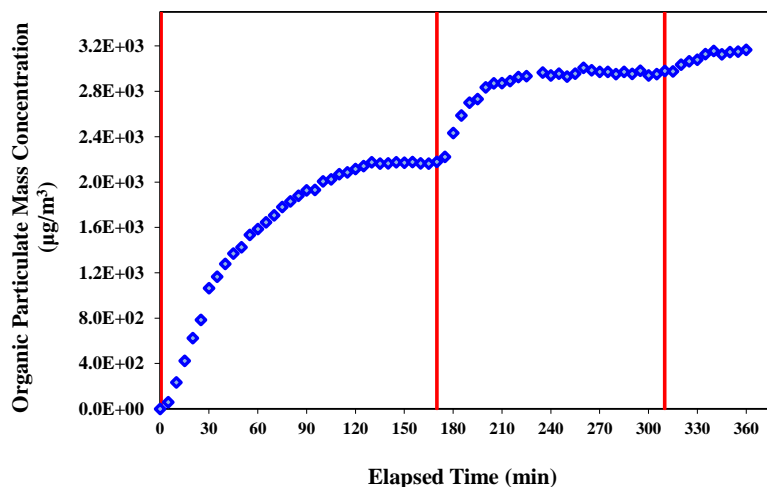


Figure 3.59 Time profile of organic particulate mass concentration during β -pinene OH-induced aging experiment ($\text{NO}_x \sim 1\text{ppm}$). The vertical red lines indicate the initiation of OH exposure (lights on).

3.4.2.1.1. Source of Additional SOA Formation during Aging

Observations from the SRM time profiles suggest that nopinone plays an important role in the additional formation of several oxidation products during aging, as discussed previously. In order to investigate how much nopinone oxidation contributes to the additional SOA mass produced during aging, a number of nopinone/OH experiments were carried out in the smog chamber. The objective was to compare the SOA mass formed from nopinone/OH experiments with the additional SOA mass produced during β -pinene OH-induced aging experiments. For this purpose, we had to maintain the same conditions for the nopinone experiments as those during β -pinene OH-induced aging experiments. One of the major parameters that needed to be kept consistent was the nopinone concentration. This means that the starting nopinone concentration in these set of experiments needed to be close to the

nopinone concentration achieved during β -pinene experiments just prior to the initiation of aging. The quantitative results obtained in our group by Zoya Dobrusin (Dobrusin, 2012) showed that the nopinone yield after completion of β -pinene oxidation in the chamber was approximately 25% which was consistent with reported literature values (Larsen et al., 2001, Wisthaler et al., 2001, Hakola et al., 1994). Therefore, since ~ 0.4 ppm β -pinene was used in our aging experiments, 0.1 ppm nopinone was injected to the chamber in the nopinone/OH experiments. In addition, similar concentrations of IPN and NO were chosen from our β -pinene aging experiments (prior to initializing the aging), as follow: 2 ppm IPN and ~ 1 ppm NO.

Figure 3.60 shows the nopinone decays in the particle phase from both the β -pinene aging experiment ($(\beta p+OH)+OH$) and the nopinone experiment ($np+OH$). It was seen that as soon as the OH radicals were generated, the nopinone signal began to decrease. A comparison between the organic particulate mass produced from $(np+OH)$ and that of $(\beta p+OH)+OH$ is shown in Fig. 3.61. These results indicate that the organic mass concentration formed during the $(\beta p+OH)+OH$ was higher than that of $(np+OH)$. The additional organic mass formed from the $(\beta p+OH)+OH$ was approximately $800 \mu\text{g cm}^{-3}$ compared to the average of $\sim 450 \mu\text{g cm}^{-3}$ formed from the $(np+OH)$. This indicates that something else other than nopinone oxidation contributes to the additional organic mass formation during the β -pinene OH-induced aging. This contribution could be from the direct oxidation of some other products (i.e. hydroxy nopinone) which generate low volatility products and thus increase organic mass. The other factor that may influence this result is the recycling of nopinone from further

oxidation of products, such as nitrates, leading to higher amount of nopinone in the system that subsequently generates more secondary products. Another factor that could contribute to this mass difference, is the dissimilarities in the number and nature of particles in β -pinene and nopinone experiments. Although seed particles were used in both β -pinene and nopinone experiments, during β -pinene aging period higher number of particles were present due to the formation of oxidation products. In addition, the nature of pre-existing particles was different during nopinone photooxidation (only inorganic seed particles) and β -pinene aging (mixture of organic and inorganic).

The results of these experiments indicate that the SOA mass generated from nopinone reaction with OH accounts for nearly half of the additional SOA mass produced during β -pinene OH-induced aging. As previously discussed there are a number of factors that can potentially impact the particle mass formation during nopinone experiments and result in a lower SOA mass. All these factors are mainly related to the absence of pre-existing oxidation products during nopinone experiments. However, we should also take into account that OH concentration may be higher in the nopinone experiments due to the presence of more gas phase intermediate products during the β -pinene OH-induced aging. This results in higher amount of nopinone to react with OH radicals during the nopinone experiments, leading to higher SOA masses.

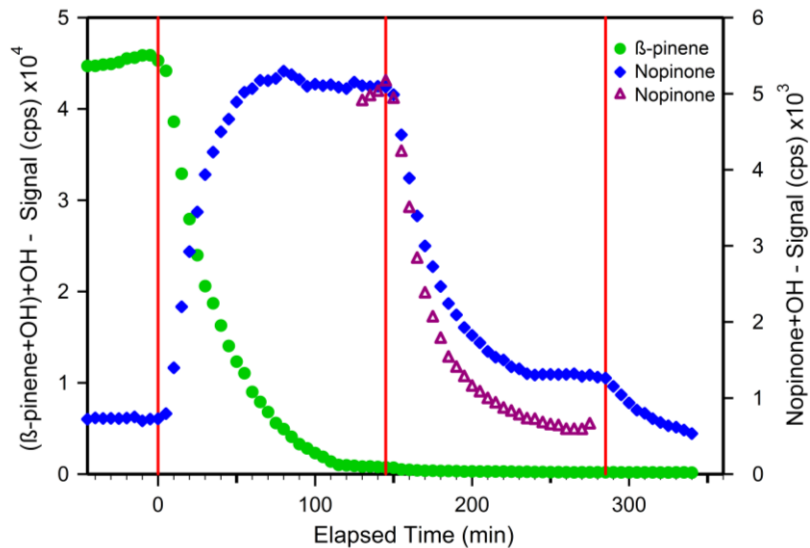


Figure 3.60 SRM time profiles for the β -pinene (green circles), nopinone (blue diamonds) during β -pinene OH-induced aging experiment and nopinone (purple triangles) during nopinone photooxidation experiment.

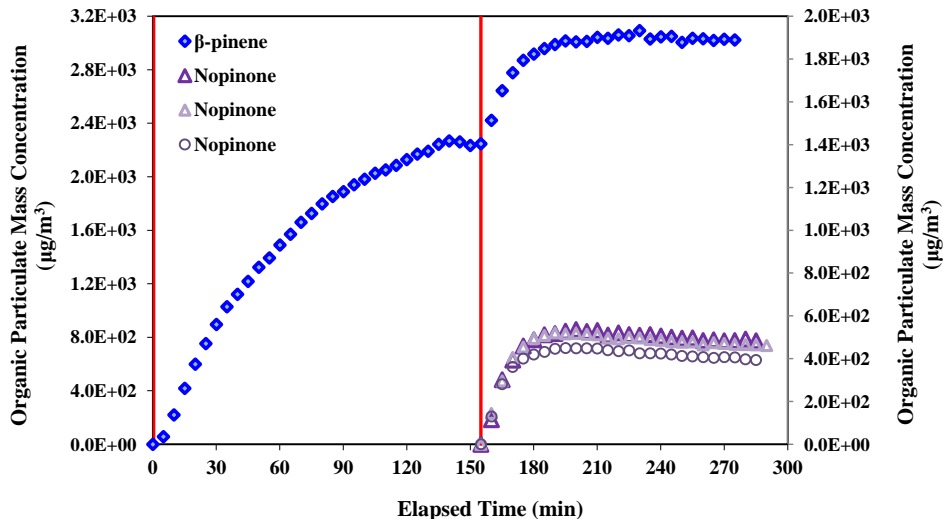


Figure 3.61 Comparison of the organic particulate mass concentration evolution from a β -pinene OH-induced aging experiment (blue diamonds) and three nopinone photooxidation experiments (purple triangles).

3.4.2.2 Ozone-induced Aging

Particle size distributions and organic particulate mass concentration were acquired during β -pinene O_3 -induced aging. We did not expect to observe any changes in particle size and particle mass during O_3 -induced aging due to the very low rate constant of nopinone reaction with O_3 . Particle size distributions within initial 5 and 15 minutes of β -pinene oxidation with O_3 are shown in Fig. 3.62, which indicates the particle growth. It also displays the particle size distribution obtained 5 and 30 minutes following the initiation of O_3 exposure to the pre-existing oxidation products (345, 375 and 380 minutes) which resulted in no particle growth.

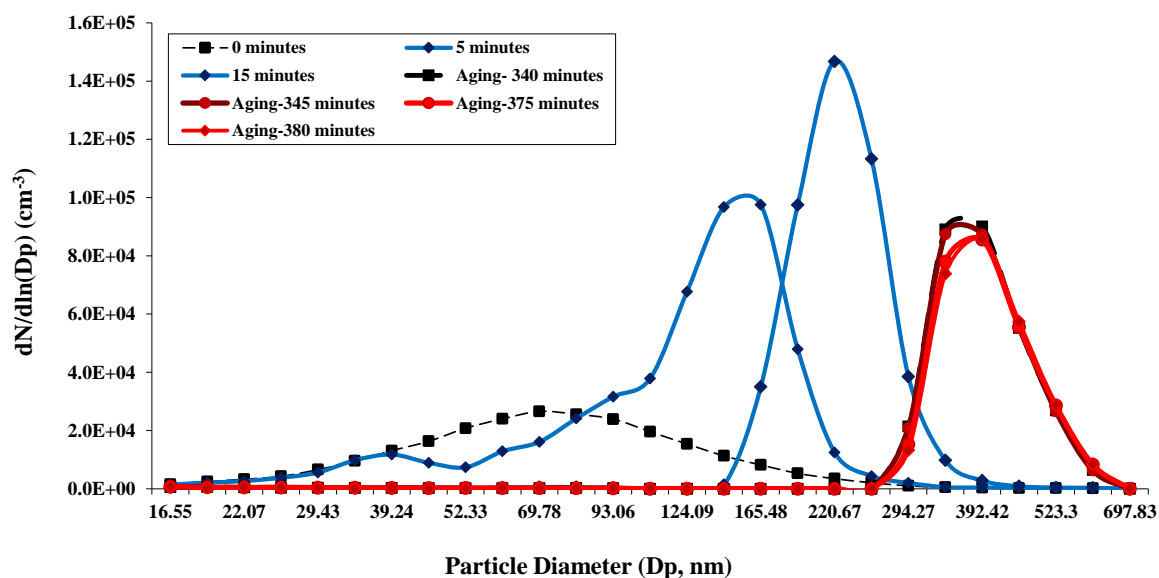


Figure 3.62 Particle size distribution during β -pinene O_3 -induced aging. The black dashed line (0 minutes) shows the time before β -pinene+ O_3 reaction started and the blue solid lines represent the particle growth while oxidizing β -pinene. The black dashed line (Aging-340 minutes) demonstrates the time before starting aging and the red solid lines show particle size distributions during aging.

The particulate mass concentration profile before and after the O₃ exposure period is illustrated in Fig. 3.63. After the first O₃ addition (time 0), an increase in particle mass was observed due to products formation from β-pinene oxidation. Arrows indicate the start of O₃ addition for aging which demonstrated no changes after 4 ppm O₃ and only a slight increase after O₃ level reached 8 ppm. Therefore, it was concluded that although O₃ had a very small influence at very high concentration level, the O₃-induced aging does not have any impacts on oxidation products. This is consistent with our expectation and also the earlier results which showed no changes in the signal of the products during O₃-induced aging.

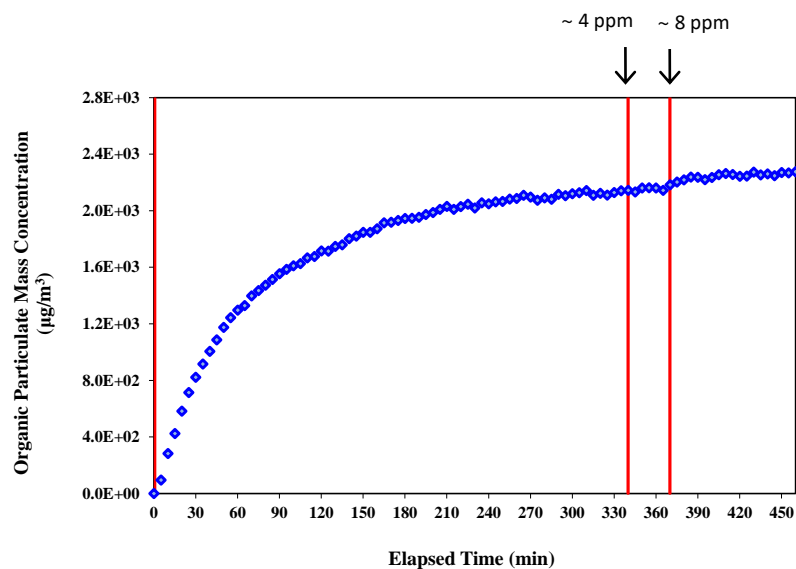


Figure 3.63 Time profile of organic particulate mass concentration during β-pinene O₃-induced aging experiment. The O₃ addition time is shown by red vertical lines and the overall O₃ levels are marked by arrows for each addition.

3.4.3. SOA Density

3.4.3.1 OH-induced Aging

As discussed in Section 3.1.2, the density of β -pinene generated particles was determined as $1.20 \pm 0.05 \text{ g cm}^{-3}$ and it was stable over the course of our experiments. In this study, we conducted a series of β -pinene OH-induced aging experiments to monitor the SOA density over the course of aging. Previously, we observed that the measured SOA density from nopinone/ NO_3 experiments was significantly higher than that of nopinone/OH experiments, likely due to the different chemical composition of organic particles. Therefore, comparison of the SOA density before and after aging could be used as an indication of changes in particle chemical composition that may occur during aging.

Figure 3.64 displays the time profiles of SOA volume, number and mass concentrations as well as SOA density before and after additional OH radical introduction. In these experiments, UV lights were turned off after the complete depletion of β -pinene followed by 2 times higher [IPN] injection. After mixing in the dark, the lights were turned on initiating the reaction.

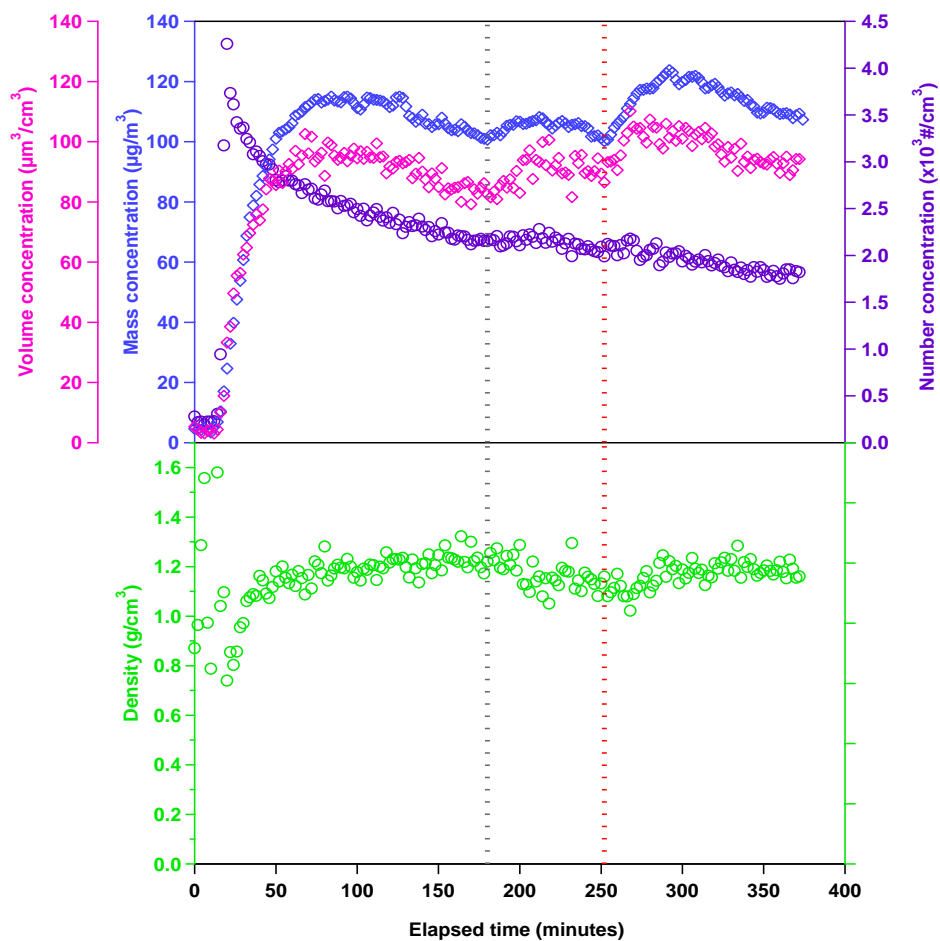


Figure 3.64 The time evolution of SOA volume, number and mass concentrations as well as SOA density in the smog chamber. Dashed grey and red lines indicate the time of the second IPN injection in the dark and turning on the UV lights, respectively. SOA density before and after aging were $1.20 \pm 0.04 \text{ g cm}^{-3}$ and $1.19 \pm 0.04 \text{ g cm}^{-3}$, respectively.

As shown in Fig. 3.64, SOA density remained constant prior to injection of additional IPN and no significant changes in SOA density were observed subsequent to exposure to additional OH radicals. There were increases in particle mass and volume concentrations and a decrease in the particle number concentration during the aging period. This indicates that the increase in particle volume is caused by the growth of the existing particles, not by

generation of new particles. These observations also indicate that the first generation semivolatile gas phase products (such as nopinone) further react with OH radicals, forming products with the same chemical composition or similar density that condense back to the pre-existing particles. This is consistent with the SOA chemical composition results from our studies which did not demonstrate any evidence of formation of high molecular-weight species or new oxidation products. The SRM profiles of products from β -pinene OH-induced aging experiments illustrated that nopinone decayed sharply upon additional OH exposure (Fig. 3.50), whereas a rise in signal was observed in the time profiles of some of the products such as carboxylic acids (Fig. 3.54). This indicates further oxidation of nopinone during aging and further formation of similar products. Hence, observing no significant changes in SOA density during aging was quite expected.

Since standards are not available for the majority of the identified products from β -pinene oxidation, it is not possible to confirm if the observed SOA density is comparable to that of carboxylic acids, as the dominant products in the particle phase. However, the density of a few carboxylic acids formed from monoterpene oxidation has been previously determined such as norpinic acid, pinic acid and pinonic acid. For crystalline pinic acid the density has been determined as $1.21 \pm 0.1 \text{ g cm}^{-3}$ (Krc, 1953). The density for cis pinonic acid is $1.22 \pm 1 \text{ g cm}^{-3}$ (Vanderhoff et al., 1986) and for norpinic acid is $1.3 \pm 0.1 \text{ g cm}^{-3}$. Since nopinone density is 0.98 g cm^{-3} , the SOA density measured during our β -pinene experiments ($\sim 1.20 \text{ g cm}^{-3}$) is more comparable to the average density of these carboxylic acids.

The measured SOA density during β -pinene aging experiment is consistent with that determined for the generated products from nopinone photooxidation. As discussed in Section 3.1.2.2, the average particle density of SOA generated from nopinone/OH was determined as $1.21 \pm 0.06 \text{ g cm}^{-3}$ which is not statistically different from that measured after aging in our OH-induced β -pinene aging experiments (t test did not show any significant differences between before and after aging at the 90 % and 68% confidence level). This further supports the fact that the chemical composition of products formed from nopinone oxidation by OH radicals is comparable to that produced from aging of β -pinene photooxidation products. Therefore, the increase in SOA mass during β -pinene aging experiments can be attributed mainly to further gas phase oxidation of nopinone and generating products with similar chemical composition.

Overall, the observed changes in the chemical composition of products and additional production of SOA mass during OH-induced aging of oxidation products derived from β -pinene photooxidation can be explained by further oxidation of semivolatile gas phase products, mainly nopinone, which produce compounds with similar chemical composition partitioning to the particle phase. This is consistent with no significant changes detected in the SOA density before and after OH-induced aging. On the contrary, O_3 -induced aging demonstrated no impact on the oxidation products and exhibited no further formation of SOA mass.

3.5. Mechanism of Formation of Identified Products

After compiling all the information gained through investigating the chemical composition of β -pinene and nopinone photooxidation products as well as the chemical aging and NO_x sensitivity of identified products, we attempted to probe the formation pathways of the identified oxidation products. The formation pathways for some of these products have been proposed in the MCM and in the literature. However, the formation mechanisms of some of the carboxylic acid and organic nitrate products identified in this study have not been proposed. Therefore, our results will help improve the current mechanisms and will extend them further. In the following Sections we will present the formation mechanisms for each category of compounds.

3.5.1. Nopinone

The formation of nopinone is proposed to occur through both primary and secondary pathways, which are compiled from MCM in Fig. 3.65. The reaction of β -pinene with OH radicals is initiated by the addition of OH to the exocyclic double bond to form β -hydroxy alkyl radicals. The subsequent addition of molecular oxygen to these alkyl radicals leads to the formation of peroxy radicals (RO_2). Reactions of the peroxy radicals with NO or RO_2 results in the formation of alkoxy radicals (RO) (76%) and organic nitrates (RONO_2) (24%). Subsequently, decomposition of the alkoxy radicals leads to the primary formation of nopinone. The proposed primary nopinone formation pathway results in an immediate nopinone onset upon β -pinene reaction with OH, as observed in Fig. 3.26.

In addition, a few secondary and higher order formation pathways to nopinone from OH-initiated oxidation of β -pinene have been proposed in Fig. 3.65. Reaction of β -pinene peroxy radicals with NO results in the formation of the C10-bicyclic hydroxy nitrate ($C_{10}H_{17}NO_4$, M 215). The subsequent oxidation of the C10-bicyclic hydroxy nitrate product with OH radicals is proposed to form either nopinone or another organic nitrate product, called C10-aldehyde nitrate ($C_{10}H_{15}NO_4$, M 213). Photolysis of the C10-aldehyde nitrate product also results in nopinone formation. Peroxy radicals also undergo self-reaction or cross-reactions with other peroxy radicals. Accordingly, the β -pinene peroxy radicals lead to the formation of the C10-dihydroxy ($C_{10}H_{18}O_2$, M 170) and the C10-hydroxy aldehyde ($C_{10}H_{16}O_2$, M 168). In addition to photolysis of the C10-hydroxy aldehyde product to nopinone, subsequent oxidation of this product with OH radicals produces a C10-hydroxy peroxyacetyl nitrate (C10-PAN) product, which can be oxidized to nopinone as well.

All these products that have been proposed to be nopinone precursors, were identified from β -pinene photooxidation in our study (Table D.1, Appendix D).

3.5.2. Hydroxyl and Carbonyl Containing Products

Several hydroxyl and carbonyl containing compounds have been identified during β -pinene photooxidation experiments in this study including oxo-nopinone, hydroxy nopinone, the C10-hydroxy aldehyde, hydroxy oxo-nopinone, the C10-dihydroxy and the C10-dihydroxy carbonyl. These products maintained the β -pinene 4- and 6-membered rings (Fig. 3.66).

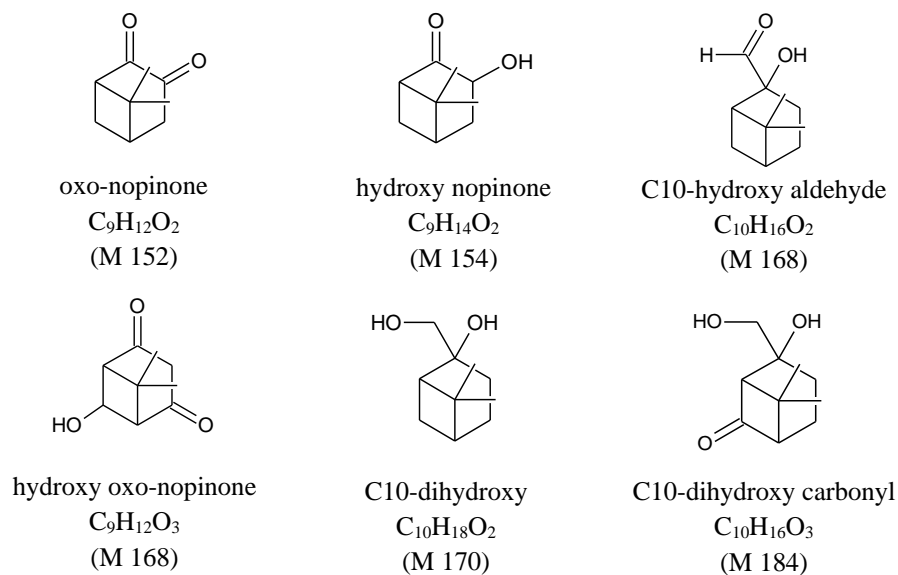


Figure 3.66 Structures of hydroxyl and carbonyl containing products identified during OH-initiated oxidation of β -pinene in this study.

The C10-hydroxy aldehyde, the C10-dihydroxy and the C10-dihydroxy carbonyl are formed via direct OH-initiated oxidation of β -pinene. The proposed mechanisms of formation for the C10-hydroxy aldehyde and the C10-dihydroxy have been demonstrated in Fig. 3.65. C10-dihydroxy carbonyl is formed through isomerization of the alkoxy radicals produced in the OH-initiated oxidation of β -pinene via a 1–5 H-shift. Then the alkyl radicals formed from the isomerization rapidly form peroxy radicals with subsequent reaction with NO to form alkoxy radicals which results in the formation of C10-dihydroxy carbonyl product (Fig. 3.67).

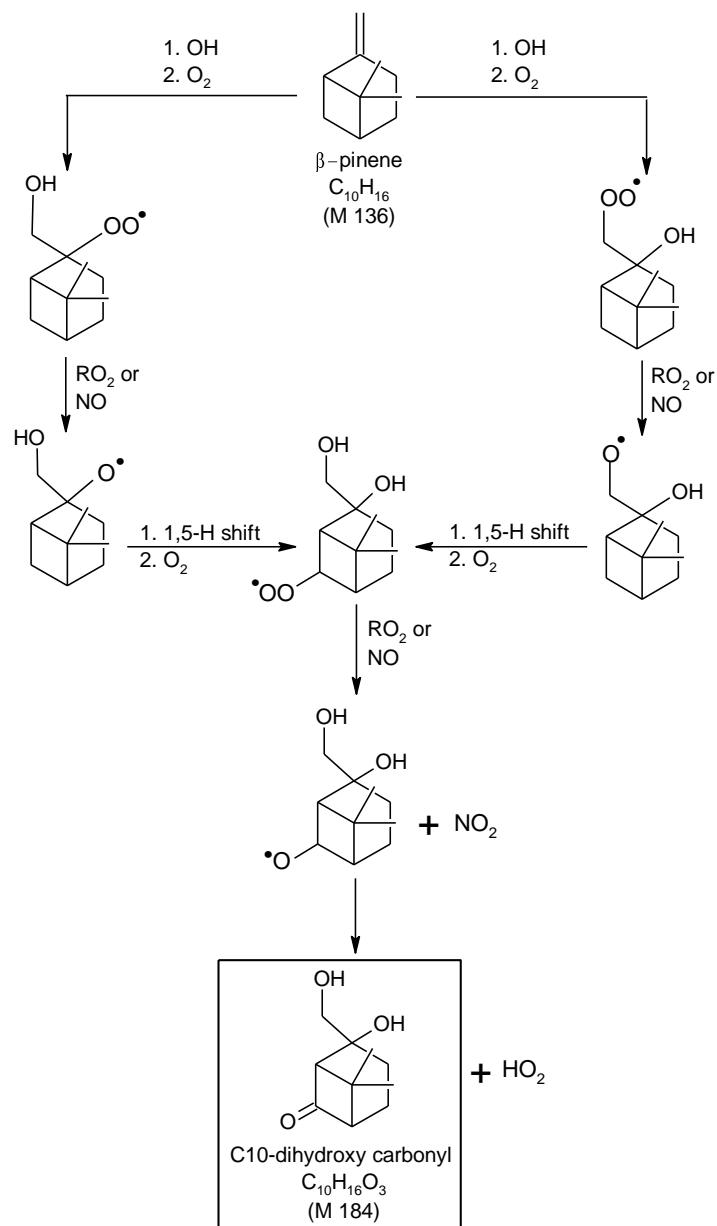


Figure 3.67 A schematic mechanism illustrating the formation pathway from β -pinene to the C10-dihydroxy carbonyl product. This mechanism has not been incorporated in the MCM, although it is presented by Davis et al. (2005).

Oxo-nopinone, hydroxy nopinone and hydroxy oxo-nopinone are formed via OH-initiated oxidation of nopinone. The proposed formation mechanisms of these products are illustrated in Fig. 3.68. The mechanistic pathway to these compounds is initiated by abstraction of an H-atom from nopinone at the 3-position. This has been proposed to be a favoured position due to resonance stabilization of the formed alkyl radical (Larsen et al., 2001). A subsequent rapid reaction with oxygen leads to the formation of a bicyclic C9-carbonyl peroxy radical, which is a key specie in the formation of a number of identified products. The subsequent reaction of the formed bicyclic C9-carbonyl peroxy radical with RO₂ radicals results in the formation of hydroxy nopinone and oxo-nopinone. Oxidation of hydroxy nopinone with OH radicals is an additional pathway to oxo-nopinone. Furthermore, hydroxy oxo-nopinone is produced via hydroxyl radical oxidation of the oxo-nopinone product.

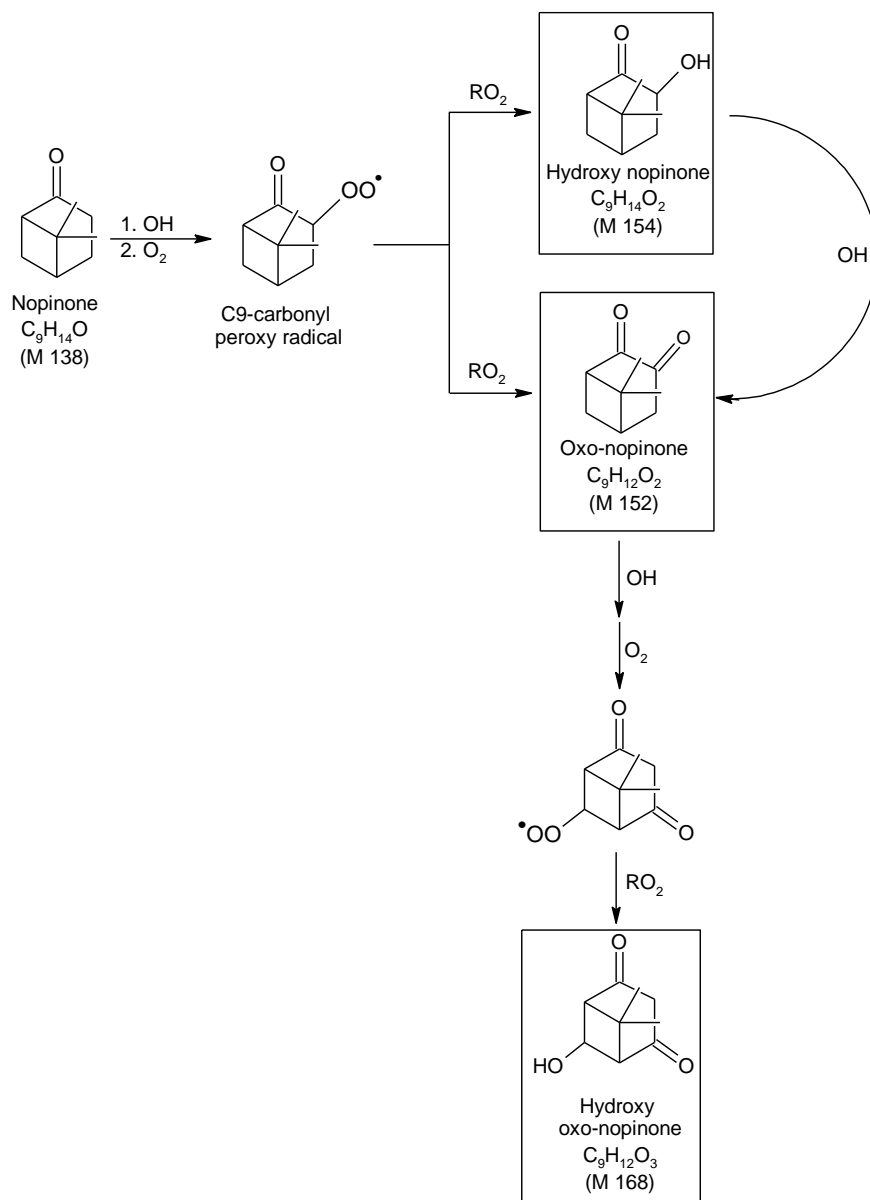


Figure 3.68 A schematic mechanism illustrating formation pathways from nopinone to hydroxy nopinone, oxo-nopinone, and hydroxy oxo-nopinone products, compiled from the MCM.

3.5.3. Carboxylic Acid Products

A number of products containing carboxylic acid functional groups have been identified during β -pinene photooxidation experiments in this study including norpinalic acid, the C8-keto acid, pinalic 3-acid, pinalic 4-acid, norpinic acid, pinic acid, homoterpenylic acid and the C10-hydroxy pinonic acid. All these products, except for homoterpenylic acid, retain the β -pinene 4-membered ring, and are formed through opening the 6-membered ring (Fig. 3.69).

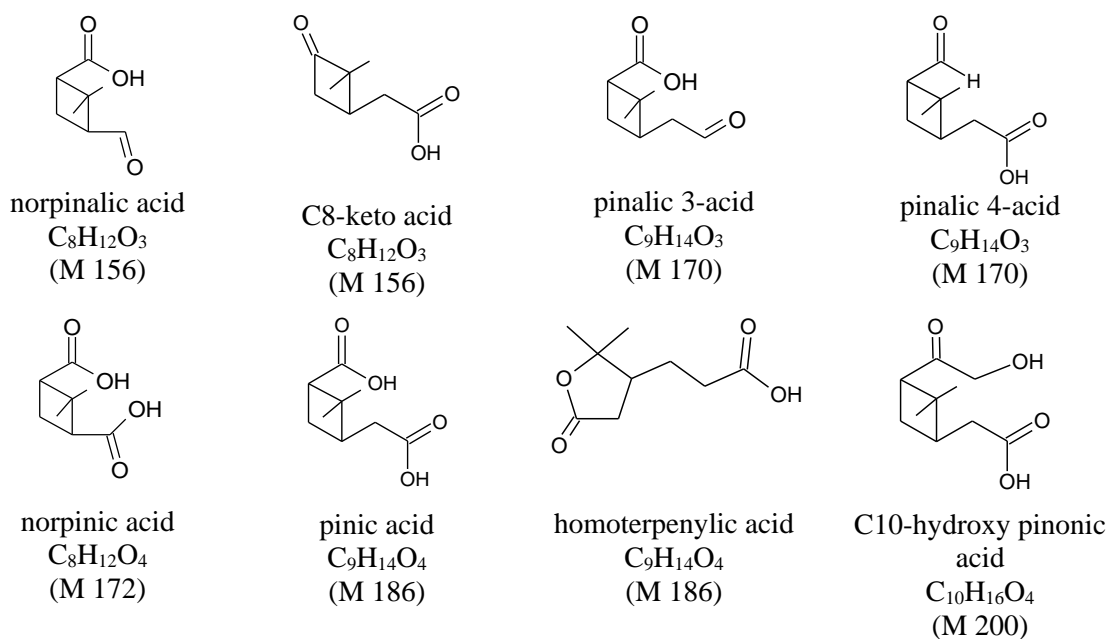
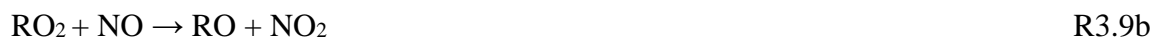


Figure 3.69 Structures of carboxylic acid products identified during OH-initiated oxidation of β -pinene in this study.

The formation of carboxylic acids is known to occur through the reaction of acylperoxy ($RC(O)O_2\bullet$) radicals with HO_2 (R3.8). Under conditions in which NO_x is present, peroxy radicals also react with NO , leading to the formation of organic nitrates (R3.9a) or the alkoxy

radical (R 3.9b). Hence, the formation of carboxylic acids is favoured under lower-NO_x conditions.



The majority of the carboxylic acids identified in this study formed via OH-initiated oxidation of nopinone, with the exception of the homoterpenylic acid and the C10-hydroxy pinonic acid. As shown in Fig. 3.68, the C9-carbonyl peroxy radical formed from nopinone oxidation can react with RO₂ to yield hydroxy nopinone and oxo-nopinone. Additionally, it can undergo reduction by reaction with NO or RO₂ and ring opening to form a C9-acylperoxy radical from which there are pathways to a number of carboxylic acids (Fig. 3.70).

After pinic acid, C10-hydroxy pinonic acid has been identified to be the most abundant product in the particle phase from β-pinene/OH (Larsen et al, 2001). The formation pathway to C10-hydroxy pinonic acid as a first generation product, is through OH addition to β-pinene (Fig. 3.71). The formed peroxy radical either reacts with NO or RO₂ to form alkoxy radical, which undergoes ring opening, or reacting with RO₂ to yield the C10-dihydroxy compound. Subsequently, the formed alkyl radical and C10-dihydroxy are further oxidized to form the C10-hydroxy pinonic acid. The formation of the homoterpenylic acid can also occur through OH addition to β-pinene, which is illustrated in Fig. 3.72.

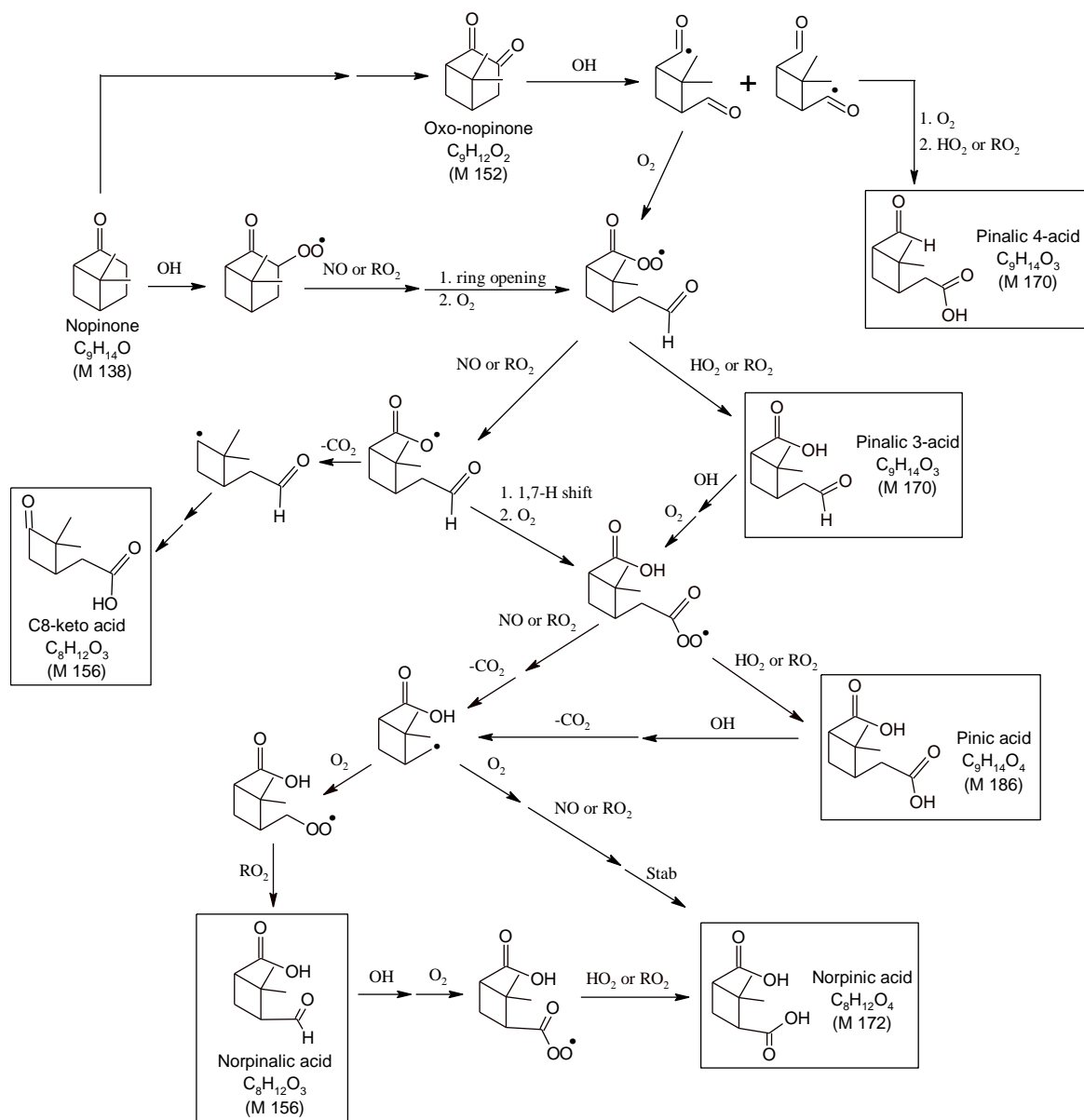


Figure 3.70 A schematic mechanism illustrating formation pathways from nopinone to a number of carbocyclic acid products (norpinalic acid, C8-keto acid, pinalic 3-acid, pinalic 4-acid, norpinic acid and pinic acid) identified in this study. These mechanisms are compiled from the MCM, Larsen et al. (2001) and Jaoui and Kamens (2003).

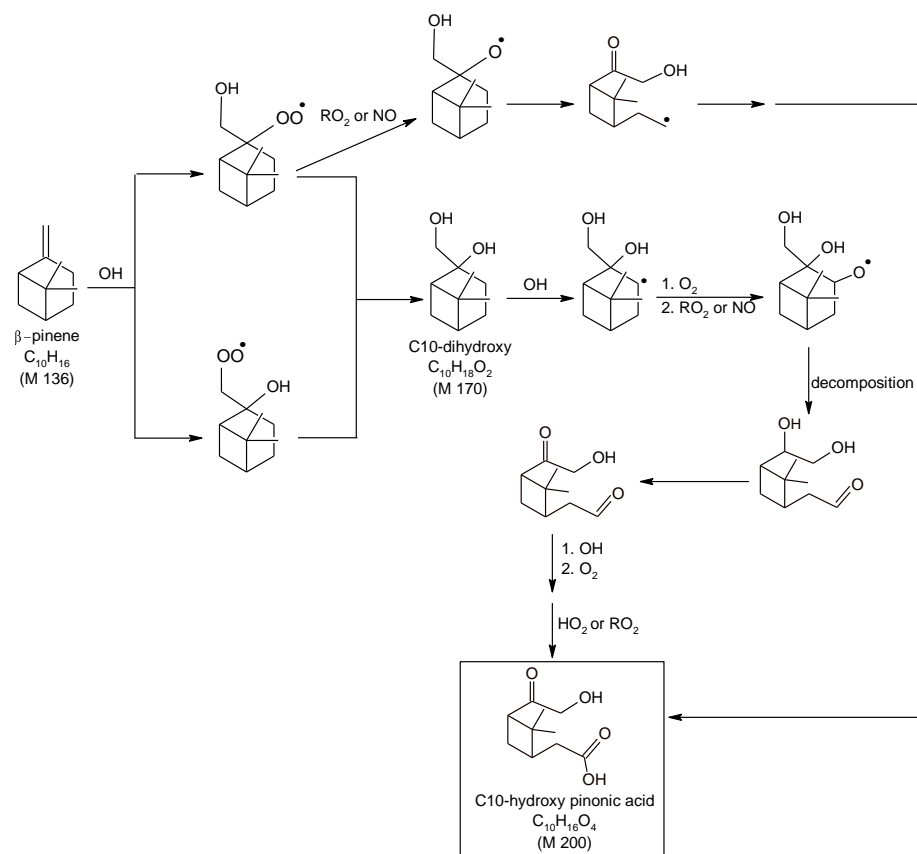


Figure 3.71 A schematic mechanism illustrating formation pathways from β -pinene to the C10-hydroxy pinonic acid (MCM; Jaoui and Kamens (2003)).

In this study, norpinalic acid (or C8-keto acid), norpinic acid, pinalic 3-acid (or pinalic 4-acid) and pinic acid have been identified during the nopinone photooxidation experiments (Section 3.2.4.1). This further supports the fact that their formation mechanisms is via OH-initiated oxidation of nopinone. In addition, the observed formation enhancement under lower- NO_x conditions for norpinic acid, pinalic 3-acid (or pinalic 4-acid), pinic acid and the C10-hydroxy pinonic acid (Section 3.3.1.2) is consistent with their formation pathway through $RC(O)O_2 + HO_2$, as illustrated in Fig. 3.70-71. However, norpinalic acid (or C8-keto

3.5.4. Organic Nitrate Products

In addition to carbonyls and acids, the photooxidation experiments in the presence of NO_x are expected to produce organic nitrates. Several organic nitrates have been identified during β -pinene photooxidation experiments in this study including the nitroxy nopinone, the C10-aldehyde nitrate, the C10-bicyclic hydroxy nitrate, the C10-monocyclic hydroxy nitrate, the C10-dihydroxy nitrate and the C10-PAN. The structure of these organic nitrates is illustrated in Fig. 3.73.

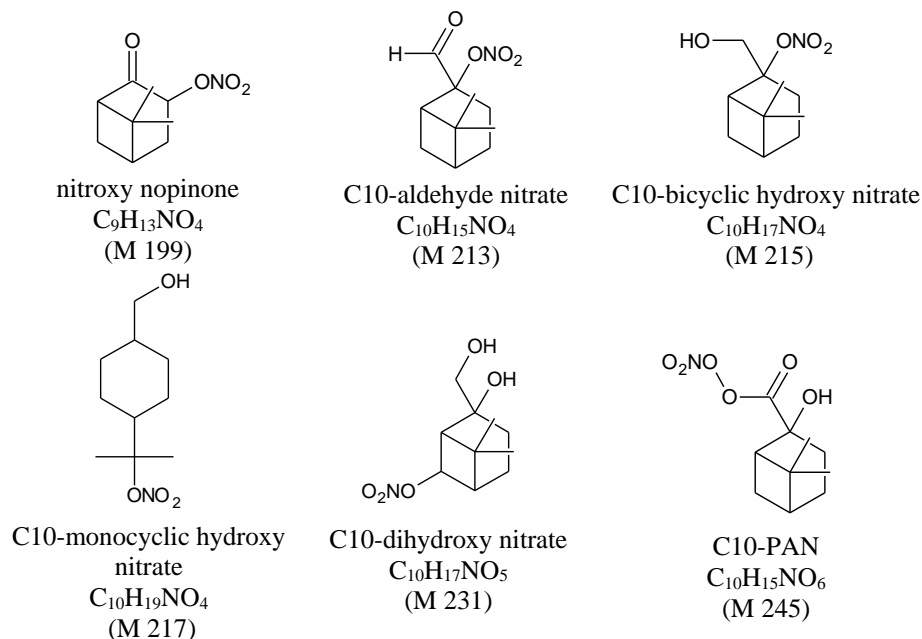


Figure 3.73 Structures of organic nitrate products identified during OH-initiated oxidation of β -pinene in this study.

As discussed previously, the nitrate functionality is formed through the reaction of peroxy radicals (RO_2) with NO (R3.9a), which is in competition with the formation of alkoxy radicals (RO , R3.9b). The formation mechanism of organic nitrates formed from hydroxyl

radical oxidation of β -pinene or nopinone have been rarely investigated. The majority of the organic nitrates confirmed in the particle phase from β -pinene photooxidation were C10, with the formation mechanism via OH addition to β -pinene. The formation pathways proposed by Aschmann et al. (1998) for the C10-bicyclic hydroxy nitrate and the C10-dihydroxy nitrate are the only available mechanisms in the literature. The mechanisms of formation for the C10-aldehyde nitrate, the C10-bicyclic hydroxy nitrate, the C10-dihydroxy nitrate and the C10-PAN are demonstrated in Fig. 3.74.

The proposed pathway for the C10-dihydroxy nitrate involves an isomerization of the alkoxy radical formed from β -pinene peroxy radical which results in the formation of several isomers of the C10-dihydroxy alkyl radical. The subsequent reaction of the dihydroxy alkyl radical with O₂ and then NO leads to the nitrate formation. Additionally, another pathway may occur through the C10-dihydroxy product which undergoes hydrogen abstraction by OH radicals.

The formation of the C10-bicyclic hydroxy nitrate is via the β -pinene peroxy radical reaction with NO. The subsequent oxidation of the C10-bicyclic hydroxy nitrate product with OH radicals is proposed to form the C10-aldehyde nitrate. However, there may be a direct pathway from β -pinene to the C10-aldehyde nitrate, which is not known at this time.

The proposed pathway for the formation of peroxyacyl nitrates (PANs) is through the reaction of acylperoxy (RC(O)O₂•) radicals with NO₂ (R3.10).



The C10-PAN formation occurs through oxidation of the C10-hydroxy aldehyde product with OH radicals, with subsequent reaction of the formed acylperoxy radicals with NO₂.

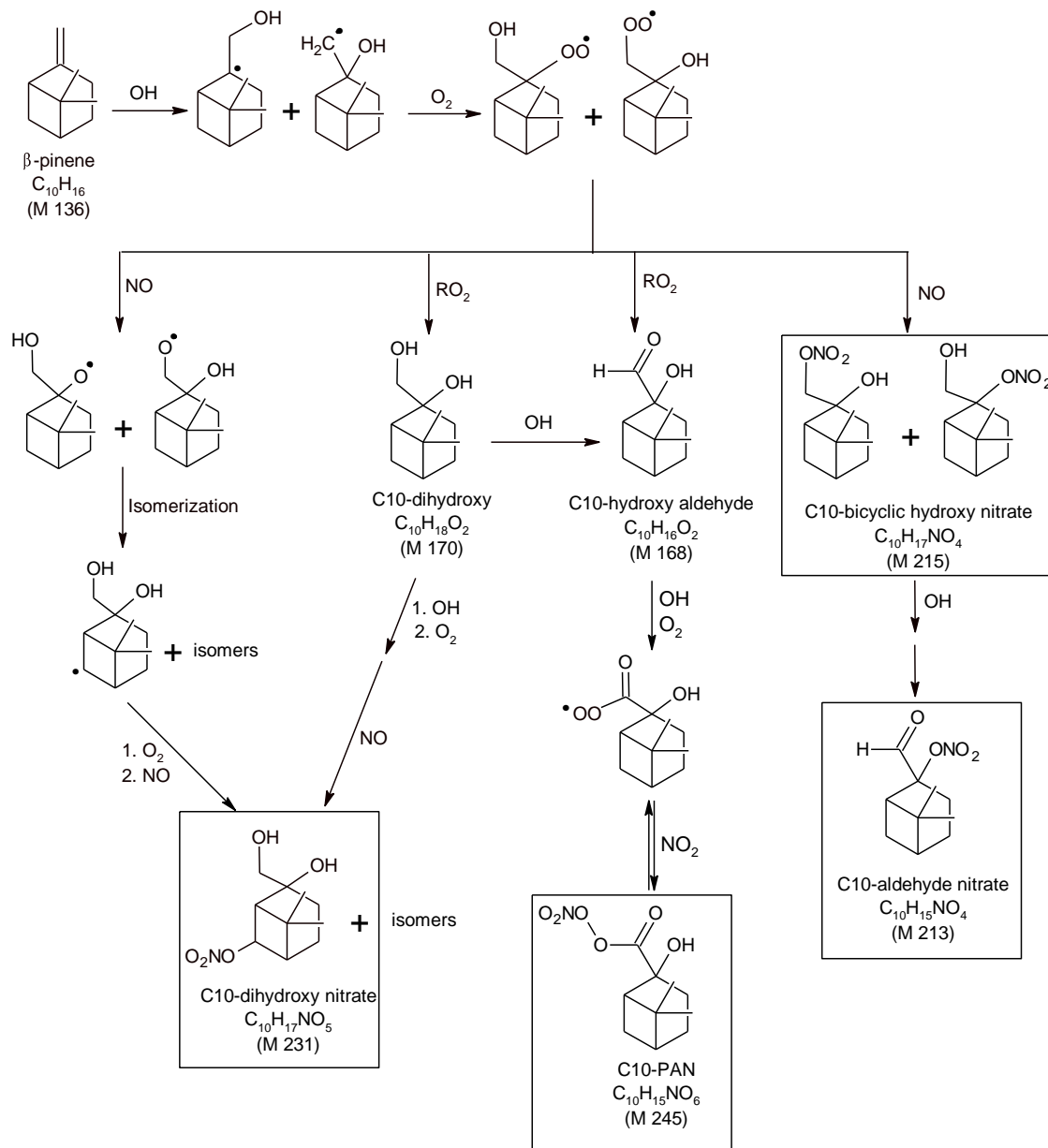


Figure 3.74 A schematic mechanism illustrating formation pathways from β -pinene to a number of organic nitrates (C10-dihydroxy nitrate, C10-bicyclic hydroxy nitrate, C10-aldehyde nitrate and C10-PAN) identified in this study.

The formation of nitroxy nopinone product is proposed in the MCM to be a primary oxidation product of nopinone, which is illustrated in Fig. 3.75.

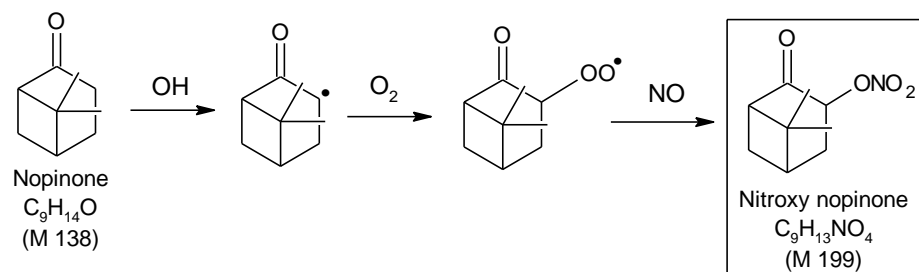


Figure 3.75 A schematic mechanism illustrating formation pathway from nopinone to nitroxy nopinone.

Overall, the majority of the identified organic nitrate products have been proposed to form through OH oxidation pathways from β -pinene. As discussed previously in Section 3.4.1.1, the results of our β -pinene OH-induced aging demonstrated no further formation of these organic nitrates (C10-aldehyde nitrate, C10-bicyclic hydroxy nitrate and C10-dihydroxy nitrate) during aging, which is consistent with their proposed formation mechanism. In addition, the low signal of the peaks associated with these nitrates during the nopinone photooxidation experiments (Section 3.2.4.1), further suggests that these organic nitrates are C10 nitrates with the formation pathway via β -pinene oxidation.

4. Conclusions and Future Directions

4.1 Conclusions

4.1.1. Chemical Composition

The chemical composition of oxidation products produced from β -pinene photooxidation was investigated in both gas and particle phases in the York University smog chamber. Integrating the counter flow membrane denuder (CFMD) and the atmospheric pressure chemical ionization mass spectrometer (APCI-MS/MS) with the smog chamber has allowed successful online analysis of the particle phase products. A number of compounds were detected from β -pinene oxidation which contained a number of functional groups including alcohols, aldehydes, ketones, carboxylic acids and nitrates. In total, 21 oxidation products have been identified in the gas and particle phase with 9 of these found predominantly in the particle phase. The formation of 18 products was confirmed in the particle phase based on the acquired accurate masses which involved differentiating between 9 isobaric compounds (Appendix D). Products that have not previously been shown experimentally to form from β -pinene photooxidation include; C6-hydroxy keto-aldehyde (m/z 145), hydroxy oxo-nopinone (m/z 169), C10-aldehyde nitrate (m/z 214), C10-monocyclic hydroxy nitrate (m/z 218) and C10-PAN (m/z 246). Moreover, three carboxylic acids (m/z 185, 199, 203) and an organic nitrate (m/z 260) were present. In addition, the results of the OH-initiated nopinone experiments revealed many similarities between the oxidation products formed from β -pinene and nopinone, confirming a number of the oxidation pathways through nopinone, with the majority of the identified products from nopinone were found to be carboxylic acids.

4.1.2. Physical Properties

Investigating the shape and physical state of generated particles with SEM revealed that laboratory generated SOA particles from β -pinene oxidation were generally spherical and ellipsoidal in shape. In addition, the SEM images showed that particles may adopt an amorphous semi-solid/liquid state, particularly for particles collected on quartz filters. However, in other chamber experiments or environments particles may be solid depending on the conditions under which the SOA particles are produced such as the precursor compound, precursor concentrations and chamber relative humidity (Bahreini et al., 2005).

For the first time, the real-time particle density was determined using the TEOM-SMPS system for the chamber generated SOA particles from β -pinene+OH, nopinone+OH and nopinone+NO₃ reactions which were found to be 1.20 ± 0.05 , 1.21 ± 0.06 and 1.39 ± 0.03 g cm⁻³ respectively. The result of our study showed that the measured SOA density from nopinone/NO₃ experiments was significantly higher than that of β -pinene/OH and nopinone/OH experiments. This is consistent with the chemical composition of particles produced from nopinone oxidation with NO₃ radicals, which revealed differences between the compositions of products formed from NO₃- and OH-induced oxidation of nopinone. The observed higher density was consistent with the high molecular weight organic nitrates (e.g. peroxyacyl nitrates (PANs, C_xH_yO₃NO₂)) identified in the nopinone/NO₃ system. The correlation between the SOA density and the chemical composition of particles points to the suitability of density measurements in providing insight into particle compositions.

4.1.3. Chemical Aging

Oxidative aging of oxidation products derived from β -pinene was investigated by exposing the products to additional hydroxyl radicals or ozone. The results indicated that the aging had a greater impact on changes in particle composition and mass for the β -pinene OH-induced aging compared with the very stable dark ozonolysis system. The observed changes in chemical composition of products and additional production of SOA mass during OH-induced aging have been attributed to the further oxidation of gas phase intermediate products, mainly nopinone, which generates compounds partitioning to the particle phase. SRM time profiles of a number of previously identified carboxylic acids, including pinalic 3-acid (or pinalic 4-acid, M 170), norpinic acid (M 172), pinic acid (M 186) and C10-hydroxy pinonic acid (M 200), demonstrated an increase in their signal during the aging period in both gas and particle phases. This was consistent with the formation mechanism of these carboxylic acids, which was proposed to form through OH-initiated oxidation of nopinone. In contrast, the majority of organic nitrates such as C10-aldehyde nitrate (M 213), C10-bicyclic hydroxy nitrate (M 215) and C10-dihydroxy nitrate (M 231), exhibited a decay in their SRM signal after exposure to additional OH radicals. This observation was in agreement with the formation pathways of these organic nitrates, which was identified to be via β -pinene oxidation and independent of nopinone formation. These findings were consistent with the results of our nopinone photooxidation experiments, which showed that the majority of the identified products from nopinone oxidation were carboxylic acids. In addition, the SOA mass generated from the nopinone photooxidation experiments accounts

for nearly half of the additional SOA mass produced during β -pinene OH-induced aging, indicating nopinone plays a significant role in further formation of oxidation products and therefore SOA mass.

In addition, SOA density was monitored during β -pinene aging experiments which demonstrated no significant changes before and after OH-induced aging. This indicates that the semivolatile products formed during aging have similar composition as the initial products before aging which was consistent with the chemical composition results obtained in our study. Moreover, no significant difference was observed between the SOA density determined from nopinone/OH experiments ($1.21 \pm 0.06 \text{ g cm}^{-3}$) and the density of SOA formed by aging the first-generation β -pinene photo-oxidation products ($1.19 \pm 0.04 \text{ g cm}^{-3}$). This further demonstrates that the chemical composition of products formed from OH-initiated oxidation of nopinone is similar to that produced upon aging of generated products from β -pinene oxidation. This was consistent with no evidence of formation of high molecular-weight species or new oxidation products during aging experiments.

4.1.4. [NO_x] and [OH] Dependence of SOA Formation

We extended this research study by investigating the NO_x dependence of SOA formation from photooxidation of β -pinene in both the York University smog chamber and the Jülich Plant Atmosphere Chamber. The impact of NO_x on SOA formation was found to be very similar to the behavior observed in other studies (Pandis et al., 1991; Zhang et al., 1992; Presto et al., 2005; Kroll et al., 2006; Camredon et al., 2007; Pathak et al., 2007; Chan et al.,

2010; Hoyle et al., 2011; Loza et al., 2014). At low-NO_x levels SOA yields increased with increasing NO_x and then decreased at higher NO_x concentrations. The increase of yield at low NO_x concentrations was caused by the NO_x-induced increase of OH concentration, most probably from OH recycling in the NO + HO₂ → NO₂ + OH reaction.

Investigating the NO_x sensitivity of individual products in this work has provided insights into the dependence of product formation pathways on NO_x level. Our results have shown that products containing different functionalities illustrate various NO_x sensitivities. Formation of nopinone was observed to be NO_x insensitive, while the majority of carboxylic acid products demonstrated a similar NO_x dependence as the SOA yield; their formation decreased with increasing NO_x. This suggested a pathway that is favored under lower-NO_x conditions, which was consistent with the general formation mechanism of carboxylic acids which is through RO₂ + HO₂ pathway. Although it was expected to find enhancement for organic nitrates under higher-NO_x levels, the dependence of their formation on NO_x was more complex due to the interplay of the OH effect with that of NO_x. Therefore, it was concluded that understanding the true impact of NO_x on the formation of all products requires isolating the impact of OH from that of NO_x.

In the JPAC experiments, the effect of OH concentration on SOA mass growth was removed by keeping the OH concentration constant. This showed that SOA yields only decrease with increasing [NO_x]. Additionally, measuring the NO_x dependence of SOA yields at lower [NO]/[NO₂] ratios showed less pronounced increases in both OH concentration and SOA yield. This result is consistent with our assumption of OH recycling by NO and to SOA

yields being dependent on OH concentrations. To our knowledge, this is the first study that proves that the observed increase in SOA yield was due to the NO_x enhancing OH and not a direct impact of NO_x on the SOA production. By probing the NO_x dependence of SOA formation in the presence of seed particles, our results indicated that a substantial fraction of the NO_x-induced decrease of SOA yields at higher NO_x levels was caused by NO_x-induced suppression of new particle formation, which subsequently limits the particle surface area where low volatiles condense.

Eliminating the effect of NO_x-induced suppression of new particle formation and NO_x-induced changes of OH concentrations in JPAC, showed that the remaining effect of NO_x on SOA mass formation was only moderate. Even at the highest NO_x level, suppression of mass yield was only 20–30 %. VOC / NO_x ratios in typical urban air are often much higher than the lower end of the [BVOC] / [NO_x] range used in our study (Cai et al., 2011; Pollack et al., 2013; Zou et al., 2015). Therefore, depending on the conditions, impacts of NO_x on SOA formation in the real atmosphere may be far less than 20–30 %.

Our study also showed that SOA yield is dependent on OH concentration. This was achieved by separate measurements in JPAC without NO_x addition but with different OH primary production rates. Our results showed that besides SOA yield dependencies on the amount of pre-existing matter and effects like partitioning, there was also a dependence on reaction conditions, in particular on oxidant levels which is believed to be caused by secondary reactions. In general, although SOA yields measured in laboratory chambers may not be indicative of the yields in the real atmosphere, their variations as a consequence of different

conditions could provide a more comprehensive description of SOA in global and climate model.

4.1.5. Formation Mechanisms

Finally, this work evaluated the formation mechanism of identified products of β -pinene photooxidation, based on all the information collected through investigating the chemical composition of products as well as the impact of chemical aging and NO_x on product formation. Our results demonstrated that in order to have a complete oxidation mechanisms it is necessary to obtain detailed information of the oxidation products. This is valuable to create more accurate predictive atmospheric models.

4.2 Future Directions

In our laboratory studies, we attempted to fully characterize the chemical and physical properties of β -pinene oxidation products. Although the results of our study have shed light on a number of unknown areas associated with reaction products, there are still some unanswered questions to be addressed in future studies. Some of these questions can be answered by further characterization of SOA formation processes and their chemical and physical properties in our study and some need to be assessed on a broader environmental scale.

Future research studies could extend the findings of this study in a few different directions. One future research direction is to improve our knowledge of the physical state of particles.

Studies on particles morphology have shown high variability in the phase state of particles, depending on the conditions under which the aerosol formed. One of the factors that is believed to affect the particle phase is the precursor concentration (Bahreini et al., 2005; Mikhailov et al., 2009). In our chamber study, we used high β -pinene concentration which resulted in very high SOA mass loadings ($> 1000 \mu\text{g cm}^{-3}$). This may enhance the partitioning of higher volatility products into the particle phase and results in liquid phase particles. To further investigate the phase of particles, it would be beneficial to lower the β -pinene concentration in the chamber and examine the phase of produced particles. This will help to distinguish if the observed semi-solid/liquid phase state is linked to the chemical composition of particles formed from β -pinene or if it is influenced by the high β -pinene concentration.

In addition, the use of the TEOM-SMPS system has proven to be a useful technique in this study to gain insight into the particle compositions. Our results demonstrated that the measured SOA density from nopinone/ NO_3 experiments was significantly higher than that of nopinone/OH experiments, pointing to the differences in the chemical composition of the generated SOA in these two systems. To further explore this, NO_3 -induced β -pinene aging experiments could be performed to monitor the changes in SOA density before and after aging. This way we can further investigate the effect of NO_3 radicals on products produced from the photooxidation of β -pinene.

We also explored the impact of NO_x and OH on SOA formation from β -pinene photooxidation in the JPAC. However, there are a few other factors that also influence the

SOA formation. One that we were unable to study was the temperature dependence of SOA formation, which has been explained in different studies as affecting the gas/particle partitioning of semivolatiles. However, it has been shown that the partitioning theory alone cannot fully explain the overall temperature dependence of SOA formation (Jonsson, 2008; Von Hessberg et al., 2008). The results of recent studies (Pathak et al., 2007; Jonsson et al., 2008; Von Hessberg et al., 2008) indicate that the impact of temperature on SOA yields not only depends on the gas/particle partitioning but also on the changes in the kinetics of reactions and the presence of water vapour. Von Hessberg et al. (2008) found that under dry conditions, the SOA yields from β -pinene ozonolysis increase by decreasing temperature whereas the SOA yields decrease linearly with decreasing temperature under humid conditions. These results exhibit significant temperature dependence of SOA yield and therefore, highlight the need for further investigation.

The future work must be also pursued on a broader scale. Although the intensive research studies in atmospheric chemistry have made substantial progress towards understanding and characterization of atmospherically relevant processes, still more extensive laboratory studies are needed to extend our current knowledge of the atmosphere. Incorporating the detailed chemistry of the atmospherically relevant processes into atmospheric models helps to develop a more accurate and comprehensive prediction system. A few examples of the areas of which yet relatively little is known about and need to be further addressed in future laboratory studies are as follows;

The chemical mechanisms for the oxidation of VOCs is very complex and the current mechanisms cannot fully explain all the tropospheric VOC oxidation processes. These mechanisms should include not only the gas-phase VOC reactions but also the chemical reactions that take place in aqueous phase (in clouds or fogs) and on the surface or within the bulk of the aerosol particles. Thus, more detailed understanding is required on the particle surface and bulk chemical composition, hygroscopic properties of particles, as well as particle phase state and morphology. Additionally, the recently identified extremely low volatility organic compounds (ELVOC) from biogenic VOCs oxidation are suggested to promote aerosol particle formation in the atmosphere (Ehn et al. 2014). However, traditional atmospheric oxidation chemistry does not fully represent this class of compounds. Therefore, for a complete understanding of ELVOCs, a detailed assessment is required to determine their chemical composition, volatility, physical properties and formation pathways.

As stated, there are many complex chemical processes that occur in the atmosphere which need to be identified and studied in detail in laboratory experiments to provide a more comprehensive data base for inclusion in models. Apart from attempts to conduct experiments under atmospheric conditions to give an accurate representation of the real atmosphere, the laboratory findings also need to be accurately parameterized for implementing into models. This requires close collaboration between atmospheric modelers and the scientists performing laboratory experiments (or field campaigns) in order to improve the quality of the atmospheric models.

Bibliography

Alfarra, M. R., Paulsen, D., Gysel, M., Garforth, A. A., Dommen, J., Prevot, A. S. H., Worsnop, D. R., Baltensperger, U., Coe, H.: A mass spectrometric study of secondary organic aerosols formed from the photooxidation of anthropogenic and biogenic precursors in a reaction chamber, *Atmos. Chem. Phys.*, 6, 5279–5293, 2006.

Aljawhary, D., Lee, A. K. Y., and Abbatt, J. P. D.: High-resolution chemical ionization mass spectrometry (ToF-CIMS): application to study SOA composition and processing, *Atmos. Meas. Tech.*, 6, 3211–3224, doi:10.5194/amt-6-3211–2013, 2013.

Aschmann, S. M., Reisseil, A., Atkinson, R. and Arey, J.: Products of the gas phase reactions of the OH radical with α - and β -pinene in the presence of NO, *J. Geophys. Res. Atmos.*, 103(D19), 25553–25561, doi:10.1029/98JD01676, 1998.

Atkinson R and Arey J: Atmospheric degradation of volatile organic compounds, *Chem. Rev.*, 103(12):4605–4638, doi:10.1021/CR0206420, 2003.

Atkinson, R., Baulch, D. L., Cox, R. A., Crowley, J. N., Hampson, R. F., Hynes, V, Jenkin, M. E., Rossi, M. J., and Troe, J.: Evaluated kinetic and photochemical data for atmospheric chemistry: Volume I – gas phase reactions of O_x, HO_x, NO_x and SO_x species, *Atmos. Chem. Phys.*, 4, 1461–1738, 2004.

Auld, J.: A smog chamber study of mechanisms for beta-pinene oxidation by hydroxyl radicals, Ph.D., York University, Canada, 2009.

Auld, J. and Hastie, D. R.: Tandem mass spectrometry and multiple reaction monitoring using an atmospheric pressure chemical ionization triple quadrupole mass spectrometer for product identification in atmospherically important reactions, *Int. J. Mass Spectrom.*, 282(3), 91–98, 2009.

Badertscher, M., Bischofberger, K., Munk, M.E., Pretsch, E.: A novel formalism to characterize the degree of unsaturation of organic molecules, *J. Chem. Inf. Comput. Sci.*, 41 (4), 889–893, 2001.

Bahreini, R., Keywood, M. D., Ng, N. L., Varutbangkul, V., Gao, S., Flagan, R. C., Seinfeld, J. H., Worsnop, D. R., and Jimenez, J. L.: Measurements of secondary organic aerosol from oxidation of cycloalkenes, terpenes, and m-xylene using an aerodyne aerosol mass spectrometer, *Environ. Sci. Technol.*, 39(15), 5674–5688, 2005.

Bauer, S. E. and S. Menon: Aerosol direct, indirect, semidirect, and surface albedo effects from sector contributions based on the IPCC AR5 emissions for preindustrial and present-day conditions, *J. Geophys. Res. Atmos.*, 117: D01206, 2012.

Bennett, J. F., Collin, F., and Hastie, D. R.: A laboratory flow reactor with gas particle separation and on-line MS/MS for product identification in atmospherically important reactions, *Atmos. Meas. Tech.*, 2, 813–823, doi:10.5194/amt-2-813-2009, 2009.

Bienenstock, Y.: Chamber studies of particulate production from OH reactions with toluene, M.Sc., York University, 2001.

Blake, R. S., Monks P. S., Ellis A. M.: Proton-transfer reaction mass spectrometry, *Chem. Rev.*, 109(3), 861–896, 2009.

Brook, R. D., Rajagopalan, S., Pope, C. A., Brook, J. R., Bhatnagar, A., Diez-Roux, A. V., Holguin, F., Hong, Y., Luepker, R. V., Mittleman, M. A., Peters, A., Siscovick, D., Smith, S. C., Whitsel, L. and Kaufman, J. D.: Particulate matter air pollution and cardiovascular disease: An update to the scientific statement from the american heart association, *Circulation*, 121(21), 2331–2378, 2010.

Bruins, A. P.: Mass spectrometry with ion sources operating at atmospheric pressure, *Mass Spectrom. Rev.*, 10(1), 53–77, 1991.

Cai, C., Kelly, J. T., Avise, J. C., Kaduwela, A. P., and Stockwell, W. R.: Photochemical modeling in California with two chemical mechanisms: model intercomparison and response to emission reductions, *J. Air Waste Manage.*, 61, 559–572, doi:10.3155/1047-3289.61.5.559, 2011.

Calogirou, A., Jensen, N. R., Nielsen, C. J., Kotzias, D. and Hjorth, J.: Gas-phase reactions of nopinone, 3-isopropenyl-6-oxo-heptanal, and 5-methyl-5-vinyltetrahydrofuran-2-ol with OH, NO₃, and ozone, *Environ. Sci. Technol.*, 33, 453–460, 1999.

Camredon, M., Aumont, B., Lee-Taylor, J. and Madronich, S.: The SOA/VOC/NO_x system: an explicit model of secondary organic aerosol formation, *Atmos. Chem. Phys.*, 7(21), 5599–5610, doi:10.5194/acp-7-5599-2007, 2007.

Capouet, M. and Müller, J.-F.: A group contribution method for estimating the vapour pressures of α -pinene oxidation products, *Atmos. Chem. Phys.*, 6, 1455–1467, 2006.

Cappa, C. D., Lovejoy, E. R., Ravishankara, A. R.: Evidence for liquid-like and nonideal behavior of a mixture of organic aerosol components, *Proc. Natl. Acad. Sci. U. S. A.*, 105, 18687–18691, 2008.

Chan, A. W. H., Chan, M. N., Surratt, J. D., Chhabra, P. S., Loza, C. L., Crouse, J. D., Yee, L. D., Flagan, R. C., Wennberg, P. O., and Seinfeld, J. H.: Role of aldehyde chemistry and NO_x concentrations in secondary organic aerosol formation, *Atmos. Chem. Phys.*, 10, 7169–7188, doi:10.5194/acp-10-7169-2010, 2010.

ChemSpider, <http://www.chemspider.com/Chemical-Structure.15907.html>, (accessed June 2016).

Claeys, M., Iinuma, Y., Szmigielski, R., Surratt, J. D., Blockhuys, F., Van Alsenoy, C., Boege, O., Sierau, B., Gomez-Gonzalez, Y., Vermeylen, R., Van der Veken, P., Shahgholi, M., Chan, A. W. H., Herrmann, H., Seinfeld, J. H. and Maenhaut, W.: Terpenylic Acid and related compounds from the oxidation of α -pinene: Implications for new particle formation

and growth above forests, *Environ. Sci. Technol.*, 43(18), 6976–6982, doi:10.1021/es9007596, 2009.

Cody, R.B., Laramée, J.A., Durst, H.D.: Versatile new ion source for the analysis of materials in open air under ambient conditions, *Anal. Chem.*, 77(8), 2297–2302, doi:10.1021/ac050162, 2005.

Dass, C.: *Fundamentals of contemporary mass spectrometry*, John Wiley and Sons, Inc., 2007.

Davidson, J. A., Cantrell, C. A., McDaniel, A. H., Shetter, R. E., Madronich, S., and Calvert, J. G.: Visible-ultraviolet absorption cross sections for NO₂ as a function of temperature, *J. Geophys. Res.-Atmos.*, 93, 7105–7112, doi:10.1029/JD093iD06p07105, 1988.

Davidson, C. I., Phalen, R. F., and Solomon, P. A.: Airborne particulate matter and human health: A Review, *Aerosol Sci. Technol.*, 39, 737–749, 2005.

Davis, M. E. and Stevens, P. S.: Measurements of the kinetics of the OH-initiated oxidation of α -pinene: Radical propagation in the OH + α -pinene + O₂ + NO reaction system., *Atmos. Environ.*, 39(10), 1765–1774, 2005.

DeCarlo, P. F., Slowik, J. G., Worsnop, D. R., Davidovits, P., and Jimenez, J. L.: Particle morphology and density characterization by combined mobility and aerodynamic diameter measurements. Part 1: Theory, *Aerosol Sci. Technol.*, 38, 1185–1205, 2004.

DeCarlo, P.F., Kimmel, J.R., Trimborn, A., Northway, M.J., Jayne, J.T., Aiken, A.C., Gonin, M., Fuhrer, K., Horvath, T., Docherty, K.S., Worsnop, D.R., Jimenez, J.L.: Field-deployable, high-resolution, time-of-flight aerosol mass spectrometer, *Analyt. Chem.*, 78, 8281–8289, 2006.

Dobrusin, Z.: *Quantitative methods for the analysis of hydrocarbon oxidation products: a smog chamber study*, MSc., York University, 2012.

Dye, A., Rhead, M., Trier, C.: The quantitative morphology of roadside and background urban aerosol in Plymouth, UK, *Atmos. Environ.*, 34, 3139–3148, 2000.

Eddingsaas, N. C., Loza, C. L., Yee, L. D., Chan, M., Schilling, K. A., Chhabra, P. S., Seinfeld, J. H., and Wennberg, P. O.: α -pinene photooxidation under controlled chemical conditions – Part 2: SOA yield and composition in low- and high-NO_x environments, *Atmos. Chem. Phys.*, 12, 7413–7427, doi:10.5194/acp-12-7413-2012, 2012a.

Eddingsaas, N. C., Loza, C. L., Yee, L. D., Seinfeld, J. H., and Wennberg, P. O.: α -pinene photooxidation under controlled chemical conditions – Part 1: Gas-phase composition in low- and high-NO_x environments, *Atmos. Chem. Phys.*, 12, 6489–6504, doi:10.5194/acp-12-6489-2012, 2012b.

Edney, E.O., Kleindienst, T.E., Conner, T.S., McIver, C.D., Corse, E.W., Weathers, W.S.: Polar organic oxygenates in PM_{2.5} at a southeastern site in the United States, *Atmos. Environ.*, 37, 3947–3965, 2003.

Ehn, M., Thornton, J. A., Kleist, E., Sipilä, M., Junninen, H., Pullinen, I., Springer, M., Rubach, F., Tillmann, R., Lee, B., Lopez-Hilfiker, F., Andres, S., Acir, I.-H., Rissanen, M., Jokinen, T., Schobesberger, S., Kangasluoma, J., Kontkanen, J., Nieminen, T., Kurtén, T., Nielsen, L. B., Jørgensen, S., Kjaergaard, H. G., Canagaratna, M., Maso, M. D., Berndt, T., Petäjä, T., Wahner, A., Kerminen, V.-M., Kulmala, M., Worsnop, D. R., Wildt, J., and Mentel, T. F.: A large source of low-volatility secondary organic aerosol, *Nature*, 506, 476–479, doi:10.1038/nature13032, 2014.

Ellison, G. B., Tuck, A. F. and Vaida, V.: Atmospheric processing of organic aerosols, *J. Geophys. Res.*, 104(D9), 11633–11641, 1999.

Ehhalt D.H., and Rohrer F.: The impact of commercial aircraft on tropospheric ozone, In: the chemistry of the atmosphere – oxidants and oxidation in the Earth's atmosphere, A.R. Bandy (Ed.), The Royal Society of Chemistry, Special Publication No. 170, p. 105–120, 1995.

Finlayson-Pitts, B. J. and Pitts, J. N.: Chemistry of the upper and lower atmosphere: theory, experiments and applications, Academic Press, San Diego, CA, USA, 2000.

Forstner, H. J. L., Flagan, R. C., Seinfeld, J. H.: Secondary organic aerosol from the photooxidation of aromatic hydrocarbons: molecular composition, Environ. Sci. Technol., 31, 1345–1358, 1997.

Frey, M. M., Brough, N., France, J. L., Anderson, P. S., Traulle, O., King, M. D., Jones, A. E., Wolff, E. W., and Savarino, J.: The diurnal variability of atmospheric nitrogen oxides (NO and NO₂) above the Antarctic Plateau driven by atmospheric stability and snow emissions, Atmos. Chem. Phys., 13, 3045–3062, doi:10.5194/acp-13-3045-2013, 2013.

Garland, R. M., Elrod, M. J., Kincaid, K., Beaver, M. R., Jimenez, J. L. and Tolbert, M. a.: Acid-catalyzed reactions of hexanal on sulfuric acid particles: Identification of reaction products, Atmos. Environ., 40, 6863–6878, doi:10.1016/j.atmosenv.2006.07.009, 2006.

Good, A., Durden, D.A., and Kebarle, P.: Ion-molecule reactions in pure nitrogen and nitrogen containing traces of water at total pressures 0.5–4 Torr. kinetics of clustering reactions forming H⁺ (H₂O)_n, J. Chem. Phys. 52, 212–221, 1970.

Griffin, R. J., Cocker, D. R., Flagan, R. C., and Seinfeld, J. H.: Organic aerosol formation from the oxidation of biogenic hydrocarbons, J. Geophys. Res., 104, 3555–3567, doi:10.1029/1998JD100049, 1999.

Guenther A., Hewitt C.N., Erickson D., Fall R., Geron C., Graedel T., Harley P., Klinger L., Lerdau M., McKay W.A., Pierce T., Scholes B., Steinbrecher R., Tallamraju R., Taylor, J. and Zimmerman P.: A global model of natural volatile organic compound emissions, J. Geophys. Res., 100(D5): 8873–8892, 1995.

Hakola, H., Arey, J., Aschmann, S. and Atkinson, R.: Product formation from the gas-phase reactions of OH radicals and O₃ with a series of monoterpenes., J. Atmos. Chem., 18(1), 75–102, 1994.

Hallquist, M., Wenger, J. C., Baltensperger, U., Rudich, Y., Simpson, D., Claeys, M., Dommen, J., Donahue, N. M., George, C., Goldstein, A. H., Hamilton, J. F., Herrmann, H., Hoffmann, T., Iinuma, Y., Jang, M., Jenkin, M. E., Jimenez, J. L., Kiendler-Scharr, A., Maenhaut, W., McFiggans, G., Mentel, Th. F., Monod, A., Prévôt, A. S. H., Seinfeld, J. H., Surratt, J. D., Szmigielski, R., and Wildt, J.: The formation, properties and impact of secondary organic aerosol: current and emerging issues, *Atmos. Chem. Phys.*, 9, 5155–5236, doi:10.5194/acp-9-5155-2009, 2009.

Harrison, R. M. and Yin, J.: Particulate matter in the atmosphere: which particle properties are important for its effects on health?, *Sci. Total Environ.*, 249, 85–101, 2000.

Hatakeyama, S., Izumi, K., Fukuyama, T., Akimoto, H., and Washida, N.: Reactions of OH with α -pinene and β -pinene in air: Estimate of global CO production from the atmospheric oxidation of terpenes, *J. Geophys. Res.*, 96, 947–958, doi:10.1029/90JD02341, 1991.

Heald, C. L., Jacob, D. J., Park, R. J., Russell, L. M., Huebert, B. J., Seinfeld, J. H., Liao, H., and Weber, R. J.: A large organic aerosol source in the free troposphere missing from current models, *Geophys. Res. Lett.*, 32, L18809, doi:10.1029/2005GL023831, 2005.

Healy, R. M., Temime, B., Kuprovskyte, K. and Wenger, J. C.: Effect of relative humidity on gas/particle partitioning and aerosol mass yield in the photooxidation of p-xylene, *Environ. Sci. Technol.*, 43, 1884–1889, 2009.

Hoffmann, T., Klockow, D., Odum, J., Bowman, F., Collins, D., Flagan, R. C., and Seinfeld, J. H.: Formation of organic aerosols from the oxidation of biogenic hydrocarbons, *J. Atmos. Chem.*, 26, 189–222, doi:10.1023/A:1005734301837, 1997.

Hoffmann, T., Bandur, R., Hoffmann, S. and Warscheid, B.: On-line characterization of gaseous and particulate organic analytes using atmospheric pressure chemical ionization mass spectrometry, *Spectrochim. Acta, Part B At. Spectrosc.*, 57B(10), 1635–1647, 2002.

Hoyle, C. R., Boy, M., Donahue, N. M., Fry, J. L., Glasius, M., Guenther, A., Hallar, A. G., Huff Hartz, K., Petters, M. D., Petäjä, T., Rosenoern, T., and Sullivan, A. P.: A review of

the anthropogenic influence on biogenic secondary organic aerosol, *Atmos. Chem. Phys.*, 11, 321–343, doi:10.5194/acp-11-321-2011, 2011.

Jacob, D. J.: Introduction to atmospheric chemistry, Princeton University Press, New Jersey, 1999.

Jang, M. S., Carroll, B., Chandramouli, B., and Kamens, R. M.: Particle growth by acid-catalyzed heterogeneous reactions of organic carbonyls on preexisting aerosols, *Environ. Sci. Technol.*, 37, 3828–3837, 2003.

Jaoui, M. and Kamens, R. M.: Mass balance of gaseous and particulate products from β -pinene/O₃/air in the absence of light and β -Pinene/NO_x/air in the presence of natural sunlight, *J. Atmos. Chem.*, 45(2), 101–141, doi:10.1023/A:1024093710794, 2003.

Jayne, J. T., Leard, D. C., Zhang, X. F., Davidovits, P., Smith, K. A., Kolb, C. E. and Worsnop, D. R.: Development of an aerosol mass spectrometer for size and composition analysis of submicron particles, *Aerosol Sci. Technol.*, 33(1–2), 49–70, 2000.

Jenkin, M. E.: Modelling the formation and composition of secondary organic aerosol from α - and β -pinene ozonolysis using MCM v3, *Atmos. Chem. Phys.*, 4, 1741–1757, doi:10.5194/acp-4-1741-2004, 2004.

Johnson, D., Jenkin, M. E., Wirtz, K., and Martin-Reviejo, M.: Simulating the formation of secondary organic aerosol from the photooxidation of aromatic hydrocarbons, *Environ. Chem.*, 2, 35–48, 2005.

Jonsson, A. M., Hallquist, M. and Ljungstrom, E.: The effect of temperature and water on secondary organic aerosol formation from ozonolysis of limonene, delta(3)-carene and α -pinene, *Atmos. Chem. Phys.*, 8, 6541–6549, 2008.

Kalberer, M., Yu, J., Cocker, D. R., Flagan, R. C., and Seinfeld, J. H.: Aerosol formation in the cyclohexene-system, *Environ. Sci. Technol.*, 34, 4894–4901, 2000.

Kleindienst, T.E., Smith, D.F., Li, W., Edney, E.O., Driscoll, D.J., Speer, R.E., Weathers, W.S.: Secondary organic aerosol formation from the oxidation of aromatic hydrocarbons in the presence of dry submicron ammonium sulfate aerosol, *Atmos. Environ.*, 33, 3669–3681, 1999.

Kostenidou, E., Pathak, R. K., and Pandis, S. N.: An algorithm for the calculation of secondary organic aerosol density combining AMS and SMPS data, *Aerosol Sci. Tech.*, 41(11), 1002–1010, 2007.

Kourtchev, I., Ruuskanen, T. M., Keronen, P., Sogacheva, L., Dal, M. M., Reissell, A., Chi, X., Vermeylen, R., Kulmala, M., Maenhaut, W. and Claeys, M.: Determination of isoprene and α/β -pinene oxidation products in boreal forest aerosols from Hyytiälä, Finland: diel variations and possible link with particle formation events, *Plant Biol (Stuttg); Plant Biol. (Stuttgart, Ger.)*, 10(1), 138–149, 2008.

Krc, J.: DL-Pinic Acid-I, *Analyt. Chem.*, 25, 1420–1421, 1953.

Kroll, J. H., Ng, N. L., Murphy, S. M., Flagan, R. C. and Seinfeld, J. H.: Secondary organic aerosol formation from Isoprene photooxidation, *Environ. Sci. Technol.*, 40(6), 1869–1877, doi:10.1021/es0524301, 2006.

Kurtenbach, R., Kleffmann, J., Niedojadlo, A. and Wiesen, P.: Primary NO₂ emissions and their impact on air quality in traffic environments in Germany, *Environ. Sci. Eur.*, 24(1), 21, 2012.

Laramee, J.A., Cody, R.B.: Chemi-ionization and Direct Analysis in Real Time (DARTtm) Mass Spectrometry. In: Gross, M.L., Caprioli, R.M. (eds.) *The Encyclopedia of Mass Spectrometry*. Vol 6: Ionization Methods. Elsevier, Amsterdam, pp 377–387, 2007.

Larsen, B. R., Di Bella, D., Glasius, M., Winterhalter, R., Jensen, N. R. and Hjorth, J.: Gas-phase OH oxidation of monoterpenes: Gaseous and particulate products, *J. Atmos. Chem.*, 38(3), 231–276, doi:10.1023/A:1006487530903, 2001.

Lee, A., Goldstein, A. H., Kroll, J. H., Ng, N. L., Varutbangkul, V., Flagan, R. C. and Seinfeld, J. H.: Gas-phase products and secondary aerosol yields from the photooxidation of 16 different terpenes, *J. Geophys. Res.*, 111(D17), D17305–D17305, doi:10.1029/2006JD007050, 2006.

Leighton, P. A.: photochemistry of Air pollution, Academic press, New York and London, 1961.

Lewandowski, M., Jaoui, M., Kleindienst, T. E., Offenberg, J. H., and Edney, E. O.: Composition of PM_{2.5} during the summer of 2003 in Research Triangle Park, North Carolina, *Atmos. Environ.*, 41, 4073–4083, 2007.

Lide, D. R.: CRC Handbook of Chemistry and Physics, 84th Edition, 2003-2004, *Handb. Chem. Phys.*, 53, 2616, doi:10.1136/oem.53.7.504, 2003.

Liggio, J. and Li, S. M.: Reactive uptake of pinonaldehyde on acidic aerosols, *J. Geophys. Res. Atmos.*, 111, 1–12, doi:10.1029/2005JD006978, 2006.

Ligocki M. E. and Pankow J. F.: Assessment of adsorption/solvent extraction with polyzethane foam and adsorption/thermal desorption with Tenax-GC for the collection and analysis of ambient organic vapors. *Analyt. Chem.*, 57, 1138–1144, 1985.

Loza, C. L., Craven, J. S., Yee, L. D., Coggon, M. M., Schwantes, R. H., Shiraiwa, M., Zhang, X., Schilling, K. A., Ng, N. L., Canagaratna, M. R., Ziemann, P. J., Flagan, R. C., and Seinfeld, J. H.: Secondary organic aerosol yields of 12-carbon alkanes, *Atmos. Chem. Phys.*, 14, 1423–1439, doi:10.5194/acp-14-1423-2014, 2014.

Malloy, Q. G. J., Nakao, S., Qi, L., Austin, R., Stothers, C., Hagino, H. and Cocker ,III, D. R.: Real-time aerosol density determination utilizing a modified scanning mobility particle sizer aerosol particle mass analyzer System, *Aerosol Sci. Technol.*, 43(7), 673–678, doi:10.1080/02786820902832960, 2009.

Mao, J., Ren, X., Brune, W. H., Olson, J. R., Crawford, J. H., Fried, A., Huey, L. G., Cohen, R. C., Heikes, B., Singh, H. B., Blake, D. R., Sachse, G. W., Diskin, G. S., Hall, S. R., and Shetter, R. E.: Airborne measurement of OH reactivity during INTEX-B, *Atmos. Chem. and Phys.*, 9, 163-173, 10.5194/acp-9-163-2009, 2009.

Marcolli, C., Luo, B., and Peter, T.: Mixing of the organic aerosol fractions: Liquids as the thermodynamically stable phases, *J. Phys. Chem. A*, 108, 2216–2224, 2004.

Master Chemical Mechanism, MCM, version 3.2, <http://mcm.leeds.ac.uk/MCM/>

Mauderly, J. L. and Chow, J. C.: Health effects of organic aerosols, *Inhal. Toxicol.*, 20(3), 257–288, 2008.

McMurry, P. H., Wang, X., Park, K., and Ehara, K.: The Relationship between mass and mobility for atmospheric particles: A new technique for measuring particle density, *Aerosol Sci. Tech.*, 36(2), 227–238, 2002.

Medley, S.S.: Energetic ion mass analysis using a radio-frequency quadrupole filter, *Rev. Sci. Instrum.*, 49(8), 1978.

Mentel, Th. F., Wildt, J., Kiendler-Scharr, A., Kleist, E., Tillmann, R., Dal Maso, M., Fisseha, R., Hohaus, Th., Spahn, H., Uerlings, R., Wegener, R., Griffiths, P. T., Dinar, E., Rudich, Y., and Wahner, A.: Photochemical production of aerosols from real plant emissions, *Atmos. Chem. Phys.*, 9, 4387–4406, doi:10.5194/acp-9-4387-2009, 2009.

Mikhailov, E., Vlasenko, S., Martin, S. T., Koop, T., Poeschl, U.: Amorphous and crystalline aerosol particles interacting with water vapor: conceptual framework and experimental evidence for restructuring, phase transitions and kinetic limitations, *Atmos. Chem. Phys.*, 9, 9491–9522, 2009.

Miller, K. A., Siscovick, D. S., Sheppard, L., Shepherd, K., Sullivan, J. H., Anderson, G. L., and Kaufman, J. D.: Long-term exposure to air pollution and incidence of cardiovascular events in women. *New England Journal of Medicine*, 356(5):447–458, 2007.

- Morris, R. E., McNally, D. E., Tesche, T. W., Tonnesen, G., Boylan, J. W., and Brewer, P.: Preliminary evaluation of the community multiscale air, quality model for 2002 over the southeastern United States, *J. Air Waste Manage. Assoc.*, 55, 1694–1708, 2005.
- Müller J.-F.: Geographical distribution and seasonal variation of surface emissions and deposition velocities of atmospheric trace gases. *J. Geophys. Res.* 97(D4): 3787–3804, 1992.
- Ng, N. L., Chhabra, P. S., Chan, A. W. H., Surratt, J. D., Kroll, J. H., Kwan, A. J., McCabe, D. C., Wennberg, P. O., Sorooshian, A., Murphy, S. M., Dalleska, N. F., Flagan, R. C., and Seinfeld, J. H.: Effect of NO_x level on secondary organic aerosol (SOA) formation from the photooxidation of terpenes, *Atmos. Chem. Phys.*, 7(4), 5159–5174, doi:10.5194/acp-7-5159-2007, 2007a.
- Ng, N. L., Kroll, J. H., Chan, A. W. H., Chhabra, P., Flagan, R. C. and Seinfeld, J. H.: Secondary organic aerosol formation from m-xylene, toluene, and benzene. *Atmos. Chem. Phys.* 7, 3909–3922, doi:10.5194/acp-7-3909-2007, 2007b.
- Noyes, W. A.: n-butyl nitrite. *Organic Syntheses*, 16:7–8, 1936.
- Odum, J. R., Hoffmann, T., Bowman, F., Collins, D., Flagan, R. C., and Seinfeld, J. H.: Gas/particle partitioning and secondary organic aerosol yields, *Environ. Sci. Technol.*, 30, 2580–2585, 1996.
- Okada, K. and Heintzenberg, J.: Size distribution, state of mixture and morphology of urban aerosol particles at given electrical mobilities, *J. Aerosol Sci.*, 34, 1539–1553, 2003.
- Pandis, S. N., Paulson, S. E., Seinfeld, J. H., and Flagan, R. C.: Aerosol formation in the photooxidation of isoprene and β -pinene, *Atmos. Environ. A-Gen.*, 25, 997–1008, doi:10.1016/0960-1686(91)90141-S, 1991.
- Pankow, J. F.: An absorption model of the gas/aerosol partitioning involved in the formation of secondary organic aerosol, *Atmos. Environ.*, 28(6), 189–193, 1994.

Pathak, R. K., Stanier, C. O., Donahue, N. M. and Pandis, S. N.: Ozonolysis of α -pinene at atmospherically relevant concentrations: Temperature dependence of aerosol mass fractions (yields), *J. Geophys. Res.*, 112(D3), D03201–D03201, doi:10.1029/2006JD007436, 2007.

Pollack, I. B., Ryerson, T. B., Trainer, M., Neuman, J. A., Roberts, J. M., and Parrish, D. D.: Trends in ozone, its precursors, and related secondary oxidation products in Los Angeles, California: A synthesis of measurements from 1960 to 2010, *J. Geophys. Res.-Atmos.*, 118, 5893–5911, doi:10.1002/jgrd.50472, 2013.

Pope III, C. A. and Dockery, D. W.: Health effects of fine particulate air pollution: Lines that connect, *J. AirWaste Manage.*, 56, 709–742, 2006.

Presto, A. A., Huff Hartz, K. E., and Donahue, N. M.: Secondary organic aerosol production from terpene ozonolysis. 2. Effect of NO_x concentration, *Environ. Sci. Technol.*, 39, 7046–7054, doi:10.1021/es050400s, 2005.

Prinn, R.G., Huang, J., Weiss, R.F., Cunnold, D.M., Fraser, P.J., Simmonds, P.G., McCulloch, A., Harth, C., Salameh, P., O'Doherty, S., Wang, R.H.J., Porter, L., Miller, B.R.: Evidence for substantial variations of atmospheric hydroxyl radicals in the past two decades, *Science* 292, 1882–1887, 2001.

Qi, L., Nakao, S., Malloy, Q., Warren, B., Cocker, David R.: Can secondary organic aerosol formed in an atmospheric simulation chamber continuously age?, *Atmos. Environ.*, 44, 2990–2996, 2010.

Renbaum-Wolff, L., Grayson, J. W., Bateman, A. P., Kuwata, M., Sellier, M., Murray, B. J., Shilling, J. E., Martin, S. T. and Bertram, A. K.: Viscosity of α -pinene secondary organic material and implications for particle growth and reactivity., *Proc. Natl. Acad. Sci. U. S. A.*, 110(20), 8014–9, doi:10.1073/pnas.1219548110, 2013.

Robinson, A. L., Donahue, N. M., Shrivastava, M. K., Weitkamp, E. A., Sage, A. M., Grieshop, A. P., Lane, T. E., Pierce, J. R. and Pandis, S. N.: Rethinking organic aerosols: semivolatile emissions and photochemical aging, *Science*, 315(5816), 1259–1262, 2007.

Rogge, W.F., Hildemann, L.M., Mazurek, M.A., Cass, G.R., Simoneit, B.R.T.: Sources of fine organic aerosol. 3. Road dust, tire debris, and organometallic brake lining dust: roads as sources and sinks, *Environ. Sci. Technol.*, 27, 1892–1904, 1993.

Rudich, Y.: Laboratory perspectives on the chemical transformations of organic matter in atmospheric particles, *Chem. Rev.*, 103(12), 5097–5124, 2003.

Saathoff, H., Naumann, K.-H., Moehler, O., Jonsson, a M., Hallquist, M., Kiendler-Scharr, a, Mentel, T. F., Tillmann, R. and Schurath, U.: Temperature dependence of yields of secondary organic aerosols from the ozonolysis of alpha-pinene and limonene, *Atmos. Chem. Phys.*, 9(5), 1551–1577, doi:10.5194/acp-9-1551-2009, 2009.

Sarrafzadeh, M., Wildt, J., Pullinen, I., Springer, M., Kleist, E., Tillmann, R., Schmitt, S. H., Wu, C., Mentel, T. F., Zhao, D., Hastie, D. R., and Kiendler-Scharr, A.: Impact of NO_x and OH on secondary organic aerosol formation from β-pinene photooxidation, *Atmos. Chem. Phys.*, 16, 11237–11248, doi:10.5194/acp-16-11237-2016, 2016.

Seinfeld, J. H. and Pandis, S. N.: *Atmospheric chemistry and physics: From Air pollution to climate change*, Wiley-Interscience, New York, 2006.

Seinfeld, J. H. and Pankow, J. F.: Organic atmospheric particulate material, *Annu. Rev. Phys. Chem.*, 54, 121–140, 2003.

Sheehan, P. E. and Bowman, F. M.: Estimated effects of temperature on secondary organic aerosol concentrations, *Environ. Sci. Technol.*, 35, 2129–2135, 2001.

Shilling, J. E., Chen, Q., King, S. M., Rosenoern, T., Kroll, J. H., Worsnop, D. R., McKinney, K. A., Martin, S. T.: Particle mass yield in secondary organic aerosol formed by the dark ozonolysis of alpha-pinene, *Atmos. Chem. Phys.*, 8, 2073–2088, 2008.

Song, C., Na, K., and Cocker III, D. R.: Impact of the hydrocarbon to NO_x ratio on secondary organic aerosol formation, *Environ. Sci. Technol.*, 39, 3143–3149, 2005.

Song, C., Na, K., Warren, B., Malloy, Q., and Cocker, D. R.: Impact of propene on secondary organic aerosol formation from m-xylene, *Environ. Sci. Technol.*, 41, 6990–6995, doi:10.1021/Es062279a, 2007.

Surratt, J. D., Murphy, S.M., Kroll, J. H., Ng, N. L., Hildebrandt, L., Sorooshian, A., Szmigielski, R., Vermeylen, R., Maenhaut, W., Claeys, M., Flagan, R. C., and Seinfeld, J. H.: Chemical composition of secondary organic aerosol formed from the photooxidation of Isoprene, *J. Phys. Chem. A*, 110(31), 9665–9690, 2006.

Sutter, B., Bemer, D., Appert-Collin, J.-C., Thomas, D. and Midoux, N.: Evaporation of liquid semi-volatile aerosols collected on fibrous filters, *Aerosol Sci. Technol.*, 44(5), 395–404, doi:10.1080/02786821003674244, 2010.

TEOM series 1400a, operation manual, 2001, Rupprecht & Patashnick Co., Inc. 25 Corporate Circle Albany, NY 12203 USA.

Thornton, J. and Abbatt, J.: N₂O₅ reaction on submicron sea salt aerosol: Kinetics, products, and the effect of surface active organics, *J. Phys. Chem. A*, 109, 10004–10012, 2005.

Thornton, J., Braban, C., and Abbatt, J.: N₂O₅ hydrolysis on submicron organic aerosols: the effect of relative humidity, particle phase, and particle size, *Phys. Chem. Chem. Phys.*, 5, 4593–4603, 2003.

TSI (2002). Model3071A electrostatic classifier. TSI Incorporated, 500 Cardigan Road St. Paul MN 55126 USA, f edition.

Twomey, S. A., Piepgrass, M. and Wolfe, T.L.: An assessment of the impact of pollution on global cloud albedo, *Tellus B*, 36B, 356, 1984.

Vanderhoff, P. A., Thompson, H. W., and Lalancette, R. A.: Structure of (+/-)-Cis-pinonic acid, *Acta Crystallogr. C*, 42, 1766–1769, 1986.

Virtanen, A., Joutsensaari, J., Koop, T., Kannosto, J., Yli-Pirila, P., Leskinen, J., Makela, J. M., Holopainen, J. K., Poeschl, U., Kulmala, M., Worsnop, D. R. and Laaksonen, A.: An amorphous solid state of biogenic secondary organic aerosol particles, *Nature*, 467(7317), 824–827, doi:10.1038/nature09455, 2010.

Volkamer, R., Jimenez, J. L., San Martini, F., Dzepina, K., Zhang, Q., Salcedo, D., Molina, L. T., Worsnop, D. R., and Molina, M. J.: Secondary organic aerosol formation from anthropogenic air pollution: Rapid and higher than expected, *Geophys. Res. Lett.*, 33, L17811, doi:10.1029/2006GL026899, 2006.

Von Hessberg, C., von Hessberg, P., Poeschl, U., Bilde, M., Nielsen, O. J. and Moortgat, G. K.: Temperature and humidity dependence of secondary organic aerosol yield from the ozonolysis of β -pinene, *Atmos. Chem. Phys.*, 9, 3583-3599, 2009.

Warscheid, B. and Hoffmann, T.: Structural elucidation of monoterpene oxidation products by ion trap fragmentation using on-line atmospheric pressure chemical ionisation mass spectrometry in the negative ion mode, *Rapid Commun. Mass Spectrom.*, 15, 2259–2272, 2001.

Warscheid, B., Kuckelmann, U. and Hoffmann, T.: Direct quantitative analysis of organic compounds in the gas and particle phase using a modified atmospheric pressure chemical ionization source in combination with ion trap mass spectrometry, *Anal. Chem.*, 75(6), 1410–1417, doi:10.1021/ac025788d, 2003.

Wildt, J., Mentel, T. F., Kiendler-Scharr, A., Hoffmann, T., Andres, S., Ehn, M., Kleist, E., M \ddot{u} sgen, P., Rohrer, F., Rudich, Y., Springer, M., Tillmann, R., and Wahner, A.: Suppression of new particle formation from monoterpene oxidation by NO $_x$, *Atmos. Chem. Phys.*, 14, 2789–2804, doi:10.5194/acp-14-2789-2014, 2014.

Wirtz, K. and Martin-Reviejo, M.: Density of secondary organic aerosols, *J. Aerosol Sci.*, 34, S223–S224, 2003.

Wisthaler, A., Jensen, N. R., Winterhalter, R., Lindinger, W., and Hjorth, J.: Measurements of acetone and other gas phase product yields from the OH-initiated oxidation of terpenes by proton-transfer-reaction mass spectrometry (PTR-MS). *Atmos. Environ.*, 35(35), 6181–6191, 2001.

Xiong, C. and Friedlander, S.: Morphological properties of atmospheric aerosol aggregates, *Proc. Natl. Acad. Sci. U. S. A.*, 98, 11851–11856, 2001.

Xu, L., Kollman, M. S., Song, C., Shilling, J. E., and Ng, N. L.: Effects of NO_x on the volatility of secondary organic aerosol from isoprene photooxidation, *Environ. Sci. Technol.*, 48, 2253–2262, 10.1021/es404842g, 2014.

Yasmeen, F., Vermeylen, R., Szmigielski, R., Iinuma, Y., Boege, O., Herrmann, H., Maenhaut, W. and Claeys, M.: Terpenylic acid and related compounds: precursors for dimers in secondary organic aerosol from the ozonolysis of α - and β -pinene, *Atmos. Chem. Phys.*, 10(19), 9383–9392, doi:10.5194/acp-10-9383-2010, 2010.

Yu, S. C., Mathur, R., Schere, K., Kang, D. W., Pleim, J., Young, J., Tong, D., Pouliot, G., McKeen, S. A., and Rao, S. T.: Evaluation of real-time PM_{2.5} forecasts and process analysis for PM_{2.5} formation over the eastern United States using the Eta-CMAQ forecast model during the 2004 ICARTT study, *J. Geophys. Res. Atmos.*, 113, D06204, doi:10.1029/2007JD009226, 2008.

Zelenyuk, A., Yang, J., Song, C., Zaveri, R. A., and Imre, D.: A new real-time method for determining particles' sphericity and density: Application to secondary organic aerosol formed by ozonolysis of α -Pinene, *Environ. Sci. Technol.*, 42(21), 8033–8038, 2008.

Zhang, S.-H., Shaw, M., Seinfeld, J. H., and Flagan, R. C.: Photochemical aerosol formation from α -pinene and β -pinene, *J. Geophys. Res.*, 97, 20717–20729, doi:10.1029/92JD02156, 1992.

Zou, Y., Deng, X. J., Zhu, D., Gong, D. C., Wang, H., Li, F., Tan, H. B., Deng, T., Mai, B. R., Liu, X. T., and Wang, B. G.: Characteristics of 1 year of observational data of VOCs,

NO_x and O₃ at a suburban site in Guangzhou, China, *Atmos. Chem. Phys.*, 15, 6625–6636, doi:10.5194/acp-15-6625-2015, 2015.

Appendices

Appendix A. Dilution Correction

The quantitative results obtained from the GC-FID, NO_x analyzer and the SMPS in the York University have been corrected for dilution caused by the continuous sampling through instruments and the purified Aadco makeup air input. An example of the calculation for the sampled particle mass concentration is given in Equation A.1.

$$[PM]_{sampled\ at\ t} = \frac{\Delta t \cdot F_D \cdot [PM]_t}{V} + [PM]_{t-\Delta t} \quad (A.1)$$

Where Δt is the time between measurements (e.g. 5 min), F_D is the diluting flow rate (L min⁻¹), $[PM]_t$ is the particle mass concentration at time t , V is the chamber volume (8 m³) and $[PM]_{t-\Delta t}$ is the particle mass concentration in the previous time frame. The calculated $[PM]_{sampled}$ in a given time frame was then added to the measured PM value of that time frame as a correction.

Appendix B. Determination of J(O¹D)

The J(O¹D) was determined by setting up the rate equation for the CSTR for only ozone and moisturized air (no VOC or NO_x in the chamber) which is presented in Equation B.1.

$$\frac{d[O_3]}{dt} = \frac{F}{V}([O_3]_{in} - [O_3]) - (J(O^1D) \cdot [O_3] \cdot f) \quad (B.1)$$

Where V is the volume of the chamber and F is the total air flow through the chamber. $[O_3]_{in}$ and $[O_3]$ are the concentrations of ozone in the inlet air and in the chamber respectively. f is the fraction of O¹D atoms reacting with water which is calculated according to Eq. B.2.

$$f = \frac{k^{O^1D+H_2O} \cdot [H_2O]}{(k^{O^1D+H_2O} \cdot [H_2O] + k^{O^1D+O_2} \cdot [O_2] + k^{O^1D+N_2} \cdot [N_2])} \quad (B.2)$$

Apart from reaction of O(¹D) atoms with water vapor, O(¹D) atoms undergo relaxation to ground state O(³P) via collisions with molecular oxygen or nitrogen (RB.1).



Ground state O(³P) atoms then react directly with molecular oxygen (O₂) leading to ozone formation (RB.2).



Therefore, the decay of O₃ had to be corrected for f . The following rate constants (Atkinson et al., 2004) were used to calculate f :

$$k^{O^{1D}+H_2O} = 2.2 \times 10^{-10}, k^{O^{1D}+O_2} = 4.0 \times 10^{-11}, k^{O^{1D}+N_2} = 3.1 \times 10^{-11} \text{ cm}^3 \text{ molecule}^{-1} \text{ s}^{-1}$$

At the water content in the JPAC, f is in the range of ~ 0.1 . Under steady state conditions solving the differential equation for $J(O^1D)$ results in:

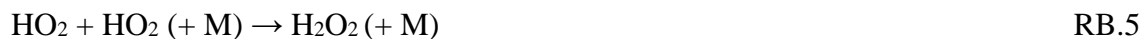
$$J(O^1D) = \frac{F}{V} \frac{([O_3]_{in} - [O_3])}{[O_3] \cdot f} \quad (B.3)$$

As a first approximation, $J(O^1D)$ can be calculated using the decay of O_3 in the chamber when the TUV lamp is switched on (Eq. B.3). This is a first approximation since additional losses of O_3 occur through reactions with OH and HO_2 radicals (RB.3-4).



These chain reactions will deplete O_3 in the chamber in addition to O_3 photolysis. Hence the exact $J(O^1D)$ value was calculated by a model developed by Thomas Mentel.

The results were also controlled by adding high amounts of CO in the JPAC. Adding CO causes conversion of OH to HO_2 and thus, at high HO_2 concentrations the decrease of O_3 is strongly reduced as the HO_2 is decreased proportionally due to Reaction RB.5.



Thus, the obtained modeled value of $J(O^1D)$ is reliable.

The linearity of $J(O^1D)$ was also controlled in the JPAC. This was done in a good approximation by measuring the decay of O_3 at different TUV gap widths and then calculating the $J(O^1D)$ value. In addition, by adding VOC and determining the OH

concentrations, it was found that the production rate of OH is proportional to $J(O^1D)$ as long as the other quantities are held constant. The calculated $J(O^1D)$ values in this study was according to this linearity.

Appendix C. Nitrate Radical (NO₃) Concentration Modelling

Accuchem model

1111

1, NO + O₃ = NO₂ + O₂ 1.95e-14

2, NO₂ + O₃ = NO₃ + O₂ 3.17e-17

3, NO₃ + NO₂ = N₂O₅ 1.0e-12

4, N₂O₅ = NO₃ + NO₂ 2.49e-11

END

O₃, 1.5e14

NO, 2.0e14

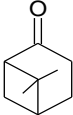
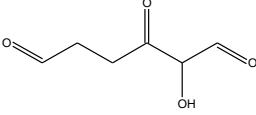
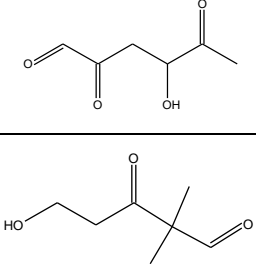
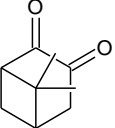
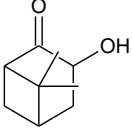
END

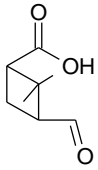
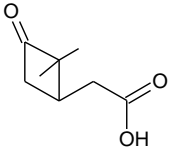
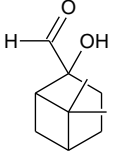
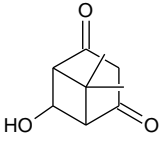
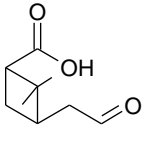
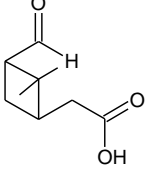
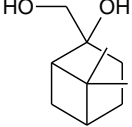
0.001

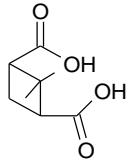
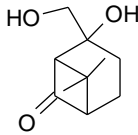
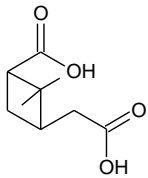
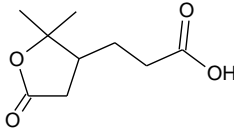
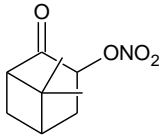
1e5

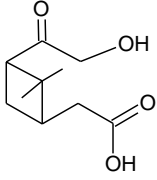
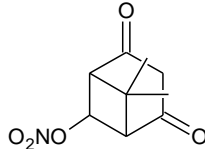
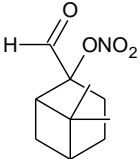
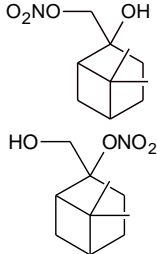
Appendix D. Summary of Identified Reaction Products

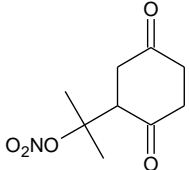
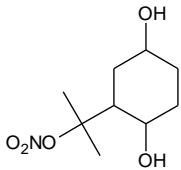
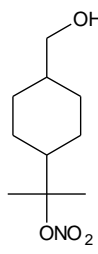
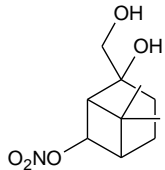
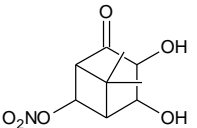
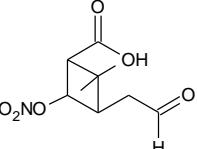
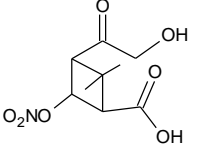
Table D.1 Summary of the molecular formula, m/z, functional groups, structure and NO_x sensitivity of identified products in the gas and particle phase. The exact masses as well as the confirmed molecular formula based on the exact mass for particle phase products are written in blue. The products that are indicated by * exist predominantly in the particle phase.

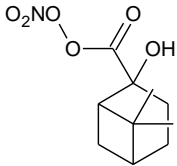
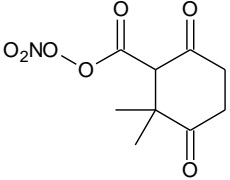
m/z [M+H] ⁺	Molecular Formula [M]	Compound Name	Structure	Evidence	NO _x Sensitivity
139 139.07	C ₉ H ₁₄ O	nopinone		MS/MS Fingerprint confirmation	NO _x insensitive
145* 145.047	C ₆ H ₈ O ₄	C6-hydroxy keto-aldehyde (multiple isomers)		MS/MS fragmentation pattern	Enhanced under low NO _x
	C ₇ H ₁₂ O ₃	C7-hydroxy keto-aldehyde			
153 153.093	C ₉ H ₁₂ O ₂	oxo-nopinone (multiple isomers)		MS/MS fragmentation pattern	Enhanced under high NO _x
155 155.071	C ₉ H ₁₄ O ₂	hydroxy nopinone ¹ (multiple isomers)		MS/MS fragmentation pattern	Enhanced under low NO _x

157 157.084	$C_8H_{12}O_3$	norpinalic acid ¹		MS/MS fragmentation pattern (SRM 157→111)	NO _x insensitive in the particle phase Enhanced under high NO _x in the gas phase
	$C_8H_{12}O_3$	C8-keto acid			
167 167.105	$C_{10}H_{14}O_2$	unknown	unknown	-----	NO _x insensitive
169* 169.087	$C_{10}H_{16}O_2$	C10-hydroxy aldehyde (multiple isomers)		MS/MS fragmentation pattern	Enhanced under low NO _x
	$C_9H_{12}O_3$	hydroxy oxo- nopinone (multiple isomers)			
171 171.104	$C_9H_{14}O_3$	pinalic 3-acid		MS/MS fragmentation pattern (SRM 171→125)	Enhanced under low NO _x
	$C_9H_{14}O_3$	pinalic 4-acid			
	$C_{10}H_{18}O_2$	C10-dihydroxy (multiple isomers)		MS/MS fragmentation pattern	undetermined

173* 173.087	$C_8H_{12}O_4$	norpinic acid ¹		MS/MS fragmentation pattern	Enhanced under low NO_x
185 185.083	$C_{10}H_{16}O_3$	C10-dihydroxy carbonyl ³ (multiple isomers)		MS/MS fragmentation pattern	NO_x insensitive
	$C_9H_{12}O_4$	carboxylic acid	unknown	MS/MS fragmentation pattern (+) and (-) MSMS	
187* 187.096	$C_9H_{14}O_4$	pinic acid ¹		MS/MS Fingerprint Confirmation (+) and (-) MSMS	Enhanced under low NO_x
	$C_9H_{14}O_4$	homoterpenylic acid ²		MS/MS fragmentation pattern (+) and (-) MSMS	undetermined
199 199.096	$C_{10}H_{14}O_4$	carboxylic acid	unknown	MS/MS fragmentation pattern (+) and (-) MSMS	Enhanced under low NO_x
200* 200.101	$C_9H_{13}NO_4$	nitroxy nopinone		MS/MS fragmentation pattern	NO_x insensitive

		(multiple isomers)			
201* 201.109	$C_{10}H_{16}O_4$	C10-hydroxy pinonic acid ¹		MS/MS fragmentation pattern (+) and (-) MS/MS	Enhanced under low NO _x
	C9 max	carboxylic acid	unknown		
203* 203.09	$C_9H_{14}O_5$	carboxylic acid	unknown	MS/MS fragmentation pattern (+) and (-) MS/MS	undetermined
214 214.102	$C_9H_{11}NO_5$	C9-bicyclic dioxo nitrate (multiple isomers)		MS/MS fragmentation pattern	Enhanced under low NO _x
	$C_{10}H_{15}NO_4$	C10-aldehyde nitrate (multiple isomers)			
216 216.12	$C_{10}H_{17}NO_4$	C10-bicyclic hydroxy nitrate ³ (multiple isomers)		MS/MS fragmentation pattern	NO _x insensitive

	$C_9H_{13}NO_5$	C9-monocyclic dioxo nitrate (multiple isomers)			
218* 218.14	$C_9H_{15}NO_5$	C9-dihydroxy nitrate (multiple isomers)		MS/MS fragmentation pattern	Enhanced under high NO_x
	$C_{10}H_{19}NO_4$	C10-monocyclic hydroxy nitrate (multiple isomers)			
232 232.12	$C_{10}H_{17}NO_5$	C10-dihydroxy nitrate ³ (multiple isomers)		MS/MS fragmentation pattern	Enhanced under high NO_x in the gas phase Enhanced under low NO_x in the particle phase
	$C_9H_{13}NO_6$	1- C9-dihydroxy-oxo nitrate ⁴			
		2- C9-oxo nitrate acid ⁴			
		3- C9-dioxo hydroxy nitrate ⁴			

246* 246.10	$C_{10}H_{15}NO_6$	C10-PAN (multiple isomers)		MS/MS fragmentation pattern	Enhanced under low NO_x
	$C_9H_{12}NO_7$	C9-PAN (multiple isomers)			
260*	$C_{10}H_{13}NO_7$	nitrate	unknown	MS/MS fragmentation pattern	Enhanced under low NO_x

¹ Identified by Larsen et al. (2001) during the particle phase β -pinene/OH reaction.

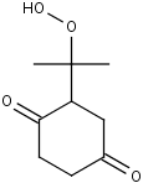
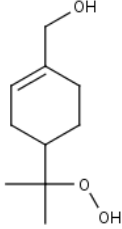
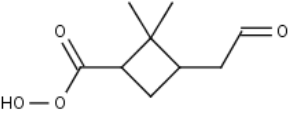
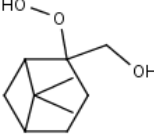
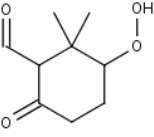
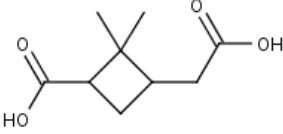
² Proposed by Claeys et al. (2009).

³ Proposed by Aschmann et al. (1998).

⁴ Proposed by Auld (2009).

Appendix E. Potential Products for m/z 187

Table E.1 List of potential products for the m/z 187, obtained from the Master Chemical Mechanism (MCM).

Structure	Chemical Composition	Structure	Chemical Composition
	peroxide		peroxide
	pinalic peroxy acid ¹		peroxide
	peroxide		pinic acid ²

¹Identified during the gas phase β -pinene photooxidation by Auld (2009).

²Identified in this study from β -pinene photooxidation in the particle phase.